U.S. Department
of Transportation

**Federal Railroad
Administration**

**Office of Research,
Development and Technology
Washington, DC 20590**

Side Impact Test and Analyses of a DOT-113C120W9 Tank Car with Cryogenic Lading

DOT/FRA/ORD-24-02

Final Report | January 2024

REPORT DOCUMENTATION PAGE	*Form Approved* *OMB No. 0704-0188*

1. REPORT DATE *(DD-MM-YYYY)* 1/16/2024	**2. REPORT TYPE** Technical Report	**3. DATES COVERED** *(From - To)* May 2022

4. TITLE AND SUBTITLE Side Impact Test and Analyses of a DOT-113C120W9 Tank Car with Cryogenic Lading	**5a. CONTRACT NUMBER** DTFR53-11-D-00008 TTCI-11-033
	5b. GRANT NUMBER
	5c. PROGRAM ELEMENT NUMBER
6. AUTHOR(S) Shaun Eshraghi** – ORCID: 0000-0002-8152-0838 Steve Belport* – ORCID: 0000-0002-8212-9873 Michael Carolan** – ORCID: 0000-0002-8758-5739 Shawn Trevithick* – ORCID: 0000-0001-6155-5526 Aswani Krishnamurthy** – ORCID: 0000-0003-3116-7797	**5d. PROJECT NUMBER**
	5e. TASK NUMBER 693JJ620F000040
	5f. WORK UNIT NUMBER
7. PERFORMING ORGANIZATION NAME(S) AND ADDRESS(ES) *MxV Rail, Inc. 55500 DOT Road, Pueblo, CO 81001-0130 **Volpe National Transportation Systems Center 55 Broadway, Cambridge, MA 02142	**8. PERFORMING ORGANIZATION REPORT NUMBER**
9. SPONSORING/MONITORING AGENCY NAME(S) AND ADDRESS(ES) U.S. Department of Transportation Federal Railroad Administration Office of Railroad Policy and Development Office of Research, Development, and Technology (RD&T) Washington, DC 20590	**10. SPONSOR/MONITOR'S ACRONYM(S)**
	11. SPONSOR/MONITOR'S REPORT NUMBER(S) DOT/FRA/ORD-24-02

12. DISTRIBUTION/AVAILABILITY STATEMENT
This document is available to the public through the FRA Web site at http://www.fra.dot.gov

13. SUPPLEMENTARY NOTES
COR: Francisco González, III

14. ABSTRACT

As part of a research program to improve transportation safety for tank cars carrying hazardous materials, the Federal Railroad Administration (FRA) sponsored Transportation Technology Center, Inc. (now MxV Rail) and the Volpe National Transportation Systems Center (Volpe) to test and analyze the side impact puncture performance of a DOT-113 tank car filled with cryogenic liquid nitrogen (LN2). The research team conducted the impact test on May 14, 2022. All test requirements were met. Researchers performed both pre-test and post-test analyses of the impact response to evaluate, validate, and improve puncture modeling capabilities. This was the last in a series of four tests on DOT-113 tank cars and tank car surrogates sponsored by FRA.

15. SUBJECT TERMS
Impact test, DOT-113C120W9 tank car, tank car performance, transportation safety, tank car, hazardous materials, rolling stock, test

16. SECURITY CLASSIFICATION OF:			**17. LIMITATION OF ABSTRACT**	**18. NUMBER OF PAGES**	**19a. NAME OF RESPONSIBLE PERSON** Francisco González, III
a. REPORT	**b. ABSTRACT**	**c. THIS PAGE**			
Unclassified	Unclassified	Unclassified		144	**19b. TELEPHONE NUMBER** *(Include area code)* 202-493-6076

METRIC/ENGLISH CONVERSION FACTORS

ENGLISH TO METRIC

LENGTH (APPROXIMATE)

1 inch (in) = 2.5 centimeters (cm)
1 foot (ft) = 30 centimeters (cm)
1 yard (yd) = 0.9 meter (m)
1 mile (mi) = 1.6 kilometers (km)

AREA (APPROXIMATE)

1 square inch (sq in, in^2) = 6.5 square centimeters (cm^2)
1 square foot (sq ft, ft^2) = 0.09 square meter (m^2)
1 square yard (sq yd, yd^2) = 0.8 square meter (m^2)
1 square mile (sq mi, mi^2) = 2.6 square kilometers (km^2)
1 acre = 0.4 hectare (he) = 4,000 square meters (m^2)

MASS - WEIGHT (APPROXIMATE)

1 ounce (oz) = 28 grams (gm)
1 pound (lb) = 0.45 kilogram (kg)
1 short ton = 2,000 pounds (lb) = 0.9 tonne (t)

VOLUME (APPROXIMATE)

1 teaspoon (tsp) = 5 milliliters (ml)
1 tablespoon (tbsp) = 15 milliliters (ml)
1 fluid ounce (fl oz) = 30 milliliters (ml)
1 cup (c) = 0.24 liter (l)
1 pint (pt) = 0.47 liter (l)
1 quart (qt) = 0.96 liter (l)
1 gallon (gal) = 3.8 liters (l)
1 cubic foot (cu ft, ft^3) = 0.03 cubic meter (m^3)
1 cubic yard (cu yd, yd^3) = 0.76 cubic meter (m^3)

TEMPERATURE (EXACT)

[(x-32)(5/9)] °F = y °C

METRIC TO ENGLISH

LENGTH (APPROXIMATE)

1 millimeter (mm) = 0.04 inch (in)
1 centimeter (cm) = 0.4 inch (in)
1 meter (m) = 3.3 feet (ft)
1 meter (m) = 1.1 yards (yd)
1 kilometer (km) = 0.6 mile (mi)

AREA (APPROXIMATE)

1 square centimeter (cm^2) = 0.16 square inch (sq in, in^2)
1 square meter (m^2) = 1.2 square yards (sq yd, yd^2)
1 square kilometer (km^2) = 0.4 square mile (sq mi, mi^2)
10,000 square meters (m^2) = 1 hectare (ha) = 2.5 acres

MASS - WEIGHT (APPROXIMATE)

1 gram (gm) = 0.036 ounce (oz)
1 kilogram (kg) = 2.2 pounds (lb)
1 tonne (t) = 1,000 kilograms (kg)
= 1.1 short tons

VOLUME (APPROXIMATE)

1 milliliter (ml) = 0.03 fluid ounce (fl oz)
1 liter (l) = 2.1 pints (pt)
1 liter (l) = 1.06 quarts (qt)
1 liter (l) = 0.26 gallon (gal)
1 cubic meter (m^3) = 36 cubic feet (cu ft, ft^3)
1 cubic meter (m^3) = 1.3 cubic yards (cu yd, yd^3)

TEMPERATURE (EXACT)

[(9/5) y + 32] °C = x °F

QUICK INCH - CENTIMETER LENGTH CONVERSION

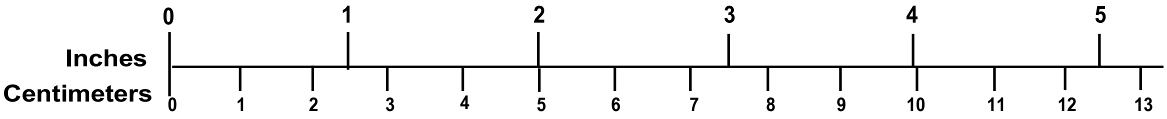

QUICK FAHRENHEIT - CELSIUS TEMPERATURE CONVERSIO

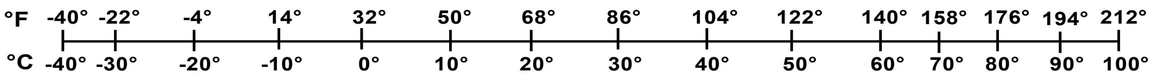

For more exact and or other conversion factors, see NIST Miscellaneous Publication 286, Units of Weights and Measures. Price $2.50 SD Catalog No. C13 10286

Updated 6/17/98

Acknowledgements

The tests described in this report were performed by Transportation Technology Center, Inc. (now MxV Rail) and the analyses described in this report were performed by the Volpe National Transportation Systems Center (Volpe) under FRA sponsorship.

The authors of this report gratefully acknowledge the cooperation and assistance of Scott Nason and Scott Blegen of Chart Industries in providing engineering drawings and design information for the Department of Transportation (DOT)-113 tank car used in this test. The authors also gratefully acknowledge the assistance provided by Union Tank Car in obtaining design information for the outer tank of the tank car used in this test.

The authors gratefully acknowledge the cooperation and assistance of John Burgess and Scott Tuttle of Airgas regarding the filling procedures and post-test procedures for testing with liquid nitrogen (LN2).

Pre-impact material testing of the outer tank's steel was performed by Rocky Mountain Engineering and Materials Technology, Inc. The authors gratefully acknowledge work done by John N. Schwartzberg, P.E., in planning and performing these material tests.

Pre-impact material testing of the inner tank's steel was performed by Composite Technology Development, Inc. The authors gratefully acknowledge work done by Mark Haynes and Paul Fabian in planning and performing these material tests.

The authors gratefully acknowledge the technical assistance of Volpe Senior Engineer Benjamin Perlman. The authors gratefully acknowledge the data and image processing and analysis performed by Engineering Student Trainee Andrew Skrzypczak, as well as his thoughtful comments on this report.

The authors gratefully acknowledge technical discussions and assistance in developing the testing plan from Mark Maday of FRA's Office of Railroad Safety and technical discussions and assistance in test planning from Karl Alexy and Charles King of FRA's Office of Railroad Safety and Bill Schoonover of PHMSA's Office of Safety.

The authors are grateful to Dr. Phani Raj of FRA's Office of Railroad Safety for his assistance in performing and reviewing filling volume calculations and for his insightful discussions during test preparations.

Contents

Illustrations

Tables

Executive Summary

As part of a research program to improve transportation safety for tank cars carrying hazardous materials, the Federal Railroad Administration (FRA) sponsored Transportation Technology Center, Inc. (now MxV Rail) and the Volpe National Transportation Systems Center (Volpe) to test and analyze the side impact puncture performance of a DOT-113 tank car filled with cryogenic liquid nitrogen (LN2). The research team conducted the impact test on May 14, 2022. All test requirements were met. Researchers performed both pre-test and post-test analyses of the impact response to evaluate, validate, and improve puncture modeling capabilities. This was the last in a series of four tests on DOT-113 tank cars and tank car surrogates sponsored by FRA.

The team filled the tank car with liquid nitrogen to achieve a 5 percent outage. The targeted pressure for the test was 30 psig. Researchers vented gaseous nitrogen (GN2) to maintain the LN2's low temperature. After venting and replacing some of the existing LN2 in the DOT-113 with "fresh" LN2, the tank car was left approximately 95-97 percent full by volume, and the remaining 3-5 percent of its volume (i.e., outage) was occupied by GN2. The pressure just prior to the test was approximately 22 psig. The team targeted a test speed of 22 mph ± 0.5 mph to approximate the threshold impact speed necessary to puncture both the outer and inner tanks of the tank car. Pre-test simulations indicated that puncture was likely but not certain at this speed.

The tank car was impacted by a 297,000 lb ram car fitted with a 12 by 12-inch ram head traveling at 22.1 mph. The impact resulted in puncture of both the inner and outer tanks of the car. Researchers used pre-test finite element (FE) modeling to estimate the overall impact response of the tank car for test planning. The pre-test simulations incorporated a phase change from GN2 to LN2 that was dependent on the initial temperature and pressure of the outage. After the test, the pre-test FE model was updated to represent the measured conditions of the test. The pre-test model run using the actual test conditions was in good agreement with the measured test data.

Note that the overall goal of the DOT-113 side impact test series was to analyze the side impact performance of a DOT-113 tank car carrying liquefied natural gas (LNG) under typical service conditions. Due to safety concerns, a DOT-113 tank car with LNG lading could not be directly tested in a full-scale side impact test. Instead, the team used DOT-113 tank cars and surrogate lading ranging from water to cryogenic LN2 and then compared the tests to companion FE analyses. The results of this testing and the lessons learned demonstrate the capabilities of the FE modeling techniques used to capture the relevant puncture behaviors of a DOT-113 tank car under cryogenic conditions. Since confidence in the FE model was achieved, this model may be used to estimate the puncture resistance of a DOT-113 tank car carrying LNG.

1. Introduction

As part of a research program to improve transportation safety for tank cars carrying hazardous materials, the Federal Railroad Administration (FRA) sponsored Transportation Technology Center, Inc. (now MxV Rail) and the Volpe National Transportation Systems Center (Volpe) to test and analyze the side impact puncture performance of a DOT-113C120W9 (DOT-113) tank car filled with cryogenic liquid nitrogen (LN2). On May 14, 2022, the research team conducted the impact test; data from the test was then used to verify and refine a computational model. This was the last in a series of four tests on DOT-113 tank cars and tank car surrogates sponsored by FRA.

1.1 Background

In the past 15 years, significant research has been conducted to analyze and improve the impact behavior and puncture resistance of railroad tank cars. Ultimately, the results of this research was used by federal regulatory agencies (i.e., FRA and the Pipeline and Hazardous Materials Safety Administration [PHMSA] in the United States) to establish performance-based testing requirements and to develop methods to evaluate the crashworthiness and structural integrity of different tank car designs when subjected to a standardized shell impact scenario. A performance-based requirement for tank car head impact protection has been defined within the current regulations [1], and an optional performance-based requirement for tank car shell impact resistance is applicable to DOT-117P tank cars [2].

FRA sponsors a continuing research program to provide the technical basis for rulemaking on enhanced and alternative performance standards for tank cars and to review new and innovative designs developed for the industry in the U.S. and abroad. In support of this ongoing research program, full-scale tests are necessary to provide the technical information to validate modeling efforts and to inform regulatory activities. These tests evaluate the crashworthiness performance of tank cars used in the transportation of hazardous materials under standardized, repeatable conditions.

A DOT-113 tank car is a specialized tank car designed to transport cryogenic liquids[1]. A cryogenic liquid is “a refrigerated liquefied gas having a boiling point colder than −90 °C (-130 °F) at 101.3 kPa (14.7 psia) absolute.”[2] DOT-113 tank cars are “tank-within-a-tank” cars, in which the inner tank is in contact with the cryogenic material and resists the pressure exerted by the lading. An outer tank surrounds the inner tank and insulating materials and carries the in-train forces. The DOT-113 tank car used in this test was constructed specifically for this shell impact test.

The Hazardous Materials Regulations (HMR) permit the transportation of several cryogenic liquids via DOT-113 tank cars, including argon and ethylene. Refrigerated liquid methane (more commonly referred to as liquefied natural gas, or LNG) was not authorized for transportation via DOT-113 tank car prior to 2020. PHMSA and FRA published a Notice of Proposed Rulemaking

---

[1] Subpart F – Specification for Cryogenic Liquid Tank Car Tanks and Seamless Steel Tanks (Classes DOT-113 and 107A) https://www.govinfo.gov/content/pkg/CFR-2018-title49-vol3/pdf/CFR-2018-title49-vol3-part179-subpartF.pdf

[2] 49 CFR 173.115(g)

(NPRM) in October 2019[3] to permit LNG to be transported in DOT-113 tank cars; however, after a side impact test of a surrogate DOT-113 tank car filled with liquid nitrogen, PHMSA and FRA published a second NPRM in November 2021[4] that suspended the transportation of LNG in DOT-113 tank cars until further research could be conducted.

Because the existing fleet of DOT-113 tank cars is small compared to the overall tank car fleet and limited accident data exist regarding the performance of these cars in derailments or collisions, a series of full-scale shell impact tests was planned to provide technical information on their puncture resistance. The first test in this series was performed on November 19, 2019 [3], and the second test was performed on June 11, 2020 [4]. After the second test, a series of finite element (FE) analyses was conducted to transition from testing and modeling a tank car filled with water to one filled with LN2 [5]. The third test was performed on July 24, 2021 [6]. After this third test, a series of FE analyses was conducted to incorporate the effects of the GN2 to LN2 phase change (i.e., condensation) into the simulations [7].

DOT-113 tank cars include several unique design features that are not found on unpressurized (e.g., DOT-117) or pressurized (e.g., DOT-105) tank cars because of the specific properties of cryogenic materials. Because the inner tank of a DOT-113 tank car will be exposed to cryogenic temperatures, it must be constructed of either ASTM A240 Type 304 or Type 304L stainless steel [7]. These steel grades maintain desirable properties at cryogenic temperatures.

Since the inner tank and lading must be kept at cryogenic temperatures during transit, the inner tank must be surrounded by highly effective insulation. This insulation may take the form of expanded perlite[5] (e.g., a granular, lightweight, natural mineral) or multiple layers of "super" insulating materials (e.g., multi-layer insulation [MLI]). Additionally, a vacuum is typically used in conjunction with either perlite or MLI to further reduce heat transfer into the inner tank. Government specification 49 CFR 179 Subpart F defines the maximum rate of heat transfer permissible through the insulation system. The inner tank and insulation must be surrounded by an external tank to contain the insulation, maintain the vacuum, and carry the in-train forces.

The DOT-113 tank car described in this report was newly manufactured for this test and included all the mechanical features of an in-service tank car; however, researchers removed the airbrake lines and handrails before testing since they would have affected the test setup. Most of the previously tested tank cars in FRA's side impact testing program have typically had an exterior jacket that was much thinner than the commodity tank. However, the DOT-113 tank used in this test featured an outer tank made of 9/16-inch carbon steel and an inner tank made of 0.296-inch stainless steel. This report documents the impact test, the FE model development and pre-test estimates, the comparisons of the test and analyses, and the subsequent post-test analyses.

---

[3] Federal Register/Vol 84, No. 206/Thursday, October 24, 2019. https://www.regulations.gov/document?D=PHMSA-2018-0025-0002

[4] Federal Register/Vol 86, No. 213/Monday, November 8, 2021. https://www.regulations.gov/document/PHMSA-2021-0058-0002

[5] The DOT-113 car used in Test 10 was equipped with perlite insulation. All other tank cars and surrogates used in this test series were equipped with MLI.

1.2 Objectives

The objective of this test was to quantify the deformation mode, impact load-time history, and puncture resistance of a DOT-113C120W9 tank car filled with LN2 in a side impact. Moreover, the impact conditions were developed so that the test was 1) safe, 2) repeatable, and 3) analyzable. The test conditions were intended to be representative of planned service conditions, with the limitation that LNG could not be used in the test due to safety concerns. This test was intended to subject a new DOT-113 tank car with a 9/16-inch-thick TC-128 outer tank to an impact with a rigid impactor having kinetic energy close to the puncture threshold for the tank car under the test conditions.

The objective of the pre- and post-test analyses was to provide estimates of the tank car impact response for pre-test planning and the validation of tank car impact and puncture modeling capabilities.

1.3 Overall Approach

Prior to this test, FRA conducted similar shell impact tests on DOT-105, DOT-111, DOT-112, DOT-117, and DOT-113 tank cars. These previous tests were accompanied by companion FE analyses and covered a wide range of tank car design, including capacities, shell diameter, shell thickness, vintage, manufacturer, outage level, outage pressure, etc. The goal of the tank car shell impact testing and modeling program is to understand how a particular tank car, filled to represent typical service conditions, performs under a standardized impact scenario. All these previously tested tank cars operate at ambient temperature compared to cryogenic temperature for DOT-113 tank cars.

To understand the behaviors of a DOT-113 tank car under impact conditions and the potential for improving its performance through design changes, the team used full-scale and laboratory testing with companion FE modeling of increasing complexity. This methodology ultimately represented a DOT-113 tank car under LNG service conditions subjected to a shell impact that punctured both inner and outer tanks. The planned approach included multiple tests and corresponding analyses to examine the influence of different materials and thicknesses used for the tank shell to 1) examine the effect(s) of modeling both the lading and the inner tank steel using properties at cryogenic conditions and 2) ultimately model a DOT-113 tank car under “representative” conditions expected for LNG service.

The observations, lessons learned, and data collected during the first impact test of a DOT-113 tank car, and the subsequent impact tests of two DOT-113 surrogate tank cars, were used as a starting point for modeling the DOT-113C120W9 tank car in this test. The desired outcome for the impact test described in this report was puncture of both the inner and outer tanks at a speed that minimized the post-puncture (i.e., residual) kinetic energy or speed of the impactor. Such a test would be an experimental demonstration of the impact energy required to puncture both tanks of a DOT-113 tank car under cryogenic loading conditions.

Before the test, the research team collaborated with FRA to determine the target test speed based on model estimates, the desired outcome of the test, and factors such as ambient conditions (e.g., wind speed influencing actual impact speed) at the time of the test. After the test, the measured internal pressure, the estimated outage volume, and the measured test speed were used to update the pre-test model to reflect the actual test conditions. Finally, the post-test model results were compared to the test measurements.

1.4 Scope

This report describes the DOT-113 tank car used in this test and compares it to the DOT-113 and DOT-113 surrogates used in the previous tests. The report includes discussion of the process of developing and executing the FE models used in this program. Some aspects of this process include modeling 1) the tank car steels, 2) the lading within the tank, and 3) the gas phase outage within the tank. Tensile tests of the steel used to build the tank car were performed to provide more accurate input for the pre-test FE models. This report presents the test results, discusses the execution of the test, summarizes the overall results of the test, and includes a discussion of the post-test modeling adjustments. Finally, the report presents a comparison between the test measurements and the model results.

This report does not include any results from further analyses using the DOT-113 tank car model, such as impact conditions outside of the conditions of the test. While this report refers to previously performed shell impact tests on tank cars of different specifications [8, 9, 10, 11, 12, 13, 14, 15], no comparison of results from those tests are included within the scope of this report. The first 10 shell impact tests have been summarized and compared previously [16]. Research into the puncture resistance of DOT-113 tank cars is ongoing [3, 4, 5], and further simulations or comparisons may be presented in future work. Further testing and simulations of the puncture responses of DOT-113 tank cars under varied impact conditions (e.g., varied outage level, varied impact speeds, varied tank thicknesses, cryogenic lading conditions, etc.) are planned in this testing and analysis program, but they will be documented in a future report.

1.5 Organization of the Report

Section 2 describes the tank car that was used for testing and analysis and describes the shell impact test setup.

Section 3 describes the instrumentation used during the test and its placement. This description includes discussion of the cameras used to capture the impact event.

Section 4 presents the results of the test, which include a description of the actual conditions of the impact, a description of the test itself, and a summary of the measured test data.

Section 5 describes the development of the FE models used in this program. This section describes the geometry used in the model, the different material models developed, and techniques used in the pre-test and post-test models.

Section 6 presents test measurements alongside the corresponding estimates from the pre- and post-test FE models.

Section 7 presents discussion on the test and model results.

Section 8 includes a summary of the report and concluding remarks.

Appendix A describes the positions of the cameras and targets used in the test.

Appendix B contains the full set of time history data measured during the test. The appendix also contains the material data measured during the tensile coupon tests for the TC-128 carbon steel that makes up the car’s outer tank as well as the T-304 stainless steel from the car’s inner tank.

Appendix C contains a full set of comparisons between test measurements and FE estimates. This appendix contains comparisons for pre-test models using three different outage modeling approaches and for the post-test model using the actual initial conditions.

Appendix D describes the geometry and mesh on each part used in the FE models.

Appendix E contains a description of the modeling techniques that were used in both the pre-test and post-test FE models.

Appendix F contains a description of how each material behavior was developed in the FE models.

Appendix G contains pressure and temperature data collected during filling the tank care with LN2 and shortly after the side impact test as well as calculations used to determine the outage volume after filling.

2. Test Conditions

Researchers performed a side (i.e., shell) impact test on May 14, 2022, at the Transportation Technology Center (TTC) in Pueblo, Colorado. The test was performed by sending a ram car into the side of a DOT-113 tank car that was mounted on skids and backed by a rigid impact barrier. The tank car was filled to approximately 95-97 percent with LN2. This section describes the tank car used in this test and the overall test setup for the side impact testing program.

2.1 DOT-113C120W9 Tank Car Specification and Features

The DOT-113 tank car is a tank-within-a-tank design. The commodity-carrying inner tank and insulation must be surrounded by an external tank to contain the insulation, maintain vacuum, and carry the in-train forces. The DOT-113C120W specification requires that the outer tank be made of carbon steel or stainless steel approved for use in tank car construction [17] with a minimum thickness of 7/16 inch. On July 24, 2020, PHMSA promulgated a final rule (85 FR 44994)[6] to authorize the transportation of methane, refrigerated liquid (more commonly referred to as liquefied natural gas [LNG]) by rail tank car [18]. In the final rule, enhanced outer tank requirements were specified for DOT-113C120W tank cars using the specification suffix "9" (DOT-113C120W9) to denote that the thickness of the outer tank shall be 9/16 inch instead of 7/16 inch. Additionally, the outer shell of a specification DOT-113C120W9 tank car must be constructed of normalized TC-128 carbon steel. A description of the alphanumeric code making up the DOT-113C120W9 specification is shown in Table 1. A summary of the outer tank requirements from the final rule is presented in Table 2.

Table 1. Description of Specification DOT-113C120W9 Tank Car

DOT	**113**	**C**	**120**	**W**	**9**
Car built to meet a U.S. Department of Transportation specification	Specification 113	Inner tank design service temperature of −260 °F (111 K)	Inner tank test pressure of 120 psig	Welded tank	Outer Tank Per Table 2

Table 2. Summary of Outer Tank Properties from Final Rule for LNG

Property	**Final Rule**
Tank Car Specification	113C120W9
Minimum Wall Thickness of the Outer Tank Shell	9/16 inch
Minimum Wall Thickness of the Outer Tank Heads	9/16 inch
Required Outer Tank Steel Type(s)	AAR TC-128, Grade B normalized steel plate

2.2 Description of DOT-113 Tank Car Used in Test

The DOT-113 tank car used in this test was constructed solely for the purpose of this side impact test.

---

[6] Pipeline and Hazardous Materials Safety Administration (PHMSA) (2020). Hazardous Materials: Liquefied Natural Gas by Rail. Washington, DC: U.S. Department of Transportation.

The inner tank was made of American Society for Testing and Materials (ASTM) A240, Type 304 (T304) stainless steel [19] with a nominal thickness of 0.296 inch. The outer tank was made of Association of American Railroads (AAR) Specification TC-128, Grade B high strength carbon-manganese steel [17] in the normalized condition with a nominal thickness of 0.5625 inch (9/16 inch).

The tank car had an outside diameter of 121 1/4 inches. The length of the outer tank was 76 feet, 2 7/8 inches over the heads. During the manufacturing process, samples taken from the material used to fabricate the inner and outer tanks were sent to the research team for material characterization testing (see Section 4.7). The outer tank experienced post-weld heat treatment and was then cut in half to allow for nesting of the inner tank. The inner tank did not experience post-weld heat treatment. The inner tank had an outside diameter of approximately 108 inches and the length over its heads was approximately 75 feet. The inner tank had a nominal capacity of 34,500 gallons of water at room temperature.[7] The car was equipped with two pressure relief valves (PRVs) with start-to-discharge (STD) pressures of 75 psig.

The two tanks were nested together and separated by a 6-inch gap. This annular space contained MLI and was held under vacuum. Based on observations made during a previous test (Test 11) of a water-filled DOT-113 surrogate tank, the MLI was expected to have a negligible effect on the structural response of the tank car during impact.

The test was performed by sending a ram car into the side of the tank car, which was mounted on skids and backed by a rigid impact barrier as shown in Figure 1.

Figure 1. DOT-113 Tank Car Mounted on Support Skids

2.2.1 Test Arrangement

Figure 2 shows an overhead view of the test with annotations indicating 1) the A-end and B-end of the tank car, 2) the east and west sides of the test site, and 3) the direction of travel of the ram car.

---

[7] Due to thermal contraction, the inner tank would have a lower capacity of cryogenic lading based on the temperature of the lading. The research team estimated the inner tank's inside diameter at 106.7 inches and capacity at 34,150 at a chilled temperature of −320 °F (77 K) based on the saturation temperature of nitrogen at atmospheric pressure. The chilled inner tank had a capacity approximately 1 percent lower than the warm inner tank.

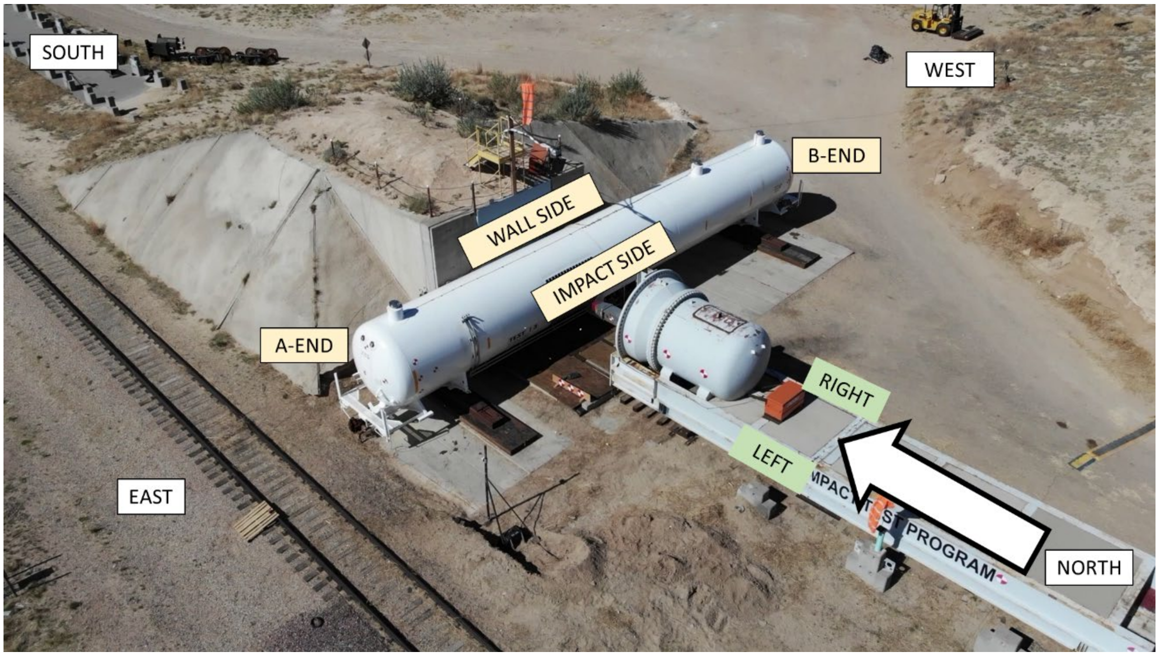

Figure 2. Overhead View of Test Setup Extracted from Drone Video, with Annotations

The DOT-113 tank car was offset approximately 11 feet toward the west, resulting in an off-center impact. The location of the impact was chosen to avoid support structures between the inner and outer tanks and to avoid the weld seams. Figure 3 shows an annotated photo of the closure weld and a diagram of the nesting process where the outer tank (brown) is closed around the inner tank (grey). The closure weld is a unique circumferential weld formed using a single-welded butt joint with a backing strip on the inside of the joint, instead of a fusion double-welded butt joint per 49 CFR 179.400-11. The closure weld is unique because it is not possible to weld from the inside of the outer tank after the inner tank is nested. As a result, the closure weld is the only circumferential weld in the inner and outer tank that is not a double-sided weld. Additionally, a post-weld heat treatment (PWHT) of the entire tank car is not possible once the inner tank is nested. Thus, the double-sided welds on the two halves of the outer tank go through a global PWHT, but the closure weld is not required to undergo a PWHT by 49 CFR 179.400-12.

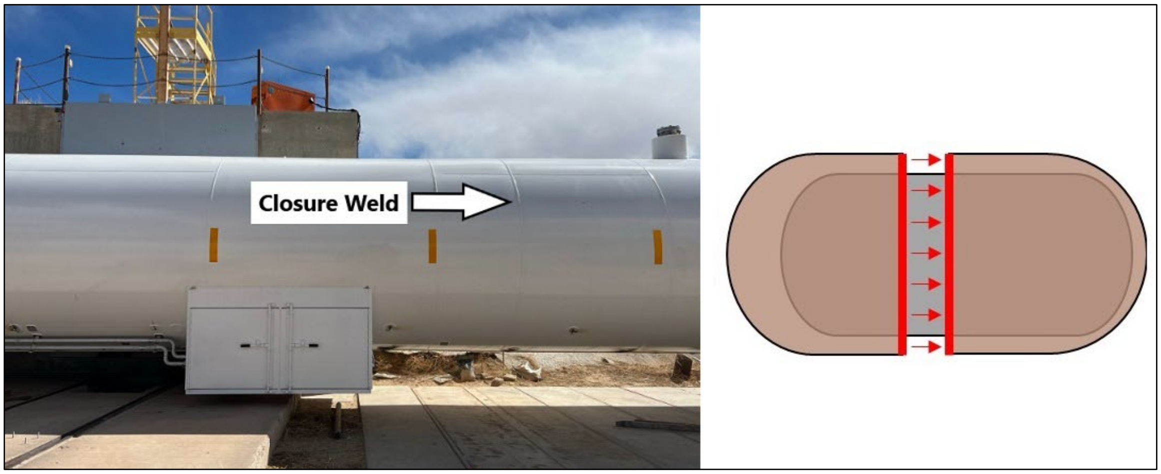

Figure 3. Photo of Closure Weld (left) and Diagram of Nesting Process (right)

Figure 4 (a) shows one of the skids on which the tank car was placed. The skid is oriented parallel to the track, with one end near the impact barrier. Two sections of I-beams were welded to each skid and to the tank car for attachment, as shown in Figure 4 (b). The tank car with the skids attached was placed on 1-inch steel plates. These steel plates were then placed on four 3/4-inch-thick stacks of plywood to raise the tank car above the concrete slab in which the rails were embedded at the impact wall. The raising of the tank was to ensure the horizontal centerline of the impactor and the horizontal centerline of the tank car were aligned as closely as possible. This test configuration was designed to minimize the tank car rollback and to allow the tank car on the skids to slide on the steel plates during the impact without contacting the concrete slab.


(a) Support Skids
(b) Welded I-beam Connection

Figure 4. Tank Support Skid System

The desired level of LN2 in the tank car was calculated based on the nominal dimensions and capacity of the inner tank as well as the desired outage pressure and volume based on in-service conditions for the transport of LNG (see Appendix G). The target lading and outage conditions are discussed in Section 2.2.2, and the actual lading and outage conditions estimated post-test are discussed in Section 4.6. A pipe (e.g., trycock line) that passed through both the inner and outer shells of the car was configured in such a way that the LN2 would begin to flow out of the pipe once the desired 5 percent outage had been achieved. Additionally, a static head pressure gauge was installed on the tank car to measure the depth of the liquid in the tank car. During the filling process, the pipe was used to verify the liquid level indicated by the gauge. Figure 5 shows a static head pressure of approximately 76.5 inches of water prior to impact.

During the planning phase of Test 13, it was decided that, in addition to the static head pressure gauge and trycock that were employed for the previous two tests, it would also be beneficial to use the weight of the car to better measure the actual liquid level. Knowing the weight of the LN2 contained in the tank car, the temperature of the LN2, and the pressure inside the tank car made it possible to calculate the actual height of the LN2 with a higher degree of confidence than solely relying on the static head pressure measurement. Four 100-kip load cells were used to weigh the car. One load cell was placed under each end of the two bolsters (see Figure 6). After the tank car was filled to the desired level, the car was raised, the load cells were removed, and the car was lowered back down onto the center bowl on the skid. The empty weight recorded for the car was 111,400 lb, and the weight recorded for the car after filling was 322,500 lb. Based on these weight measurements, the tank car contained approximately 211,100 lb of LN2. It should be noted that the weight measured by the load cells drifted upward by approximately 1.5 percent when left idle for an extended period. This drift was noticed after the empty car was first placed on the load cells and left overnight and the weight indicated by the load cells the next day was different from the reading on the previous afternoon. This trend continued while filling the tank car. Although attempts were made to identify the reason for the discrepancy, no clear answer was found. One possible cause was that the change in temperature over the course of the day created small changes in the resistance of the wiring that carried the signal from the load cell to the data recording device, thus also changing the voltage reading.

[redacted]

Figure 5. Static Head Pressure Gauge

Figure 6. Load Cell with Hydraulic Ram Positioned on Top to Transfer Weight from Center Plate to Load Cell

The indenter was positioned to align as closely as possible with the mid-height of the target tank car. The ram car (a photo from a previous test is shown in Figure 7) was a modified flat car with an 8-foot ram installed on the leading end. This ram car, which was used in previous tank car tests, has a shortened tank attached to the ram end. A 12 by 12-inch indenter with 1.0-inch radii on the edges and corners was used in the test. The same indenter was used in the impact test of a DOT-111 tank car [11], a DOT-112 tank car [12], a DOT-117 tank car [14], a DOT-105 tank car [13], and a second DOT-111 tank car meeting voluntary industry standard CPC-1232 [16]. This same indenter was also used on the previous tests of a legacy DOT-113 [3] and DOT-113 surrogate [4], which were both filled with water, and a DOT-113 surrogate filled with LN2 [6].

Figure 7. Ram Car and Head

Figure 8 shows the 12 by 12-inch indenter attached to the ram car from a previous test.

Figure 8. Ram Arm with 12 by 12-inch Indenter

Figure 9 shows the ram car aligned with the tank car. The ram car was weighed before the test to confirm the actual weight, which was 297,000 lb.

Figure 9. Ram Arm with 12 by 12-inch Indenter Aligned with the Impact Zone on the Tank Car

2.2.2 Target Lading and Outage Conditions

The third test in this series (Test 12) was the first test to use cryogenic LN2 to fill the inner tank [6]. Using a cryogenic liquid presented new challenges compared to the previous DOT-113 tests that used water in the test setup, including the need to use a stand-in cryogenic liquid (e.g., LN2) rather than the cryogenic liquid that the tank was designed to carry (e.g., LNG). As the test preparations progressed, the lading conditions ultimately chosen for the test also evolved. The Test 12 report contains a detailed discussion of how the cryogenic lading, initial pressure, lading volume, and initial temperature of the lading were selected for that test [6]. These considerations remain relevant to Test 13 and thus, the discussion is not repeated in this report. This Section describes the initial lading conditions targeted for Test 13.

Four lading conditions were defined prior to the test: 1) the lading to be used in the test; 2) the volume of lading (and thus, the volume of vapor space or “outage”) to be placed in the car; 3) the desired pressure for the outage; and 4) the desired temperature for the outage. Several conditions affecting the lading were initially chosen to match the previously conducted DOT-113 tests in this series, or to be consistent with the expected service conditions for LNG tank cars [21].

The target lading and outage conditions chosen for the current test are summarized in Table 3. Pre-test models (Section 6.1) were used to help with the selection of the outage level and pressure for this test. Based on the modeling results, it was determined that a range of pressures (15 to 35 psig) would be acceptable. The chosen outage volume target was five percent.

Table 3. Summary of Lading and Outage Conditions Targeted for Test 13

Parameter	Target Value for Test
Commodity in Tank	LN2
Outage Volume	5%
Outage Pressure	15 to 35 psig

Note that the values shown in Table 5 were the values targeted for the test. The commodity in the tank (i.e., LN2) did not change as test preparations progressed but the actual outage volume and pressure at the time of the test varied from these target values. These differences are discussed in Section 4.6.

2.3 Comparison of DOT-113 Test Conditions

Table 4 presents a summary of the test conditions in 1) the 2019 test of a DOT-113C120W, 2) the 2020 test of a DOT-113 surrogate tank car filled with water, 3) the 2021 test of a DOT-113 surrogate tank car filled with LN2, and 4) this 2022 test of a DOT-113C120W9 filled with LN2. The test conditions not detailed in Table 4 were consistent between the tests where possible. After Test 10, the insulation was changed from perlite to MLI to better represent a modern DOT-113. In Test 11, the annular space was held at atmospheric pressure to simplify the design and construction of the surrogate tank car (this was not expected to have a significant effect on puncture). For Test 11 and Test 12, both the inner tank volume and the length over the heads were reduced. Again, this was done to simplify the design and construction of the DOT-113 surrogates and was not expected to have a significant effect on puncture speed [4]. After Test 10, the outer tank was intentionally changed from a 7/16-inch A516, Grade 70 (A516-70) carbon steel to a 9/16-inch TC-128 carbon steel to evaluate the crashworthiness improvement obtained by using a higher strength, thicker steel in the outer tank. While it would have been preferrable to use a 9/16-inch-thick outer tank for Test 12 as well, a 0.608-inch TC-128 outer tank was used due to availability for manufacturing the surrogate. The thickness of the outer tank for Test 13 was 9/16 inch. The target test speed was increased in each test compared to the previous one (16.5 ± 0.5, 17.2 ± 0.5, 17.7 ± 0.5, and 22 ± 0.5 mph, respectively) to ensure that the kinetic energy of the impactor was greater than or equal to the previous test. A much higher speed was targeted for Test 13 to increase the probability of puncture of the car.

It should be noted that the changes to the insulation, outer tank thickness and strength, lading, and outage volume were expected to have a large effect on the structural response of a DOT-113 tank car. Post-test FE analyses performed after the November 2019 test indicated that the presence of perlite in the annular space stiffened the force versus impactor travel response of the tank car. This resulted in puncture at a lower impactor velocity than that predicted in analyses without perlite. While it is preferable to change only one variable (e.g., insulation type or outer tank steel) between tests, the high cost and time commitment associated with running a full-scale side impact test made it necessary to change multiple variables between tests. However, once confidence is built in a validated FE model of a DOT-113 side impact test, this FE model can be used to carefully investigate the effect of each test variable on the structural response of the tank car to a side impact collision.

Table 4. Summary of DOT-113 Side Impact Test Conditions

Test Date	**November 19, 2019**	**June 11, 2020**	**July 24, 2021**	**May 14, 2022**
Test Number	Test 10 [3]	Test 11 [4]	Test 12 [6]	Test 13 (this report)
Test Article	DOT-113C120W	DOT-113 Surrogate	DOT-113 Surrogate	DOT-113C120W9
Thickness (Outer Tank)	7/16 inch	9/16 inch	0.608 inch	9/16 inch
Material (Outer Tank)	A516-70 Carbon Steel	TC-128 Carbon Steel	TC-128 Carbon Steel	TC-128 Carbon Steel
Diameter (Outer Tank)	~119 inches	~120 inches	~117 inches	~120 inches
Length (Outer Tank)	~74 feet	~45 feet	~46 feet	~75 feet
Thickness (Inner Tank)	1/4 inch	1/4 inch	1/4 inch	0.296 inch
Material (Inner Tank)	T304 Stainless Steel	T304 Stainless Steel	T304 Stainless Steel	T304 Stainless Steel
Diameter (Inner Tank)	~106 inches	~106 inches	~103 inches†	~108 inches†
Volume (Inner Tank)	32,900 gallons	19,300 gallons	17,900 gallons†	34,500 gallons†
Tank Lading	Water	Water	LN2	LN2
Outage (Actual)	17.6%	17.6%	~9%	3 to 5%
Pressure (Actual)	50 psig	50 psig	30 psig	22 psig
Insulation	Perlite	MLI	MLI	MLI
Annular Pressure	Vacuum	Atmospheric	Vacuum	Vacuum
Impact Speed (Actual)	16.7 mph	17.3 mph	18.3 mph	22.1 mph
Outcome	Puncture	No Puncture	No Puncture	Puncture of both inner and outer tanks

† The inner tank values reported here are at room temperature; however, Test 12 and Test 13 were conducted at cryogenic temperature with LN2. The inner tank volume was reduced by approximately 1 percent due to thermal contraction.

3. Test Instrumentation

3.1 Overview

The test configuration and instrumentation were consistent with the specifications of the test implementation plan [22]. Table 5 is a list of all instrumentation used for this test. Additional descriptions of the various types of instrumentation are provided in the following subsections.

Table 5. Instrumentation Summary

Type of Instrumentation	Channel Count
Accelerometers	11
Speed Sensors	2
Pressure and Temperature Transducers	4
Thermocouples	6
String Potentiometers	4
Laser Displacement Transducers	15
Total Data Channels	**42**
Digital Video	4 High Speed Cameras, 3 Go-Pros, and 1 Thermal Imaging Camera

3.2 Ram Car Accelerometers and Speed Sensors

The local acceleration coordinate systems were defined relative to the ram car. Positive x, y, and z directions were forward, left, and up relative to the lead end of the ram.

Three triaxial accelerometers were mounted on the longitudinal centerline of the ram car at the front, rear, and near the middle of the car. Two uniaxial accelerometers were mounted on the left and right sides of the car to supplement recording of longitudinal acceleration. Figure 10 illustrates the positions of these accelerometers. Table 6 provides a summary of the ram car accelerometer ranges and positions.

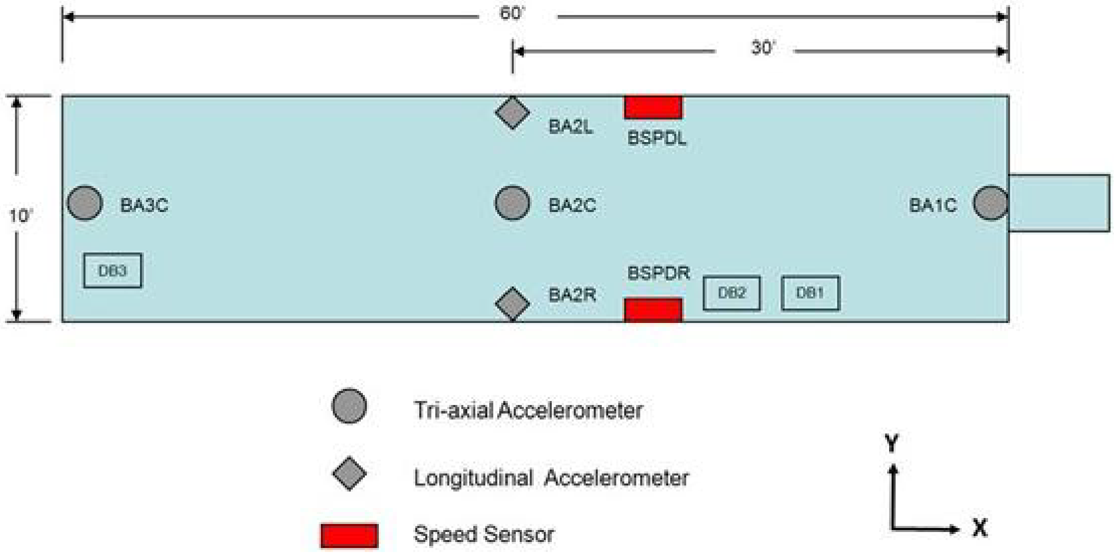

Figure 10. Ram Car Instrumentation

Table 6. Ram Car Accelerometers

Channel Name	Sensor Description	Range
BA1CX	Leading End, Centerline, X Accel	200 g
BA1CY	Leading End, Centerline, Y Accel	100 g
BA1CZ	Leading, Centerline, Z Accel	200 g
BA2LX	Middle, Left Side, X Accel	100 g
BA2CX	Middle, Centerline, X Accel	50 g
BA2CY	Middle, Centerline, Y Accel	50 g
BA2CZ	Middle, Centerline, Z Accel	50 g
BA2RX	Middle, Right Side, X Accel	100 g
BA3CX	Trailing End, Centerline, X Accel	200 g
BA3CY	Trailing End, Centerline, Y Accel	100 g
BA3CZ	Trailing End, Centerline, Z Accel	200 g

Speed sensors (i.e., reflector-based light sensors) were mounted on both sides of the ram car to provide an accurate measurement of the car's velocity within 20 inches of the impact point. These sensors use reflectors on the ground that are separated by a known distance in conjunction with light sensors mounted on the car. The sensors were triggered as the car passed over the reflectors. The last reflector was positioned so that it would align with the sensor when the ram head was within a few inches of the impact point. The time interval between the car's passing over the reflectors was recorded, and the speed was calculated from distance and time. A handheld radar gun was also used to take supplemental speed measurements.

3.3 Tank Car String Potentiometers and Thermocouples

The local displacement coordinate systems (except for the tank heads) were defined relative to the tank car. Positive x, y, and z directions were forward, right (away from the wall), and up relative to the A-end of the tank car. Tank head displacements were positive toward the impact wall.

Four string potentiometers were used to measure the tank motions at the ends of the tank car. Two potentiometers were attached to the skids mounted on the tank car and the remaining two potentiometers were attached to the center of the tank heads. The fixed anchor positions were established so that they measured the longitudinal motions of the tank heads and skids. Figure 11 and Figure 12 show the string potentiometer locations. Table 7 lists the string potentiometers and their information.

Table 7. Tank Car String Potentiometers

Area	Location	Axis	Channel Name	Range
Tank Head	A-End	Y	TDAend	50 in
Tank Head	B-End	Y	TDBend	50 in
Skid	A-End	Y	TDAskid	50 in
Skid	B-End	Y	TDBskid	50 in

Six thermocouples were installed inside the inner tank, mounted in stainless steel tubes that extended into the inner tank. Three thermocouples located 53.5 inches below the top of the inner tank measured the temperature of the liquid nitrogen. The remaining thermocouples were located 5.25 inches from the top of the inner tank and measured the temperature in the vapor space. Figure 11 and Figure 12 and show the thermocouple locations. Table 8 below lists the thermocouples and their information.

Table 8. Tank Car Thermocouples

Location	Sensor Description	Channel Name	Range
A Top	A-End Vapor Space	TT1VS	−328 °F to 122 °F (73.15 K to 323.15 K)
A Center Line	A-End Liquid	TT1L	−328 °F to 122 °F (73.15 K to 323.15 K)
B Mid Top	B-Middle Vapor Space	TT2VS	−328 °F to 122 °F (73.15 K to 323.15 K)
B Mid Center Line	B-Middle Liquid	TT2L	−328 °F to 122 °F (73.15 K to 323.15 K)
B Top	B-End Vapor Space	TT3VS	−328 °F to 122 °F (73.15 K to 323.15 K)
B Center Line	B-End Liquid	TT3L	−328 °F to 122 °F (73.15 K to 323.15 K)

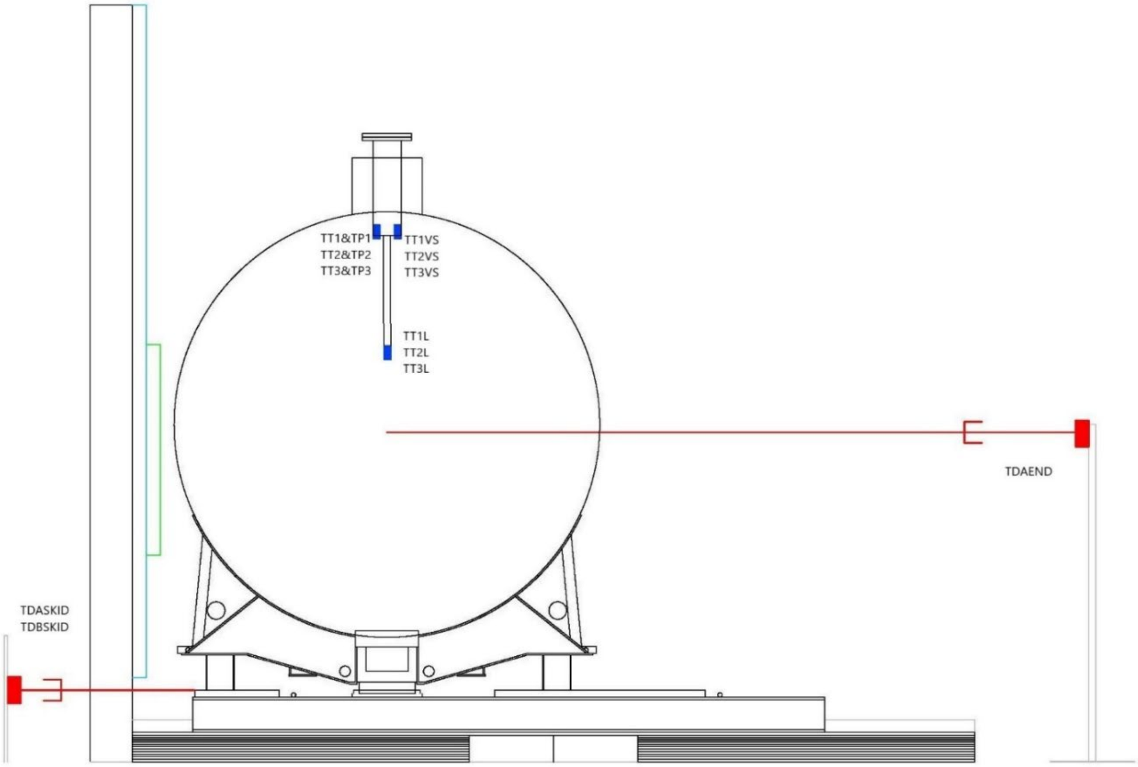

Figure 11. Tank Car String Potentiometer and Thermocouple Locations (end view)

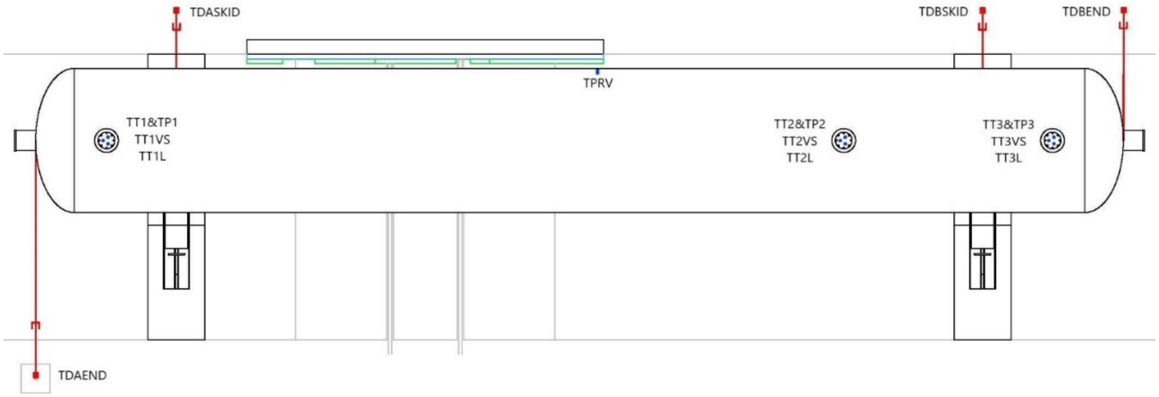

Figure 12. Tank Car String Potentiometer and Thermocouple Locations (overhead)

3.4 Tank Car Combination Pressure and Temperature Sensors

Three combination pressure and temperature transducers were mounted in the vapor space next to the thermocouples. These transducers were used to measure the pressure and temperature in the outage during the impact. A fourth pressure and temperature transducer was mounted just upstream from the pressure relief valve. The positions of the combination pressure and temperature transducers are shown in Figure 11 and Figure 12 and summarized in Table 9.

Table 9. Tank Car Combination Pressure and Temperature Transducers

Location	Channel Name	Range
A-End	TT1 / TP1	0 to 250 psig −320 °F to 70 °F (77.6 K to 294.3 K)
Between Center and B-End	TT2 / TP2	0 to 250 psig −320 °F to 70 °F (77.6 K to 294.3 K)
B-End	TT3 / TP3	0 to 250 psig −320 °F to 70 °F (77.6 K to 294.3 K)
Line to PRV	TPRV	0 to 250 psig −320 °F to 70 °F (77.6 K to 294.3 K)

3.5 Laser Displacement Transducers

A series of laser displacement transducers mounted to the face of the ram car and in the recesses cut into the offset plate attached to the crash wall were also used to record the tank car's response. Fifteen laser displacement transducers were set up to record the tank crush displacements around the immediate impact zone during the test. Four transducers were mounted to the ram car to measure the dent formation of the tank at locations 24 inches and 48 inches on either side of the impact point. A fifth laser transducer was mounted on the ram car to measure the distance of the ram car from the crash wall. Five pairs of lasers were mounted in pockets in the standoff plate attached to the crash wall; one laser of each pair measured distances that were extremely close to the wall, while the other laser of the pair measured longer distances. This pairing was necessary due to the designed measurement ranges and resolutions of the lasers. One of the laser pairs was mounted in line with the center of impact and the other four pairs were mounted 24 inches and 48 inches on either side of the impact point.

Table 10 provides a list of the laser displacement transducers used during the test. Figure 13 shows the positions of the lasers mounted to the ram car, Figure 14 shows the lasers mounted to the crash wall, and Figure 15 shows the relative positions of the crash wall lasers.

Table 10. Laser Displacement Transducers

Location	Channel Name	Sensor Description	Range (mm)
Ram Car	BD1X	Displacement EAST	50 – 12,000
Ram Car	BD2X	Displacement 2nd from EAST	50 – 12,000
Ram Car	BD3X	Displacement 3rd from EAST Aimed at Crash Wall Above Tank Car	50 – 12,000
Ram Car	BD4X	Displacement 4th from EAST	50 – 12,000
Ram Car	BD5X	Displacement 5th from EAST	50 – 12,000
Crash Wall	TD1XS	Displacement Short Range EAST	35 – 110
Crash Wall	TD1XL	Displacement Long Range EAST	100 – 1,000
Crash Wall	TD2XS	Displacement Short Range 2nd from EAST	35 – 110
Crash Wall	TD2XL	Displacement Long Range 2nd from EAST	100 – 1,000
Crash Wall	TD3XS	Displacement Short Range 3rd from EAST	35 – 110
Crash Wall	TD3XL	Displacement Long Range 3rd from EAST	100 – 1,000
Crash Wall	TD4XS	Displacement Short Range 4th from EAST	35 – 110
Crash Wall	TD4XL	Displacement Long Range 4th from EAST	100 – 1,000
Crash Wall	TD5XS	Displacement Short Range 5th from EAST	35 – 110
Crash Wall	TD5XL	Displacement Long Range 5th from EAST	100 – 1,000

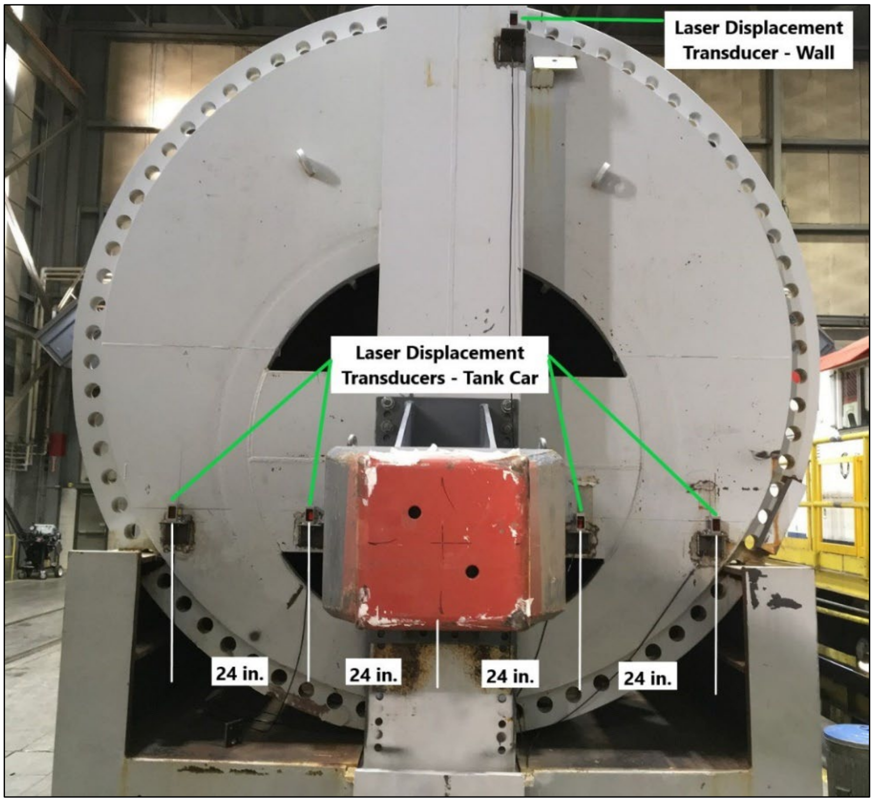

Figure 13. Lasers Displacement Transducers on Ram Car

Figure 14. Lasers Displacement Transducers on Crash Wall

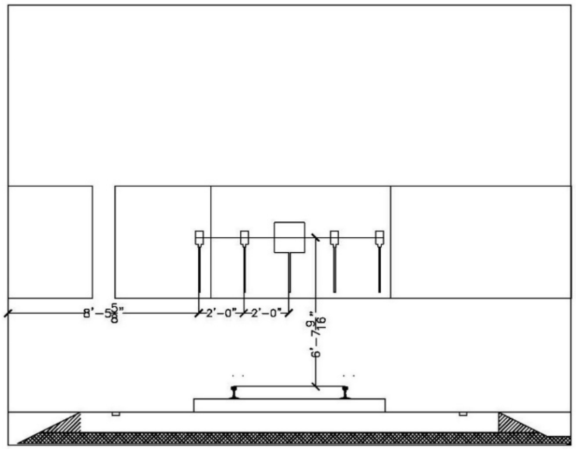

Figure 15. Relative Positions of Crash Wall Laser Transducers

3.6 Real Time and High-Speed Photography

Four high-speed (HS) and four real-time high-definition (HD) video cameras documented the impact event. Figure 16 shows a schematic of the camera position setup. Additionally, a thermal imaging camera was mounted to a drone to capture additional details of the LN2 release in the event of a tank puncture.

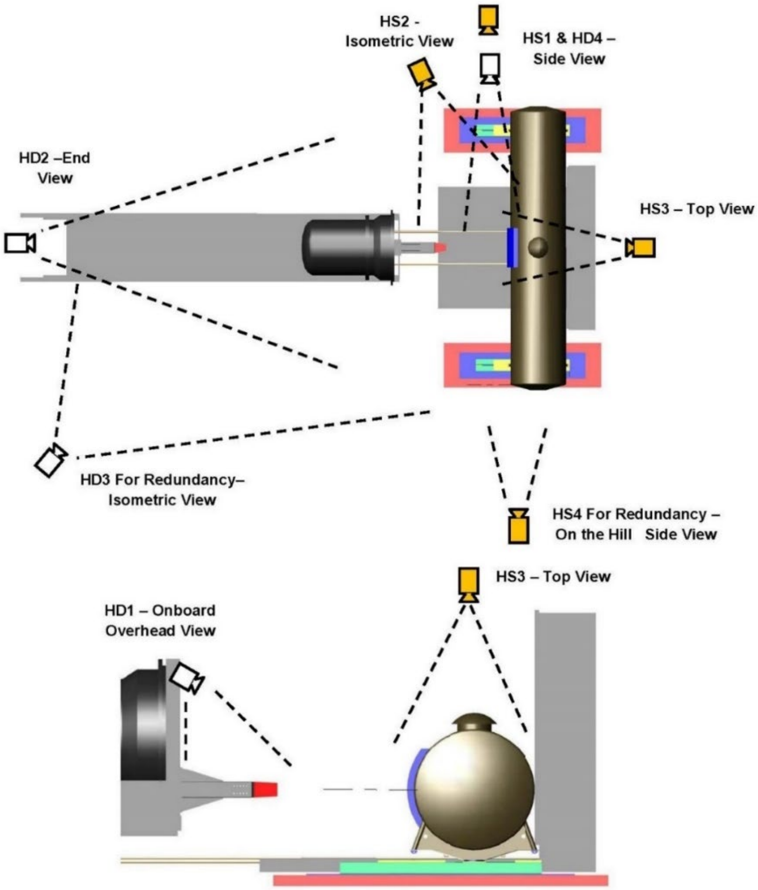

Figure 16. Camera Views

All the HS cameras were crashworthy and rated for peak accelerations of 100 g. The final alignment and sighting-in of the cameras was done prior to the start of the test when the ram car was positioned at the impact point.

Both the ram car and the impact barrier were painted with flat light gray paint, and the tip of the indenter was painted red. High-contrast targets were applied to the ram car, the indenter, and at select ground reference points to aid in video analysis, should video analysis have been necessary.

3.7 Data Acquisition

A set of 8-channel, battery-powered onboard data acquisition systems was used to record the data from the instrumentation mounted on the ram car. These systems provided 1) excitation to the instrumentation, 2) analog anti-aliasing filtering of the signals, 3) analog-to-digital conversion, and 4) a recording of each data stream. A similar set of ground-based data acquisition systems was used to record data from the pressure transducers and string potentiometers on the tank car.

The data acquisition systems were GMH Engineering Data BRICK Model III units. The data acquisition complied with the appropriate sections of Society of Automotive Engineers (SAE) J211 [22]. The data from each channel was anti-alias filtered at 1,735 Hz, then sampled and recorded at 12,800 Hz. The data recorded on the data bricks was synchronized to time zero when the tape switches were closed by the initial impact. The time reference came from the closure of the tape switches on the front of the test vehicle. Each data brick was ruggedized for shock loading up to at least 100 g. Onboard battery power was provided by GMH Engineering 1.7 Amp-hour 14.4 Volt NiCad Packs. Tape Switches, Inc. model 1201-131-A tape switches provided event initial contact.

Software in the data bricks was used to determine zero levels and calibration factors rather than relying on set gains and expecting no zero drift. The data bricks were set to record one second of data before initial impact and four seconds of data after initial impact.

4. Results

This section describes the actual conditions of the test, some of which varied from the target conditions summarized in Section 2. This section also presents photographic results and a discussion of the damage to the tank car as well as graphs of test data. The results of post-test laser scans of the inner and outer tanks are also included in this section.

4.1 Test Conditions

As described in Section 2 and Section 3, this test was a side impact of a DOT-113C120W9 tank car, performed on May 14, 2022. The test involved a 22.1 mph side impact by a structurally rigid 297,000-lb ram car with a 12-inch-square impactor head into the side of a tank car backed by a rigid impact barrier. The tank car was filled to approximately 95-97 percent capacity with LN2 to simulate the standard commodity lading volume of a DOT-113 tank car. The pressure in the inner tank was approximately 22 psig.

At the time of the test, the ambient conditions included a wind speed of 1 mph out of the NW with gusts up to 7 mph and an air temperature of 66° F.

4.2 Test Result Details

Pre-test simulations estimated a puncture speed range of 20-23 mph. The team chose a target test speed of 22 ±0.5 mph because it was thought that it would provide sufficient energy to puncture both the outer and inner tanks without leaving a large amount of residual kinetic energy in the ram car after the puncture. Section 6 contains discussion of the pre-test simulations used to help select the target test speed. The actual calculated impact speed from the speed sensors was 22.1 mph.

The ram punctured both the outer and inner tanks. The indenter punctured the outer tank on the left-hand side of the indenter. The initial puncture created a tear in the outer tank that spread circumferentially as the impactor continued to travel forward. The inner tank was punctured after the outer tank, releasing LN2 into the annular space between the two tanks and through the tear in the outer tank. At the time the inner tank punctured, the ram car's residual speed was approximately 7 mph. The high residual speed at the time of puncture resulted in the ram being imbedded in the tank car. The continued forward travel of the impactor following the puncture of the inner tank created additional tearing and damage to both tanks until the ram came to a stop. Figure 17 below shows the ram arm imbedded in the tank car. Note the presence of frost on the exterior of the car, which indicates 1) that this photograph was taken immediately following the test and 2) that the outer tank experienced a significant drop in temperature following release of the LN2.

Figure 18 shows the post-test position of the tank car relative to the supporting wall. This photograph was taken from the east (A) end of the tank car, looking toward the west. The tank car has rebounded slightly from the wall even though the impact punctured both tanks.

Figure 19 contains side-by-side photographs taken prior to the ram's removal from the tank car. The left-side photograph was taken from outside the tank from the west side of the test setup (i.e., looking toward the east, or A-end). The right-side of this image shows the interior view of the final position of the ram head and arm inside the inner tank. The damaged inner tank is visible behind the ram head.

Figure 20 shows the damage to the impacted side of the tank car following removal of the ram car. Figure 21 shows a more detailed view of the impact zone.

Figure 17. Ram Arm Embedded in Tank Car After Conclusion of Test

Figure 18. Post-test Position of Tank Car (wall side)

Figure 19. Exterior (left) and Interior (right) Views of Tank Damages from West Side Prior to Impactor Removal

Figure 20. Tank Car after Separating from the Ram Car (impact side)

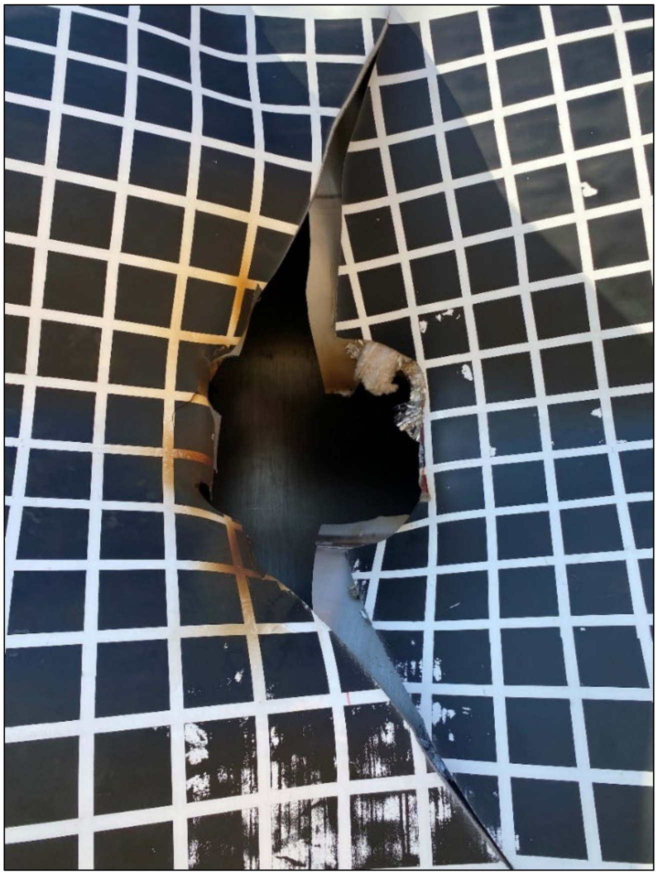

Figure 21. Close-Up View of Impact Zone after Separating from the Ram Car

4.3 Laser Scanning

Following the test, complete light detection and ranging (LIDAR) scans of the outside and inside of the tested tank car were performed to document the deformation that occurred during the test. Figure 22 shows the post-test scan of the DOT-113 tank car. The area of impact is shown to the left side of the cabinets in this figure and the indentation has a diamond shape that is typical in side impact tests [16]. Square sections of the outer and inner tank were cut away near the B-end bolster (right) to access the inner tank for LIDAR scanning and to fabricate samples for material testing (refer to Section 4.6).

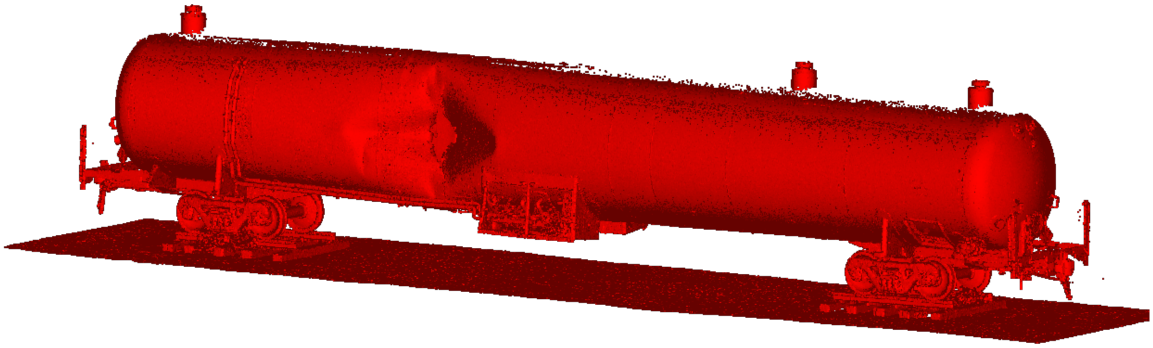

Figure 22. LIDAR Isometric Front View

4.4 Tank Car Damage

In addition to the direct damage caused by the impact, the release of LN2 into the annular space between the inner and outer tanks and the dousing of the outside of the outer tank with LN2 caused the bottom of the outer tank to split from induced stresses. The outer tank was exposed to LN2 while still carrying its own weight, which could have caused a brittle fracture of the outer tank's material. Figure 23 shows the bottom of the outer tank's shell looking toward the B (west) end of the tank car. This photograph was taken immediately after impact, with visible frost observable on the bottom of the tank. MLI from within the annular space has been partially ejected through the crack in the outer tank's shell.

Figure 23. Split in Bottom of Tank Caused by Thermal Stress

Figure 24 shows a view of the outer tank crack passing through a double-sided circumferential weld between two shell plates. A possible lack of fusion in the inside of the weld is indicated in this image. This possible lack of fusion is not believed to have contributed to the brittle crack's initiation or propagation.

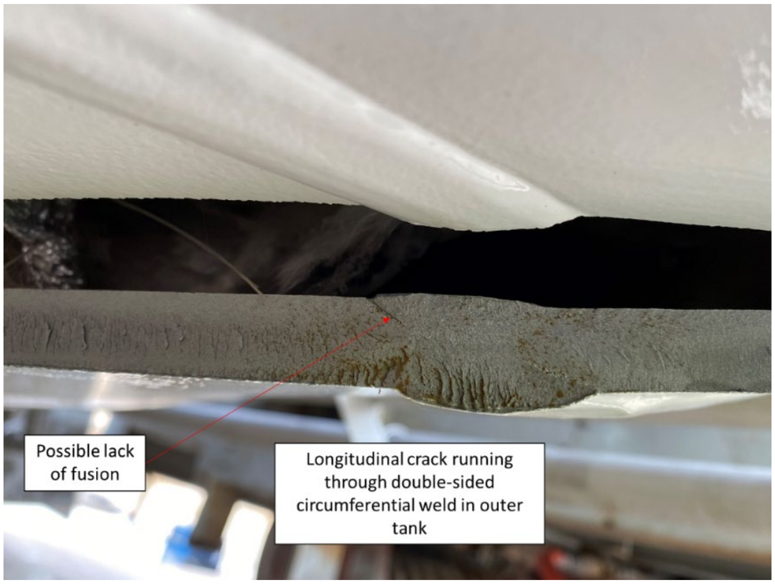

Figure 24. Crack Passing Through Double-sided Circumferential Weld

Figure 25 contains a photograph of a tape measure placed along the fracture surface of the crack. The outer tank of the DOT-113 was made of TC-128B steel having a nominal thickness of 9/16 inch. This measurement confirmed that the crack in the outer tank propagated without reducing the tank shell's thickness.

Figure 25. Thickness of Outer Tank Along Thermal Crack

Figure 26 contains a photograph of the puncture zone after the impactor was removed.

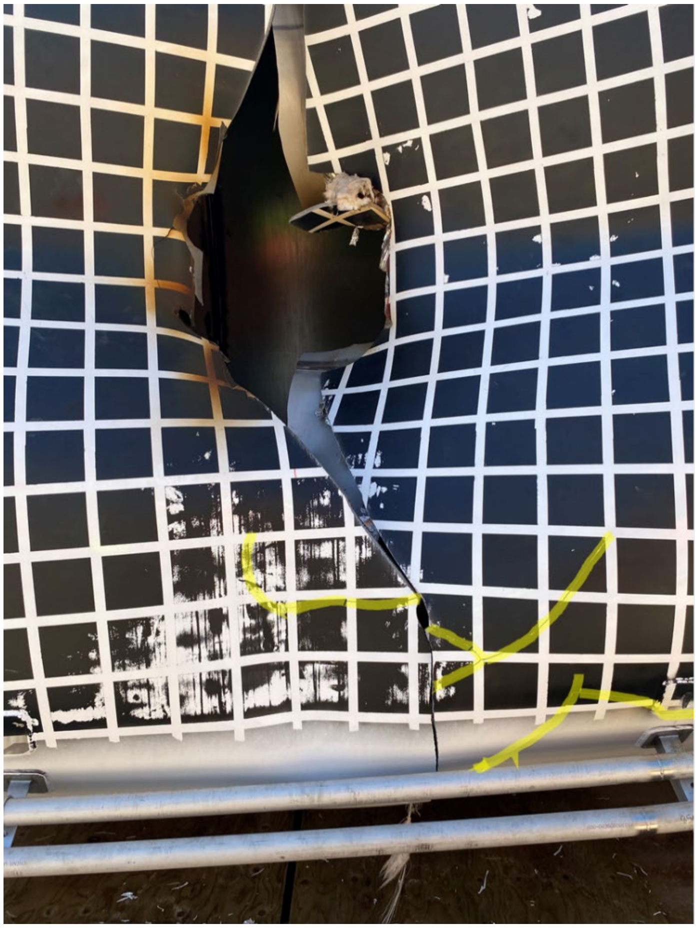

Figure 26. Photograph of Puncture Zone After Impactor Removal with Branching Cracks Highlighted

Several cracks that branch off the main puncture have been highlighted. These branching cracks are not typically observed in tank car puncture tests using water lading. Researchers believe these cracks, like the longitudinal crack on the bottom of the tank, were caused by the outer tank being doused with LN2 while still carrying the stresses of its own weight. Note that these branching cracks are only seen below the point of impact. The bottom half of the tank car is both the location that would experience tensile stresses from its own weight when supported on its bolsters and the location where LN2 would pool due to gravity.

Figure 27 contains a composite image showing two photographs of the impact zone taken at different times. The left side of this image shows the impact zone immediately after puncture, as evidenced by the visible frost on the outside of the tank car. The termination of one of the branching cracks is highlighted. Note that the crack terminates with a vertical orientation. The right hand photograph was taken two days after the test. The tank car was drained of LN2 by this time and had warmed to ambient temperature. At the time the right photograph was taken, the impactor was still embedded within the tank car. In this photograph, the original crack termination is highlighted. By two days post-impact, a new horizontal crack had branched from the original crack. This new crack is supporting evidence of brittle thermal cracking of the outer tank, which was only loaded by its own weight once the impactor came to rest.

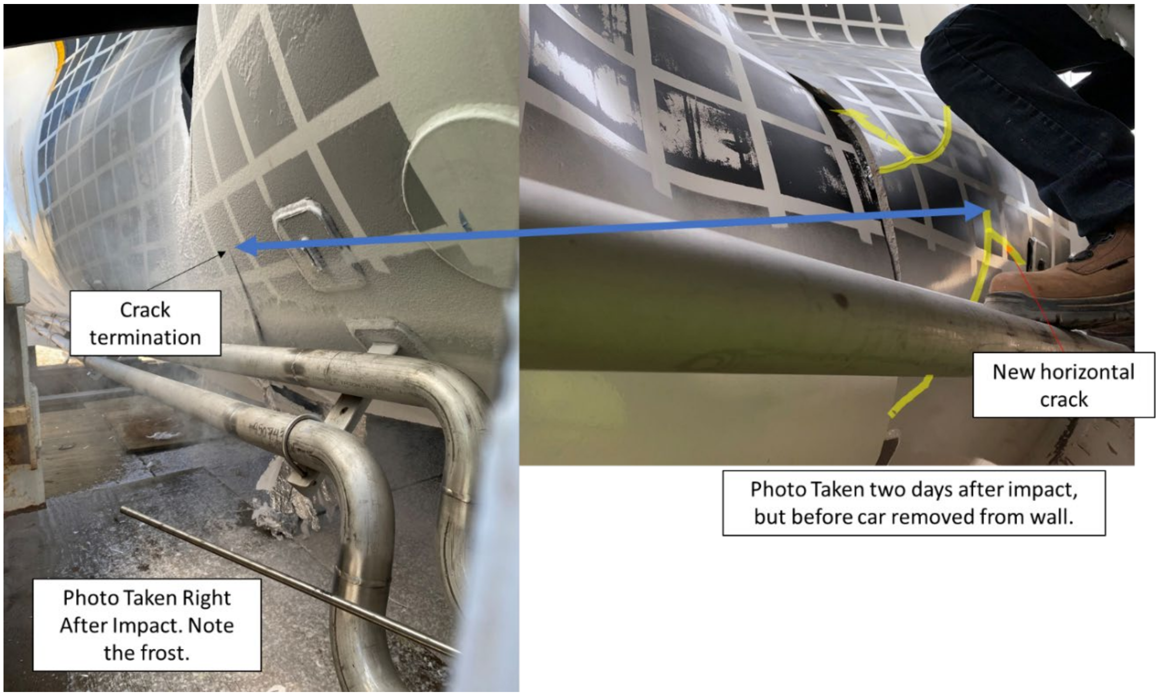

Figure 27. Composite Image Showing Extent of Cracking Immediately after Impact (left) and Two Days after Impact (right)

Several small fragments of outer tank steel were found on or around the tank car following the impact test. Figure 28 shows a photograph of one fragment of the outer tank found after the test. The presence of red paint on this fragment demonstrates that this fragment was contacted by the tip of the ram, which had been painted red.

Red paint transfer from end of impactor

Figure 28. Fragment of Outer Tank Found Post-impact

Figure 29 contains a composite image showing front and side views of a second outer tank fragment. This second fragment also exhibited red paint, indicating it was contacted by the end of the ram. This image shows a side view of the fragment on the left and a front view on the right. Alignment arrows have been added to indicate where features on the front and side views align with one another. The side view shows significant thinning of the material in the area that was in contact with the impactor with no observable thinning outside of the impact area. This behavior suggests the puncture resulting from the impactor was a ductile fracture, while the subsequent fracture after exposure to released LN2 was a brittle fracture.

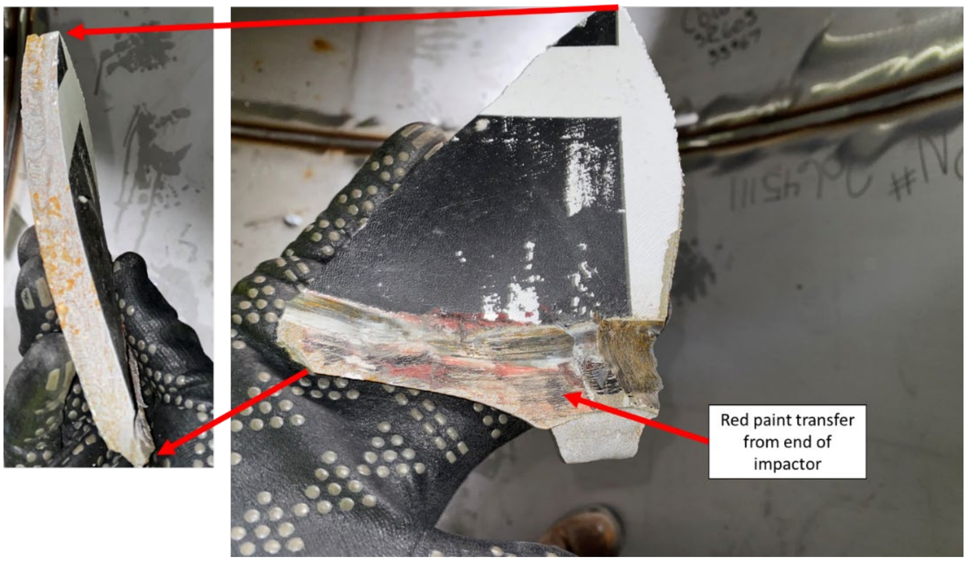

Red paint transfer from end of impactor

Figure 29. Second Fragment of Outer Tank Found Post-impact Showing Side (left) and Front (right) Views

4.5 Measured Data – Impact Test

The data collected in the test were initially processed (i.e., offset corrections, filtering, etc.) by the test team and then compared with the FE analyses. The offset adjustment procedure ensured that the plotted and analyzed data included only impact-related accelerations and strains and excluded electronic offsets or steady biases in the data. The data collected before impact were averaged to determine the necessary offset correction. This offset was then subtracted from the entire data set for each channel. This post-test offset adjustment was independent of, and in addition to, the pre-test offset adjustment made by the data acquisition system.

The post-test filtering of the acceleration data was accomplished with a phaseless four-pole digital filter algorithm consistent with the requirements of SAE J211 [22]. A 60 Hz channel frequency class (CFC) filter was applied for the filtered acceleration data shown in this report. A summary of the measured data is provided in this section. Appendix B contains the plots of the filtered data from all transducers.

The longitudinal acceleration of the ram car was one of the primary measurements in the test. Multiple accelerometers were installed on the ram car to capture this data. The data were then used to determine the impact energy, the deceleration of the ram car, and the contact forces between the ram and target tank car. The ram car's average longitudinal acceleration history, calculated from the onboard accelerometer data, is shown in Figure 30. It should be noted that the longitudinal accelerometer BA1CX was culled from this average, as the data it recorded showed significant deviation from the remaining accelerometers after about 0.16 seconds.

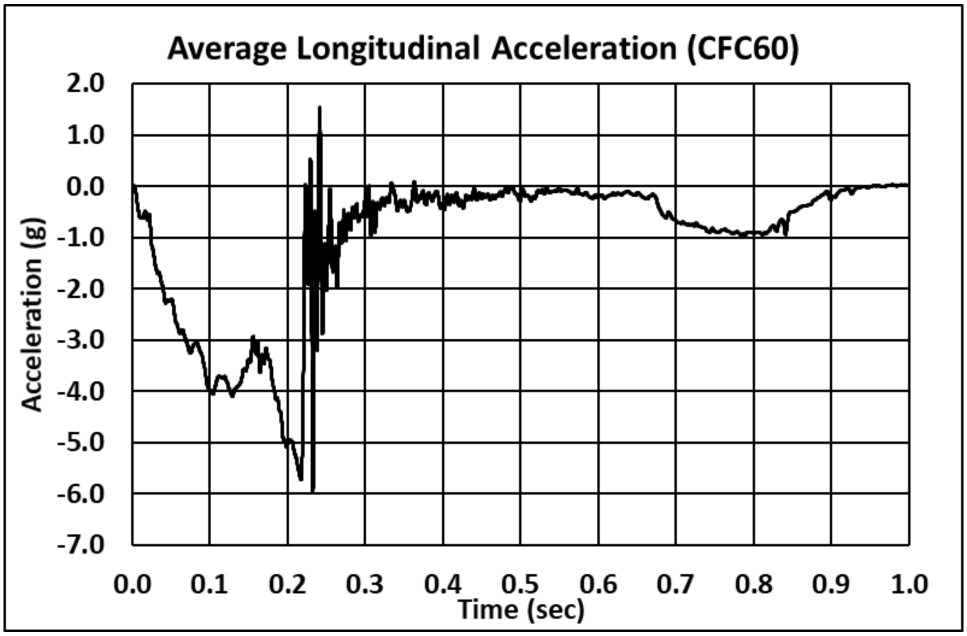

Figure 30. Longitudinal Acceleration Data (Averaged)

The ram car velocity history for this test was calculated by integrating the average longitudinal acceleration of the ram car and using the measured impact speed as an initial condition. The contact forces between the ram and target tank car were calculated as the product of the average acceleration and the mass of the ram car. Figure 31 shows both the force-time and velocity-time histories for the ram car.

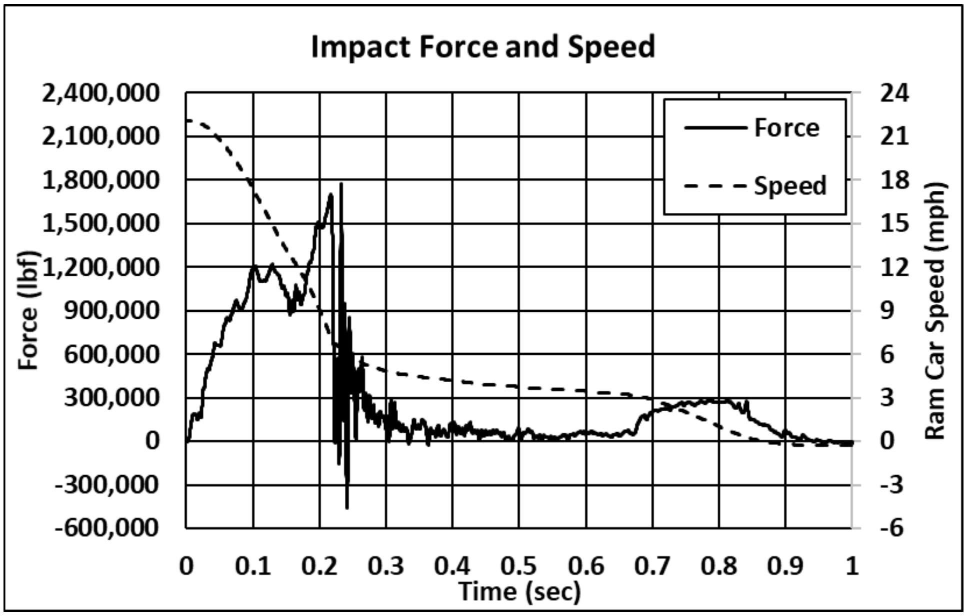

Figure 31. Impact Force and Ram Car Speed

Similarly, the kinetic energy was calculated based on the speed-time history and mass of the ram car. The energy absorbed by the tank car at any point in time was calculated as the difference between the ram car's current kinetic energy and its kinetic energy at the time of impact. Figure 32 shows the kinetic energy time history of the ram car and the energy absorbed by the tank car. The energy absorbed by the tank car increases rapidly until the puncture of the inner tank (at around 0.22 seconds), after which time it slowly increases until it reaches the point where the ram car's forward motion ends at approximately 0.85 seconds. As with the average acceleration calculations, accelerometer BA1CX was not included in the calculations for impact force and energy.

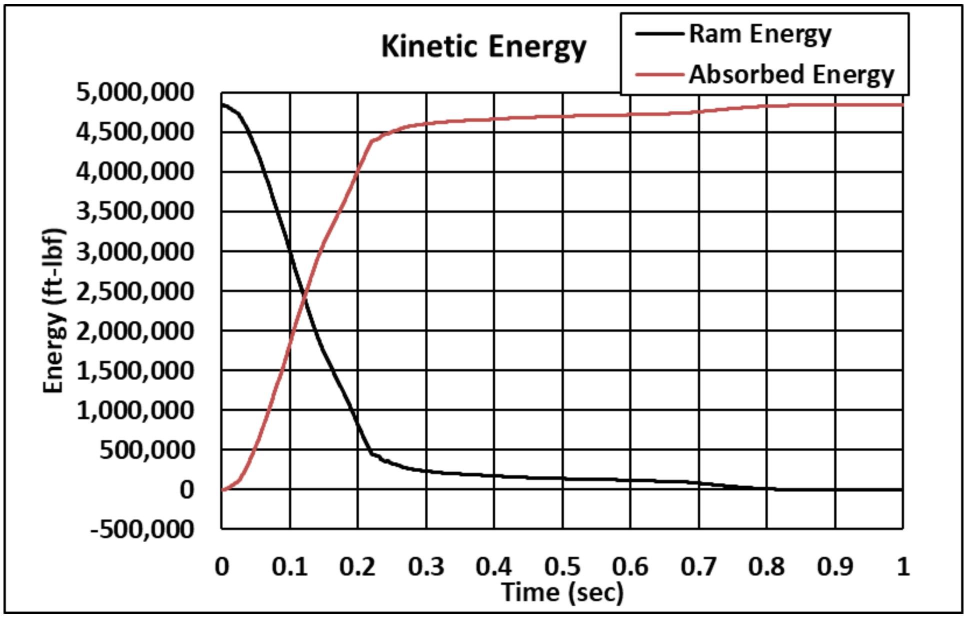

Figure 32. Kinetic Energy Time-history of Ram Car

The total kinetic energy of the ram car at the time of impact was slightly under 4.84 million ft-lbf. The energy absorbed by the tank car at the time the inner tank punctured was almost 4.4 million ft-lbf. While additional energy was transferred from the ram car to the tank car after the puncture of the outer and inner tanks, as the ram car continued moving forward and enlarging the puncture holes, the energy absorbed up to the point of puncture was the most important result. Based on the ram car's mass, the absorbed energy corresponds to an impact speed of approximately 21 mph to just cause puncture.

Another significant impact response measured during the test was the effect of the internal pressure as the tank indentation formed and reduced the volume of the tank. The tank was initially filled to approximately 95-97 percent with LN2 (see Section 4.6) and the pressure in the tank car was about 22 psig prior to impact. As described in Section 3.4, three combination temperature and pressure transducers were mounted at the A-end, the B-end, and in between the B-end and the center of the tank car to measure pressure and temperature in the outage.

Figure 33 shows the pressure data from the outage. The graph shows two distinct sets of peak pressures. The first (and lower) set occurs just prior to puncture of the outer tank (approximately 0.15 seconds). The second (and higher) set of peak pressures occurs at about the same time as the puncture of the inner tank (approximately 0.22 seconds), which would also correspond to the point of maximum tank car deformation, as expected. The maximum pressure recorded for transducers TP1, TP2, and TP3 were 156.2, 150.9, and 175.7 psig, respectively. It should be noted that, for the data recorded just prior to impact and after the system had resettled post-impact, TP3 recorded pressures that were about 2 psi lower than the other two combination pressure and temperature transducers.

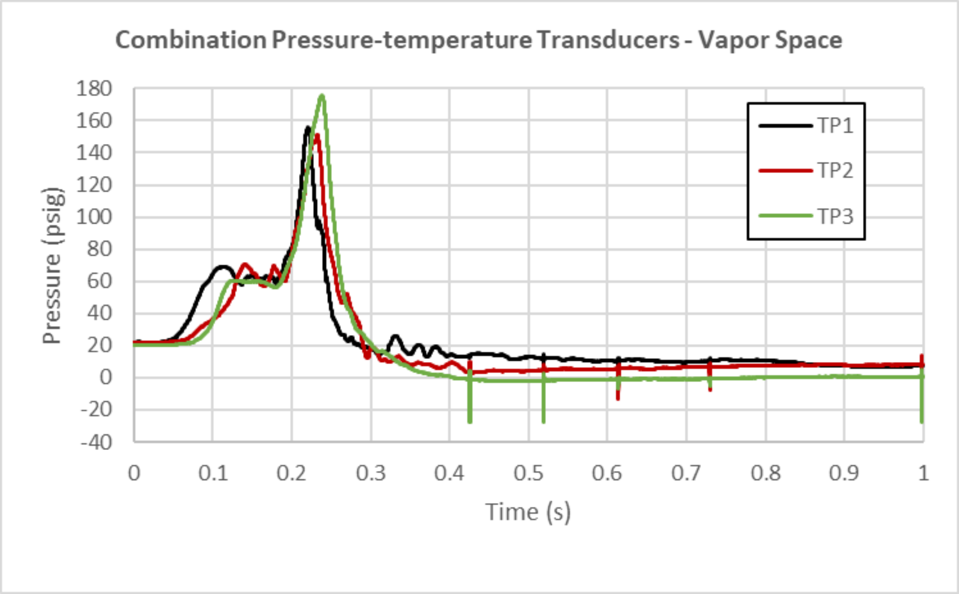

Figure 33. Pressure Data from the Outage

Figure 34 shows the pressure response at the PRV. The tank car used in this test had two PRVs, with both set to discharge at 75 psig; however, only one PRV was active at a time. Only the PRV on the back side of the tank car (facing the crash wall) had a pressure transducer installed to monitor the response. The first sets of peaks (i.e., shoulders) on the graph occur around the same time as the puncture of the outer tank (0.15 seconds). The maximum pressure recorded was 57.8

psig and occurred at 0.324 seconds, approximately 0.1 seconds after puncture of the inner tank (0.22 seconds).

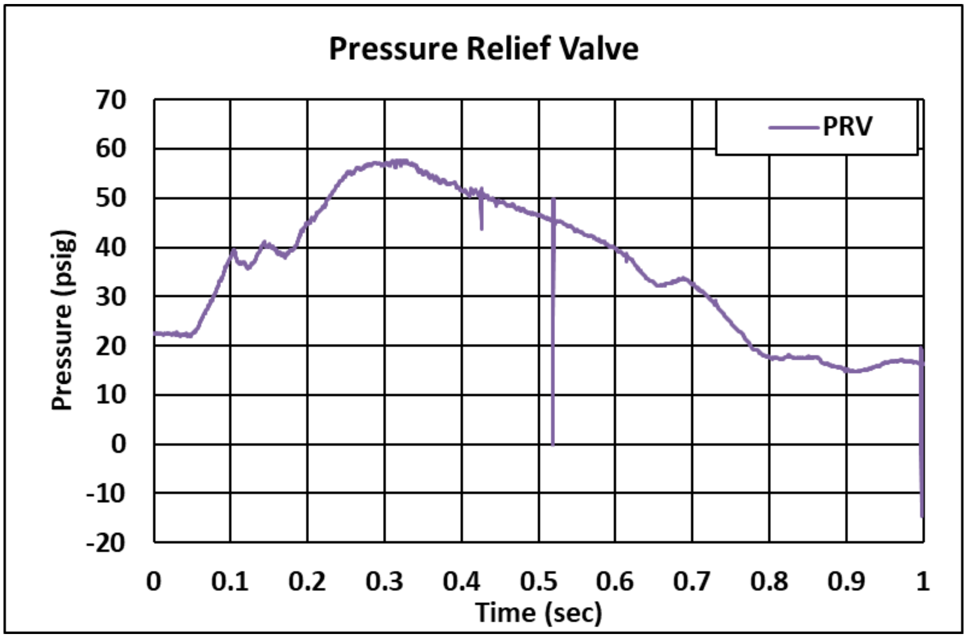

Figure 34. Pressure Data at the Pressure Relief Valve

The longitudinal movements (i.e., toward or away from the impact wall) at both ends of the tank car were recorded with string potentiometers, and the external tank deformations were recorded with laser displacement transducers. The layout of the string potentiometers was described in Section 3.3. The layout of the lasers was described in Section 3.5.

Figure 35 shows the deformation of the tank at positions 24 inches (BD2X) and 48 inches (BD1X) to the left of the impact centerline and 24 inches (BD4X) and 48 inches (BD5X) to the right of the impact centerline.

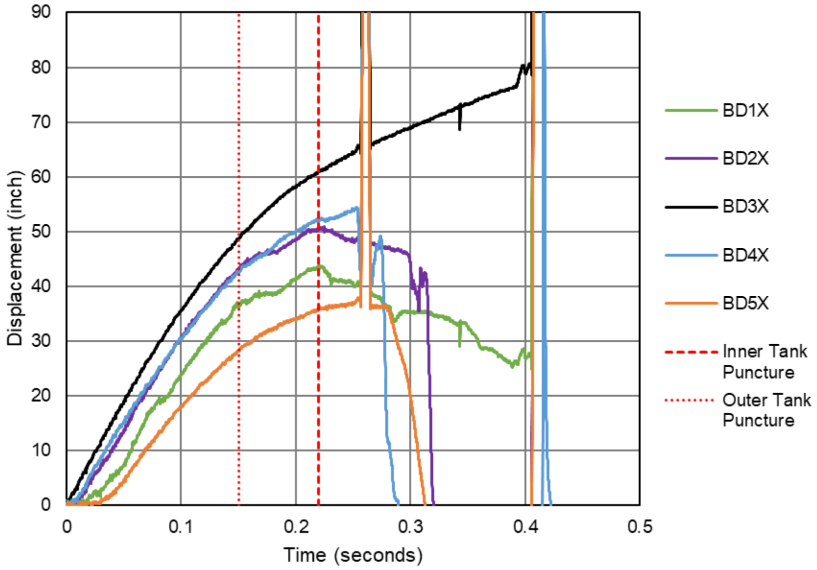

Figure 35. Tank Car Deformation Measured with Laser Displacement Transducers

The deformation of the tank at the impact centerline was measured using a laser transducer on the ram car (BD3X) that reflected off the impact wall. The deformation of the tank at the offset positions was calculated using the lasers on the front of the ram car. For each of the positions, except for the impact centerline (BD3X), the deformation of the outer tank was calculated by subtracting the displacement from the front of the ram car (e.g., BD1X) from BD3X and adding the displacement from the wall (e.g., TD1XS) after zeroing all the laser transducer channels at the time of impact. It should be noted that the long range laser transducers on the wall (e.g., TD1XL) did not record a usable measurement because the tank car remained close to the wall during the impact, and the lasers were obscured by a cloud of water vapor after puncture.

Shortly after the inner tank punctured at 0.22 seconds, the measurements became unstable, then dropped out. This was the result of a thick cloud of water vapor created by the release of LN2 / GN2 interfering with the laser beams. Based on the various HS camera views, lasers BD1X and BD2X on the left side of the ram car were completely obscured by 0.42 seconds. Lasers BD4X and BD5X on the right side of the ram car were completely obscured by 0.34 seconds. The maximum deformations of the tank car at the time the inner tank punctured (0.22 seconds) were approximately 42 inches at BD1X, 50 inches at BD2X, 51 inches at BD4X, and 35 inches at BD5X. The maximum deformation recorded at the impact centerline (BD3X) at the time the inner tank punctured (0.22 seconds) was about 62 inches. The overall maximum deformations at locations BD1X, BD4X, and BD5X occurred just after the inner tank punctured and were about 43 inches, 54 inches, and 37 inches, respectively. The overall maximum deformation at the impact centerline should have occurred at about the time of puncture because after that point the metal would begin to displace laterally, around the impactor as it shoved into the tank, as opposed to longitudinally, compressing the tank.

The displacements measured by the tank car external string potentiometers are shown in Figure 36 for the tank heads and Figure 37 for the support skids.

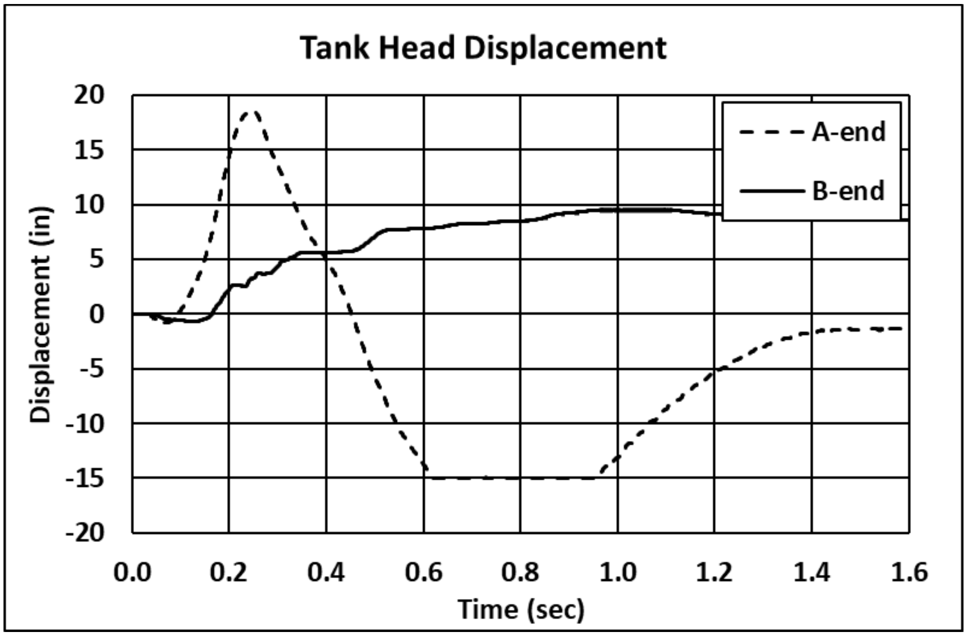

Figure 36. External Longitudinal Displacements – Tank Car Heads

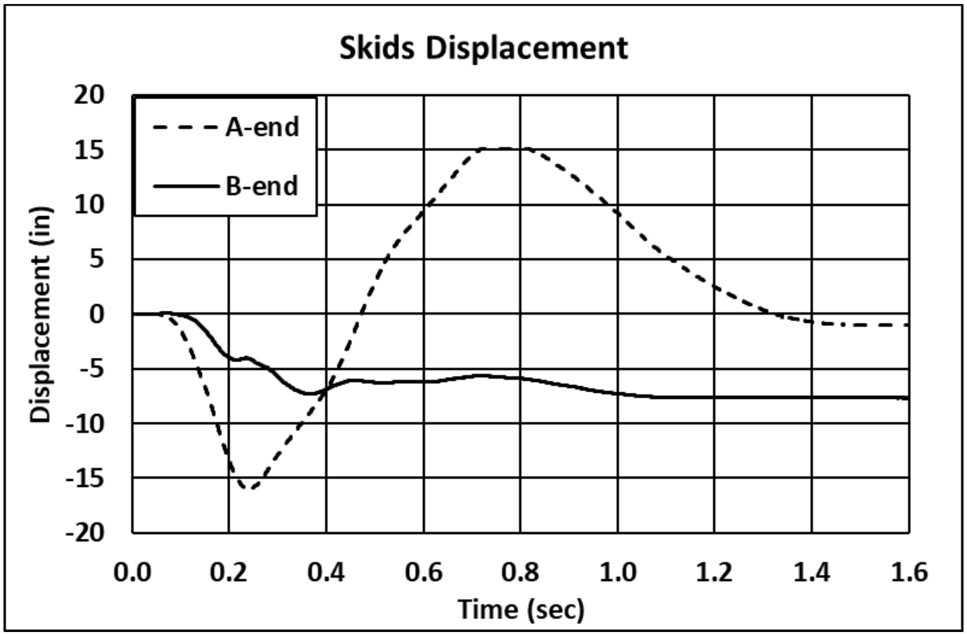

Figure 37. External Longitudinal Displacements – Skids

The displacements of the ends of the car were significantly delayed compared to the motions in the impact zone, and little displacement is seen for the first 0.1 second of the response. There is a large difference in response from one end of the car to the other. This is the result of the approximately 11-foot offset toward the A-end of the impact location, resulting in a much larger inertial moment at the B-end. The A-end head string potentiometer reached its travel limit of −15 inches in Figure 36, and the A-end skid string potentiometer reached its travel limit of +15 inches in Figure 37. Also note that after 0.22 seconds the LN2 was escaping the tank car and may have affected subsequent external measurements. Lastly, the research team inverted the polarity of the B-end head string potentiometer with respect to Figure 11 to match at the polarity of the A-end head.

The temperature inside the tank during the impact was recorded by thermocouples and combination pressure and temperature transducers (see Figure 35, Figure 36, and Figure 37). The temperature readings from the thermocouples remain relatively constant until about 0.2 seconds after the initial contact. After this point, the temperature in both the lading and the vapor space oscillated. The temperature readings from these transducers vary significantly, and while the temperature reading from TT3 is closer to the actual temperature of the vapor space, it is still considered to be too high. It is believed that this was caused by the heating of the transducer itself. This, in turn, was a result of the fact that the end of the transducer, which connects the data and electrical cable, was located on the outside of the tank car. The temperature reading from the liquid nitrogen is also considered to be too high, given the chemical properties of liquid nitrogen and the conditions inside the tank car (see Section 4.6). It is possible that this was partly due to a slightly higher temperature inside the stainless-steel tubes in which the thermocouples were mounted because, as with the combination pressure and temperature sensors, the opposite ends of the tubes were located on the outside of the tank car. It is also possible that the high readings were a result of a pocket of vapor forming around the thermocouples, preventing them from being in contact with the liquid.

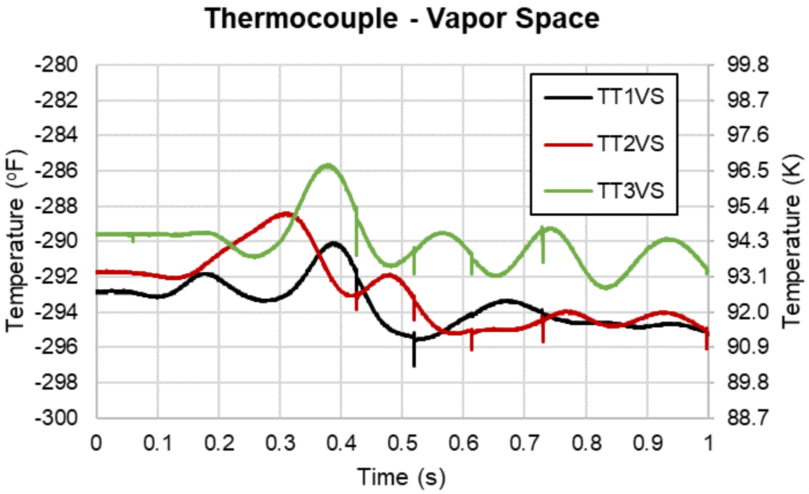

Figure 38. Temperature Recorded by Thermocouples in the Vapor Space

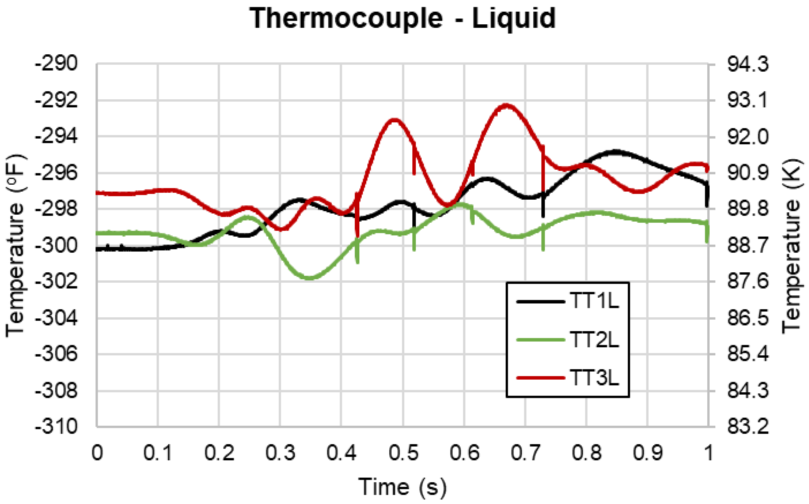

Figure 39. Temperature Recorded by Thermocouples in the Liquid Nitrogen

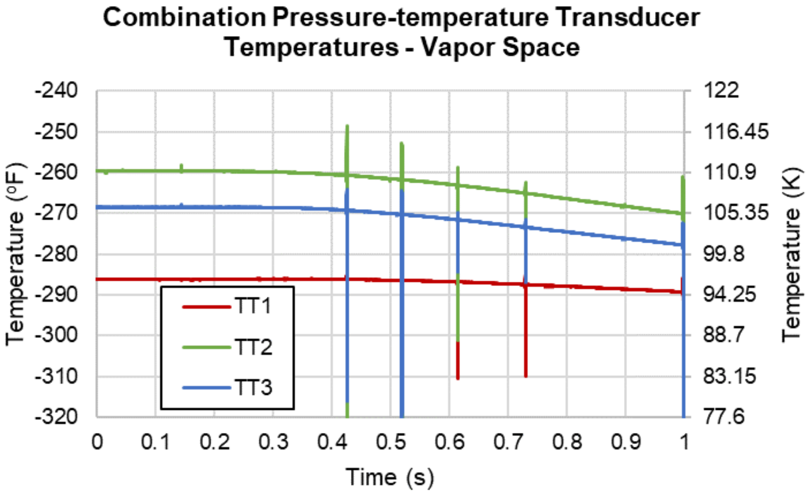

Figure 40. Temperature Recorded by Combination Pressure-temperature Transducers in the Vapor Space

4.6 Summary of Actual Lading and Outage Conditions

Section 2.2.2 described the target values for pressure, temperature, and filling volume of LN2 and GN2. The actual lading and outage conditions at the time of the test differed somewhat from the target lading and outage conditions. Some of the differences were known to exist prior to the test, while other variations were identified upon examination of the test measurements. The estimated actual lading and outage conditions from Test 13 are summarized in Table 11.

Table 11. Summary of Actual Initial Lading and Outage Conditions in Test

Parameter	**Actual Value from Test**
Commodity in Tank	LN2
Commodity Temperature	−314 to −306 °F (81 to 85 K)
Outage Volume	3 to 5%
Outage Pressure	22 psig

4.6.1 Initial Pressure

Data were recorded from 1 second prior to impact until 30 seconds after the impact. The pressure-time histories measured during the impact event were previously shown in Figure 33 and Figure 34. Additional plots of the pressure measurements recorded 1 second prior to impact and at the end of the 30 second window are shown in Appendix G.

The average pressures over the 1 second prior to impact are shown in Table 12. In the second before impact the conditions within the tank were stable, and the average value represents a steady-state value over the entire second.

Table 12. Average Pressures Measured Before Impact

Channel	Units	Pressure
TP1	psig	22.0
TP2	psig	22.0
TP3	psig	20.3
PRV	psig	22.4
Average	psig	21.7

Additionally, a mechanical pressure gauge measured a pressure of between 24 and 25 psig prior to impact (see Figure 41). This value is slightly higher than the average pre-test pressures measured by the pressure transducers.

[redacted]

Figure 41. Mechanical Pressure Gauge Prior to Test

4.6.2 Initial Temperature

Researchers encountered several challenges while interpreting the temperature data from the nine temperature sensors inside the inner tank. Six thermocouples were installed at various positions inside the inner tank to determine the average bulk temperature of the LN2 and GN2. Three thermocouples were submerged below the liquid and three thermocouples were initially positioned within the vapor space. An additional three combination pressure and temperature transducers were installed at the very top of the vapor space. The locations of these temperature sensors are shown on Figure 11 and Figure 12. Additional discussion on the challenges researchers encountered with interpreting temperature data is provided in Appendix G.

At 22 psig, LN2 can only exist at a temperature at or below the saturation temperature. All the recorded temperatures measured via thermocouple remained above the saturation temperature before, during, and after the impact test, despite several thermocouples being installed below the liquid level. The temperatures measured at each location averaged over the second before impact are shown in Table 13. In the second prior to impact the temperatures within the tank were stable.

Table 13. Average Temperatures Measured Before Impact

Location	**A-End**	**Middle**	**B-End**	**Average**
Top of Inner Tank	−286.2 °F (96.4 K)	−259.6 °F (111.2 K)	−268.5 °F (106.2 K)	−271.4 °F (104.6 K)
Mid-height of GN2	−292.9 °F (92.7 K)	−291.7 °F (93.3 K)	−289.6 °F (94.5 K)	−291.4 °F 93.5(K)
Mid-height of LN2	−300.2 °F (88.6 K)	−299.3 °F (89.1 K)	−297.1 °F (90.3 K)	−298.9 °F (89.3 K)
Saturation Temperature at 22 psig [20]				**−306 °F (85 K)**

Researchers determined that the temperatures recorded within the inner tank could not be relied upon to describe the properties of the LN2. Prior to impact the sensors reported temperatures at which LN2 could not exist as a liquid at the corresponding pressure, yet LN2 was known to exist within the tank. The team believes that the surfaces of the thermocouples below the liquid level were not in contact with liquid, but rather with a thin film of vapor that had formed between the thermocouple and the LN2. While the thermocouples do not appear to have malfunctioned, the temperatures measured prior to and during the test do not directly describe the average temperature of the LN2 as intended.

4.6.3 Initial Volume of Lading

The researchers used three tools to estimate the volume of liquid lading prior to the impact test:

(1) A liquid level valve (i.e., trycock) was located approximately 96.2 inches above the bottom of the chilled inner tank, corresponding to a 95 percent full liquid level. The trycock valve can only be used to indicate whether the liquid level is below or above the trycock height (i.e., 95 percent full).

(2) A static head pressure gauge was installed that measured a pressure differential between the top and bottom of the inner tank in units of inches of water. This measurement can be

converted to a liquid level for LN2 by using the density of LN2 relative to water. However, the density of LN2 is dependent on its temperature and pressure.

(3) Four load cells were placed under the tank car to measure the weight of lading inside. However, the scales experienced drift over the several days needed to fill the tank car. Therefore, they were only used as a check on the measurement from the static head pressure gauge.

The static head pressure gauge on the tank reported a pressure differential corresponding to 76.5 inches of water on the morning of the test (see Figure 5). Because the thermocouples positioned inside the liquid all reported temperatures above the saturation temperature of LN2 (refer to Section 4.6.2), the researchers could not directly use the measured temperatures to calculate the density of LN2. Researchers had to assume that the LN2 was at or below its saturation temperature of approximately −306 °F (85 K) at the measured pressure of 22 psig (34.3 psia) averaged 1 second prior to the impact. Using the saturation temperature, researchers determined that the minimum density of the LN2 was 6.413 lbf/gal (768.5 kg/m^3) [20]. Thus, a gauge reading of 76.5 inches of water corresponded to a maximum of 99.5 inches of LN2 at the saturation temperature, placing the liquid level at a maximum of 3.3 inches above the trycock position. Given the chilled inner tank's inside diameter of approximately 106.7 inches, this filling level placed the top of the liquid 7.2 inches below the top of the tank. The calculated minimum outage height of 7.2 inches was approximated as 7.3 inches in the pre- and post-test FE models corresponding to an outage volume of 3 percent.

Prior to impact, researchers opened the trycock valve and witnessed liquid ejecting. This confirmed that the liquid level was over 95 percent. Therefore, researchers could calculate the maximum density of LN2 as 6.591 lbf/gal (789.8 kg/m^3) [20], and they calculated the corresponding minimum bulk temperature of LN2 as −314 °F (81 K). This means that the volume of LN2 was somewhere between 95 and 97 percent, and the average LN2 temperature was somewhere between −314 °F (81 K) and −306 °F (85 K). The relationship between average LN2 temperature and lading volume is shown in Table 14. Given the uncertainties in the average temperature of LN2, the researchers could not determine an exact lading volume and conducted FE modeling at both 95 and 97 percent lading volumes. Refer to Appendix G for more discussion on calculations of the outage volume.

Table 14. Assumed Bulk LN2 Temperature Versus Lading Volume

Temperature (°F)	Temperature (K)	Lading Volume (%)
−306	85.4	97%
−308	84.3	96.5%
−310	83.2	96%
−312	82.0	95.5%
−314	80.9	95%

4.7 Steel Tensile Testing

In most of the prior side impact tests, the tensile properties of the steels composing the tanks were not measured prior to the tests due to the risk of structurally compromising the tank [16]. Tensile coupons were cut after the test, and the pre-test FE model was updated with the actual material properties when creating the post-test FE model. Tests 11, 12, and 13 were unique side impact tests in the overall program where a tank car or tank car surrogate was constructed for the purpose of the side impact test.

4.7.1 AAR TC-128, Grade B Carbon Steel

For the TC-128 outer tank, the pre- and post-test FE models for Test 13 used the results from the pre-test material characterizations performed on the Test 11 DOT-113 surrogate tank car because the TC-128 properties from Test 11 were determined to be typical. Before assembly of the Test 11 surrogate tank car, the manufacturer of the outer tank excised a representative section of the 9/16-inch TC-128 outer shell in the PWHT condition and machined ASTM E8 smooth round bar (SRB) coupons with a 2-inch gauge length (GL) and 0.5-inch diameter. The pre-Test 11 SRB coupons were tested at quasi-static strain rate and room temperature, and the measured tensile properties were used to define the material behavior in the pre- and post-test FE models for Test 11 [4].

Prior to Test 13, samples of TC-128 carbon steel were excised from areas of the outer tank that were removed during fabrication and subjected to tensile testing. The results of those tests (provided in Appendix B) confirmed that the mechanical properties of the Test 13 TC-128 were similar to the properties of the Test 11 and Test 12 TC-128. Therefore, the Test 13 FE model did not need to be updated using the new material test data. The average yield strength (YS), ultimate tensile strength (UTS), and elongation at break (EB) in a 2-inch gauge length (EB-2in) measured in various coupons taken from the Test 11 and Test 12 cars and the average corresponding properties for samples taken from shell plates in the Test 13 outer tank are shown in Table 15.

Table 15. Comparison of Test 11, Test 12, and Test 13 TC-128 Mechanical Properties

Steel	**YS**	**UTS**	**EB-2in**
-	**ksi**	**ksi**	**%**
Test 11 TC-128 (pre-test, average)	64.9	88.8	31.4
Test 12 TC-128 (post-test, average)	60.2	86.2	37.5
Test 13 TC-128 (pre-test, average)	63.2	88.4	29.3[8]

4.7.2 ASTM A240, Type 304 Stainless Steel

For the T304 inner tank, the pre- and post-test FE models for Test 13 used the results from the pre-test material characterization performed on the Test 13 DOT-113 tank car. Prior to Test 13, portions of the inner tank removed during fabrication had ASTM E8 subsize DogBone (DB) coupons cut out for tensile testing. The T304 coupons had a 2-inch GL[9], 0.5-inch width, and 0.24-inch thickness, and they were subjected to tensile testing at various combinations of strain

---

[8] Of the three specimens tested from Test 13, only one fractured between the gauge marks. Thus, the EB-2in reported is the value from this specimen, not the average.

[9] One specimen tested at room temperature used a 2.5 inch gauge length.

rates and temperatures. The T304 coupons were tested at room temperature and −320 °F (77 K). The room temperature specimens were tested at a quasi-static (QS) strain rate, and the 77K specimens were tested at both a QS strain rate and a strain rate of 0.1 s^{-1}. The results of the tensile testing performed on the Test 13 T304 are reported in Appendix B.

The pre-test average YS, UTS, and EB from the Test 13 DOT-113 tank car are shown in Table 16.

Table 16. Summary of Pre-test Test 13 T304 Mechanical Properties

Temperature	Strain Rate	YS	UTS	EB
Kelvin	*s^{-1}*	*ksi*	*ksi*	*%*
295	8.33e-5	42.4	109.1	67.7 (2/2.5 in)
77	8.33e-5	54.6	237.5	N/A†
77	0.1	63.0	193.3	30.6 (2-in)

† The first specimen exceeded the maximum load of the test frame, the second specimen exceeded the extension limits of the test frame, and the third specimen failed in the grip section.

4.8 Observations from Test Videos

After the test, the team examined the test videos alongside the other data measured during the test. An analysis of the videos yielded several insights into behaviors measured during the impact test; Table 17 summarizes these key events. In this section, the test data and corresponding still frames from test videos are discussed to better understand the sequence of events that occurred during this test. Based on the test video and test data correlation described in this section, the outer tank was confirmed to have torn first and the inner tank to have torn subsequently. This discussion is focused on the first 222 ms of the impact event, as that is the period during which the two tanks punctured. The averaged acceleration-time data presented in this section excludes accelerometer BA1CX.

Table 17. Summary of Key Events Observed in Test Data and Test Videos

Event	Source of Event Time	Time (ms)	Impactor Travel (in)	Impact Force (kips)	Absorbed Energy (million ft-lbf)	Outage Pressure (psig)
First peak force	Test data	125	42.6	1217.4	2.61	60.3
Visible tear in outer tank	Onboard camera	150	48.8	938.2	3.18	62.3
Global peak force	Test data	213	60.3	1702.5	4.33	127.9
First frame with visible leakage (onboard camera)	Onboard camera	217	60.8	775.4	4.39	140.1
Global peak pressure	Test data	221	61.3	284.0	4.40	143.1
First frame with visible leakage (HS Camera)	HS camera	222	61.4	504.2	4.40	142.3

4.8.1 Time of Impact

The ram car's onboard camera was not equipped with a trigger to synchronize it with the data acquisition system. The video from this camera was synchronized with the time of contact between the ram car and the tank car. Figure 42 shows the last frame in which daylight is visible between the shadows of the ram car and tank car, indicating the ram car has not yet contacted the tank car. The following frame is shown in Figure 43, where no daylight is visible between the two shadows. This frame was denoted Frame 0. The onboard camera recorded video at 240 frames per second. Thus, the uncertainty between these two frames is 4.167 ms (i.e., contact could have occurred anytime within a 4.167 ms window based on this approach).

Figure 42. Frame Prior to Contact, Showing Daylight Between Impactor and Outer Tank

Figure 43. First Frame Showing Contact Between Impactor and Outer Tank

4.8.2 Plateau Peak Force

The averaged force-time history data from the onboard accelerometers was filtered with a CFC60 filter. The impact force initially rose before reaching a plateau value. Figure 44 shows the force-time history measured during the test, with a callout indicating the time and amplitude of the peak force to occur during the initial force plateau. This plateau peak force of 1,193 kips occurred at approximately 0.125 seconds. This peak occurs just prior to a drop in force at the end of the plateau.

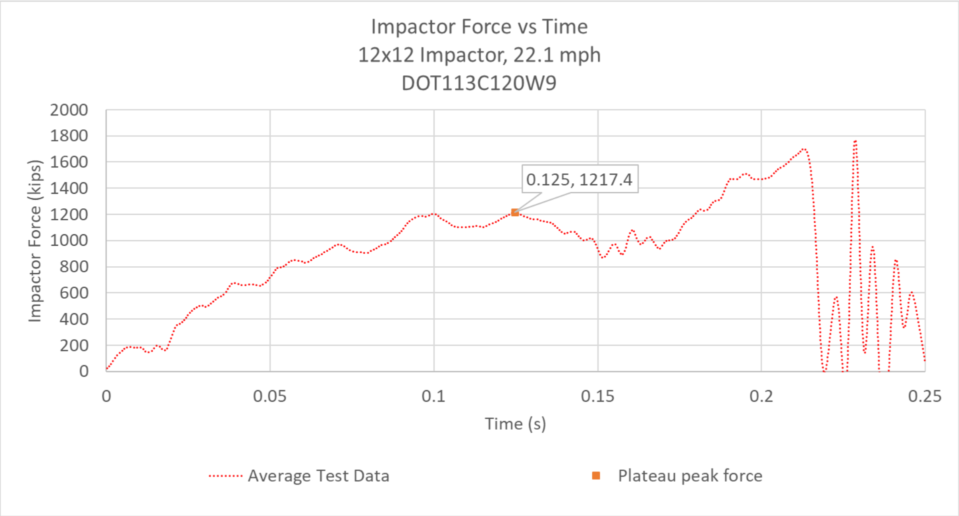

Figure 44. Impactor Force Versus Time with Plateau Peak Force Annotated

Figure 45 shows a frame extracted from a 1000 fps HS isometric camera at 0.125 seconds. At that time, the indentation in the outer tank is apparent but there is no evidence of tank tearing.

Figure 45. Frame from Isometric HS Video at 0.125 s

4.8.3 Visible Tear in Outer Tank

Figure 46 contains a plot of impactor force versus time with an annotation at the time at which a visible tear in the outer tank was first observed in a frame from the onboard video. The error bars around this data point indicate ± 4.167 ms due to uncertainty around the exact time. From this figure, it is apparent that the time of visible tearing of the outer tank occurred right after a decrease in force after the end of the force plateau.

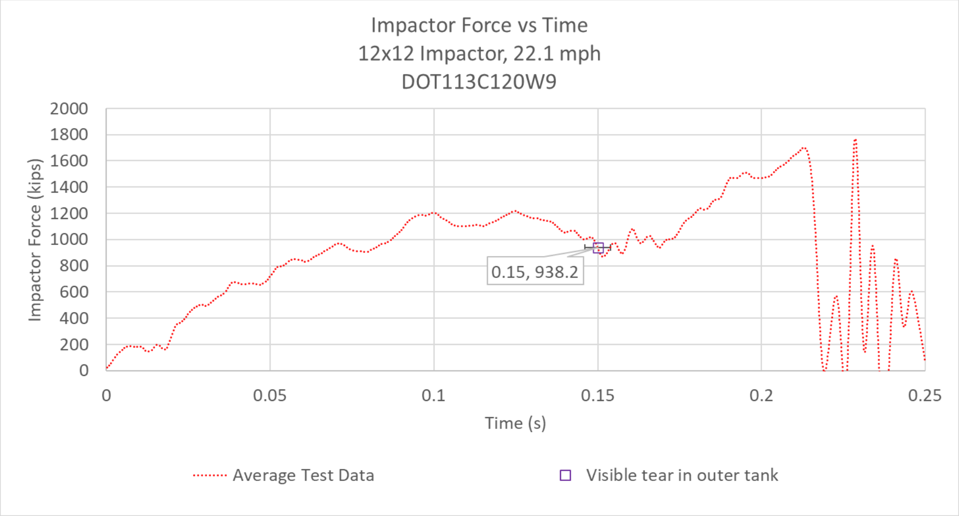

Figure 46. Impactor Force Versus Time with Time of Outer Tank Visible Tear Annotated

Figure 45 contains a still frame extracted from the onboard video at 0.150 seconds, with an inset image featuring a close-up view of the point of impact. This frame was the first frame with an observed tear in the outer tank.

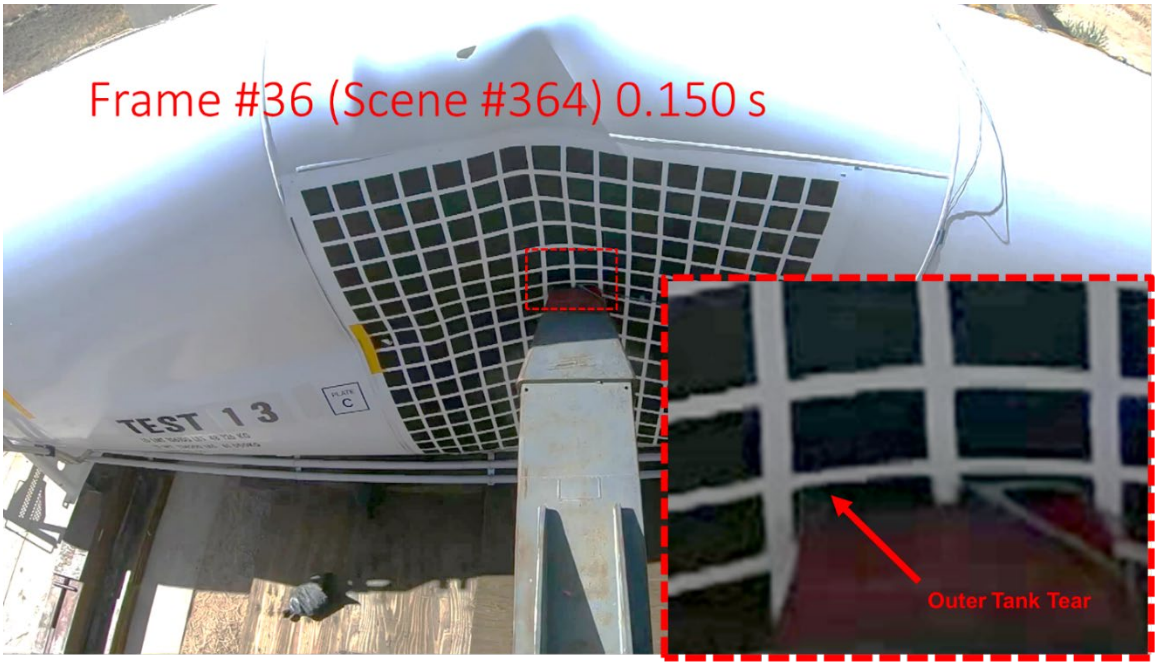

Figure 47. Frame from Onboard Video at 0.150 s

4.8.4 Pre-puncture Peak Force

Figure 48 contains a plot of impactor force versus time with an annotation for the time at which the maximum peak force was measured prior to the inner tank's puncture. This pre-puncture peak force occurred immediately prior to a near-total reduction in impactor force. Note that following puncture a higher peak force was measured during the oscillations as the tank drained and the impactor came to rest embedded within the shells.

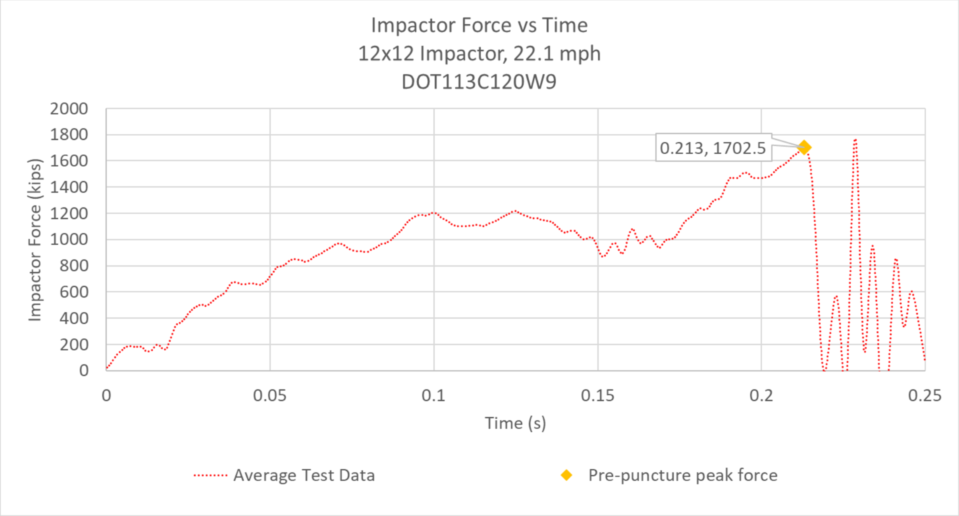

Figure 48. Impactor Force Versus Time with Time of Global Peak Force Annotated

Figure 49 contains a frame extracted from the isometric HS video at 0.213 seconds. The indentation in the tank car has grown larger since the previous frame shown from this video (Figure 45). No evidence of N2 leakage from the inner tank is visible in Figure 49.

Figure 49. Frame from Isometric HS Video at 0.213 s

4.8.5 Visible Leakage

Figure 50 contains a plot of impactor force versus time with annotations for the times at which N2 escaping the torn outer tank was first observed in a frame from the onboard video (0.217 s) and the HS isometric video (0.222 s). The error bars around the onboard data point indicate ± 4.167 ms due to uncertainty around the exact time. Taking the uncertainty into account, N2 leakage was observed in both videos at essentially the same time. This provides a good indication that the estimated time from the onboard video is reasonably close to the time triggered in the HS isometric video.

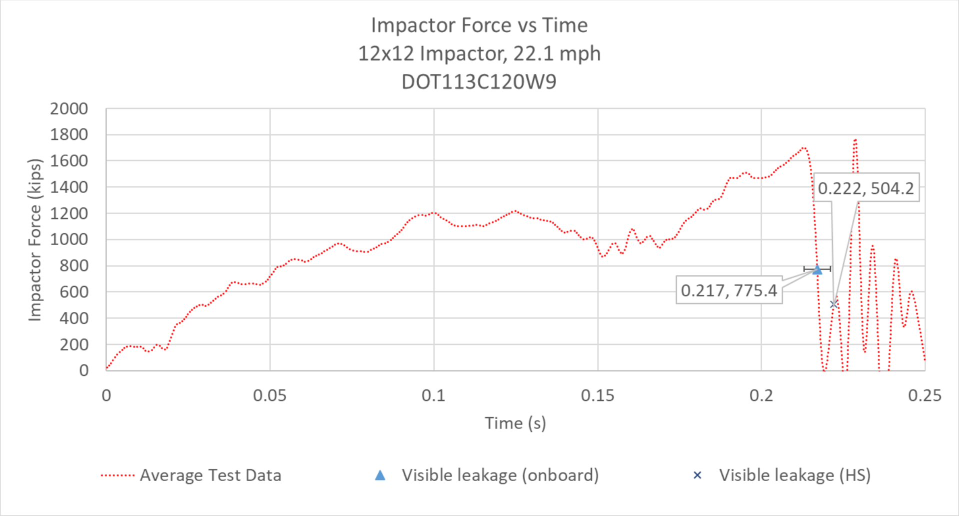

Figure 50. Impactor Force Versus Time with Times of Visible Leakage from Onboard and HS Cameras Annotated

Figure 51 contains a frame extracted from the onboard video at 0.217 seconds.

Figure 51. Frame from Onboard Video at 0.217 s

This frame contains an inset image with a zoomed-in view of the impactor, with an annotation indicating the visible leakage through the newly created tear in the outer tank. By 0.217 seconds, the impactor force had dropped to 406.4 kips from the global peak force (1,689 kips) that occurred at 0.213 seconds. This rapid drop in force is associated with the inner tank puncturing.

Figure 52 contains a still frame extracted from the isometric HS video of the test at 0.222 seconds, the approximate time at which the inner tank punctures. This figure shows the extent of the deformation that occurred up to that point.

Figure 52. Still Frame from HS Video Taken at 0.222 s

Figure 53 is a composite of video frames from the isometric HS camera at 0.220 seconds (left), 0.222 seconds (center), and 0.224 seconds (right). The frames have been zoomed in to 200 percent and show the escape of LN2 (circled in yellow) from the inner tank. The LN2 first becomes visible at the upper and lower corners of the impactor at 0.222 seconds.

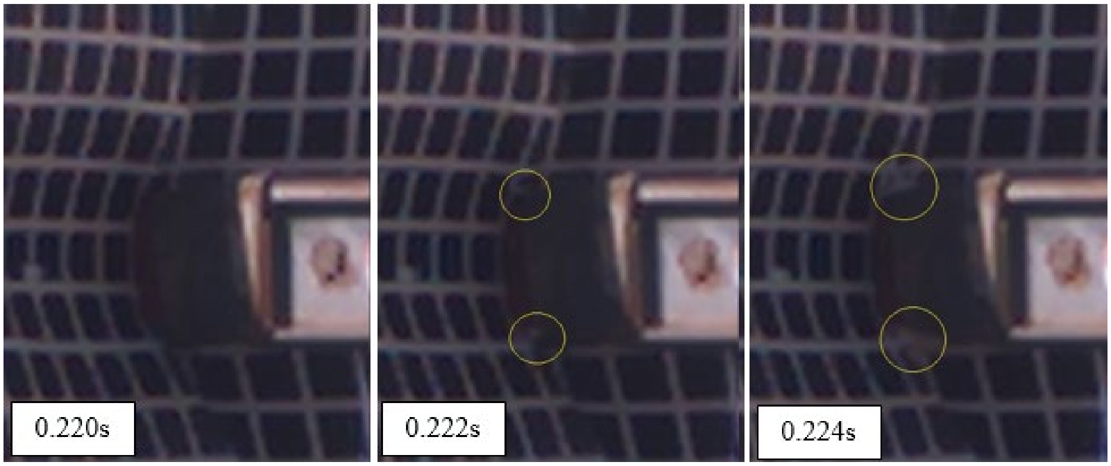

Figure 53. Composite of Zoomed Frames from Isometric Camera at 0.220 s, 0.222 s, and 0.224 s

4.8.6 Global Peak Internal Pressure

Figure 54 contains a plot of the average outage pressure versus time with an annotation indicating the peak outage pressure of 143.1 psig was reached at approximately 0.221 seconds.

This peak outage pressure is significantly above the 75 psig STD pressure of the PRV installed on the tank car. As can be seen in this figure, the pressure only exceeds 75 psig for slightly more than 50 ms. As previously shown in Figure 34, the pressure in the piping leading to the PRV did not reach the 75 psig STD pressure.

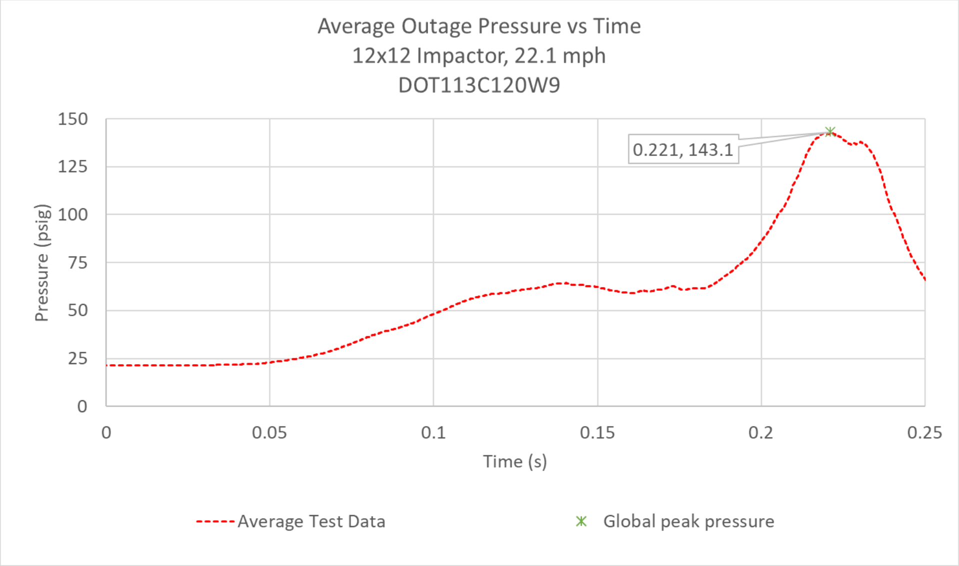

Figure 54. Average Outage Pressure Versus Time with Time of Global Peak Internal Pressure Annotated

Figure 55 contains a plot of the average force versus time with an annotation indicating the impactor force at the time the peak internal pressure occurred. This figure shows that the peak pressure lagged significantly behind the peak impactor force. At the time the peak internal pressure was measured the outer and inner tanks had both already punctured. The time of the peak force measurement occurs between the time visible leakage was observed in the onboard video and when visible leakage was visible on the high-speed video.

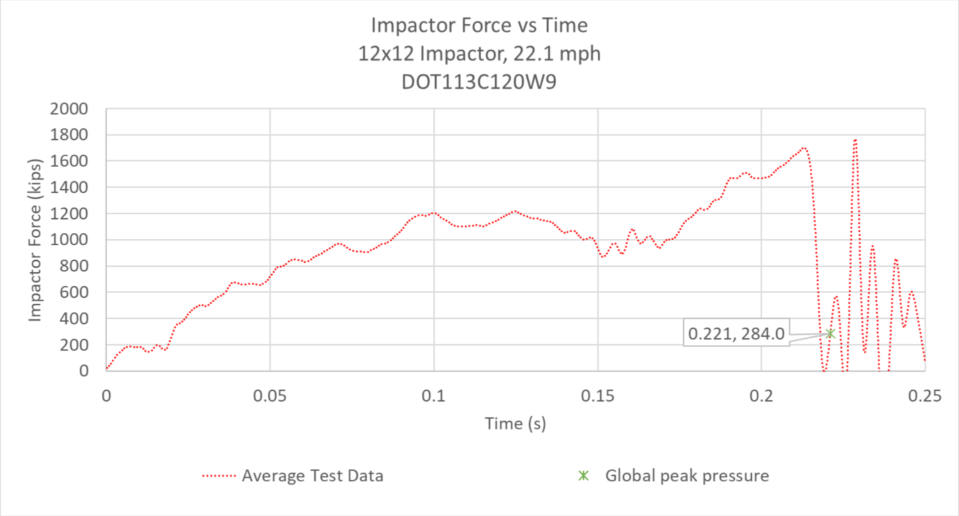

Figure 55. Impactor Force Versus Time with Time of Global Peak Internal Pressure Annotated

4.8.7 *Summary of Impact Sequence*

Figure 56 contains an annotated force versus time plot showing each of the events on a single plot. Figure 57 contains a similar plot for the average internal pressure versus time data. Review of the test data and videos confirms that the outer tank punctured prior to the inner tank. Leakage was observable in two different videos very soon after the global peak force was reached, indicating that the global peak force corresponded to puncture of the inner tank. The global peak pressure occurred late in the impact event, after the global peak force.

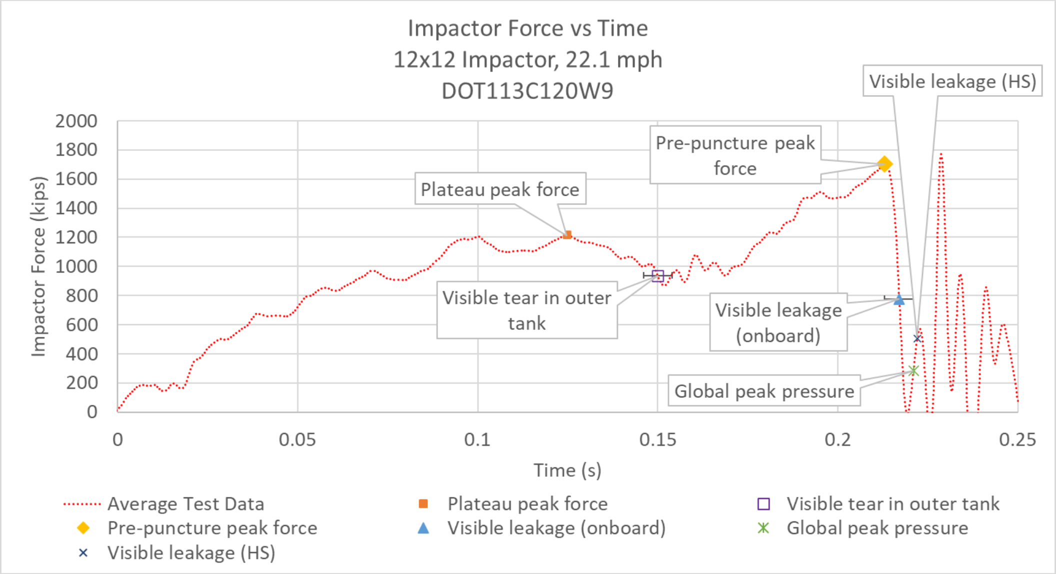

Figure 56. Annotated Plot of Impactor Force Versus Time

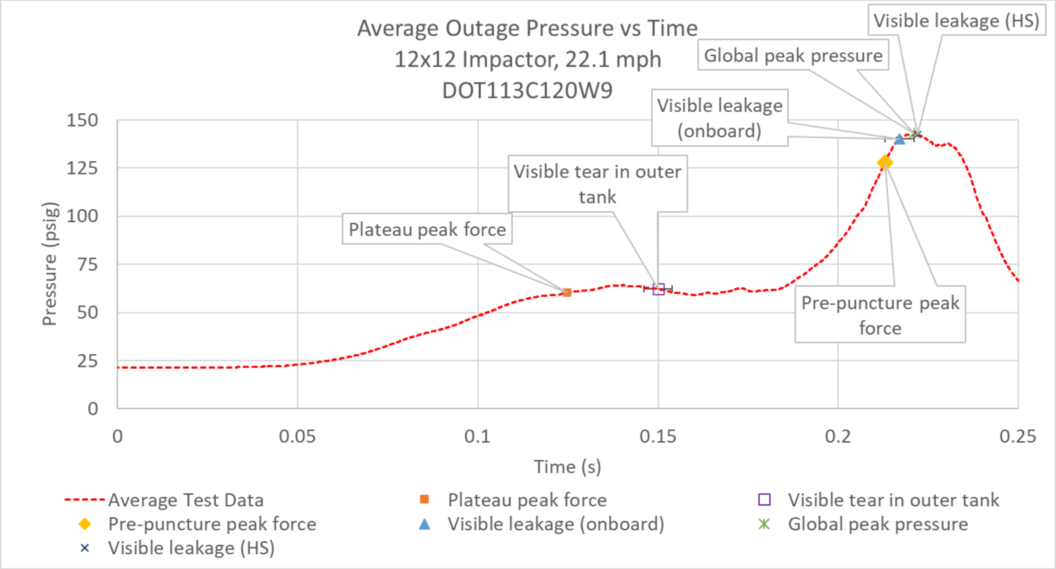

Figure 57. Annotated Plot of Average Outage Pressure Versus Time

5. FE Model Development

Researchers developed pre-test FE models of the DOT-113 tank car to help determine the targeted impact speed. The pre-test FE models provided estimates of the speed range where puncture could be expected to occur while considering uncertainties in the exact puncture speed, lading conditions, etc. The team developed FE models that incorporated and expanded upon several modeling techniques used during simulations of previous tank car impact tests [8, 9, 10, 11, 12, 13, 14, 15, 16, 6]. The DOT-113 models required definition of the tank car geometry, geometry of the impact setup (e.g., impact wall, impactor, etc.), definition of boundary conditions, constraints, initial conditions, and the development of several material models. Additionally, modeling features such as element types, mesh sizes, and fluid/structure interactions were selected.

The models were developed using the Abaqus/CAE preprocessor and executed in Abaqus/Explicit [23]. Abaqus/Explicit is a commercially available, general purpose, nonlinear FE solver capable of simulating dynamic impacts involving complex material behaviors such as plasticity and puncture. The solid mechanics simulation features used in the DOT-113 models included defining material models to describe the elastic-plastic behavior and fracture behavior of the inner and outer steel tanks. The team used the Bao-Wierzbicki (B-W) triaxiality-based damage initiation model to model damage initiation for fracture [24].

The Abaqus software also includes several modeling techniques to represent the gas and liquid phases of the lading, permitting these two phases to be modeled explicitly. The LN2 and GN2 of the tank were modeled using Lagrangian Equation-of-State (EOS) and pneumatic cavity approaches, respectively. Between Tests 12 and 13, simulation studies were conducted to examine several different modeling techniques to include a GN2 to LN2 condensation behavior into the model based on the outcome of Test 12 [6]. The results of these simulation studies were published in a standalone report [7].

5.1 Overview of Models

A DOT-113 tank car filled with LN2 presents several unique FE modeling challenges compared to modeling single-walled tank cars filled with water. These include:

1. Specific modeling techniques were required to simulate puncture of two tanks because a DOT-113 tank car features outer and inner tanks.
2. The inner tank was at a cryogenic temperature and its steel needed to be modeled with material definitions capturing the temperature and strain rate dependence of its plasticity and fracture behavior.
3. The GN2 in the outage could not be modeled directly as an ideal gas because the model needed to capture a phase change from gas to liquid (i.e., condensation) once the saturation pressure was exceeded during the impact.

The pre-test FE model for this test used material property definitions for the inner and outer tank steels developed based on tensile characterizations. The development of the FE model material inputs for the TC-128 outer tank material responses is described in detail in the Test 11 report [4]. The development of the FE model material inputs for the T304 inner tank material is described in detail in Appendix F.

Puncture-capable FE models feature more complex material definitions and meshes than non-puncture models. These models include inner and outer tanks with refined meshes in the impactor contact areas and material modeling behaviors to simulate element degradation and removal. For the DOT-113 tank car, the refined area was meshed using solid elements on both the inner tank and the outer tank. While the desired outcome of the DOT-113 test was puncture of both tanks, the solid patch of elements on the outer tank needed to be large enough to not only capture the initial tearing of the tank (which typically occurs beneath a corner of the impactor) but also to allow the tear to propagate until such a time as the inner tank punctured. This required a much larger solid patch of elements on the outer tank than for single-walled tanks to allow the tear to propagate fully without being artificially arrested by reaching the limits of the solid patch, as that could result in the modeled DOT-113 placing less demand on the inner tank than would be experienced during an impact test.

Experience in previous DOT-113 tank car and surrogate tests indicated that the MLI between the inner and outer tanks would not substantially contribute to the structural response during the impact test. The Test 13 FE model included a pressure load to represent the vacuum on the annular space but did not include a representation of the MLI, like the Test 12 model [6].

The point of impact on the tested DOT-113 tank car was planned to be offset (approximately 11 feet) from the centerline of the car. Both the pre- and post-test models included the full-length of the tank car without a symmetry condition. The tank car's geometry was simplified, and small structures expected to have an insignificant effect on the puncture speed were omitted. These simplifications have a relatively minor effect on the impact response of the tank under the test conditions. The FE model is shown in Figure 58.

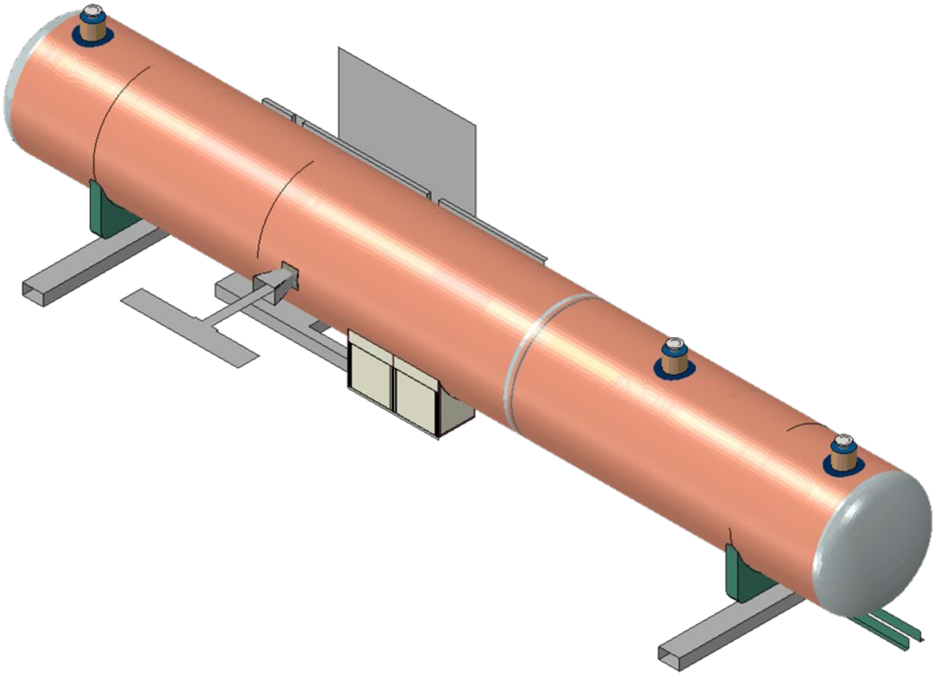

Figure 58. DOT-113 with LN2 FE Model

The LN2 lading in the Test 13 FE model was represented using a Lagrangian EOS for the LN2. A Lagrangian EOS approach was previously used to model the water in a test of a DOT-117 tank car [13] and a DOT-111 tank car meeting voluntary industry standard CPC-1232 [15], and to model the LN2 in a prior test of a DOT-113 surrogate (Test 12) [6].

The outage in recent shell impact FE models (Tests 6-12) was represented with a pneumatic cavity. The pneumatic cavity approach is a simplified modeling technique that represents a gas using uniform pressure over its entire volume. This uniform pressure will change over the course of the impact simulation by solving the ideal gas equation as the volume enclosing the pneumatic cavity is reduced through tank deformation. The cavity approach is commonly referred to as the uniform pressure method (UPM) in FE models of air bags in automotive crash simulations. The pneumatic cavity approach can be applied using either an adiabatic or an isothermal assumption. The team consistently used an isothermal assumption in tank car side impact simulations due to the relatively long duration of the pressurization in the outage compared to simulations where an adiabatic assumption might be used (e.g., the deployment of an airbag).

The parts included in the model can generally be divided into three categories: rigid bodies, deformable bodies made of steel, and deformable bodies made of other materials (e.g., membrane and lading). A section view, with the cutting plane passing through the center of the impactor, is shown in Figure 59. This image includes annotations denoting the various parts comprising the assembly of the DOT-113 tank car FE model.

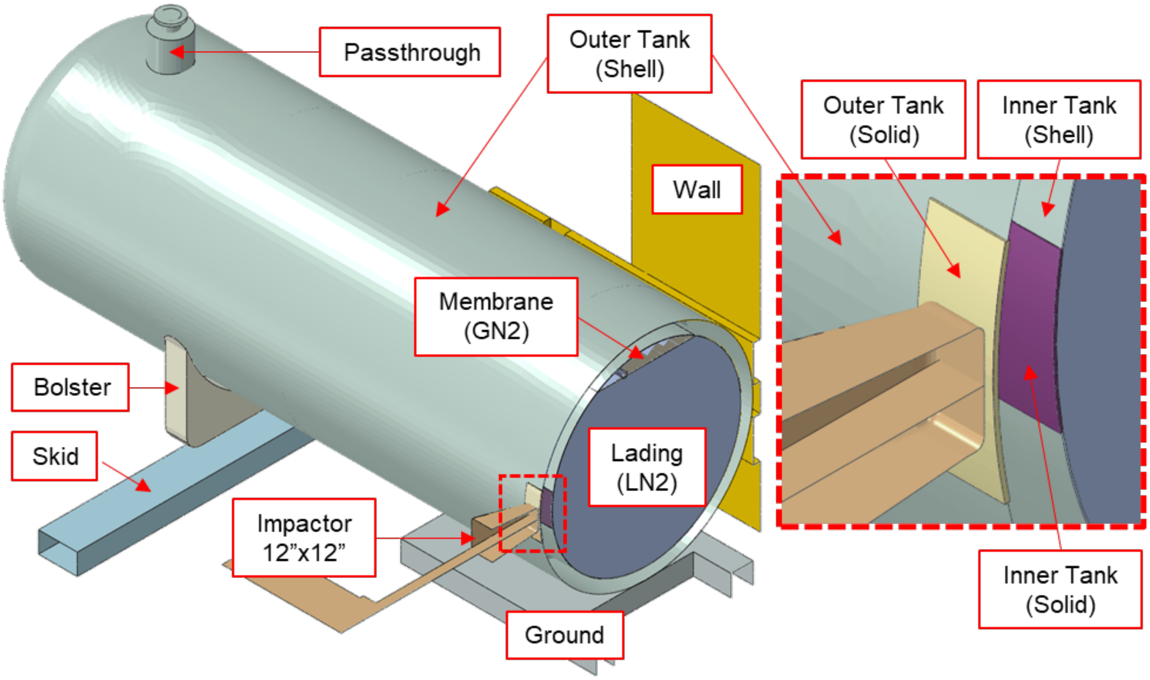

Figure 59. Section View through Impact Plane with Annotated Parts

Table 18 contains a summary of the parts comprising the FE model used in the post-test puncture simulation. This table contains the weight of the part in the FE model and the number of elements in that part's mesh. Due to parameterization of the outage volume (3 and 5 percent), the meshes and part weights were slightly different for the lading and membrane in different versions of the FE models. The parts are summarized in Table 18 using an outage of 3 percent. A full description of each part in the pre-test and post-test models can be found in Appendix D.

Table 18. Summary of Parts in FE Models (3% Outage)

Part Name	Type of Body	Material	Number of Elements	Part Weight
-	-		#	*lbf*
Impactor	Rigid	-	78,906	297,200
Wall	Rigid	-	1,658	-
Skids (x 2)	Rigid	-	736	7,000
Ground	Rigid	-	1,664	-
Outer Tank (Shell)	Deformable	TC-128	56,421	61,656
Outer Tank (Solid)	Deformable	TC-128	474,880	70
Inner Tank (Shell)	Deformable	T304	45,144	29,219
Inner Tank (Solid)	Deformable	T304	413,440	24
Bolsters and Stub Sills	Deformable	TC-128	3,484	8,085
Passthroughs	Deformable	T304	16,104	1,437
Piping	Deformable	T304	49,428	610
Lading	Deformable	LN2	98,430	215,080
Internal Membrane	Deformable	Other	12,792	469

The total weight of the parts in the FE model corresponding to the entire DOT-113 tank car (inner and outer tanks, LN2, etc.) was approximately 317,000 lbf. As previously discussed in Section 2.2.2, LN2 was used in the test to accomplish the following:

1. Account for the fluid mass
2. Consider the dynamic effects of a fluid-filled tank at a cryogenic temperature
3. Chill the stainless steel inner tank and alter its material properties

The tested DOT-113 tank car is designed to carry a cryogenic material (i.e., LNG) having a lower density than that of LN2.The tested tank car was intentionally overloaded (by weight) to ensure that the filling level (by volume) was not overly low. Based on previous experiments, researchers determined that the filling level would have a larger effect on puncture energy compared to lading weight.

5.2 Material Behaviors in FE Models

Several material definitions were used in both the pre-test and post-test FE models: ASTM A240 Type 304 stainless steel, AAR TC-128, Grade B carbon steel, a membrane material, GN2, and LN2. The material definitions for TC-128 steel, the membrane, and LN2 were the same as described in the Test 12 report [6]. The updated material properties input to the Test 13 FE model are summarized in this section for the T304 stainless steel and GN2. Complete descriptions of the development of the stainless steel and carbon steel material models are provided in Appendix F.

The results of the tensile characterization revealed that the TC-128 outer tank and T304 inner tank met their respective requirements in AAR Specifications for Tank Cars Appendix M-1002 [17] and ASTM A240 [7], respectively, for YS, UTS, and EB-2in. The average mechanical properties from eight TC-128 samples and three T304 samples used in the calibration of material definitions in the Test 13 DOT-113 FE model are summarized in Table 18. The T304 stainless steel material properties shown in this table were obtained from samples tested at a temperature of 77 K, which is the saturation temperature of LN2 at atmospheric pressure. The T304 had a higher strength and ductility at QS rates than at the tested elevated strain rate. The team set the strain rate at 0.1 s^{-1} for T304 to calibrate the behavior of the Test 13 FE model as a conservative estimate of puncture onset.

Table 19. Summary of Average YS, UTS, and EB from Tensile Tests used in FE Model Calibration

Steel	Temp.	Strain Rate	YS	UTS	EB-2in
	Kelvin	*s^{-1}*	*ksi*	*ksi*	*%*
T304 Stainless Steel	77	0.1	63.0	193.3	30.6
TC-128 Carbon Steel	294	QS	64.9	88.8	31.4

5.2.1 ASTM A240 Type 304 Stainless Steel

Prior to the side impact test, a section of the tank car's T304 inner tank was cut into flat ASTM E8 tensile coupons, as discussed in Section 4.6. Tensile tests were performed on nine DB coupons having typical dimensions of 2-inch GL, 0.5-inch gauge width, and 0.24-inch thickness. Three groups of three tensile tests were conducted at 1) QS strain rate and room temperature, 2) QS strain rate and cryogenic temperature, and 3) elevated strain rate (0.1 s^{-1}) and cryogenic temperature.

An FE model of the T304 coupons was created in Abaqus/Explicit using similar modeling techniques (i.e., mesh size, step time, mass scaling, etc.) to the tank car puncture model to calibrate a material input to the puncture model. A more detailed description of the calibration procedure of the T304 material input is contained in Appendix F. Figure 42 shows that the calibrated T304 material input was able to match the average UTS and EB results from the tensile tests at 77 K and 0.1 s^{-1}.

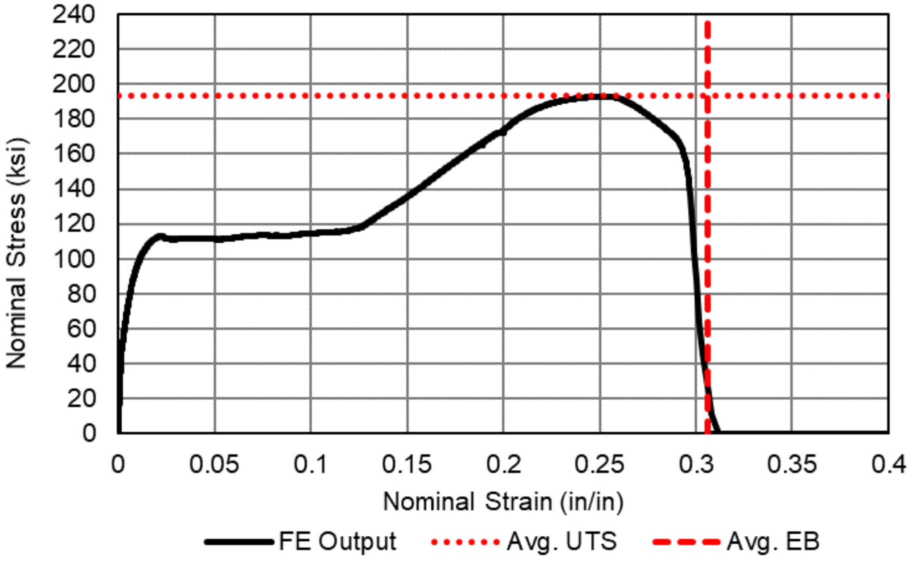

Figure 60. Nominal Stress-Strain Response from the T304 Stainless Steel Coupon FE Model (solid black) with Average Tensile Properties (dashed red) for Comparison at 77 K and 0.1 s^{-1}

Table 20 summarizes the material properties used for the T304 stainless steel inner tank in the FE models of the DOT-113 tank car. Damage progression was only specified for the solid patch.

Table 20. Summary of Material Properties for T304 Stainless Steel

Parameter	**Value**
Mass Density	7.35×10^{-4} lbf-s^2/in^4
Modulus of Elasticity	3×10^7 psi
Poisson's Ratio	0.25
Plasticity	Isotropic Hardening (see Appendix F)
Damage Initiation	Ductile Damage (see Appendix F)
Damage Progression	Displacement = 0.005 in/in^2, exponent = −2
Mesh Implementation	0.059-inch Reduced Integration Brick (C3D8R) Elements

5.2.2 AAR TC-128 Carbon Steel

The same TC-128 material input from Test 11 [4] and Test 12 [6] was used in the Test 13 pre- and post-test models. As discussed in Section 4.6, a spare section of the outer tank from Test 11 was cut into smooth round bar ASTM E8 tensile coupons during manufacturing. Tensile tests were performed on eight coupons having typical dimensions of 2-inch GL and 0.5-inch diameter. An FE model of the TC-128 tensile coupon geometry was used to calibrate a material model to match the average YS, UTS, and EB-2in (see Figure 61).

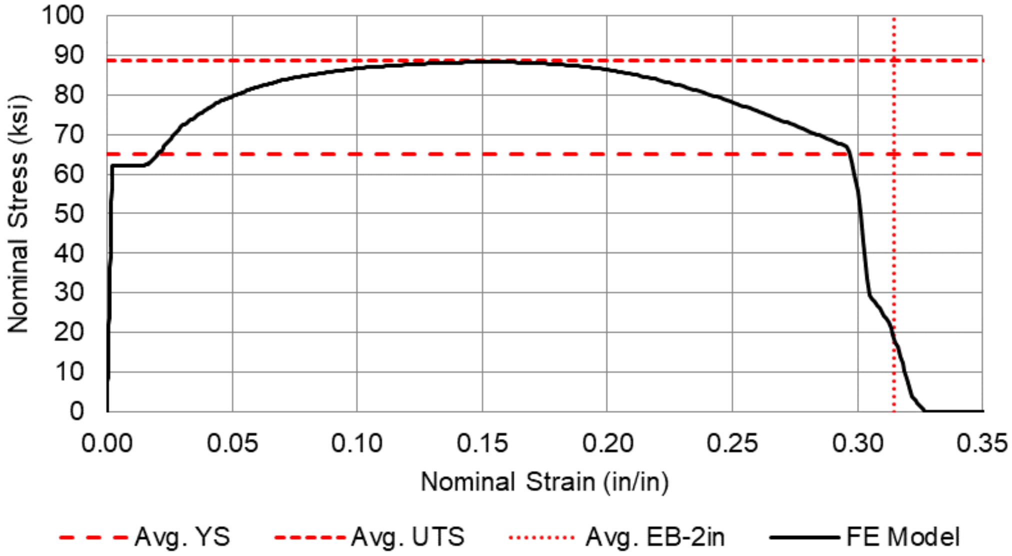

Figure 61. Nominal Stress-Strain Response from the TC-128 Carbon Steel Coupon FE Model (solid black) with Average Tensile Properties (dashed red)

The material properties of TC-128 steel used in the outer tank of the FE models is summarized in Table 21. Damage progression was only specified for the solid patch.

Table 21. Summary of Material Properties for TC-128 Carbon Steel

Parameter	Value
Mass Density	7.35×10^{-4} lbf-s^2/in^4
Modulus of Elasticity	3×10^7 psi
Poisson's Ratio	0.3
Plasticity	Isotropic Hardening (see Test 11 report [4])
Damage Initiation	Ductile Damage (see Test 11 report [4])
Damage Progression	Displacement = 0.005 in/in^2, exponent = −1
Mesh Implementation	0.08-inch Reduced Integration Brick (C3D8R) Elements

The DOT-113 FE model for this test (Test 13) used the same TC-128 material properties as the last two DOT-113 surrogate FE models (Test 11 and 12) because the material characterization conducted on the Test 13 outer tank revealed that its TC-128 was similar in ductility and strength to the TC-128 in Test 11 and Test 12. The team determined that the mechanical properties of TC-128 from Test 11 were typical, and it was expected that a slight difference in TC-128 fracture toughness would not significantly affect the FE model results.

5.2.3 Membrane

As described in Appendix D, an artificial surface was modeled within the tank to define the limits of the hydraulic and pneumatic cavities. Because this surface does not correspond to any physical structure within the tank, modeling techniques were chosen to minimize the increase in either artificial mass or stiffness introduced to the model by the membrane, while negatively impacting the FE model's stability or runtime. The material properties of the membrane are summarized in Table 22.

Table 22. Material Properties Defined for Membrane Material

Parameter	Value
Density	7.35×10^{-6} lbf·s^2/in^4
Modulus of Elasticity	1×10^4 psi

5.2.4 Gaseous Nitrogen (GN2)

The gas phase of the lading was modeled as GN2 within Abaqus using a pneumatic cavity with fluid leakage to represent condensation of GN2 to LN2. The fluid cavity with leakage technique was developed following Test 12, based on the determination that GN2 had condensed into LN2 during that test. The process of developing and calibrating a fluid cavity with leakage model was previously discussed in a separate report [7]. Figure 62 shows the fluid cavity leakage definition used to represent condensation of GN2 to LN2 at an isothermal temperature of −290.5 °F (94 K) in the pre- and post-test FE models.

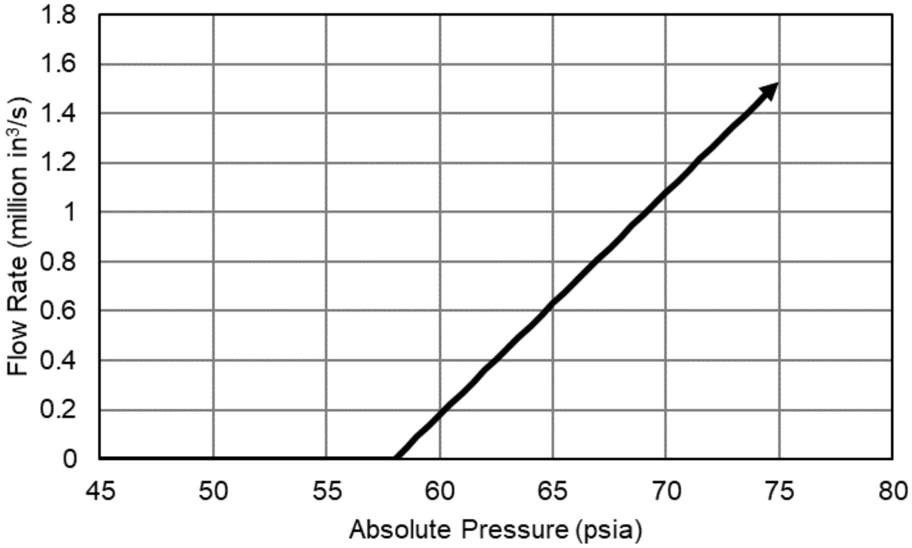

Figure 62. Volumetric Flow Rate Versus Gauge Outage Pressure

Researchers used different outage volumes and temperatures in the pre-test models based on their experience in Test 12 [6] where the outage volume and temperature were difficult to control with cryogenic lading. The initial pressure in the pre-test model was set to 30 psig to repeat the initial condition from Test 12. The pre-test outage volume was set at 3 and 5 percent based on uncertainties in the lading volume.

After the test, the post-test model was updated to reflect the initial pressure of 22 psig that was averaged 1 second prior to impact (refer to Section 4.6.1). The outage volume was still set to 3 and 5 percent because the volume of LN2 could not be measured accurately prior to impact (refer to Section 4.6.3).

The initial pressure and temperature are discussed further in Appendix E. The modeling inputs defined for the GN2 phase of the model are summarized in Table 23, using the unit system used in the FE models.

Table 23. Properties for GN2 (Pneumatic Cavity)

Property	**Pre-test Value**	**Post-test Value**	**Reference**
Universal Gas Constant ©	73.583 in-lbf/(mol·K)	73.583 in-lbf/(mol·K)	[26]
Molecular Weight (*MW*)	1.60 x 10^{-4} lbf·s^2/(in·mol)	1.60 x 10^{-4} lbf·s^2/(in·mol)	[21]
Outage Volume	3 and 5%	3 and 5%	
Isothermal Temperature	94 K	94 K	
Initial Pressure	30 psig	22 psig	
Molar Specific Heat at Constant Pressure ($c_{p,m}$)	257.59 in-lbf/(mol-K)	257.59 in-lbf/(mol-K)	[21]

The molar specific heat capacity at constant pressure ($c_{p,m}$) for GN2 was calculated according to Equation 1. Values for the specific heat capacity of GN2 at constant pressure (c_p) were obtained from published values [21].

$$c_{P.m} = c_P \cdot MW \qquad \text{Eq. 1}$$

5.2.5 Liquid Nitrogen (LN2)

The pre-test target initial conditions for the side impact test were set to an outage volume of 3 and 5 percent and internal pressure of 30 psig. Within Abaqus, a Lagrangian Mie-Grüneisen EOS with the linear Us – Up Hugoniot form was used to describe the behavior of the LN2. The key material properties that must be input to this material model are the material's density, speed of sound, and viscosity. The necessary material properties were obtained from the NIST Chemistry WebBook, SRD 69 [21]. Additionally, a tensile cutoff stress of zero was specified for the EOS material so that the LN2 could not hold a tensile stress. The authors have specified a tensile cutoff stress of zero in all previous tank car side impact FE models [6, 14, 16] that used a Lagrangian EOS representation of the lading. However, the team encountered an input error in the pre-test FE model, and the tensile cutoff stress was not included; researchers corrected the input error in the post-test versions of the FE model. Initial conditions are discussed further in Appendix E.

The fluid's bulk modulus (K) can be determined from the speed of sound © and density (ρ) according to the Newton-Laplace equation given in Equation 2 [27]. Abaqus calculates the bulk modulus internally using this equation to determine the compressibility of the fluid.

$$K = c^2 \rho \qquad \text{Eq. 2}$$

The material properties of LN2 were determined at 86 K (−305 °F) and 42.3 psia (30 psig) in the pre-test models based on the planned test conditions at the time of the modeling. After the test, the post-test properties of LN2 models were determined at 85 K (−307 °F) and 34.3 psia (22 psig) based on the measured pressures before the impact test. The temperature was lowered slightly (1 K) to ensure that it was below the saturation temperature at the updated post-test pressure. Table 24 shows a summary of the material properties of LN2 used in the pre- and post-test models. This table includes the specific units used in the unit system of the FE model.

Table 24. Properties of LN2 Used in FE Models

Property	Pre-test Value	Post-test Value	Reference
Mass Density (ρ)	7.162×10^{-5} lbf·s^2/in^4	7.206×10^{-5} lbf·s^2/in^4	[21]
Speed of Sound ©	3.001×10^{4} in/s	3.041×10^{4} in/s	[21]
Bulk Modulus (K)	6.450×10^{4} psi	6.664×10^{4} psi	Eq. 2
Viscosity (μ)	1.699×10^{-8} psi·s	1.760×10^{-8} psi·s	[21]

An initial hydrostatic compression stress corresponding to the outage pressure was applied to the LN2 in the pre-test (30 psig) and post-test (22 psig) models to maintain equilibrium with the pressure from GN2. The material property definition of LN2 was not updated in the FE model to account for the LN2 being below its saturation temperature (81 K vs 85 K) for the higher outage case (3 vs 5 percent outage). The team determined that LN2 was relatively incompressible when compared with GN2, and the slight difference in LN2 temperature would likely not affect the puncture outcome of the models.

5.3 Modeling Techniques Adjusted Between Pre-test and Post-test Models

A few modeling parameters were adjusted from the pre- to post-test models. The adjustments were made based on the actual test conditions and considerations of model runtime. These modeling techniques and their adjustments are summarized in Table 25.

Table 25. Summary of Adjustments Made Between Pre- and Post-test Models

Modeling Feature	Condition in Pre-test Model	Condition in Post-test Model	Explanation
Impact Speed	Varied	22.1 mph	The impact speed was adjusted to match test speed.
Fluid Pressure	30 psig	22 psig	The pre-test outage initial pressure was based on the initial condition from Test 12 [6] and was updated to reflect Test 13 in the post-test model.
Tensile Cutoff Stress	Not enabled	Enabled	The team identified an error in the pre-test FE model that allowed the LN2 to hold a tensile stress.

5.3.1 Impact Speed

Pre-test FE models were used to simulate impacts over a range of speeds from 18 to 23 mph. The purpose of the pre-test models was to aid in test planning by estimating the outcomes (e.g., impact forces, puncture of one or both tanks, etc.) over a range of speeds so that a target impact speed could be chosen. The pre-test results presented in this report used an impact speed of 22 mph which was the closest to the actual measured speed of 22.1 mph. Post-test FE models were run using 22.1 mph. The post-test FE models were run at the same speed as the test to facilitate comparison of test and model results as part of a model validation program.

5.3.2 Initial Pressure

The initial pressure assigned to GN2 and LN2 in the pre-test model was set at 30 psig based on the initial pressure measured in Test 12 [6]. The post-test model was updated to the average initial pressure measured in the outage in Test 13. The post-test model used 22 psig, the average measured pressure just prior to impact (see Section 4.6.1).

5.3.3 Tensile Cutoff Stress

The LN2 in the FE model used an EOS material input with a tensile cutoff stress of zero, as discussed in Section 5.2.5. The pre-test models encountered an input error where the zero tensile cutoff stress was not included in the FE model, allowing the LN2 to hold a tensile stress. As a result, the force versus impactor travel response from the pre-test FE model was stiffer than it should have been once the LN2 was sloshing. The team corrected the input error and included the zero tensile cutoff stress in the post-test models.

6. Comparison of Test Responses to Finite Element Analyses

This section compares the result from the pre- and post-test FE models with test measurements. While the post-test model was run at the measured test speed of 22.1 mph and measured initial pressure of 22 psig, the pre-test models were not run with these parameters as they were unknown prior to the test. The force-displacement results and pressure-time history results from analyses using the pre-test model are presented for comparison with the test measurements below in Section 6.1. The post-test model was updated from the pre-test version as discussed in Section 5.3, and the results from the post-test model are compared with test measurements in Section 6.2.

6.1 Pre-test FE Model Comparison

One of the intended uses of the pre-test models was to estimate the range of impact speeds over which puncture of both the inner and outer tanks would be likely to occur. Due to uncertainties in the expected test conditions prior to Test 13, the pre-test model was run at 3 and 5 percent outage. The internal pressure was initially set at 30 psig based on the pre-test target and the isothermal outage temperature was set at 94 K based on the post-test FE model from Test 12 [6]. These initial conditions were later updated in the post-test FE model.

The authors used earlier versions of the pre-test FE model to investigate variations in outage volume, isothermal outage temperature, stainless steel fracture toughness, etc.; however, these model results have been excluded from this report for brevity. The pre-test model results presented in this report were run in the week before the side impact test because the results of cryogenic temperature and elevated strain rate pre-test material characterization of the inner tank's T304 stainless steel (see Section 4.7.2) were available ten days prior to the test.

The target speed for the test was set at 22 ± 0.5 mph (actual impact speed 22.1 mph) based on these pre-test FE results because a puncture outcome was desired. The team decided to target an impact speed that would likely result in puncture with the knowledge that there could be significant residual speed after puncture due to a smaller than anticipated outage volume.

Figure 63 compares the impact force versus impactor travel for the pre-test FE models at 22 mph with the outage temperature set to 94 K and an initial pressure of 30 psig. The pre-test model set the initial outage volumes at 3 and 5 percent based on static head pressure gauge measurements made during filling. It should be noted that the team discovered an error in the material input for the LN2 in the pre-test model that allowed the liquid to hold a tensile stress. This error was corrected in the post-test FE model as discussed in Section 5.3.3.

While the FE model used a rigid impactor with a single acceleration-time history, the ram car in the test featured five longitudinal accelerometers. The test force reported in this section is the average of four of the longitudinal accelerometer channels excluding BA1CX. Both the test and FE forces reported in this section were filtered using a CFC60 filter [22]. The pre-test models were intended to bound the test response, but did not accurately predict the plateau in force from approximately 48 to 54 inches of impactor travel observed in the test data.

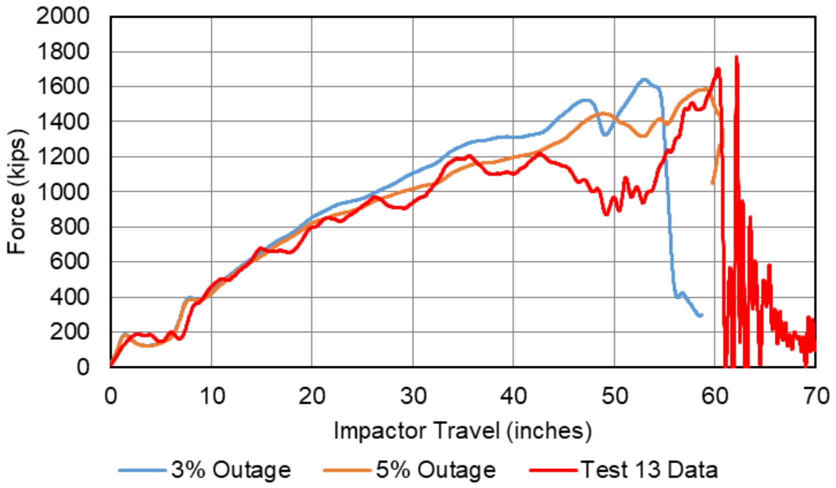

Figure 63. Force-displacement Responses from Pre-test FEA at 3 and 5% Outage Compared to Test Results

Figure 64 compares the GN2 pressure-time histories from the pre-test FE models shown in Figure 63 with the average test pressure measured in the outage. The test measurements were made using 3 combination pressure-temperature transducers placed in passthroughs leading to the top of the inner tank's outage.

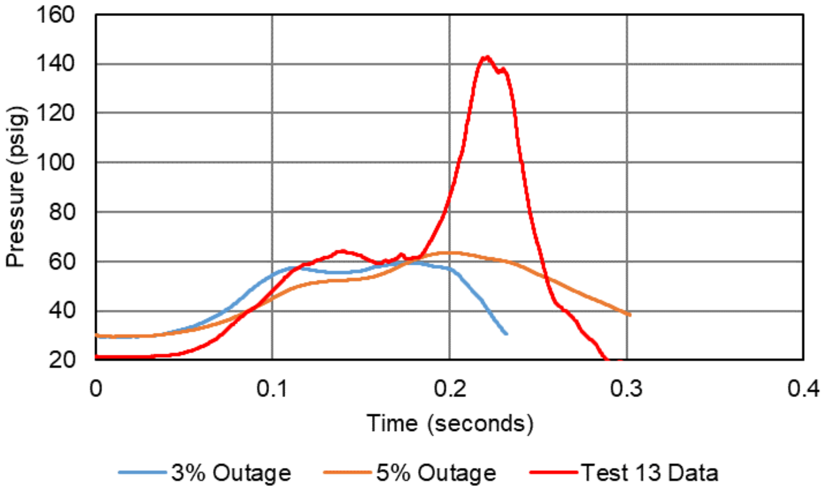

Figure 64. GN2 Pressure-time Responses from Pre-test FEA at 3 and 5% Outage Compared to Test Results

6.2 Post-test FE Model Comparison

The pre-test FE models were updated as discussed in Section 5.3 to reflect the actual test conditions. In this section, comparisons are made between the post-test FE model and the test measurements. Researchers found that the post-test FE model was in reasonable agreement with the test results.

Figure 65 compares the impact force versus impactor travel responses from the post-test FE model with the average test measurements. The post-test models used modeling techniques directly from the pre-test models. The initial conditions of the post-test model have been updated as previously described in Section 5.3.

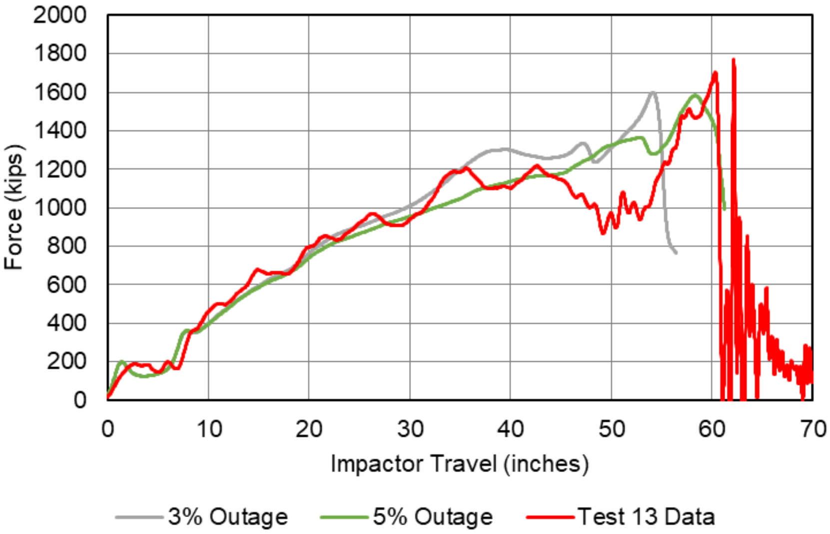

Figure 65. Force-displacement Responses from the Post-test Model at 3 and 5% Outage Compared to Test Results

The post-test model was in excellent agreement with the test's force-displacement behavior up to approximately 35 inches of impactor travel for both outage levels. After that displacement the test data exhibited a plateau in force while the model data continued to rise. While both the test data and the post-test model exhibited a drop in force prior to the global peak force, the magnitude of this drop was larger in the test than in the model. The peak force reached by the model is slightly lower than the test measurement and occurred at a lower displacement.

Figure 66 compares the GN2 pressure time histories from the post-test FE models with the average of the test measurements. The test measurements were made using three combination pressure-temperature transducers positioned in passthroughs connected to the top of the outage (TP1, TP2, and TP3).

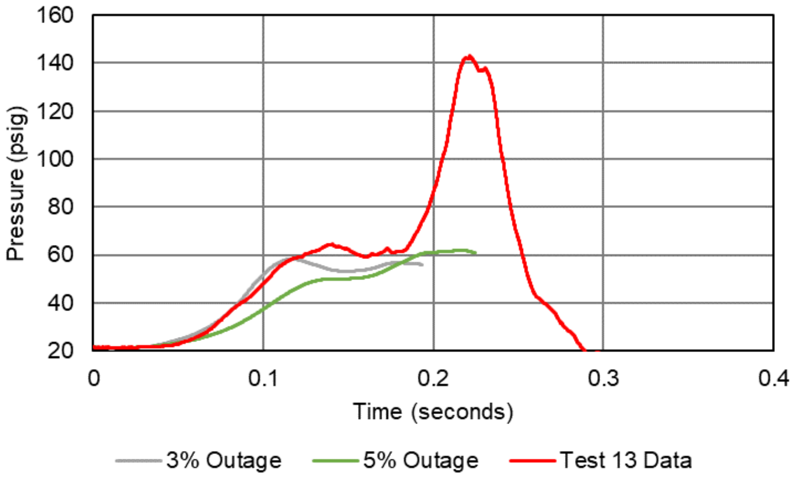

Figure 66. GN2 Pressure Time History from the Post-test FE Model at 3 and 5% Outage Compared to Test Results

Table 26 summarizes the results at the time of pre-puncture peak force from the post-test FE models and compares them with the test results. The peak results were not directly compared due to model termination shortly after puncture.

Table 26. Comparison of Results from Post-test FEA and Test at Time of Peak Force

Peak Measurement	**Test**	**Post-test FEA 3% Outage**	**Post-test FEA 5% Outage**
Impactor Acceleration (g)	5.7	5.4	5.3
Impactor Force (kip)	1702	1600	1583
Impactor Travel (inch)	60.3	54.1	58.4
East Skid Displacement (inch)	-15.1	-9.5	-11.2
West Skid Displacement (inch)	-4.2	0.0	-0.4
East Head Displacement (inch)	-17.0	-11.2	-13.4
West Head Displacement (inch)	-2.7	0.4	-0.3
Avg. GN2 Pressure (psig)	127.6	56.7	61.1

7. Comparison of Results with Previous DOT-113 Tests

This test was the last in a series of four tests conducted on DOT-113 tank cars and tank car surrogates. The overall objective of this test series was to examine the potential improvement in shell puncture resistance for a DOT-113 tank car with an outer shell made of 9/16-inch-thick TC-128 steel compared with a baseline DOT-113 tank car using 7/16-inch-thick A516-70 steel under LNG service conditions. Four tests were planned, with each successive test increasing in both complexity and realism compared to the previous test. The team conducted companion FE modeling for each test, with the FE model increasing in complexity as results and observations from each test were studied and synthesized. Details of the testing sequence are summarized in Table 27.

Table 27. Summary of DOT-113 Side Impact Test Conditions

Test Number	Test 10 [3]	Test 11 [4]	Test 12 [6]	Test 13 (this report)
Test Date	November 2019	July 2020	July 2021	May 2022
Test Article	DOT-113C120W	DOT-113 surrogate	DOT-113 surrogate	DOT-113C120W9
Thickness (Outer Tank)	7/16 inch	9/16 inch	0.608 inch	9/16 inch
Material (Outer Tank)	A516-70	TC-128	TC-128	TC-128
Diameter (Outer Tank)	~119 inches	~120 inches	~120 inches	~120 inches
Length (Outer Tank)	~74 feet	~45 feet	~46 feet	~75 feet
Thickness (Inner Tank)	¼ inch	¼ inch	¼ inch	0.296 inch
Material (Inner Tank)	T304 stainless steel	T304 stainless steel	T304 stainless steel	T304 stainless steel
Diameter (Inner Tank)	~106 inches	~106 inches	~106 inches†	~108 inches†
Volume (Inner Tank)	32,900 gal	19,300 gal	17,900 gal†	34,500 gal†
Tank Lading	Water	Water	LN2	LN2
Outage	17.6%	17.6%	9% (estimated)	3 to 5%
Pressure	50 psig	50 psig	30 psig	22 psig
Insulation	Perlite	MLI	MLI	MLI
Annular Pressure	Vacuum	Atmospheric	Vacuum	Vacuum
Impact Speed	16.7 mph	17.3 mph	18.3 mph	22.1 mph
Outcome	Puncture	No Puncture	No Puncture	Puncture

† The inner tank values reported here are at room temperature; however, Test 12 and Test 13 were conducted at cryogenic temperature with LN2. The inner tank volume was reduced by approximately 1 percent due to thermal contraction.

Figure 67 shows force-displacement responses from all the DOT-113 tank cars and surrogates tested in the series. The legacy DOT-113 tank car from Test 10 and the DOT-113C120W9 in Test 13 punctured, while the surrogates in Test 11 and Test 12 did not puncture. The legacy

DOT-113 tank car in Test 10 punctured at a lower force (800 kips) and impactor displacement than the Test 13 tank car. The legacy DOT-113 tank car was unable to resist a 16.7 mph impact. The Test 11 DOT-113 surrogate tank car resisted an impact of 17.3 mph and the Test 12 DOT-113 surrogate tank car resisted an impact of 18.3 mph. The Test 13 DOT-113 punctured from a 22.1 mph impact after absorbing approximately 4.4 million ft-lbf of energy. The 297,000 lbf ram car would have 4.4 million ft-lbf of kinetic energy when traveling at approximately 21 mph. Thus, the target impact speed of 22 ± 0.5 mph only slightly exceeded the speed necessary to cause puncture. If the team had chosen a lower target impact speed (e.g., 21 ± 0.5 mph), then there is a possibility that Test 13 would not have resulted in a puncture. With the completion of Test 13, additional FEA using LNG in the model and setting the inner tank at LNG’s temperature are planned to evaluate the performance of the DOT-113C120W9 under LNG service conditions.

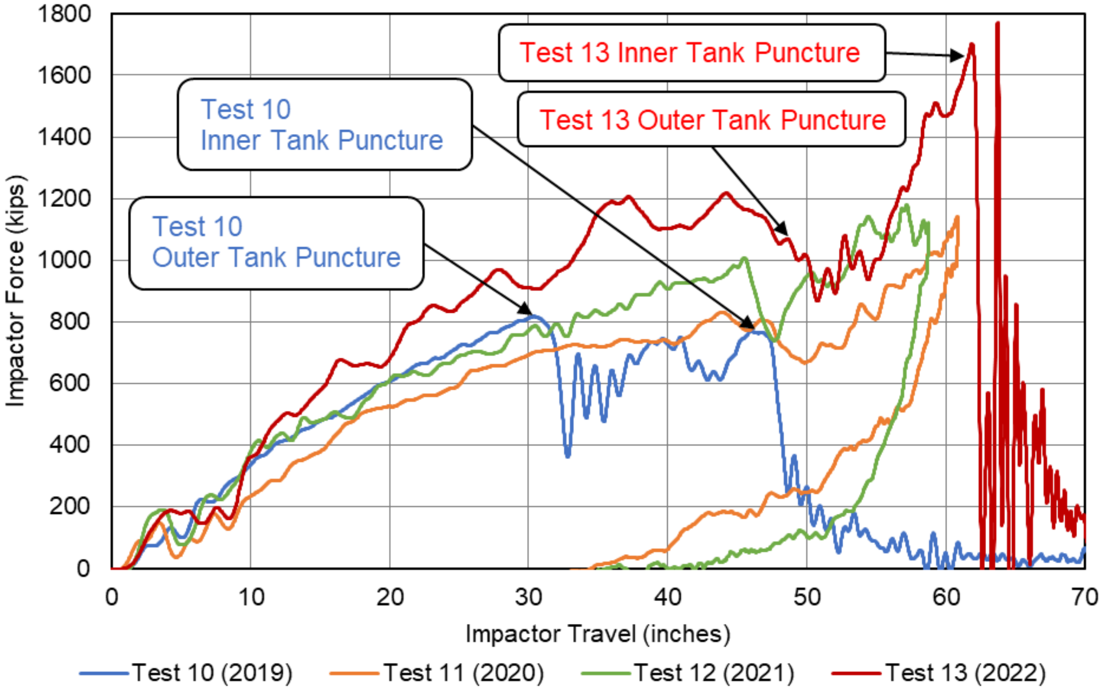

Figure 67. Comparison of Force-Displacement Responses from Test 10, 11, 12, and 13

8. Conclusion

As part of a series of DOT-113 tank car side impact tests, FRA sponsored a research team to test and analyze the side impact puncture performance of a DOT-113C120W9 tank car using a cryogenic lading. At the time of the test, the inner tank was filled to between 95 and 97 percent of its volume with LN2 and the pressure inside the inner vessel was approximately 22 psig. The test was intended to cause an impact to the tank car at a speed high enough to puncture both tanks. The tank car was impacted by a 297,000 lb ram car equipped with a 12 by 12-inch impactor at a speed of 22.1 mph. The test resulted in the puncture of both the inner and outer tanks. The energy absorbed by the tank car at the time the inner tank punctured was almost 4.4 million ft-lbf, equivalent to the 297,000 lb ram car traveling at approximately 21 mph.

Pre-test analyses predicted that puncture of the tank car was likely but not certain under the range of initial conditions and fluid behaviors investigated. Due to uncertainties in the initial conditions and fluid behavior, the goal of the pre-test modeling was to bound the observed behavior in the test, not to predict the exact threshold puncture speed. The test measurements confirmed that the modeling techniques provided a good representation of the cryogenic fluid behavior within the tank car. The model successfully captured the test behavior.

While numerous technical challenges arose during the pre-test planning, modeling, and execution phases, the test was successful in providing meaningful scientific data to understand the complexities of cryogenic stainless steel and cryogenic fluid behavior. The four tests of DOT-113 tank cars and surrogates over the course of this program culminated in the safe, successful puncture test of a DOT-113 tank car under cryogenic conditions. The FE modeling techniques developed during this program and shown to produce reasonable agreement with test measurements for cryogenic tank car impact can be adapted to additional cryogenic impact scenarios (e.g., different filling levels, different pressures, different cryogenic ladings) in future studies.

This testing and analysis support FRA’s tank car research program to provide a technical basis for rulemaking on enhanced and alternative performance standards for tank cars.

9. References

[1] Pipeline and Hazardous Materials Safety Administration (PHMSA) (2015). Tank-head puncture-resistance systems.

[2] PHMSA (2015). Performance standard requirements (DOT-117P).

[3] Trevithick, S., Carolan, M., Eshraghi, S., & Wilson, N. (2021). Side Impact Test and Analyses of a Legacy DOT-113 Tank Car (Report No. DOT/FRA/ORD-21/28). Federal Railroad Administration.

[4] Wilson, N., Carolan, M., Trevithick, S., & Eshraghi, S. (2021). Side Impact Test and Analyses of a DOT-113 Surrogate Tank Car with Water (Report No. DOT/FRA/ORD-21/35). Federal Railroad Administration.

[5] Eshraghi, S., Krishnamurthy, A., & Carolan, M. (2022). Finite Element Analyses of Side Impacts to DOT-113 Surrogate Tank Cars with Water and Liquid Nitrogen (Report No. DOT/FRA/ORD-22/22). Federal Railroad Administration.

[6] Belport, S., Carolan, M., Trevithick, S., Eshraghi, S., & Krishnamurthy, A. (2022). Side Impact Test and Analyses of a DOT-113 Surrogate Tank Car with Cryogenic Lading (Report No. DOT/FRA/ORD-22/33). Federal Railroad Administration.

[7] Carolan, M., Eshraghi, S., & Krishnamurthy, A. (N.D.). Modeling and Analysis of Phase Change in a DOT-113 Tank Car Surrogate Filled with Liquid Nitrogen (Report No. Pending). Federal Railroad Administration.

[8] ASTM International (2019). *ASTM A240/A240M: Standard Specification for Chromium and Chromium-Nickel Stainless Steel Plate, Sheet, and Strip for Pressure Vessels and for General Applications.* Conshocken, PA.

[9] Kirkpatrick, S. (2010). Detailed Puncture Analyses of Various Tank Car Designs - FInal Report - Revision 1. Applied Research Associates.

[10] Carolan, M., Jeong, D., Perlman, B., Yellapu, M., Namboodri, S., Kurtz, B., Elzey, R., Anankitpaiboon, S., Tunna, L., & Fries, R. (2013). Application of Welded Steel Sandwich Panels for Tank Car Shell Impact Protection (Report No. DOT/FRA/ORD-13/19). Federal Railroad Administration.

[11] Kirkpatrick, S., & Rakoczy, P. M. R. (2015). Side Impact Test and Analyses of a DOT-111 Tank Car (Report No. DOT/FRA/ORD/15-30). Federal Railroad Administration.

[12] Rakoczy P., & Carolan, M. (2016). Side Impact Test and Analysis of a DOT-112 Tank Car (Report No. DOT/FRA/ORD-16/38). Federal Railroad Administration.

[13] Carolan M., & Rakoczy, P. (2019). Side Impact Test and Analyses of a DOT-105 Tank Car (Report No. DOT/FRA/ORD-19/12). Federal Railroad Administration.

[14] Rakoczy, P., Carolan, M., Gorhum, T., & Eshraghi, S. (2019). Side Impact Test and Analyses of a DOT-117 Tank Car (Rerport No. DOT/FRA/ORD-19/13). Federal Railroad Administration.

[15] Wilson, N., Eshraghi, S., Trevithick, S., Carolan, M., & Rakoczy, P. (2020). Side Impact Test and Analyses of a DOT-105 Tank Car- 6x6 Inch Indenter (Report No. DOT/FRA/ORD-20/38). Federal Railroad Administration.

[16] Eshraghi, S., Trevithick, S., Carolan, M., Rakoczy, P., & Wilson, N. (2020). Side Impact Test and Analyses of a DOT 111 (CPC-1232) Tank Car (Report No. DOT/FRA/ORD-20/43). Federal Railroad Administration.

[17] Krishnamurthy, A., Trevithick, S., Carolan, M., Spangenberg, U., Wilson, N., Eshraghi, S., & Kirkpatrick, S. (2022). Review of Tank Car Side Impact Test Research and Analyses of 2007–2019 (Report No. DOT/FRA/ORD-22/14). Federal Railroad Administration.

[18] Association of American Railroads (2014). AAR Manual of Standards of Recommended Practices, Section C-III, Standard M-1002, Specifications for Tank Cars, Appendix M.

[19] Federal Register (2020). Vol 85, No. 143, Rules and Regulations.

[20] ASTM International (2020). Standard Specification for Chromium and Chromium-Nickel Stainless Steel Plate, Sheet, and Strip for Pressure Vessels and for General Applications (Report No. ASTM A240/A240M-19).

[21] Lemmon, E. W., Bell, I. H., Huber, M. L., & McLinden, M. O. (2023). Thermophysical Properties of Fluid Systems. *NIST Chemistry WebBook, NIST Standard Reference Database Number 69*, P. J. Linstrom and W. G. Mallard, Eds. National Institute of Standards and Technology.

[22] Transportation Technology Center, Inc. (2019). Test Implementation Plan for FRA Tank Car Side Impact, Revision 2. TTCI, Pueblo, CO.

[23] SAE International (2007). Instrumentation for Impact Test - Part 1: Electronic Instrumentation (Report No. J211/1_202208). SAE, Warrendale, PA.

[24] Dassault Systèmes Simulia Corp. (2019). *Abaqus 2019, Test Configurations for Abaqus 2019 Products*.

[25] Bao Y. & Wierzbicki, T. (2004). On fracture locus in the equivalent strain and stress triaxiality space. *International Journal of Mechanical Sciences, 46,* 81-98.

[26] Engineering Toolbox (2004). Universal and Individual Gas Constants.

[27] Smits, A. J. (2000). A Physical Introduction to Fluid Mechanics. New York: John Wiley and Sons.

[28] ASTM International (2013). *ASTM E8/E8M: Standard Test Methods for Tension Testing of Metallic Materials.* ASTM, West Conshocken, PA.

[29] Engineering Toolbox (2003). Air - Altitude, Density and Specific Volume.

[30] United States Geological Survey (USGS) (2002). Geographic Names Information System (GNIS) Detail - City of Pueblo. [Accessed 18 January 2022].

[31] Paredes, M., Sarzosa, D., Savioli, R., Wierzbicki, T., Jeong, D., & Tyrell, D. (2018). Ductile Tearing Analysis of TC128 Tank Car Steel Under Mode I Loading. *Theoretical and Applied Fracture Mechanics, 96,* 658-675.

[32] Swift, H. W. (1952), Plastic instability under plane stress. *Journal of the Mechanics and Physics of Solids, 1,* 1-18.

[33] Voce, E. (1948). The relationship between stress and strain for homogenous deformations. *Journal of the Institute of Metals, 74,* 537-562.

[34] Lee, Y.-W. & Wierzbicki, T. (2004). *Quick Fracture Calibration for Industrial Use*. MIT Impact & Crashworthiness Laboratory, Cambridge.

[35] Lee, Y.-W. (2005). Fracture Prediction in Metal Sheets. MIT Impact & Crashworthiness Laboratory, Cambridge.

[36] Paredes, M., Grolleau, V., & Wierzbicki, T. (2020). On Ductile Fracture of 316L Stainless Steels at Room and Cryogenic Temperature Level: An Engineering Approach to Determine Material Parameters. *In Press.*

[37] Federal Register (2019). Hazardous Materials: Liquefied Natural Gas by Rail (Vol 84, No. 206).

[38] American Society of Heating, Refrigerating and Air-Conditioning Engineers (1969). ASHRAE Thermodynamic Properties of Refrigerants. New York, NY.

[39] Engineers Edge (2022). Specific Heat Capacity of Metals Table Chart.

[40] Jensen, J. E., Tuttle, W. A., Stewart, R. B., Brechna, H., & Prodell, A. G. (1980). Brookhaven National Laboratory Selected Cryogenic Data Notebook. Brookhaven National Laboratory Associated Universities, Inc.

[41] Strobridge, T. R. (1962). Technical Note 129 - The Thermodynamic Properties of Nitrogen from 64 to 300 K Between 0.1 and 200 Atmospheres. United States Department of Commerce - Office of Technical Services, Washington, DC.

[42] Code of Federal Regulations (2023). 49 CFR Part 179 Subpart F -- Specification for Cryogenic Liquid Tank Car Tanks and Seamless Steel Tanks (Classes DOT-113 and 107A). [Accessed 5 April 2022]

[43] Reid, R. C., Prausnitz, J. M., Poling, B. E., & Sherwood, T. K. (1987). Properties of Gases & Liquids, 4th Edition. New York: McGraw Hill.

Appendix A.
Camera and Target Positions

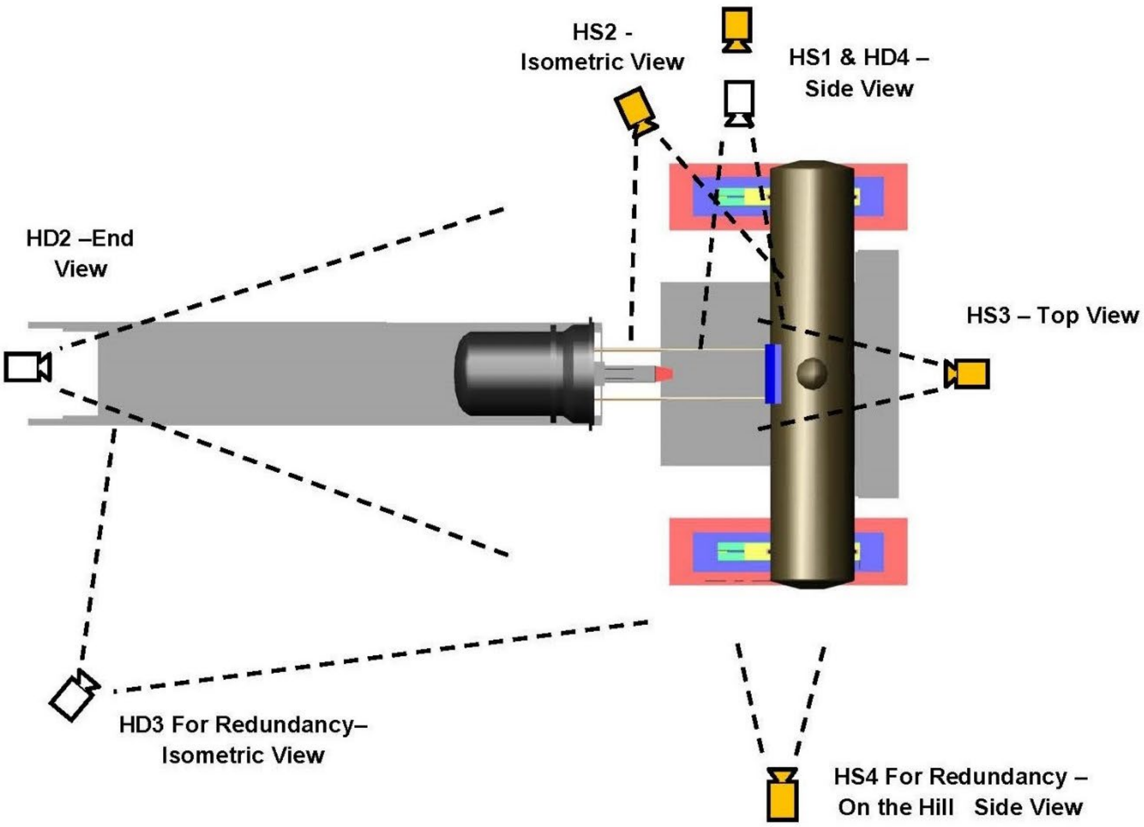

Figure A1. Camera Positions (Top) — High Speed (HS), High Definition (HD)

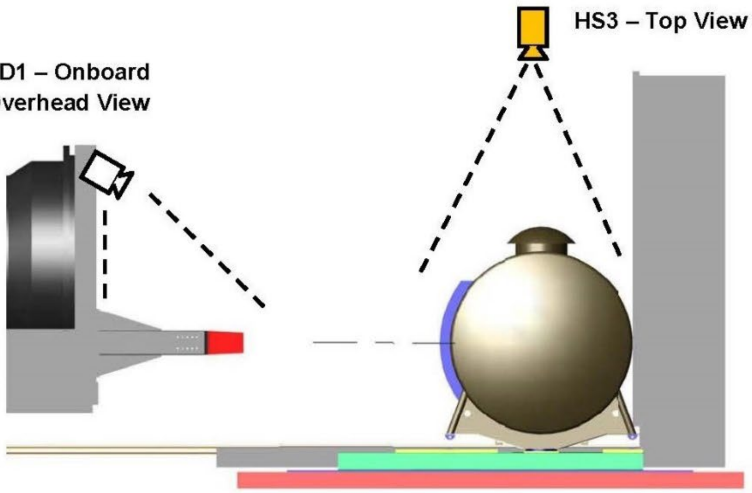

Figure A2. Camera Positions (Side) — High Speed (HS), High Definition (HD)

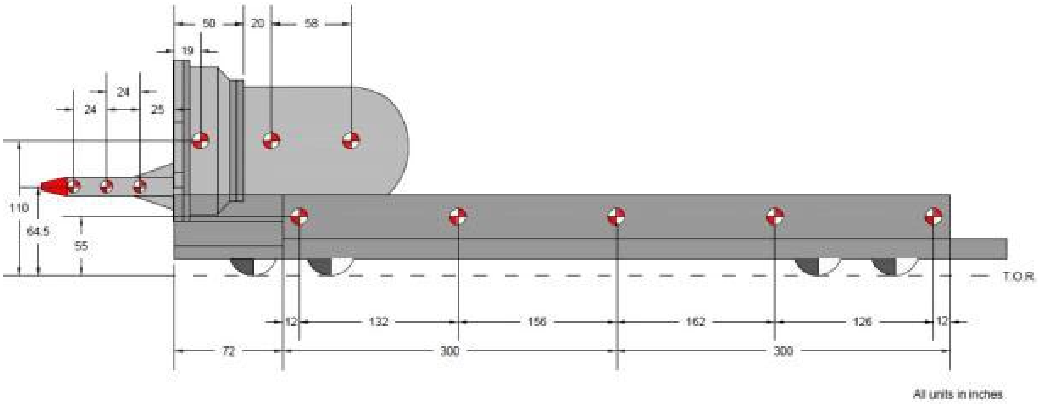

Figure A3. Ram Car Target Positions

Appendix B.
Test Data

This appendix contains raw and filtered test data. The research team processed the raw accelerations and internal pressures measured on different locations on the impact car by averaging the test data from −1 second to −0.1 second on each channel, and this value was subtracted from the test measurements to remove any initial offsets in the data. Each channel was then filtered to channel frequency class CFC60, using the procedures given in SAE J211 [22]. Displacement data did not require any filtration.

B1. Accelerations

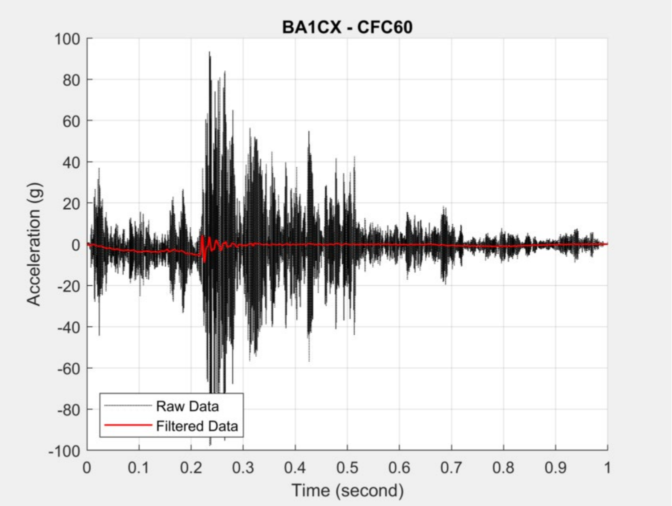

Figure B1. Raw and CFC60 Filtered Acceleration-Time Data from BA1CX

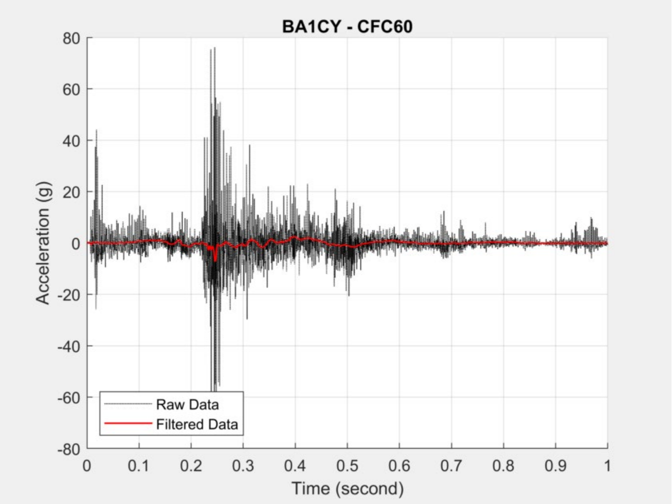

Figure B2. Raw and CFC60 Filtered Acceleration-Time Data from BA1CY

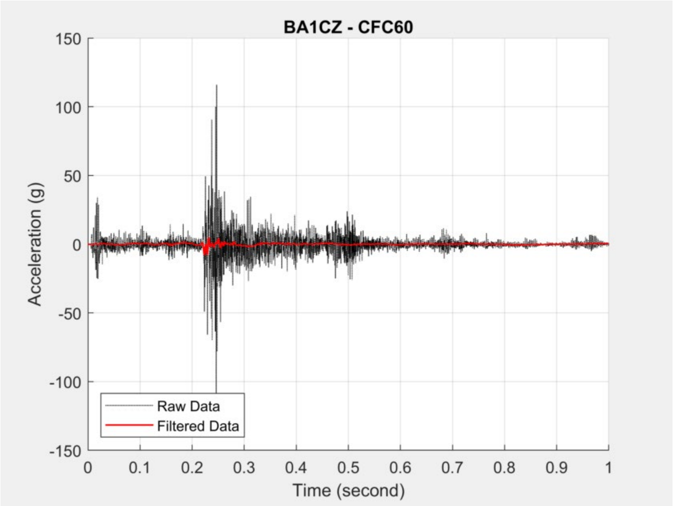

Figure B3. Raw and CFC60 Filtered Acceleration-Time Data from BA1CZ

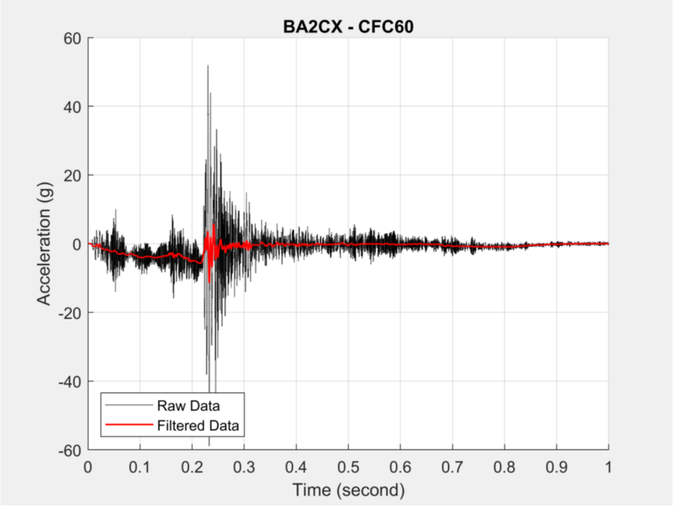

Figure B4. Raw and CFC60 Filtered Acceleration-Time Data from BA2CX

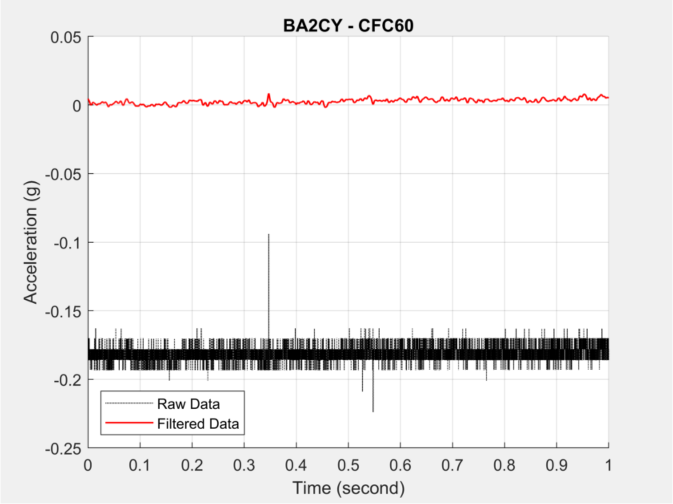

Figure B5. Raw and CFC60 Filtered Acceleration-Time Data from BA2CY

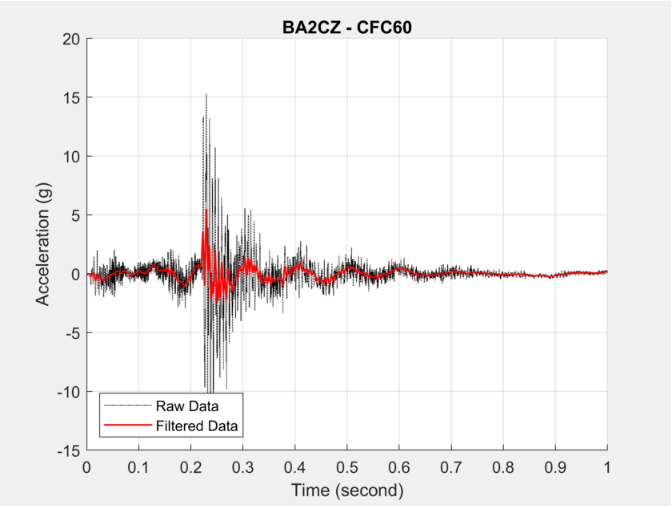

Figure B6. Raw and CFC60 Filtered Acceleration-Time Data from BA2CZ

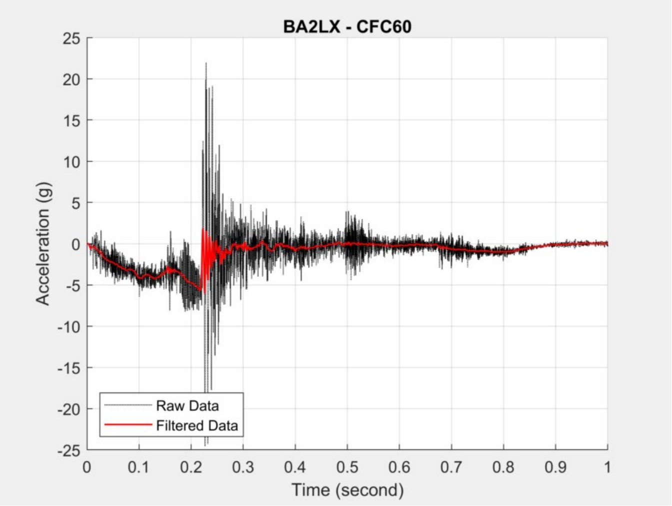

Figure B7. Raw and CFC60 Filtered Acceleration-Time Data from BA2LX

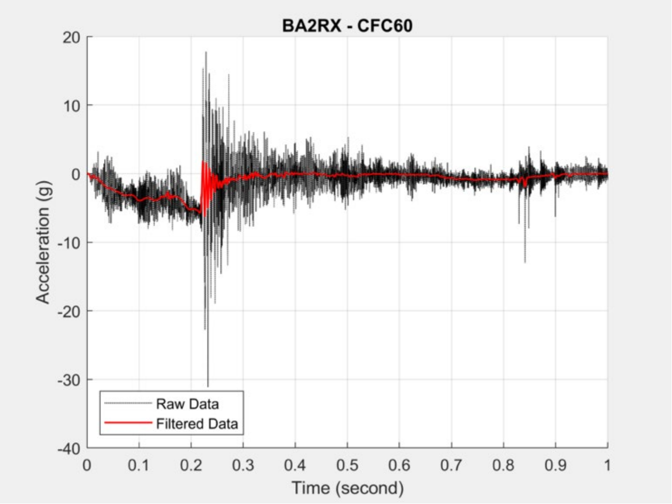

Figure B8. Raw and CFC60 Filtered Acceleration-Time Data from BA2RX

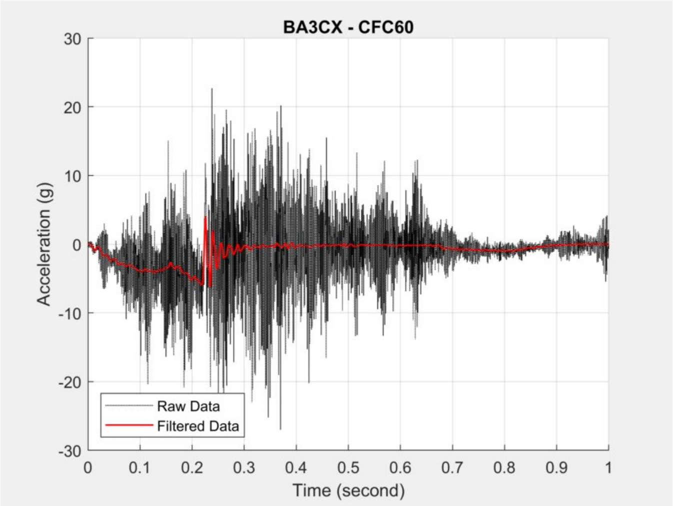

Figure B9. Raw and CFC60 Filtered Acceleration-Time Data from BA3CX

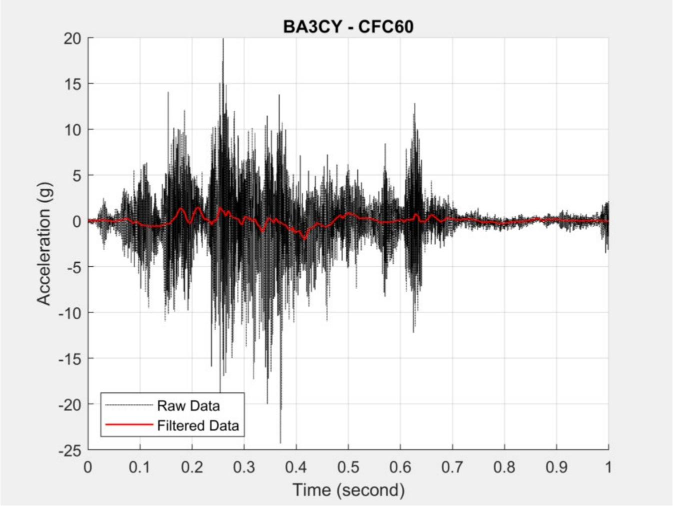

Figure B10. Raw and CFC60 Filtered Acceleration-Time Data from BA3CY

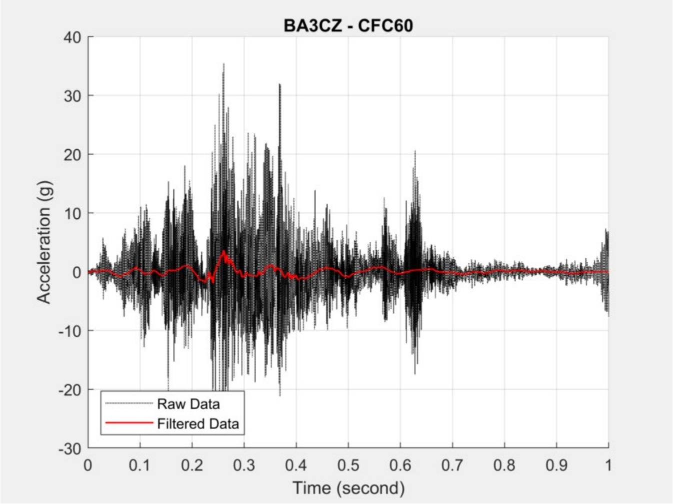

Figure B11. Raw and CFC60 Filtered Acceleration-Time Data from BA3CZ

B2. Pressures

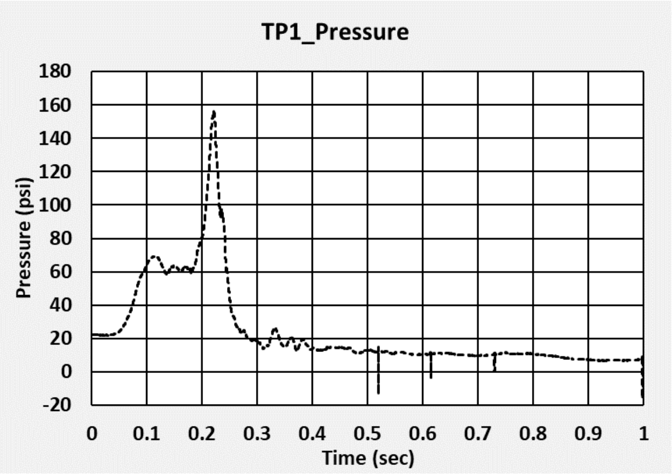

Figure B12. Raw Pressure-Time Data from TP1

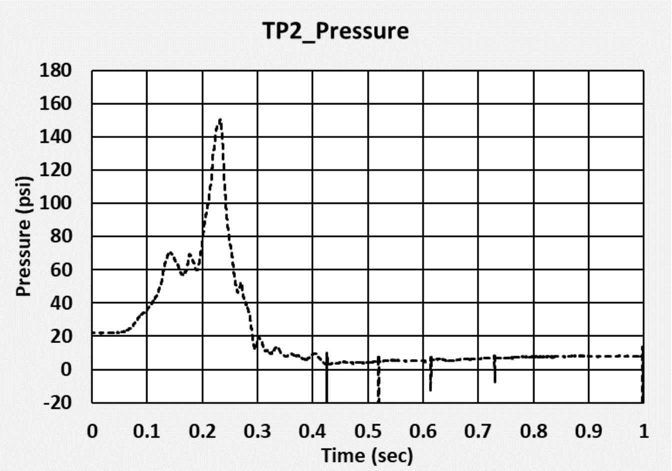

Figure B13. Raw Pressure-Time Data from TP2

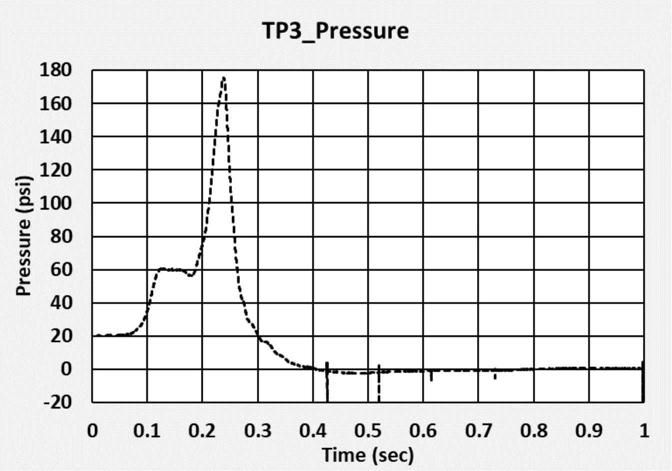

Figure B14. Raw Pressure-Time Data from TP3

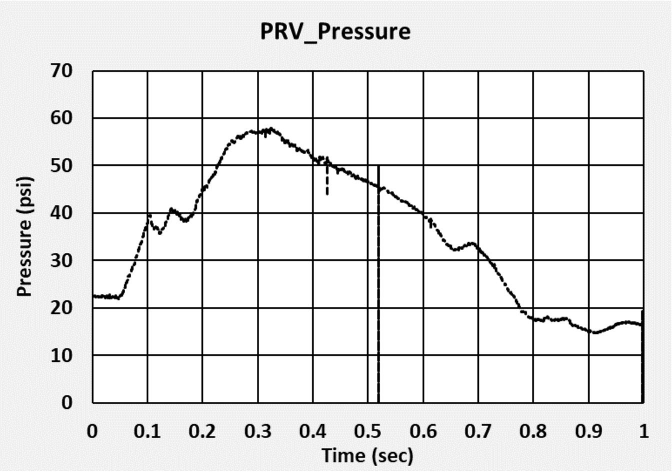

Figure B15. Raw Pressure-Time Data from PRV

B3. Displacements

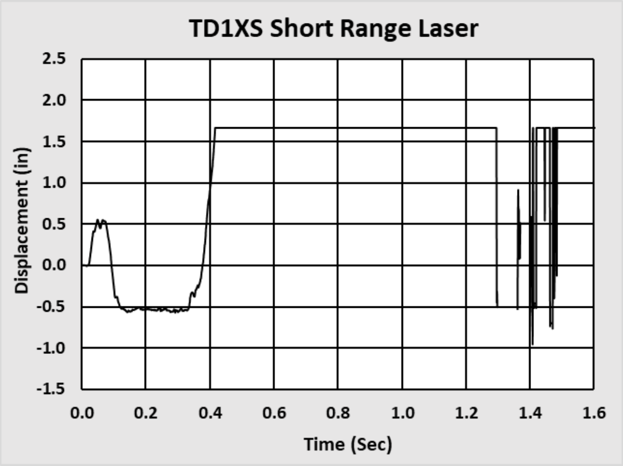

Figure B16. Raw Displacement-Time Data from Short Range Wall Mounted Laser Displacement Transducer (Range: 1.4 in to 4.3 in)

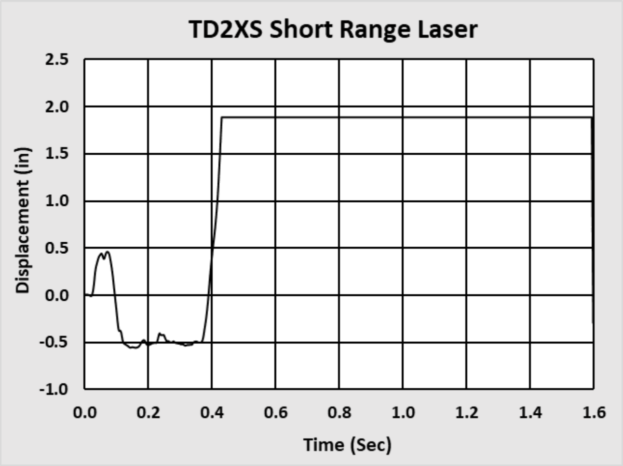

Figure B17. Raw Displacement-Time Data from Short Range Wall Mounted Laser Displacement Transducer (Range: 1.4 in to 4.3 in)

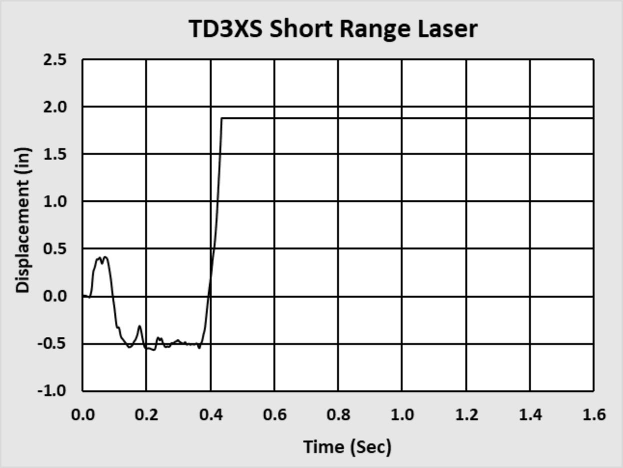

Figure B18. Raw Displacement-Time Data from Short Range Wall Mounted Laser Displacement Transducer (Range: 1.4 in to 4.3 in)

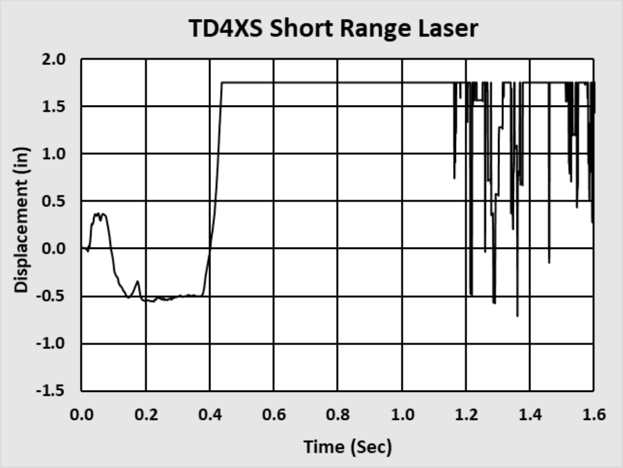

Figure B19. Raw Displacement-Time Data from Short Range Wall Mounted Laser Displacement Transducer (Range: 1.4 in to 4.3 in)

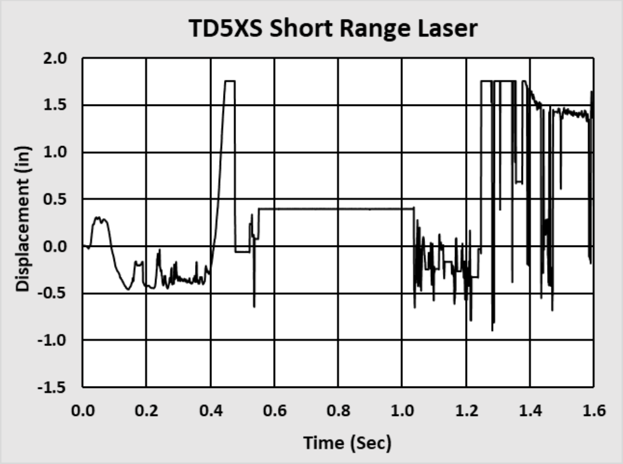

Figure B18. Raw Displacement-Time Data from Short Range Wall Mounted Laser Displacement Transducer (Range: 1.4 in to 4.3 in)

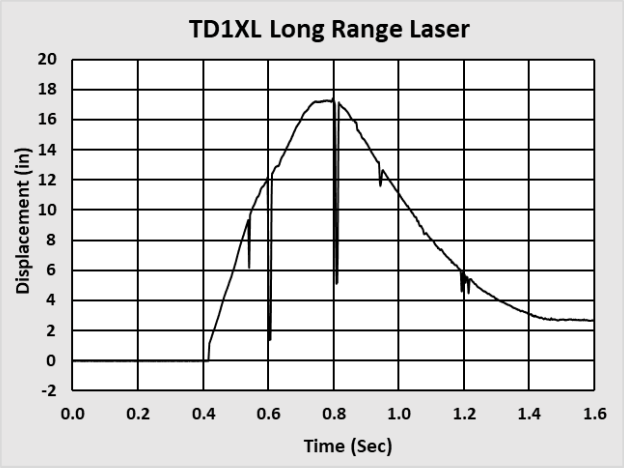

Figure B19. Raw Displacement-Time Data from Long Range Wall Mounted Laser Displacement Transducer (Range: 4 in to 39 in)

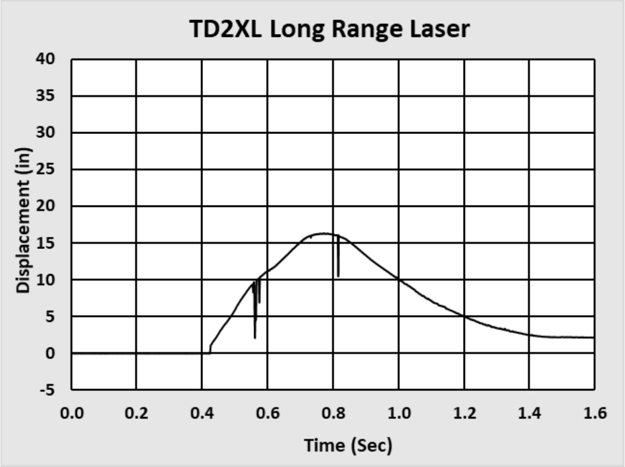

Figure B20. Raw Displacement-Time Data from Long Range Wall Mounted Laser Displacement Transducer (Range: 4 in to 39 in)

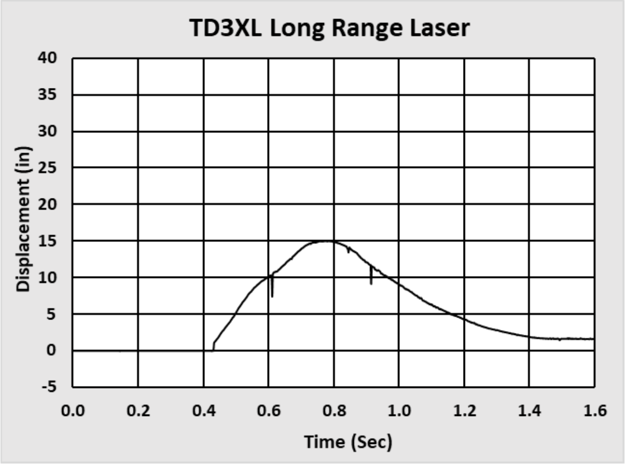

Figure B21. Raw Displacement-Time Data from Long Range Wall Mounted Laser Displacement Transducer (Range: 4 in to 39 in)

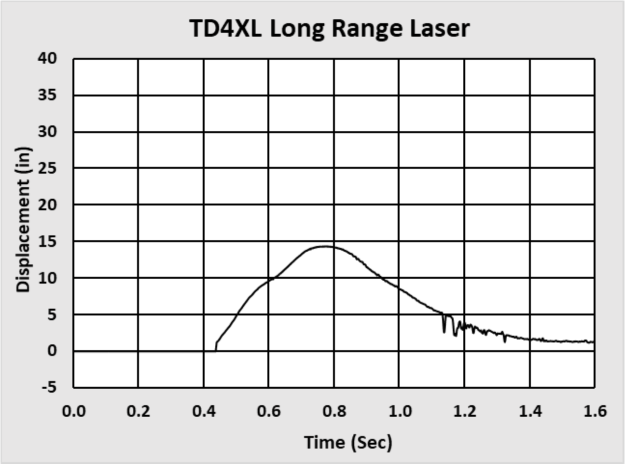

Figure B22. Raw Displacement-Time Data from Long Range Wall Mounted Laser Displacement Transducer (Range: 4 in to 39 in)

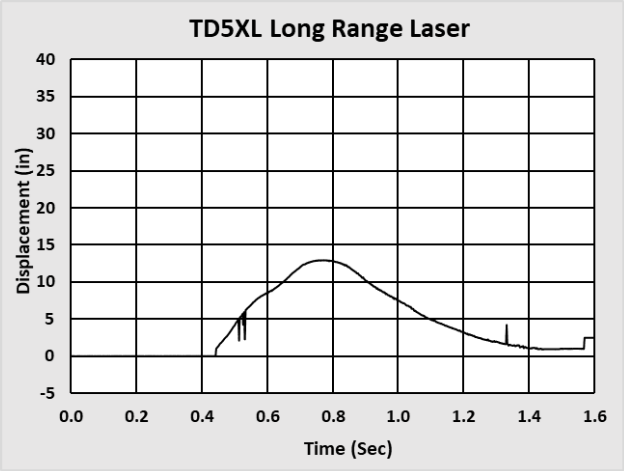

Figure B23. Raw Displacement-Time Data from Long Range Wall Mounted Laser Displacement Transducer (Range: 4 in to 39 in)

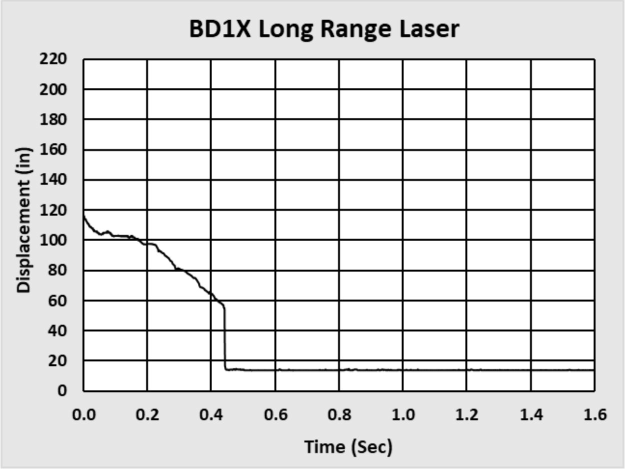

Figure B24. Raw Displacement-Time Data from Long Range Ram Car Mounted Laser Displacement Transducer (Range: 2 in to 39 ft)

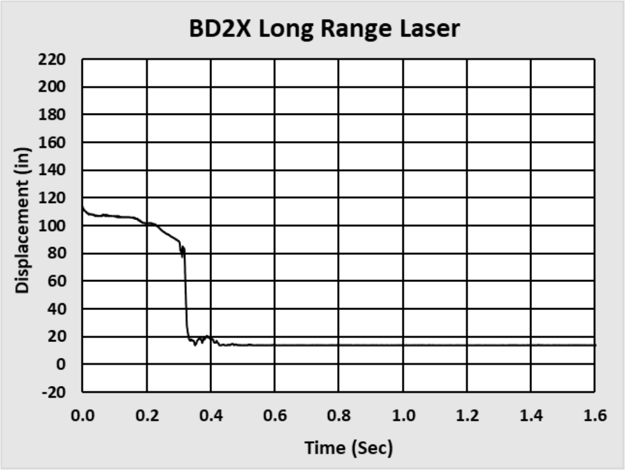

Figure B25. Raw Displacement-Time Data from Long Range Ram Car Mounted Laser Displacement Transducer (Range: 2 in to 39 ft)

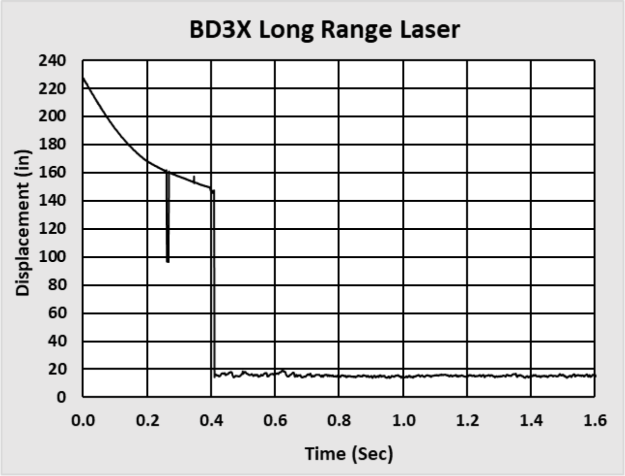

Figure B28. Raw Displacement-Time Data from Long Range Ram Car Mounted Laser Displacement Transducer (Range: 2 in to 39 ft)

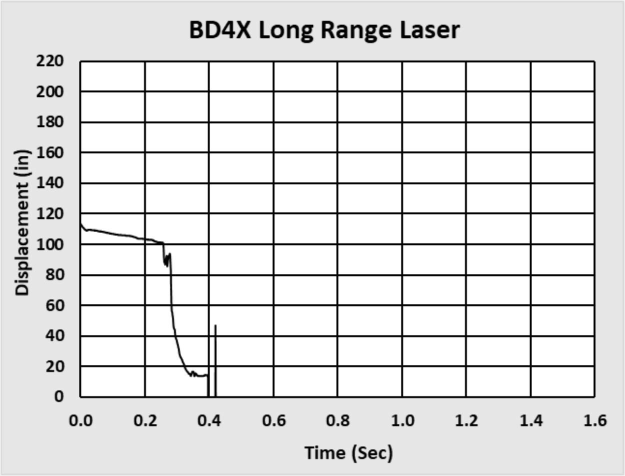

Figure B29. Raw Displacement-Time Data from Long Range Ram Car Mounted Laser Displacement Transducer (Range: 2 in to 39 ft)

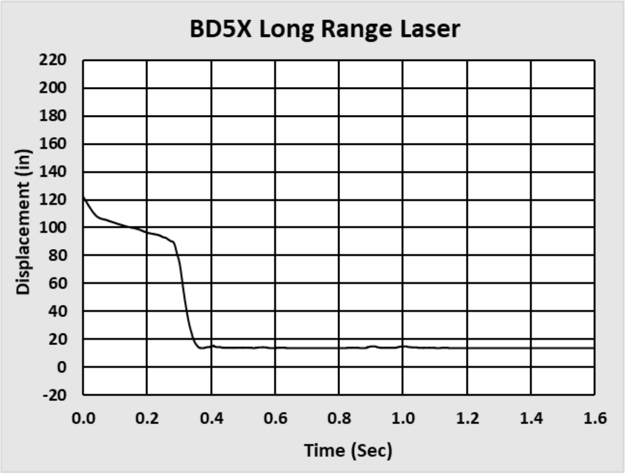

Figure B30. Raw Displacement-Time Data from Long Range Ram Car Mounted Laser Displacement Transducer (Range: 2 in to 39 ft)

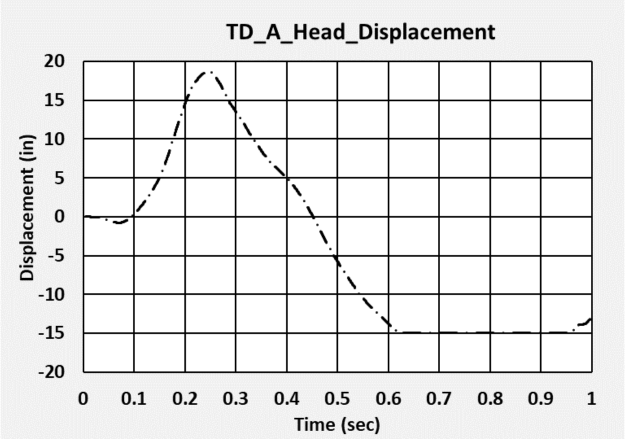

Figure B26. Raw Displacement-Time Data from Displacement Transducer on A-End Head

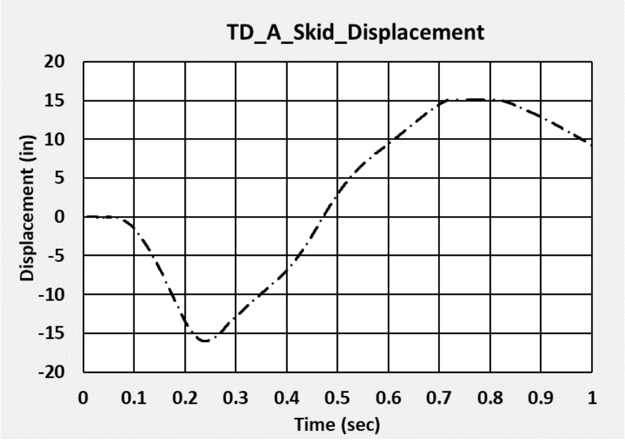

Figure B27. Raw Displacement-Time Data from Displacement Transducer on A-End Skid

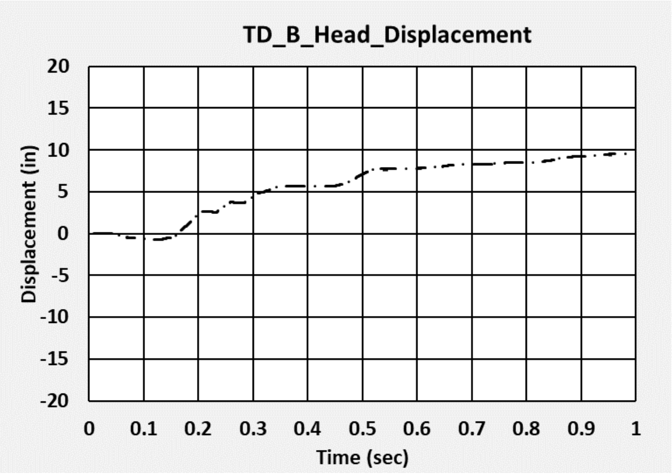

Figure B28. Raw Displacement-Time Data from Displacement Transducer on B-End Head

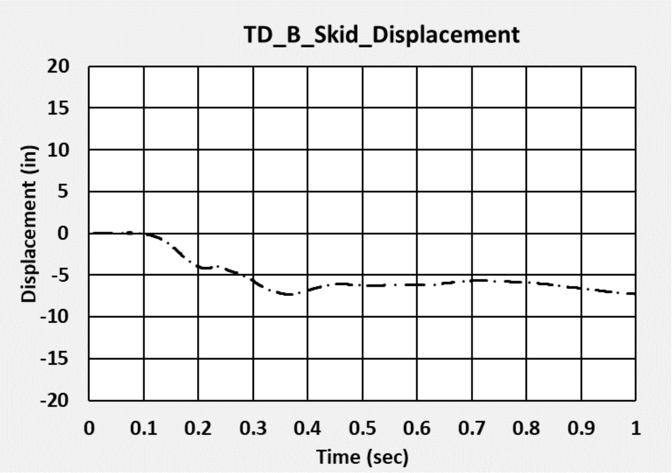

Figure B29. Raw Displacement-Time Data from Displacement Transducer on B-End Skid

B4. Thermocouples and Combination Pressure-temperature Sensors

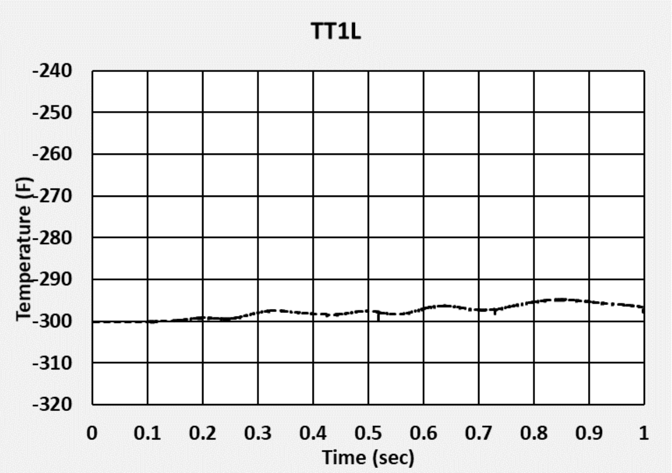

Figure B30. Raw Temperature-Time Data from Thermocouple at A-End in Liquid

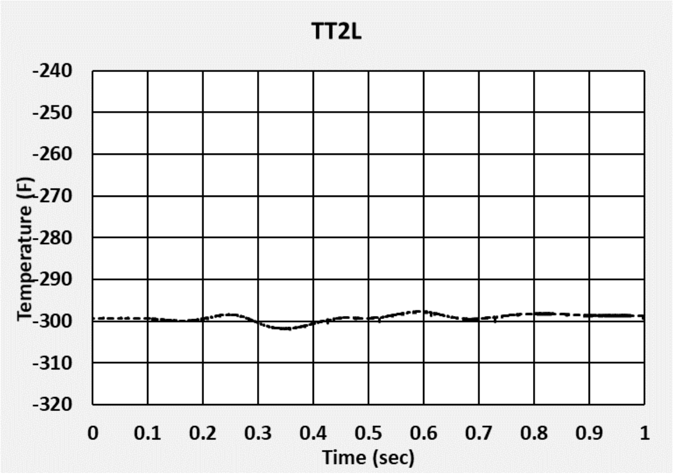

Figure B31. Raw Temperature-Time Data from Thermocouple Between B-End and Center of Car in Liquid

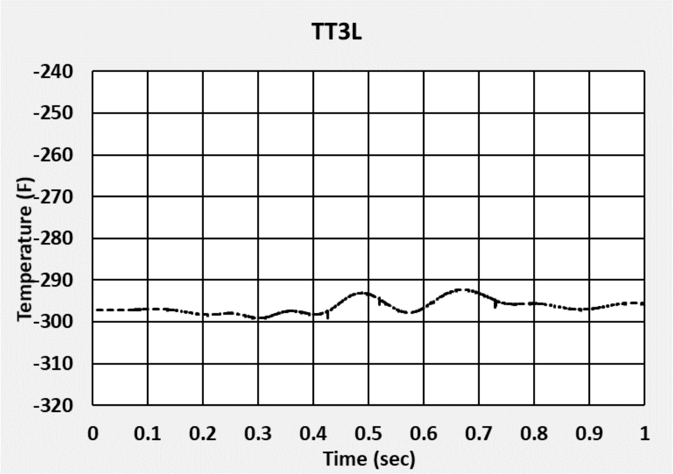

Figure B32. Raw Temperature-Time Data from Thermocouple at B-End in Liquid

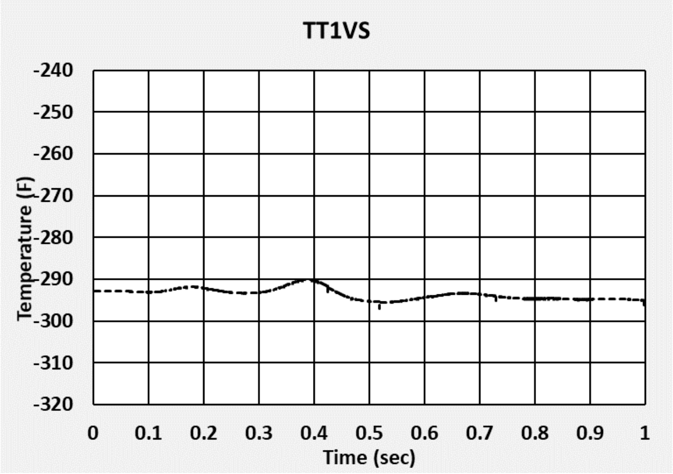

Figure B38. Raw Temperature-Time Data from Thermocouple at A-End in Vapor Space

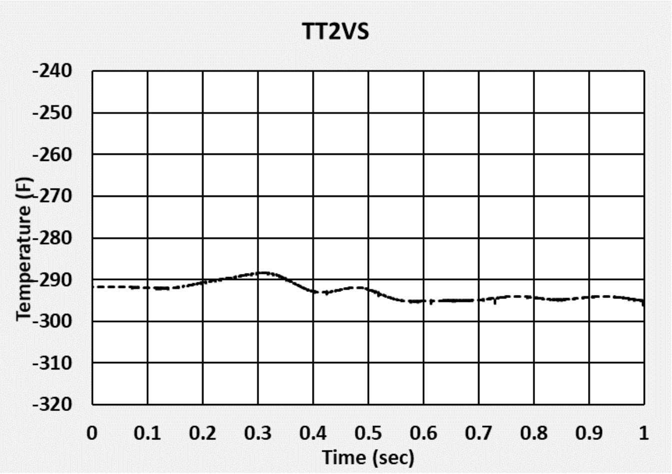

Figure B39. Raw Temperature-Time Data from Thermocouple Between B-End and Center of Car in Vapor Space

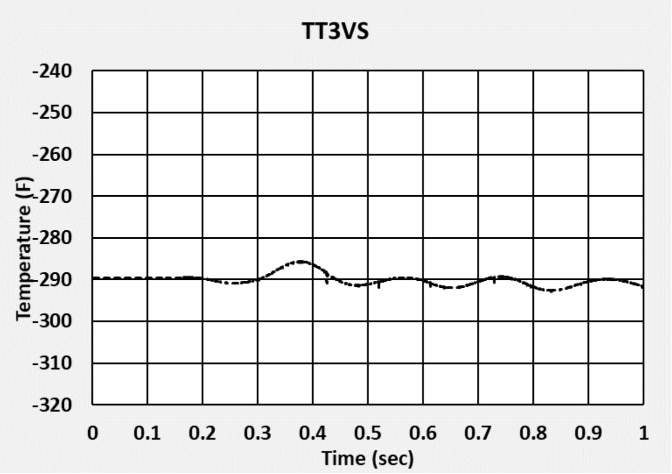

Figure B40. Raw Temperature-Time Data from Thermocouple at B-End in Vapor Space

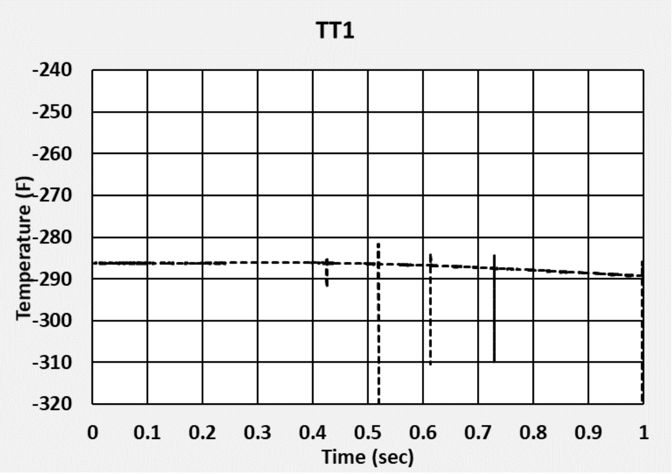

Figure B41. Raw Temperature-Time Data from Combination Pressure-temperature Transducer at A-End in Vapor Space

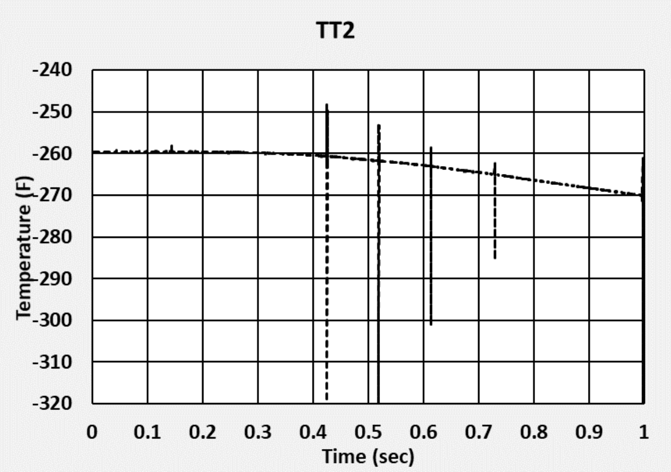

Figure B42. Raw Temperature-Time Data from Combination Pressure-temperature Transducer between B-End and Center of Car in Vapor Space

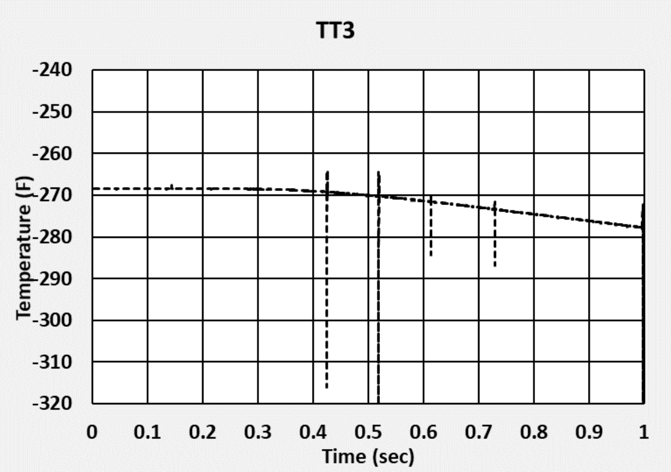

Figure B43. Raw Temperature-Time Data from Combination Pressure-temperature Transducer at B-End in Vapor Space

B5. Material Characterization Results

Material characterization tests were performed on both the TC-128 carbon steel used in the outer tank and the T304 stainless steel used in the inner tank prior to the test.

B5.1 AAR TC-128 Carbon Steel (Pre-test)

The outer tank of the DOT-113 tank car used in this test (Test 13) was characterized by tensile testing prior to the side impact test.

Researchers contracted with an independent test lab (Rocky Mountain Engineering and Materials Technology, Inc.) to conduct tensile testing on the TC-128 carbon steel used to fabricate the outer tank. A section of the Test 13 outer tank that was cut away during the process of tank car fabrication was used for tensile testing. Two-inch gauge length coupons were machined from this plate. The nominal thickness of the tank was 0.5625 inch. However, the combination of coupon thickness and material strength led to difficulty maintaining a grip on the coupon within the test fixture. The laboratory reduced the thickness of the specimens to approximately 0.367 inch.

The research team provided the lab with four specimens for tensile testing according to ASTM E-8 [27]. One of the specimens (Specimen 2) was rejected by the lab during post-processing of the results due to a problem gripping the sample which may have led to an initial yielding of the material. Additionally, Specimens 1 and 3 fractured outside of their gauge lengths, making the elongation at break lower than expected for a specimen that fractured between the gauge marks. The results of the remaining three specimens taken from the Test 13 tank car are summarized in Table B1, alongside the average properties measured during pre- and post-impact material testing of the Test 11 tank car [4] and the post-impact material testing of the Test 12 tank car [6]. The average YS and UTS properties measured for the three Test 13 specimens are similar to the average properties for the TC-128 taken from the Test 11 tank car. The EB-2in from specimen 13-4 is in reasonable agreement with the Test 11 pre-test EB-2in. Based upon these similarities, the TC-128 material response developed using Test 11 properties was not changed in the Test 13 pre- and post-test FE models.

Table B1. Summary of AAR TC-128 Steel Tensile Test Results

Specimen	**YS**	**UTS**	**EB-2in**
-	**ksi**	**ksi**	**%**
Test 13 – 1	59.7	83.7	18.0
Test 13 – 3	64.3	90.1	17.9
Test 13 – 4	65.5	91.5	29.3
Test 13 − Average	*63.2*	*88.4*	*21.7*[10]
Test 11 – Average (pre-test)	*64.9*	*88.8*	*31.4*
Test 11 – Average (post-test)	*64.5*	*86.5*	*37.1*
Test 12 – Average (post-test)	*60.2*	*86.2*	*37.5*

The full lab report is included in the following four pages.

---

[10] Of the three specimens from Test 13, only one fractured between the gauge marks (Test 13 – 4).

Rocky Mountain Engineering and Materials Technology, Inc.
An Engineering Consulting Firm
925 West Kenyon Avenue, Unit 1
Englewood, Colorado 80110
(303) 306-0660

May 1, 2022

Shawn Trevithick
Transportation Tech Center, Inc.
55500 DOT Road
Pueblo, CO 81001

Ref: Rocky Mountain EMTEC, Inc. File No. 201502
Tensile Testing/PO 90397

Dear Mr. Trevithick

Rocky Mountain Engineering and Materials Technology, Inc. has completed tensile testing of material submitted by Transportation Tech Center, Inc. Results of the tensile testing are conveyed in this engineering letter report.

Four flat steel tensile specimens were submitted for testing. The three steel flat specimens were marked "1" through "4," and are nominally 0.367-inch in thickness with a gage section of approximately a half inch in width. The specimens were machined and ready to test when submitted.

METHODOLOGY

The three specimens were tested in accordance with ASTM E8, Standard Test Methods for Tension Testing of Metallic Materials. A 2-inch extensometer was modified to increase the measurable strain range and used to determine specimen extension, from which strain was calculated. The extensometer was kept in place until after the peak load was achieved and was removed after the onset of the plastic instability but prior to fracture. Yield strength was determined by the 0.2% offset method. Specimens were tested as submitted.

FINDINGS

All four tensile specimens were tested. Results of Specimen No. 2 were removed from the data set, as the results indicate strain hardening due to issues with slippage of the grips.

Results of the remaining specimens show that the yield strength of the specimens ranges from about 60 ksi to 65.5 ksi, with tensile strength values ranging from about 84 ksi to 91.5 ksi. The elongation ranges from about 18% to 29%. The average yield strength is 63.2 ksi, while the average tensile strength is 88.4 ksi. The average elongation is 21.8% in 2-inches.[1] A summary of the tensile test data is presented in Table 1. Stress-strain curves are appended hereto. Data files for the stress-strain curves are provided separately.

Table 1
Summary of Tensile Test Data

Specimen	**Yield Strength, ksi †**	**Tensile Strength, ksi**	**Elongation, % in 2-inch**
1	59.7	83.7	18.0
3	64.3	90.1	17.9
4	65.5	91.5	29.3
Average	***63.2***	***88.4***	***21.8***

†0.2% Offset Method

Rocky Mountain EMTEC, Inc, has been pleased to be of service in this matter. Should you have questions or require additional technical assistance, please do not hesitate to contact the undersigned directly.

Reviewed by:

COLORADO REGISTERED PROFESSIONAL ENGINEER
JOHN NEIL SCHWARTZBERG
31745
5/2/2022

John N. Schwartzberg, P.E.
Senior Metallurgical Engineer
Rocky Mountain EMTEC, Inc.

---

[1] Two of the three tensile specimens fractured outside the marked 2-inch gage length. Thus, the average elongation is lower than would be expected for specimens fracturing between the gage marks. Specimen No. 4, which did fail between the gage marks, exhibits an elongation of 29.3%

APPENDIX

Full-Range Stress-Strain Curves for Tensile Tests

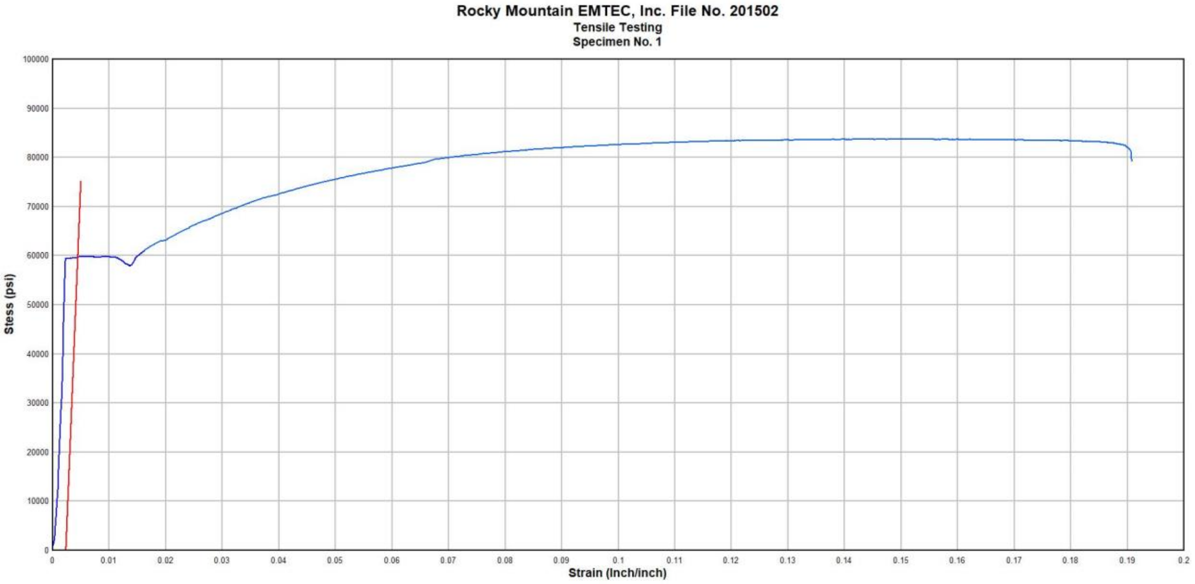

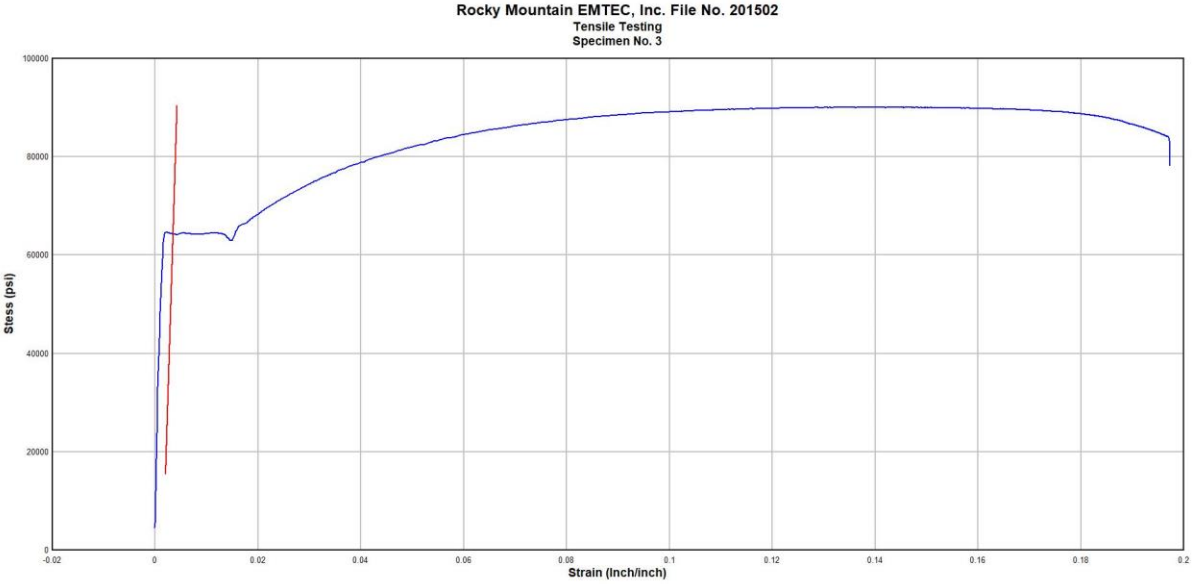

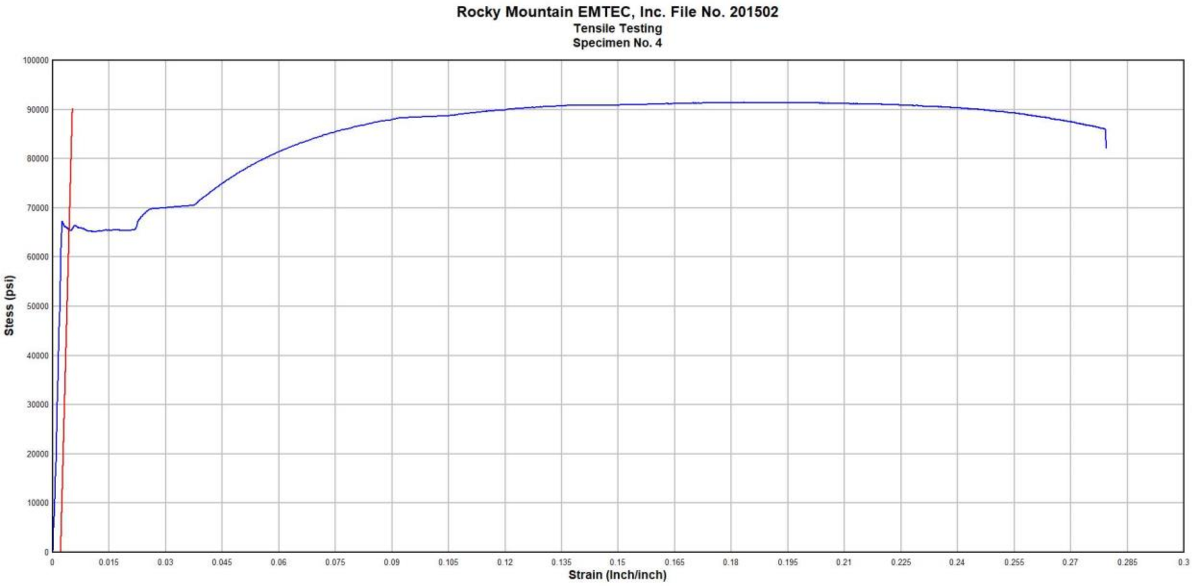

Rocky Mountain EMTEC, Inc. File No. 201502
Tensile Testing
Specimen No. 4

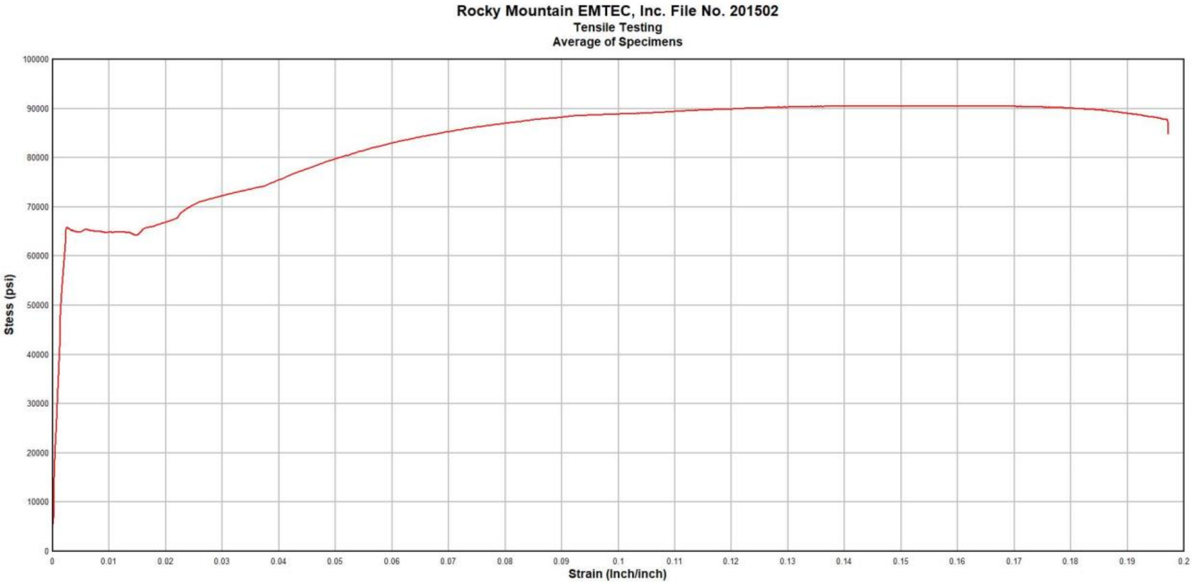

Rocky Mountain EMTEC, Inc. File No. 201502
Tensile Testing
Average of Specimens

B5.3 ASTM A240, Type 304 Stainless Steel (Pre-test)

Tensile coupons were obtained from cutouts made to the outer tank of the DOT-113 during its fabrication. Researchers contracted with an independent test lab (Composite Technology Development, Inc.) to conduct QS tensile testing at room temperature, cryogenic temperature, and at elevated strain rates.

Table B2 shows the material characterization test matrix of T304 stainless steel at room temperature (295 K) and the saturation temperature of nitrogen at sea level (77 K), and strain rates from 8.33 x 10^{-5} (standard rate) s^{-1} to 0.1 s^{-1} (rapid rate) for uniaxial tensile coupons. The specimens tested at 295 K and standard rate, and those tested at 77 K and a rapid rate all fractured between the gauge marks. None of the specimens tested at 77 K and standard rate fractured between the gauge marks. Standard rate 77 K Specimens 4 and 5 did not fracture as the extension limits of the load frame were reached. While the standard rate 77 K Specimen 6 did fracture, the fracture occurred in the radiused section between the grip and gauge sections of the specimen, not in the gauge section itself.

Table B2. Temperature and Strain Rate Test Matrix of T304 Stainless Steel

Temperature (K)	*295*	*77*	*77*
Displacement Rate (in/s)	*1.67E-04*	*1.67E-04*	*2.00E-01*
Gauge Length (in)	*2*	*2*	*2*
Strain Rate (s^{-1})	*8.33E-05*	*8.33E-05*	*1.00E-01*
YS (ksi)	43.8[11]	54.8	60.7
YS (ksi)	42.4	55.0	64.1
YS (ksi)	41.0	54.2	64.4
Average YS (ksi)	**42.4**	**54.7**	**63.1**
UTS (ksi)	109.9[11]	230.4	192.5
UTS (ksi)	108.3	244.5	194.2
UTS (ksi)	107.2	238.0	196.4
Average UTS (ksi)	**108.5**	**237.6**	**194.4**
EB-2 (%)	68.0[11]	20.3[12]	31.5
EB-2 (%)	67.3	27.9[12]	29.7
EB-2 (%)	65.4	26.8[12]	29.2
Average EB-2 (%)	**66.9**	-[12]	**30.1**
%RA	66.3[11]	15.0[12]	55.2
%RA	68.0	19.3[12]	49.0
%RA	71.5	17.1[12]	49.2
Average %RA	**68.6**	-[12]	**51.1**

The T304 tensile coupons had a flat, rectangular ASTM-E8 geometry with a 2-inch GL (except for one 295 K specimen, which used a 2.5 inch GL), nominal 0.55-inch width, and 0.24-inch thickness.

The full lab report is included in the following 22 pages.

---

[11] Specimen used a 2.5-inch gauge length.

[12] No 77 K standard load rate (8.33E-05 s^{-1}) specimens fractured between the gauge marks.

COMPOSITE TECHNOLOGY DEVELOPMENT, INC.

ENGINEERED MATERIAL SOLUTIONS

Final Test Report

T304 SS Testing at 295 K and 77 K

Purchase Order No. 90751
May 11, 2022

Prepared for:
Transportation Tech Center Inc.
Attn: Shawn Trevithick
55500 DOT Road
Pueblo, CO 81001

Prepared by:
Composite Technology Development, Inc.
2600 Campus Drive, Suite D
Lafayette, CO 80026

Report Signature Page

Prepared by: Mark M. Haynes
Mark Haynes, Test Engineer

Reviewed by: Paul E. Fabian
Paul Fabian, Program Manager

Approved by: Holly Babcock
Holly Babcock, Quality Assurance Manager

Table of Contents

Introduction

This report provides the final results of the testing performed by Composite Technology Development, Inc. (CTD) for Transportation Technology Center Inc. (TTCI) on purchase order 90751. The goal of this test program was to characterize the tensile properties of T304 stainless steel at room and cryogenic temperatures. The specimens were provided to CTD by TTCI and prepared for testing by CTD.

The test program consisted of performing tensile testing on three T304 specimens each at 295 K, 77 K and three at 77 K at a rapid load rate (0.2”/second).

The tests were performed on 20 and 100 kip capacity servo-hydraulic load frames using 20 kip and 100 kip capacity load cells. The cryogenic test temperatures were monitored by a Lakeshore Silicon Diode temperature sensor and were monitored by a Lakeshore 340 Cryogenic Temperature Controller using Liquid Nitrogen as necessary as the cooling cryogen.

Table 1 identifies all equipment used in this program, including the next calibration due date. Calibration certificates for all equipment used in this program are available upon request.

Table 1. Test Equipment

Description	Model Number	Serial No.	Calibration Due	Comments
MTS Systems Corp.-100 kip Load Frame				
100 kip Load Cell	661.23E-01	104498	09/13/2023	
LVDT	NA	106826	09/13/2023	
Vishay Micromeasurements				
Strain Scanner	8000-8-SM	214818	09/07/2022	
Strain Scanner	8000-8-SM	214819	09/07/2022	
LakeShore Cryotronics				
Temperature Controller	340	341622	12/07/2022	
Silicon Diode	DT470-LR-13-1.4L	D87900	10/23/2022	
MTS Systems Corp.-20 kip Load Frame				
20 kip Load Cell	661.21A-03	1653	09/12/2023	
LVDT	NA	538	09/12/2023	
Vishay Micromeasurements				
Strain Conditioner	2120A	10030	01/24/2023	
Measurement Equipment				
Micrometer, Mitutoyo	293-344	DY6789	11/18/2022	
Caliper, Mitutoyo	CD-6CS	615075	11/18/2022	
Torque Wrench, CDI	1002MFRH-CDI	708712148	11/18/2022	
LakeShore Cryotronics				
Temperature Controller	340	342586	10/05/2022	
Silicon Diode	DT470-LR-13-1.4L	D79582	07/14/2023	

All mechanical data was recorded through an MTS data acquisition system, all thermal data was monitored through a data acquisition system designed by CTD, using data sampling frequencies of 10 Hz and 50Hz as necessary for the mechanical data.

Electronic versions of all original data files and all modified (for analysis purposes) data files recorded during all tests are included on a USB Flash Drive provided to TTCI in conjunction with this report.

Test Methods

Testing was performed in a manner according to ASTM E8 and E1450 for flat plate specimens initially using the test fixturing shown in Figure 1 at a displacement rate of 0.01 inches per minute per the ASTM test standard.

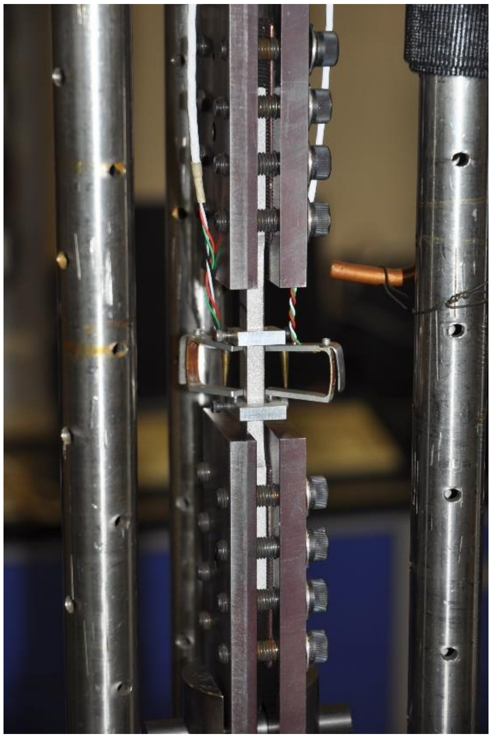

Figure 1: Initial Grip setup (295K)

The ultimate loads required for failure of the 304SS specimens at 77 K was in excess of the grip capacity of the simple clamp-style grips in Figure 1, as well as the capacity of the 20,000 lb_f load frame. Testing was moved to the 100,000 lb_f load frame and a change in the grip style which provided support at the radius to the gage section was necessitated as seen in Figure 2.

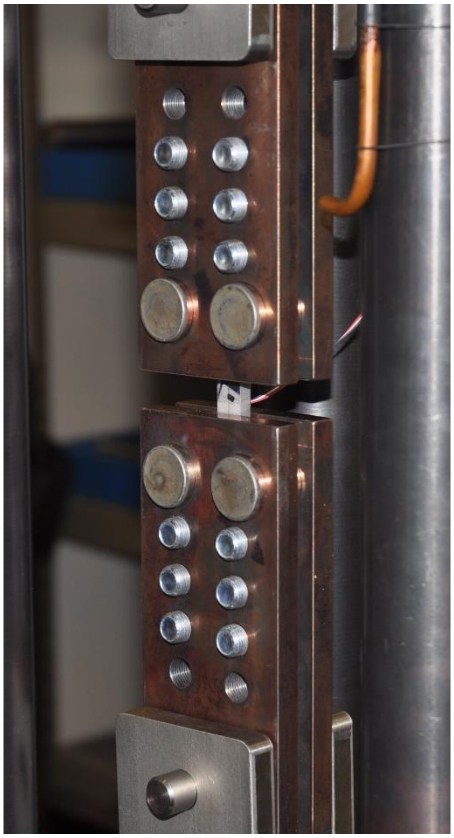

Figure 2: Test Fixture and Specimen

The original quotation specified the use of extensometers to measure the induced strain, however the length of the gage section of the specimens combined with change in grip style necessitated a change in strain acquisition methods. Single axis strain gages were bonded to the low temperature (77 K) specimens to enable accurate strain data.

Three tests were performed at both 295 K and 77 K at a load rate of 0.01 in/minute while three additional tests were performed at 77 K at a load rate of 0.2 in/second.

Cooling of the specimens and fixturing was carried out by slowly submerging the cryostat and fixture in a cryogenic chamber (dewar) filled with Liquid Nitrogen while holding a 25lb_f load to ensure continued alignment to the axis of loading. After achieving the specified test temperature, the specimens were held within the test temperature range for a minimum of 5 minutes prior to initiating the test.

Test Results

Data averages show an increase in strength values of 117.7% at 77 K from room temperature (237.5 ksi vs 109.1 ksi @ 295 K), and an elongation decrease at cryogenic temperatures and similar load rates (24.1% vs 67.7% at 295 K). Young's modulus values remained fairly consistent regardless of temperature at this load rate (29.7Msi vs 28.4Msi @ 295 K).

The rapid rate 77 K test results displayed a lower ultimate strength (193.3 ksi), but a higher Young's Modulus, Elongation, Offset Yield Strength and reduction in area than the lower load rate as can be seen in data summaries, Tables 2-4 below.

T304 @ 295K	Ultimate Strength (ksi)	Tensile Modulus (Msi)	Elongation Increase (%)	Reduction of Area (%)	0.2% Offset Yield Strength (ksi)
Average	**109.1**	**28.4**	**67.7**	**67.2**	**42.4**
Std. Dev.	**1.10**	**0.78**	**0.48**	**1.24**	**1.39**
CV	**0.01**	**0.03**	**0.01**	**0.02**	**0.03**

Table 2: T304 Results at 295 K

T304 @ 77K	Ultimate Strength (ksi)	Tensile Modulus (Msi)	Elongation Increase (%)	Reduction of Area (%)	0.2% Offset Yield Strength (ksi)
Average	**237.5**	**29.7**	**24.1**	**17.2**	**54.6**
Std. Dev.	**9.95**	**2.15**	**5.36**	**3.05**	**0.40**
CV	**0.04**	**0.07**	**0.22**	**0.18**	**0.01**

Table 3: T304 Results at 77 K

T304 @ 77K Rapid Rate	Ultimate Strength (ksi)	Tensile Modulus (Msi)	Elongation Increase (%)	Reduction of Area (%)	0.2% Offset Yield Strength (ksi)
Average	**193.3**	**32.3**	**30.6**	**52.1**	**63.0**
Std. Dev.	**1.21**	**0.17**	**1.25**	**4.38**	**2.02**
CV	**0.01**	**0.01**	**0.04**	**0.08**	**0.03**

Table 4: T304 Rapid Rate Results at 77 K

Full Stress-Strain curves for each data set are included in Appendix B.
Pictures of all failed specimen groups are presented in Appendix C.

Anomalies encountered during the testing included the following:
Specimen T304 #1 295 K, was initially tested using conventional compression grips, which failed to hold to the requisite load (9577.9 lb_f, 80.78 ksi stress), although the specimen did reach its yield point. Young's modulus determination was made from the initial run, ultimate strength and elongation were determined from the second test using the shoulder supported grip system.

All subsequent tests were performed using the shoulder supported, bolted grip system.
All 295 K specimens displayed some distortion at the shoulder due to slippage within the grips as seen in Figure 3.

Figure 3: 295 K Specimens displaying the minor deformation at the shoulders

During the first T304 test at 77 K (T304 #4), the specimen reached the maximum load allowable for the load frame (19499 Lbs, 168.8 ksi Stress). Testing was then moved to the 100 kip capacity load frame for all subsequent tests.

The 77 K specimens all showed similar distortions, the tests of Specimens 4 and 5 were ended prior to tensile failure of the material due to extension limits of the load frame. Specimen #6 failed through the radiused section as seen in Figure 4.

Figure 4: 77 K standard load rate specimens

All of the rapid rate 77 K specimens held appropriately and failed within normal parameters in a ‘cup and cone’ fashion as demonstrated in Figure 5.

Figure 5: 77 K Rapid Rate specimens

Complete data summaries are presented in Tables 5 through 7 on Pages 7 through 9.

Specimen Return

All specimens were returned to TTCI. A copy of the Specimen Return Inventory Sheet documenting the specimen return is included in Appendix D.

Conclusion

The specimens supplied to CTD by TTCI were tested within the test conditions required in the test contract. Based on the data available, CTD concludes that the data presented is an accurate representation of the material's performance under tensile loading.

Table 5: 295 K T304 Test Summary

TEST CONDITIONS

Customer:	**TTCI**	***Test Date:***	**4/11,19,20/2022**
Customer P.O.:	**90751**		
CTD Program #:	**7369-373**	***Load Frame:***	**20 Kip**
		Load /Displacement Rate:	**0.01 in/min**
Material Reference:	**Stainless Steel**	***Load Cell:***	**+/-20 Kip**
Alloy Designation:	**T304**		
ASTM Reference:	**E-8**	***Strain Measurement:***	**Two Extensometers**
Specimen Type:	**Tension**		
Test Fixture:	**E8**		
		Temperature Controller:	**NA**
Test Temperature:	**295K**	***Temperature Sensor:***	**Silicon Diode**
Temperature Hold Time:	**NA**	***Diode SN:***	**D79582**
Specimen Conditioning:	**NA**		

TEST RESULTS

Specimen #	Initial Width (in)	Initial Thickness (in)	Initial Gage Length (in)	Ultimate Load (in)	Final Gage Length (in)	Final Width (in)	Final Thickness (in)	Ultimate Strength (ksi)	Tensile Modulus (Msi)	Elongation Increase (%)	Reduction of Area (%)	0.2% Offset Yield Strength (ksi)
T304-1	0.492	0.241	2.500	13030	4.20	0.308	0.130	109.9	28.9	68.0	66.3	43.8
T304-2	0.497	0.237	2.026	12761	3.39	0.293	0.129	108.3	27.8	67.3	68.0	42.4
T304-3	0.498	0.244	2.032	13021	3.36	0.302	0.115	107.2	29.2	65.4	71.5	41.0
							Average	**109.1**	**28.4**	**67.7**	**67.2**	**42.4**
							Std. Dev.	**1.10**	**0.78**	**0.48**	**1.24**	**1.39**
							CV	**0.01**	**0.03**	**0.01**	**0.02**	**0.03**

Table 6: 77 K T304 Test Summary

TEST CONDITIONS

Customer:	**TTCI**	***Test Date:***	**4/20, 21, 22, 25/2022**
Customer P.O.:	**90751**		
CTD Program #:	**7369-373**	***Load Frame:***	**20 Kip**
		Load /Displacement Rate:	**0.01 in/min**
Material Reference:	**Stainless Steel**	***Load Cell:***	**+/-20 Kip**
Alloy Designation:	**T304**		
ASTM Reference:	**E-8**	***Strain Measurement:***	**Uniaxial Strain Gage**
Specimen Type:	**Tension**	***Gage Type:***	**SK-06-125AD-350**
Test Fixture:	**E8**		
		Temperature Controller:	**lakeShore 340**
Test Temperature:	**77K**	***Temperature Sensor:***	**Silicon Diode**
Temperature Hold Time:	**5 Minutes**	***Diode SN:***	**D87900**
Specimen Conditioning:	**NA**		

TEST RESULTS

Specimen #	Initial Width (in)	Initial Thickness (in)	Initial Gage Length (in)	Ultimate Load (in)	Final Gage Length (in)	Final Width (in)	Final Thickness (in)	Ultimate Strength (ksi)	Tensile Modulus (Msi)	Elongation Increase (%)	Reduction of Area (%)	0.2% Offset Yield Strength (ksi)
T304-4	0.498	0.232	2.028	26623	2.44	0.462	0.213	230.4	28.2	20.3	15.0	54.8
T304-4	0.496	0.238	2.033	28863	2.60	0.447	0.213	244.5	31.2	27.9	19.3	55.0
T304-6	0.496	0.232	2.019	27384	2.56	0.450	0.212	238.0	31.4	26.8	17.1	54.2
							Average	**237.5**	**29.7**	**24.1**	**17.2**	**54.6**
							Std. Dev.	**9.95**	**2.15**	**5.36**	**3.05**	**0.40**
							CV	**0.04**	**0.07**	**0.22**	**0.18**	**0.01**

Table 7: 77 K Rapid Rate T304 Test Summary

TEST CONDITIONS

Customer:	**TTCI**	***Test Date:***	**5/4/2022**
Customer P.O.:	**90751**		
CTD Program #:	**7369-373**	***Load Frame:***	**100 Kip**
		Load /Displacement Rate:	**0.2 in/sec**
Material Reference:	**Stainless Steel**	***Load Cell:***	**+/-100 Kip**
Alloy Designation:	**T304**		
ASTM Reference:	**E-8**	***Strain Measurement:***	**Axial Strain Gage**
Specimen Type:	**Tension**	***Gage Type:***	**SK-06-125AD-3560**
Test Fixture:	**E8**		
		Temperature Controller:	**LakeShore 340**
Test Temperature:	**77K**	***Temperature Sensor:***	**Silicon Diode**
Temperature Hold Time:	**5 Minutes**	***Diode SN:***	**D87900**
Specimen Conditioning:	**NA**		

TEST RESULTS

Specimen #	Initial Width (in)	Initial Thickness (in)	Initial Gage Length (in)	Ultimate Load (in)	Final Gage Length (in)	Final Width (in)	Final Thickness (in)	Ultimate Strength (ksi)	Tensile Modulus (Msi)	Elongation Increase (%)	Reduction of Area (%)	0.2% Offset Yield Strength (ksi)
T304-7	0.497	0.233	2.008	22290	2.64	0.358	0.145	192.5	32.4	31.5	55.2	60.7
T304-8	0.494	0.238	2.020	22832	2.62	0.368	0.163	194.2	32.2	29.7	49.0	64.1
T304-8	0.492	0.242	2.005	23382	2.59	0.369	0.164	196.4	31.7	29.2	49.2	64.4
							Average	**193.3**	**32.3**	**30.6**	**52.1**	**63.0**
							Std. Dev.	**1.21**	**0.17**	**1.25**	**4.38**	**2.02**
							CV	**0.01**	**0.01**	**0.04**	**0.08**	**0.03**

APPENDIX A

CERTIFICATE OF ANALYSIS

TEST SPECIMEN CERTIFICATE OF ANALYSIS

CTD Job #: 7369-373 **Customer P.O. #:** 90751

Customer: TTCI
55500 DOT Road
Pueblo, CO 81001
ATTN: Shawn Trevithick

Test Specimen Type: Tensile

Quantity: 9

Specimen Dimensions (nominal): 0.25” X 0.75” X 7”

Inspection Results:

Specimen No.	Appearance	Tab Adhesion	Strain Gage Operation	Other
T304 #1	Good	NA	NA	
T304 #2	Good	NA	NA	
T304 #3	Good	NA	NA	
T304 #4	Good	NA	Good	
T304 #5	Good	NA	Good	
T304 #6	Good	NA	Good	
T304 #7	Good	NA	Good	
T304 #8	Good	NA	Good	
T304 #9	Good	NA	Good	

APPENDIX B

STRESS-STRAIN CHARTS

Figure 1: 295 K Stress-Strain Curves

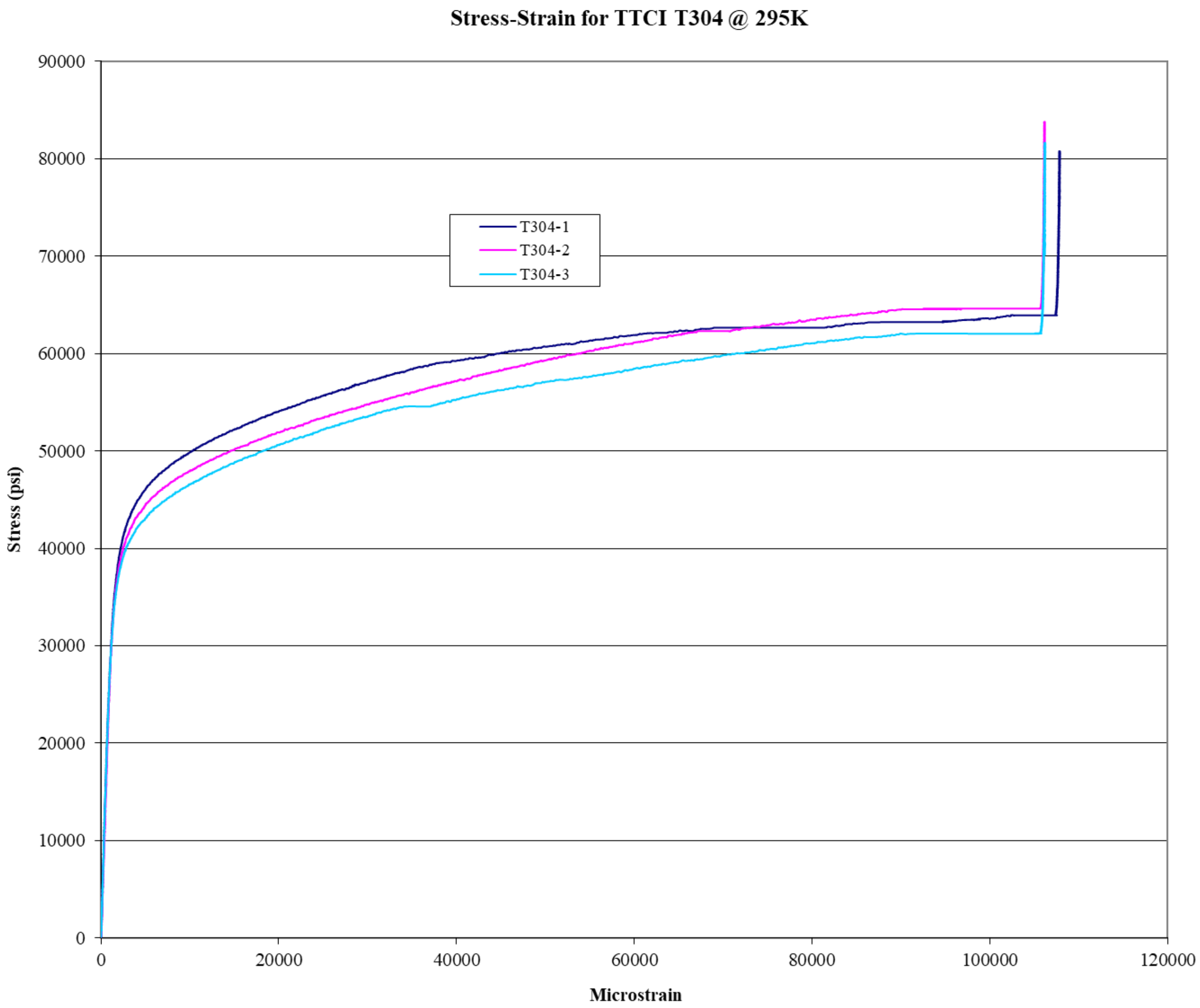

Figure 2: Stress-Strain for 77K Specimens

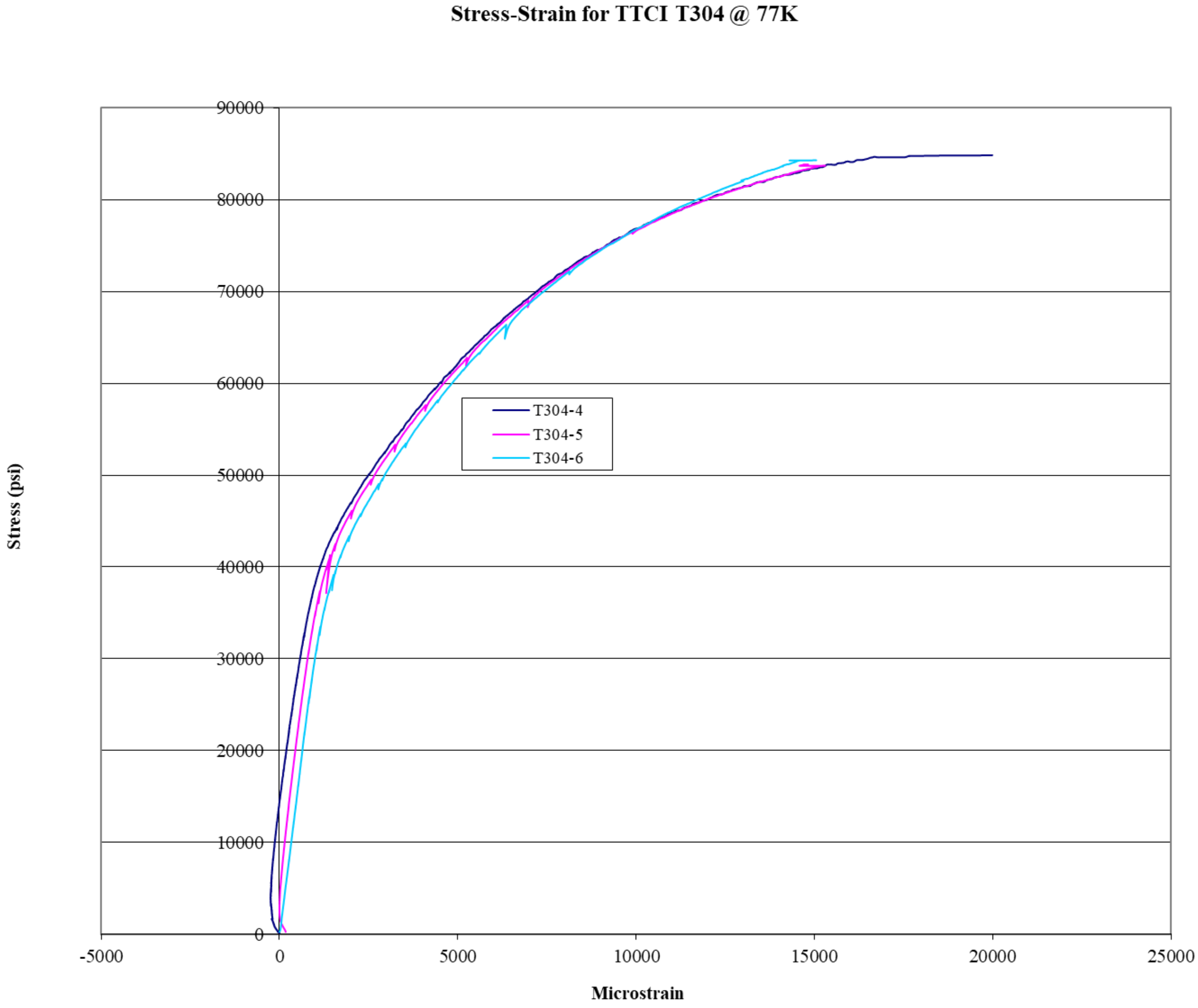

Figure 3: Stress-Strain for 77K Rapid Rate Specimens

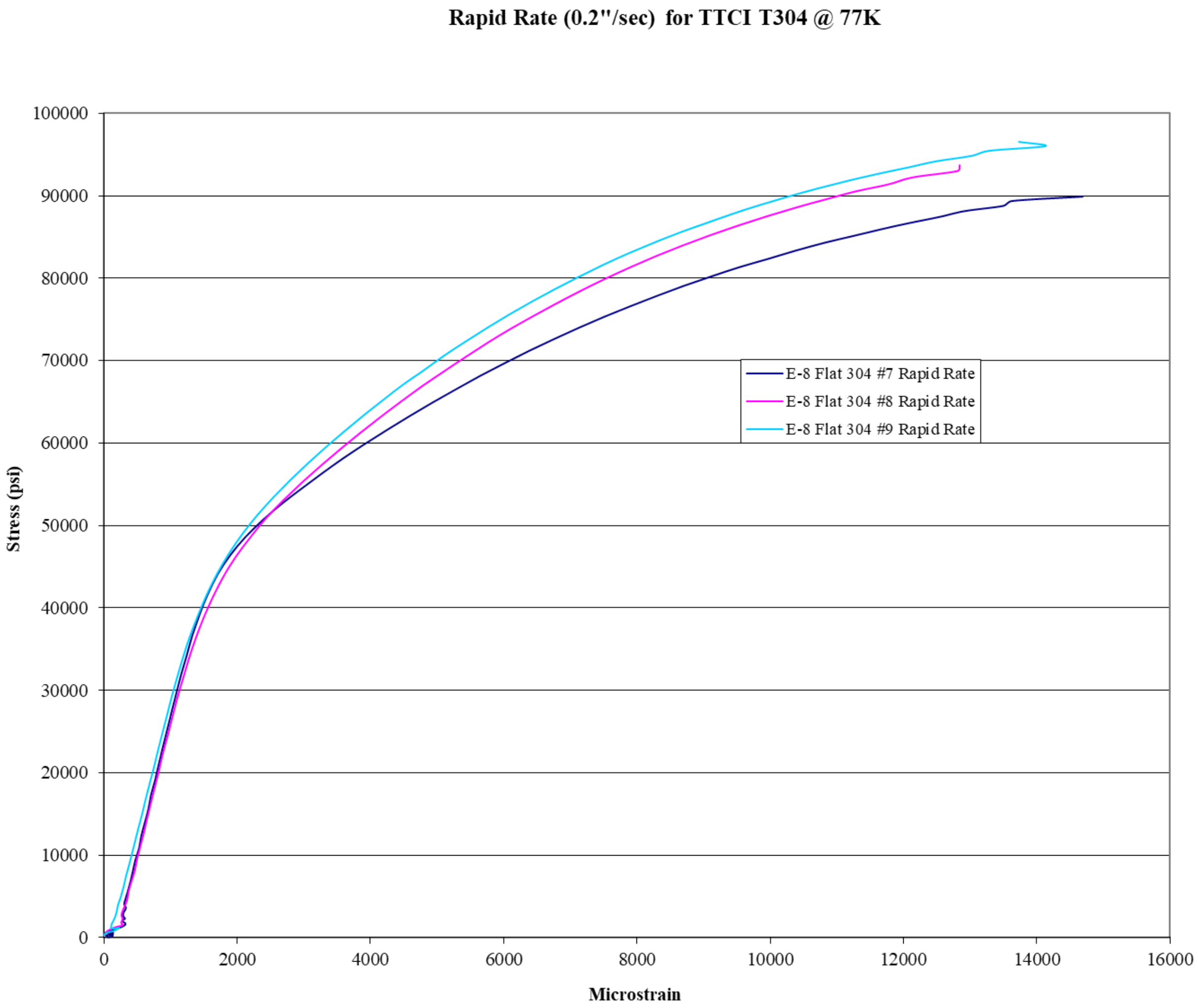

APPENDIX C

FAILED SPECIMEN PHOTOGRAPHS

Figure 1: T304 295K Failures

Figure 2: T304 200 K Failures

Figure 3: T304 77 K Rapid Rate Failures

APPENDIX D

SPECIMEN RETURN INVENTORY SHEET

TEST SPECIMEN RETURN INVENTORY SHEET

CTD Job #: **7369-373** **Customer P.O. #:** **90751**

Customer: **TTCI**
55500 DOT Road
Pueblo, CO 81001
ATTN: Shawn Trevithick

Return Inventory:

Ship Date	Specimen Type	Quantity	Specimen Number	Specimen Condition
05-13-2022	T304 Tensile	3	#1, #2, #4	Tested @295 K, Broken
	T304 Tensile	3	#4, #5, #6	Tested @77 K, Broken
	T304 Tensile	3	#7, #8, #9	Tested @77K Rapid Rate, Broken
	T304 Tensile	1	NA-Rate Test	Tested @77K Rapid Rate, Broken
	T304 Tensile	1	NA-Rate Test	Untested, Intact

Appendix C.
Post-test FEA and Test Results

For all results presented in this appendix, the acceleration data from the test and output from the FE model have been filtered using a CFC60 filter. The initial outage volume was parameterized at 3 and 5 percent due to uncertainties in the actual outage volume discussed in Section 4.6.3. This appendix contains detailed results from the post-test FE model presented in Section 6.2.

The research team inverted the east (A-end) head displacement plotted in Figure C8 with respect to the string potentiometer instrumentation layout shown in Section 3.3. This was done to orient all the plots for string potentiometers presented in this appendix in the same direction for ease of comparison, i.e., a positive value indicates motion away from the wall.

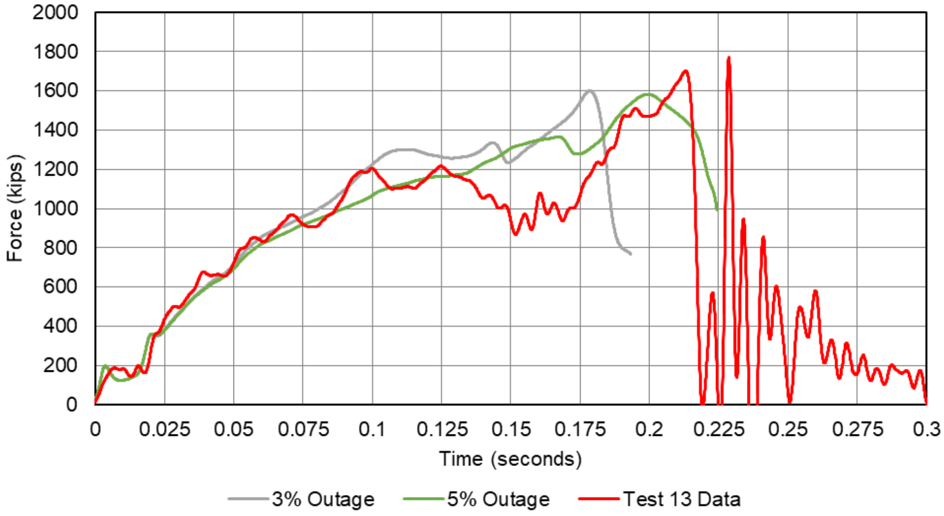

Figure C1. Impactor Force Versus Time

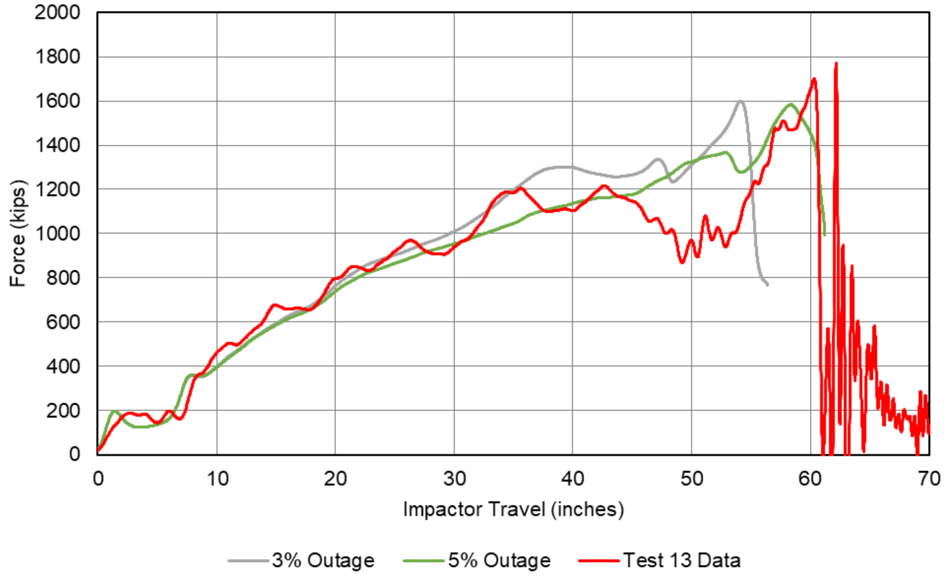

Figure C2. Impactor Force Versus Travel

Figure C3. Impactor Velocity Versus Time

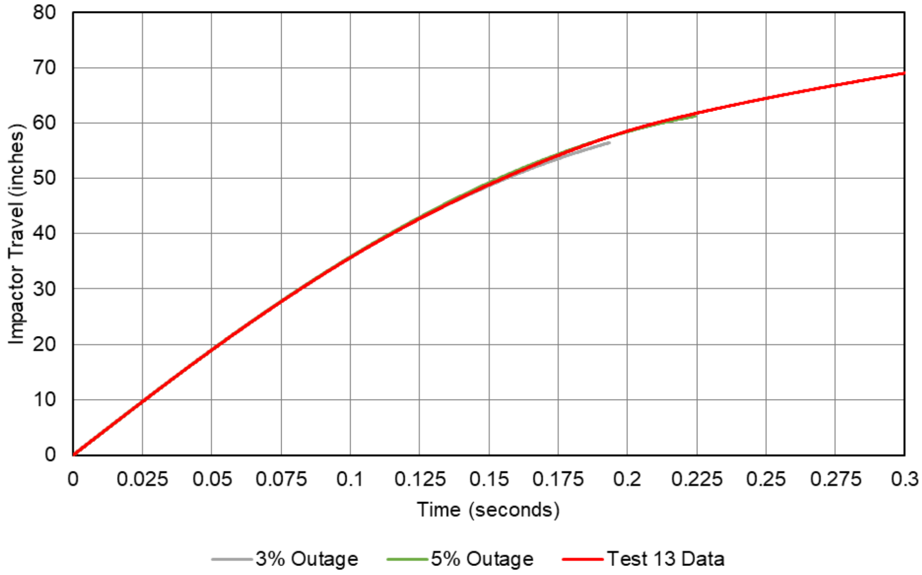

Figure C4. Impactor Travel Versus Time

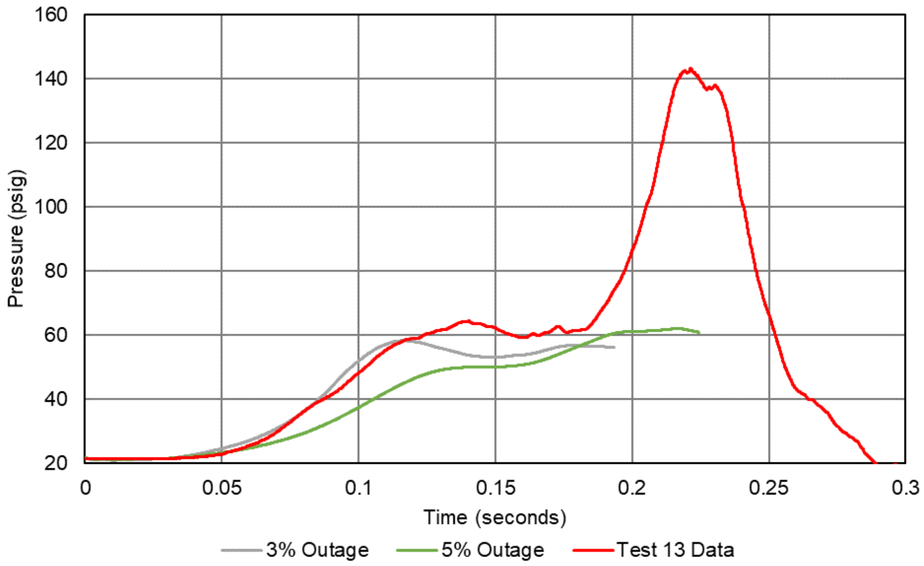

Figure C5. Outage Pressure Versus Time

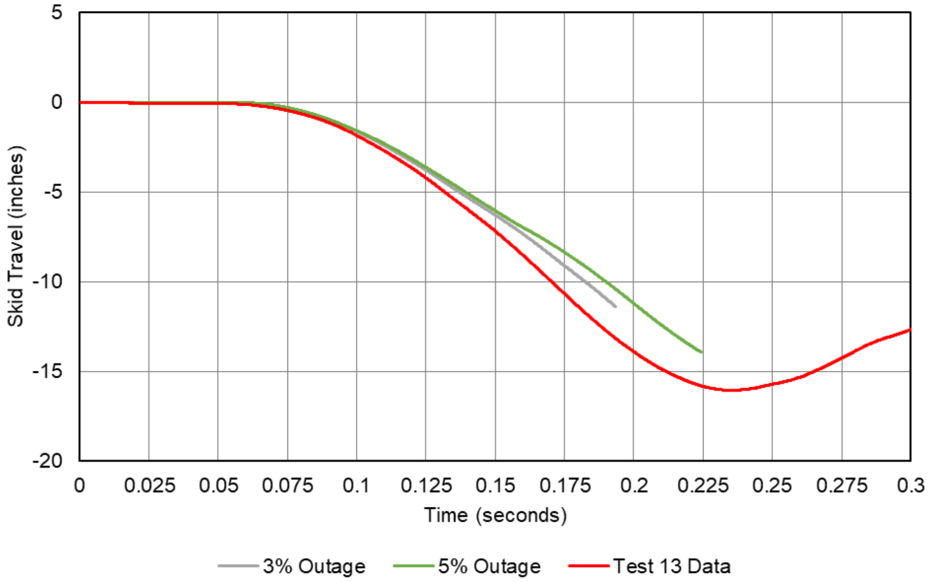

Figure C6. East (A-End) Skid Travel Versus Time

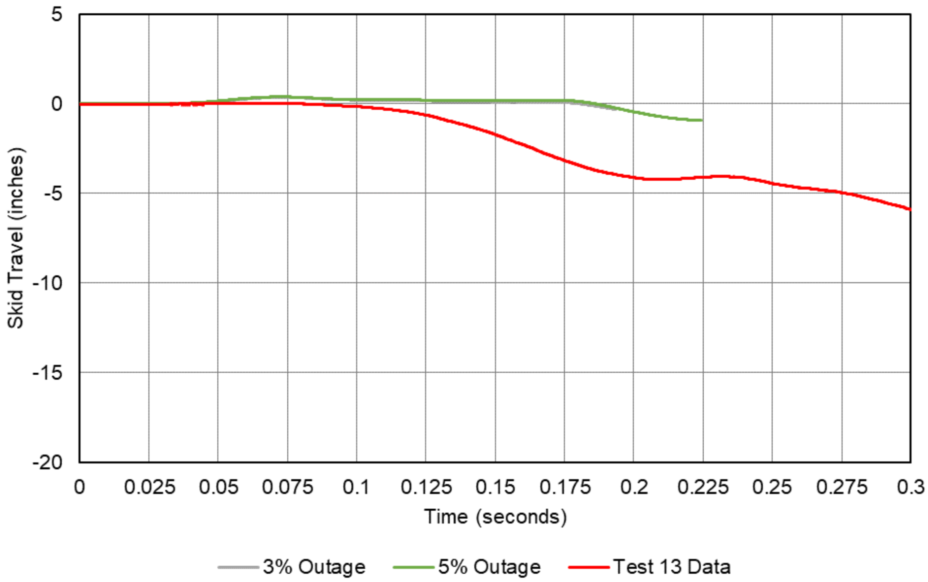

Figure C7. West (B-End) Skid Travel Versus Time

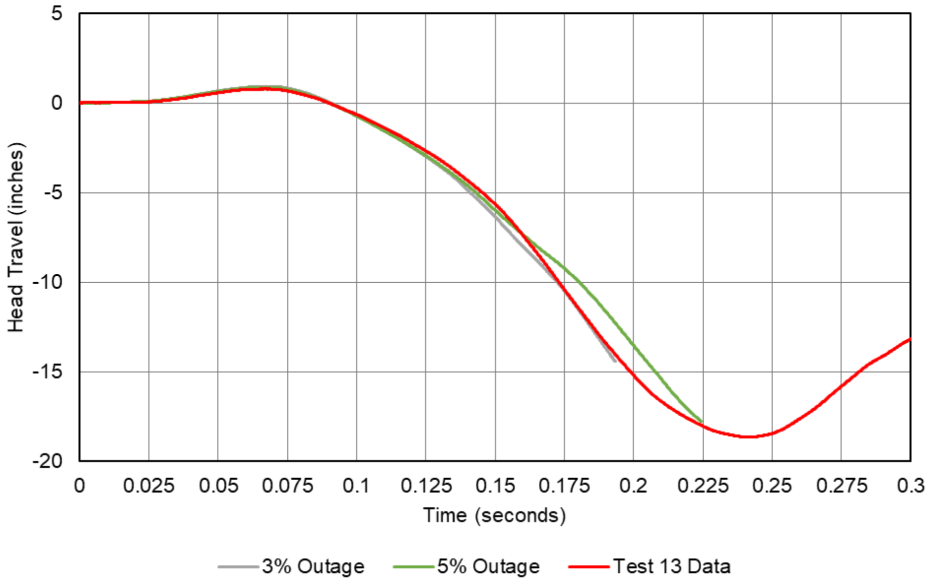

Figure C8. East (A-End) Head Travel Versus Time

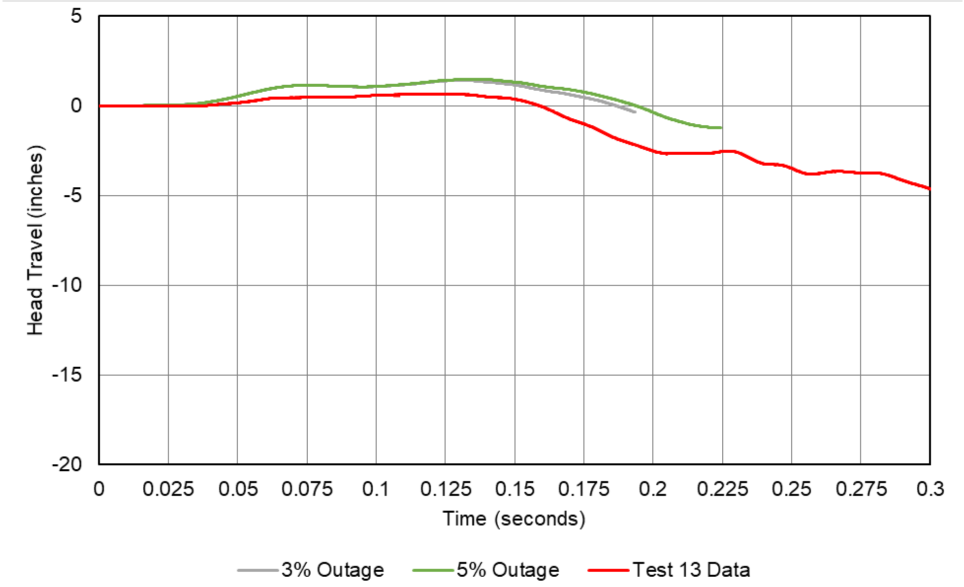

Figure C9. West (B-End) Head Travel Versus Time

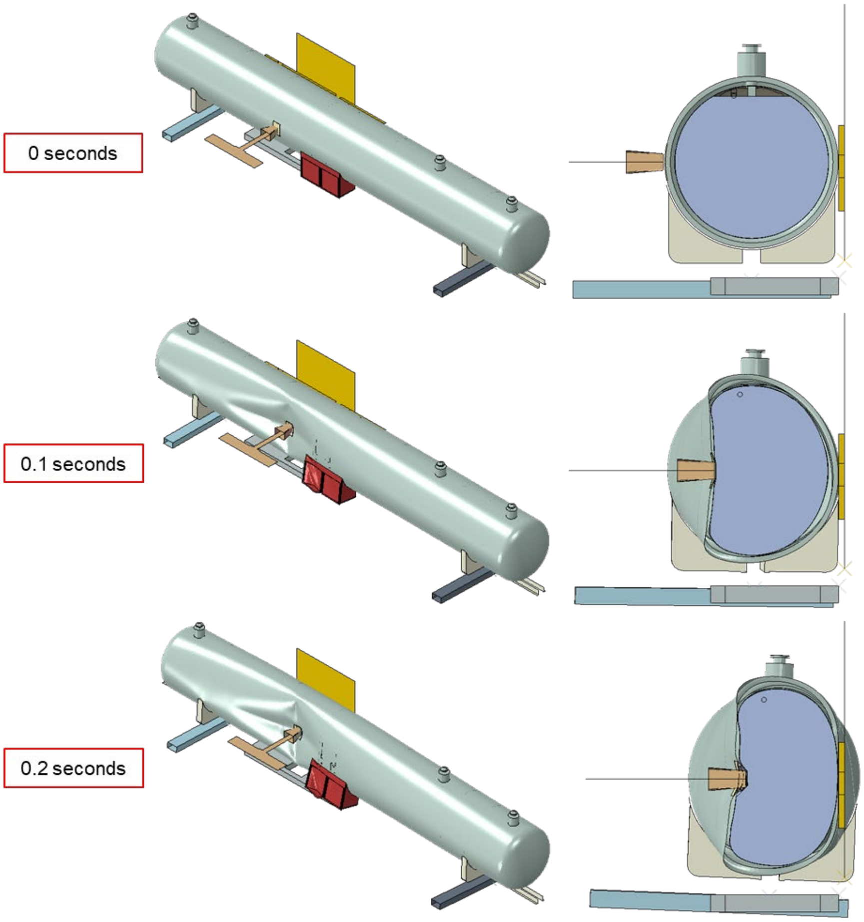

Figure C10. Isometric (left) and Side Section (right) Views of Post-test FE Model Impact Sequence at 3% Outage

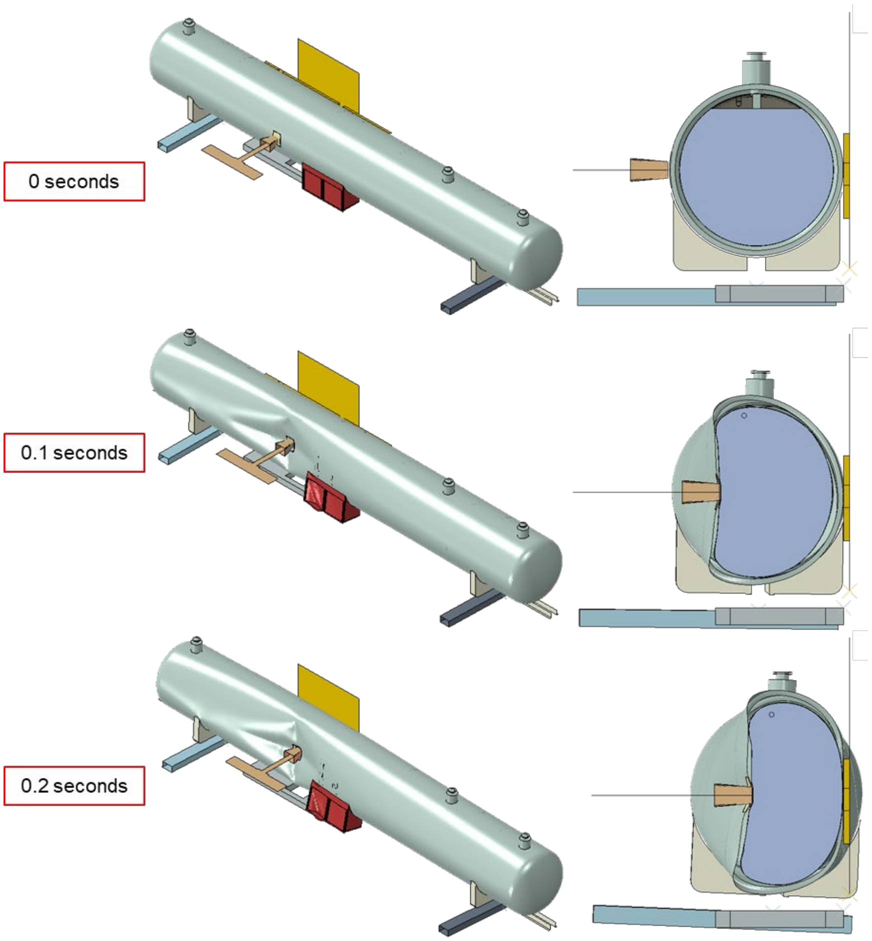

Figure C11. Isometric (left) and Side Section (right) Views of Post-test FE Model Impact Sequence at 5% Outage

Appendix D.
Geometry in Pre-test and Post-test FE Models

This appendix contains a discussion of each of the parts that comprised the assemblies for the pre- and post-test FE models. Rigid parts were used when it was important to include a part for its inertia or for its interaction through contact, but where the deformation of the part could be neglected in the calculations. Four parts were modeled as rigid bodies, and the remaining bodies were modeled as deformable bodies. A summary of the element types used to mesh the model assembly is provided in Table D1.

Table D1. Summary of Element Types [23]

Element Designation	Description
C3D8	8-node linear brick element, fully integrated
C3D8R	8-node linear brick element, reduced integration
CONN3D2	Connector element between two nodes or ground and a node
DCOUP3D	Three-dimensional distributing coupling element
M3D3	3-node triangular membrane element
M3D4R	4-node quadrilateral membrane element (reduced integration)
MASS	Point mass
R3D3	3-dimensional, 3-node triangular facet rigid element
R3D4	3-dimensional, 4-node bilinear quadrilateral rigid element
RNODE3D	3-dimensional reference node
S3R	3-node triangular general-purpose shell, finite membrane strains (identical to element S3)
S4R	4-node general-purpose shell, reduced integration with hourglass control, finite membrane strains
SPRINGA	Axial spring between two nodes, whose line of action is the line joining the two nodes – this line of action may rotate in large-displacement analysis

D1. Rigid Impactor

The impactor was modeled as a rigid body in the DOT-113 FE models. The geometry was a 12 by 12-inch square impactor with 1-inch radii edges around the impact face. The geometry included the impact face, the tapered cone back to the portion of the impactor where the impactor attached to the ram car, and a representation of the ram arm and width of the ram car's body. The impactor is shown in Figure D1 for the post-test model, and the mesh is summarized in Table D2.

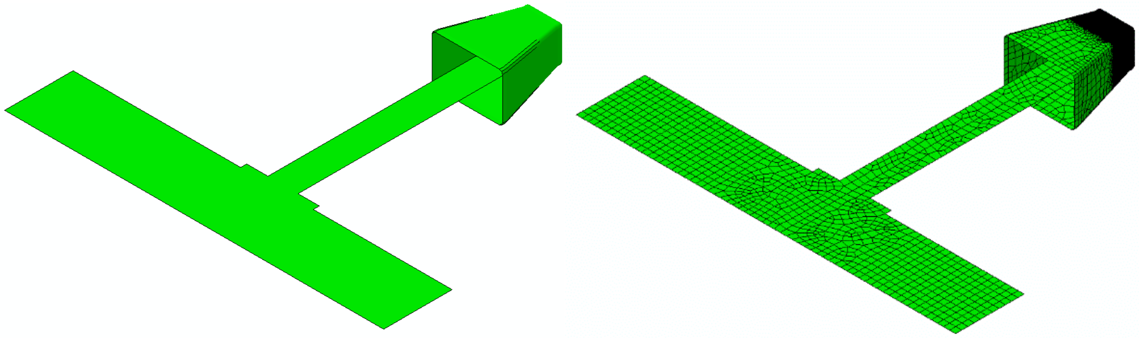

Figure D1. Impactor Geometry (left) and Mesh (right) Post-test

Table D2. Properties of Impactor Mesh

Property	Pre-test and Post-test Models
Type of Part	Rigid
Number of Elements	R3D4: 86,772 R3D3: 216 RNODE3D: 17 MASS: 1
Approximate Mesh Size	0.08 – 2 inches
Approximate Part Weight	297,200 lbf

D2. Rigid Wall

The impact wall was modeled as a rigid body. Because the wall was constrained against motion in any direction, no mass needed to be defined for this part. The wall's geometry and mesh are shown in Figure D2 for the post-test model, and the properties are summarized in Table D3.

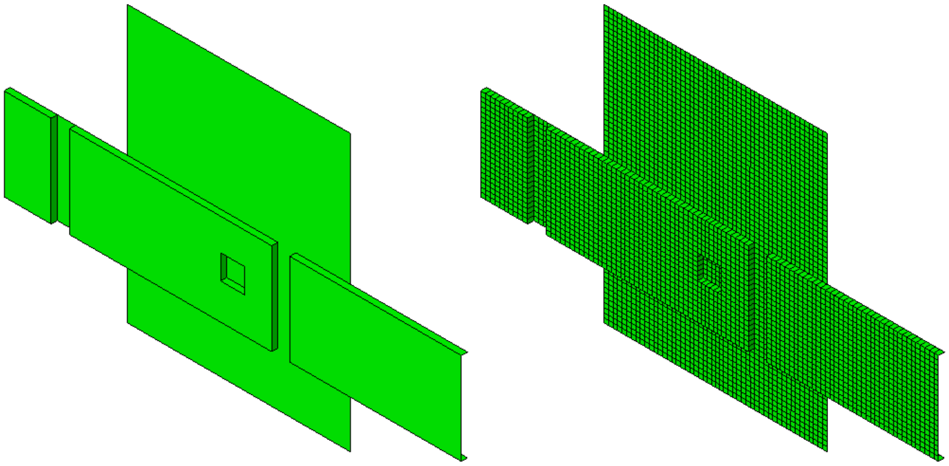

Figure D2. Rigid Wall Geometry (left) and Mesh (right) Pre- and Post-test

Table D3. Properties of Rigid Wall Mesh

Property	Pre- and Post-test Models
Type of Part	Rigid
Number of Elements	R3D4: 4,465 RNODE3D: 8
Approximate Mesh Size	3 inches

D3. Rigid Skid

The bolster of the car rested directly upon a set of skids, which themselves rested upon steel plates (see Figure 4). The skids were designed to inhibit roll of the tank car following rebound from the rigid wall during a test and were introduced early in the shell impact test series. The skid geometry and mesh are shown in Figure D3.

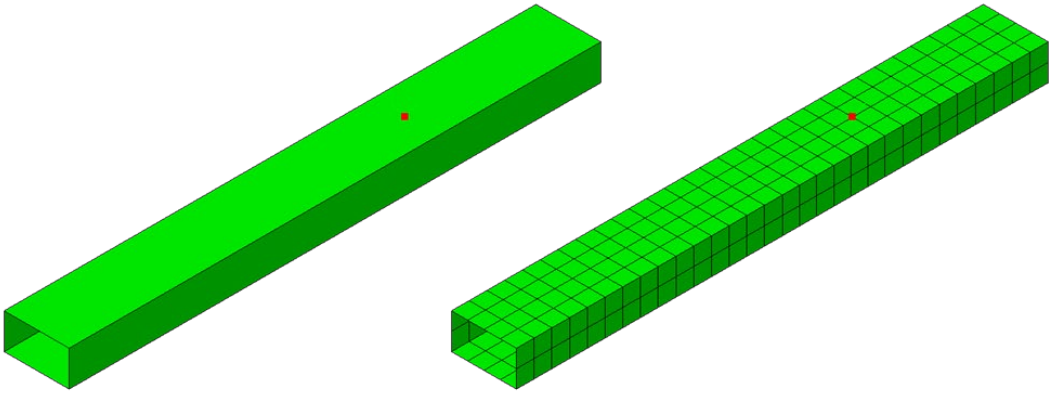

Figure D3. Skid Geometry (left) and Mesh (right) Pre- and Post-test

The rigid skids used in the test weighed approximately 3,500 lb each. This mass was included in the model using a point mass at the rigid body reference node of each skid which is shown as a red dot in Figure D3. In previous models the mass of each bolster and stub sill was lumped into the corresponding skid; however, the skids in this model did not account for the masses of the bolsters and stub sills because they were modeled with deformable shell elements. The mesh and point mass properties are summarized in Table D4.

Table D4. Properties of Skid Mesh and Point Mass

Property	**Pre-test and Post-test Models**
Type of Part	Rigid
Number of Elements	R3D4: 368 MASS: 1 RNODE3D: 1
Approximate Mesh Size	6 inches
Weight of Point Mass	3,500 lbf

D4. Rigid Ground

For both the pre-test and post-test models, the rigid ground was modeled with all six degrees-of-freedom (DOF) fixed. Figure D4 shows the rigid ground, and Table D6 summarizes the mesh properties.

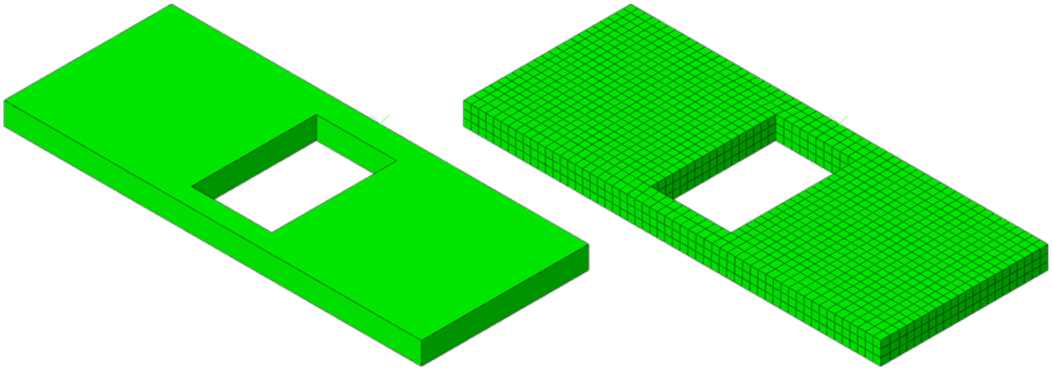

Figure D4. Rigid Ground Geometry (left) and Mesh (right)

Table D5. Properties of Rigid Ground Mesh

Property	Pre-test and Post-test Models
Type of Part	Rigid Body
Number of Elements	R3D4: 1,664 RNODE3D: 6
Approximate Mesh Size	4 inches

D5. Inner Tank – Shell Elements

The inner tank was modeled using two different techniques. In the impact zone, the inner tank was modeled using solid "brick" elements. This part is described in Section D6. Away from the impact zone, the inner tank was modeled using shell elements. The shell portion of the tank is described in this section.

Figure D5 shows the shell portion of the inner tank, and Table D7 summarizes the mesh properties. This part was globally meshed using quadrilateral reduced integration (S4R) elements and a small number of triangular shell (S3R) elements. At the edges of the impact zone, the mesh was refined (0.12 inch) to provide a transition between the fine solid mesh of the impact zone and the coarse shell mesh of the distant tank. A technique referred to as shell-to-solid coupling (SSC) was used to attach the solid patch to the edges of the shell mesh on the tank. The shell part of the tank represents the midplane surface of the tank.

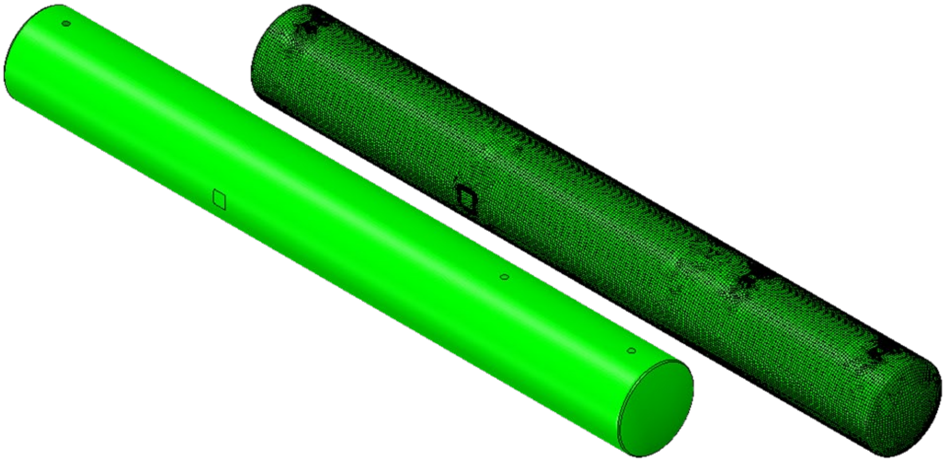

Figure D5. Post-test FE Model Inner Tank Shell Geometry (left) and Mesh (right)

Table D6. Properties of Inner Tank Shell Mesh

Property	Pre-test and Post-test Models
Type of Part	Deformable, Shell
Number of Elements	S4R: 44,828 S3R: 316
Approximate Mesh Size	0.12 to 3 inches
Material	T304 Stainless Steel
Shell Thickness	0.296 inch
Head Thickness	0.296 inch
Approximate Part Weight	29,219 lbf

D6. Inner Tank – Solid Elements

The inner tank was modeled using two different techniques. Away from the impact zone, the inner tank was modeled using shell elements. This part is described in Section D5. In the impact zone, the inner tank was modeled using solid "brick" elements as described in this section.

Figure D6 shows the solid portion of the tank, and Table D8 summarizes the mesh properties. Note that because of the fine mesh, the right image appears to show the mesh as a solid-colored part. The part was meshed using five elements through the thickness of the part. This corresponded to a global mesh seed of 0.059 inch. The mesh consisted of 8-noded reduced integration hexahedral "brick" (C3D8R) elements. The solid tank mesh was attached to the shell tank mesh along the outer and inner edges using SSC. The elements along the inner and outer edges of the solid tank that were involved in the SSC were given the same elastic and plastic material responses as the rest of the solid patch but did not have failure behaviors defined. This was done to prevent elements involved in the SSC coupling from being removed from the model, as that could cause the coupling itself to fail and the simulation to terminate.

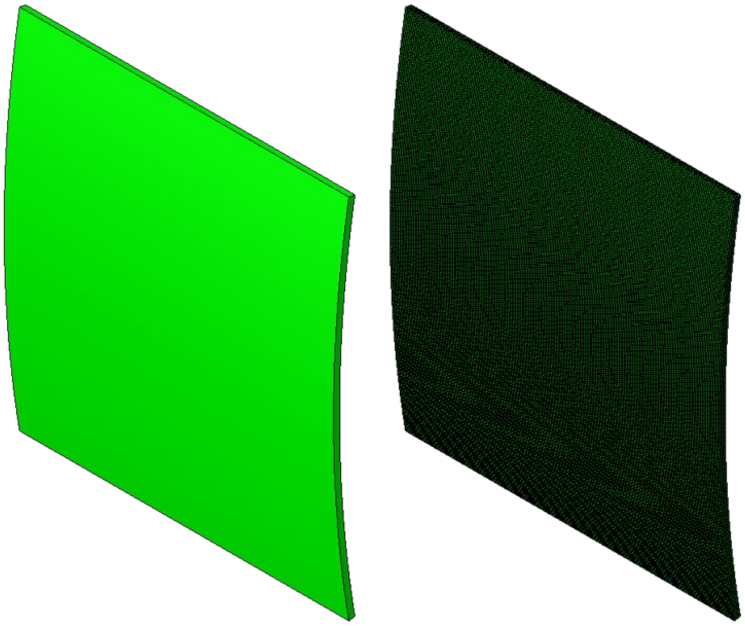

Figure D6. Inner Tank Solid Geometry (left) and Mesh (right)

Table D7. Properties of Inner Tank Solid Mesh in FE Models

Property	Pre-test and Post-test Models
Type of Part	Deformable, Solid
Number of Elements	C3D8R: 413,440
Approximate Mesh Size	0.059 inch
Material	T304 Stainless Steel
Thickness	0.29 inch
Approximate Part Weight	24 lbf

D7. Outer Tank – Shell Elements

The outer tank was modeled using two different techniques. In the impact zone, the outer tank was modeled using solid "brick" elements. This part is described in Section D8. Away from the impact zone, the outer tank was modeled using shell elements. The shell portion of the tank is described in this section.

Figure D7 shows the shell portion of the outer tank from the post-test model, and Table D9 summarizes the mesh properties. The part includes the stiffener channels, support structure for the inner tank, manway, and connections for piping on the head (right side). This part was globally meshed using 3-inch quadrilateral reduced integration (S4R) elements and a small number of triangular shell elements (S3R). At the edges of the impact zone, the mesh was refined to 0.16 inch to provide a transition between the fine solid mesh of the impact zone and the coarse shell mesh of the distant tank. The mesh was also refined near the passthrough and piping connections to 0.5 inch. While most of the outer tank was 9/16-inch-thick TC-128 carbon steel, the support structure, passthroughs, and piping connections were composed of various thicknesses of T304 stainless steel. The shell part of the tank represents the midplane surface of the tank.

Figure D7. Outer Tank Shell Geometry (left) and Mesh (right) Post-Test

Table D8. Properties of Outer Tank Shell Mesh in FE Models

Property	**Pre-test and Post-test Models**
Type of Part	Deformable, Shell
Number of Elements	S4R: 70,955 S3R: 1,570
Approximate Mesh Size	0.16 to 3 inches
Materials	TC-128 Carbon Steel T304 Stainless Steel
Shell Thickness	9/16 inch
Head Thickness	9/16 inch
Approximate Part Weight	63,093 lbf

D8. Outer Tank – Solid Elements

The outer tank was modeled using two different techniques. Away from the impact zone, the outer tank was modeled using shell elements. This part is described in Section D7. In the impact zone, the outer tank was modeled using solid "brick" elements. This part is described in this section.

Figure D8 shows the solid portion of the outer tank, and Table D10 summarizes the mesh properties. Note that because of the fine mesh, the right image appears to show the mesh as a solid-colored part. The outer tank solid patch was meshed using seven elements through the thickness. This corresponded to a global mesh seed of 0.08 inch. The solid portion of the tank was meshed using C3D8R elements. The solid tank mesh was attached to the shell tank mesh along the outer and inner edges using SSC. The elements along the inner and outer edges of the solid tank that were involved in the SSC were given the same elastic and plastic material responses as the rest of the solid patch but did not have failure behaviors defined. This was done to prevent elements involved in the SSC from being removed from the model, as that could cause the coupling itself to fail and the simulation to terminate.

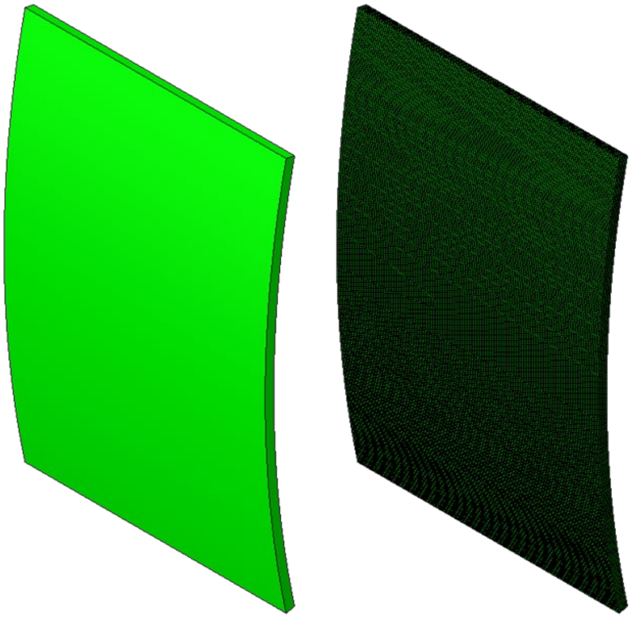

Figure D8. Outer Tank Solid Geometry (left) and Mesh (right)

Table D9. Properties of Outer Tank Solid Mesh in FE Models

Property	**Pre-test and Post-test Models**
Type of Part	Deformable, Solid
Number of Elements	C3D8R: 474,880
Approximate Mesh Size	0.08 inch
Material	TC-128 Carbon Steel
Thickness	9/16 inch
Approximate Part Weight	70 lbf

D9. Bolster and Stub Sill

The A-end and B-end bolster and stub sill of the DOT-113 tank car were represented with the same part mirrored across the center of the car. Figure D9 shows the bolster and stub sill part, and Table D11 summarizes the mesh properties. The bolster and stub sill were tied to the outer tank shell through tied constraints along the approximate weld locations.

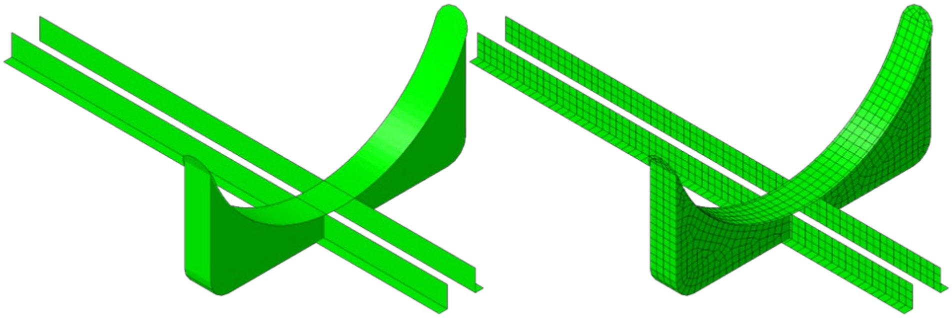

Figure D9. Bolster and Stub Sill Geometry (left) and Mesh (right)

Table D10. Properties of Bolster and Stub Sill Mesh

Property	Pre-test and Post-test Models
Type of Part	Deformable, Shell
Number of Elements	S4R: 1,712 S3R: 30
Approximate Mesh Size	3 inches
Material	TC-128 Carbon Steel
Approximate Part Weight	4,043 lbf

D10. Lading

The LN2 lading inside the inner tank was modeled as a Lagrangian EOS solid with fully integrated 4-inch "brick" elements. Figure D10 shows the lading part with a 3 percent outage from the pre- and post-test models, and Table D12 summarizes the mesh properties. The lading was also modeled at a 5 percent outage in the pre- and post-test models.

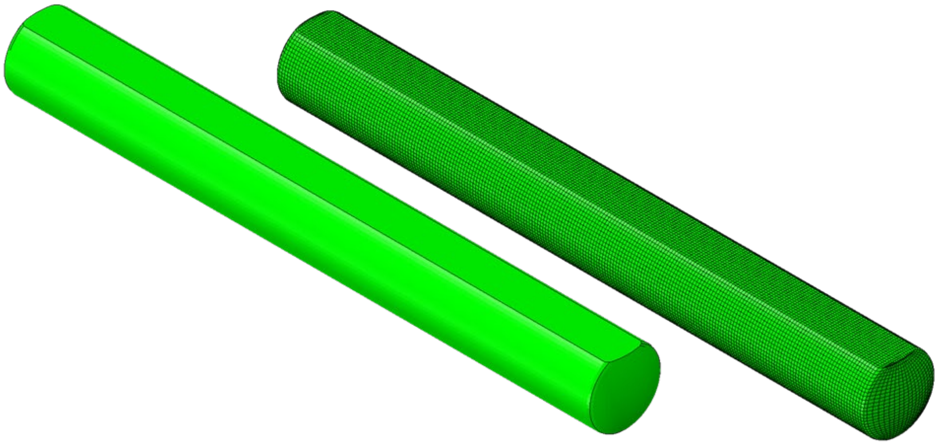

Figure D10. Lading Geometry (left) and Mesh (right) at 3% Outage

Table D11. Properties of Lading Mesh in Pre- and Post-test Models

Property	**3% Outage**	**5% Outage**
Type of Part	Deformable, Solid	Deformable, Solid
Number of Elements	C3D8: 98,430	C3D8: 100,224
Approximate Mesh Size	4 inches	4 inches
Material	Liquid Nitrogen	Liquid Nitrogen
Approximate Part Weight	215,080 lbf	209,185 lbf

D11. Membrane

The FE model of the DOT-113 tank car included a non-physical deformable membrane part that represented the extents of the outage. The gas phase (GN2) contents of the tank were modeled within the tank using a pneumatic cavity which used the membrane as an external surface to apply contact forces to the surrounding inner tank and lading.

The pneumatic cavity approach was a simplified method of capturing the pressure effects of changing the outage volume while compressing the inner tank during the impact. The solver calculated the uniform pressure and temperature in each time increment during the impact. As the tank deformed from the impact, the GN2 and LN2 changed shape. Because the LN2 was relatively incompressible compared to the GN2, the indentation of the tank mostly reduced the volume of the GN2 in the outage. The pneumatic cavity modeled the GN2 as an ideal gas with user-defined initial pressure and temperature and a universal gas constant. Thus, as the volume of the tank was reduced, the volume of the pneumatic cavity decreased and the pressure within the pneumatic cavity increased.

Because a pneumatic cavity only calculates the uniform pressures and temperatures within the cavity and not the fluid pressure or temperature at discretized points throughout the volume of the lading, this approach reduced the simulation runtime compared to techniques that represented the fluid explicitly as a Lagrangian or Eulerian mesh or collection of particles, as in smooth particle hydrodynamics (SPH). However, the uniform behavior simplification may not be well suited to all conditions, such as an impact that features an extremely small outage, or an outage that is divided into smaller volumes by a sloshing liquid.

A pneumatic cavity requires a geometric surface to be defined within the model that represents its boundary, and a reference point defined within the volume of the cavity. This reference point is used to define the interior of the cavity and is the point to which initial temperatures and pressures are defined.

The membrane part was meshed using membrane-type elements for both the portion of the part that is in contact with the interior of the tank and the portion of the part that defined the interface between the LN2 and the GN2 within the tank. Frictionless hard contact was specified between the membrane and surrounding parts. The membrane mesh was refined in the region around the manway to match its mesh size and facilitate contact. The geometry and mesh of the membrane part with a 3 percent outage are shown in Figure D11, and the mesh is summarized in Table D13.

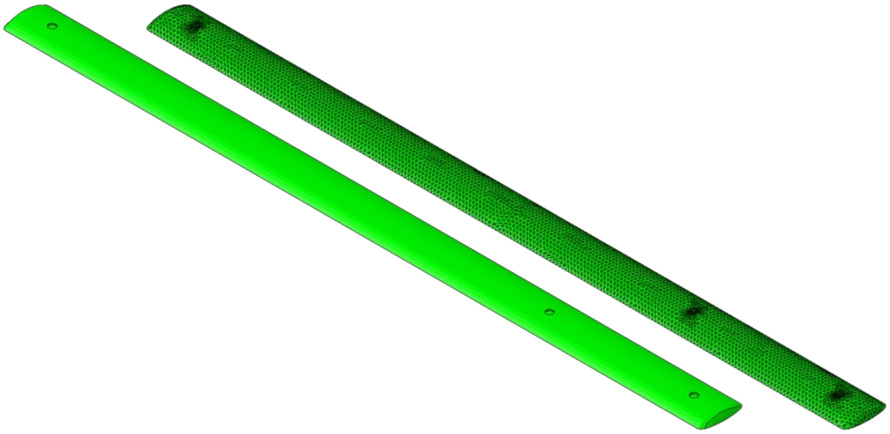

Figure D11. Membrane Geometry (left) and Mesh (right) at 3% Outage

Table D12. Properties of Membrane Mesh in FE Model

Property	3% Outage	5% Outage
Type of Part	Deformable, Membrane	Deformable, Membrane
Outage	3%	5%
Number of Elements	M3D3: 12,792	M3D3: 14,722
Membrane Thickness	0.05 inch	0.05 inch
Material	Membrane	Membrane
Approximate Mesh Size	0.5 to 3 inches	0.5 to 3 inches
Approximate Part Weight	469 lbf	561 lbf

Because the membrane represents geometry that is not physically present within the tank, a membrane element representation was chosen to be as thin and flexible as practical within the model without causing the model to terminate due to excessively distorted membrane elements. With these constraints, a thickness of 0.05 inch was chosen for the membrane.

The height of the horizontal plane (measured from the top of the lading to the top of the inner tank) was adjusted to yield the desired outage. The outage height was set to approximately 7.3 inches to yield a 3 percent outage and at 10.5 inches to yield a 5 percent outage in the pre- and post-test models. Figure D12 shows the outage height reference measurements in the FE models.

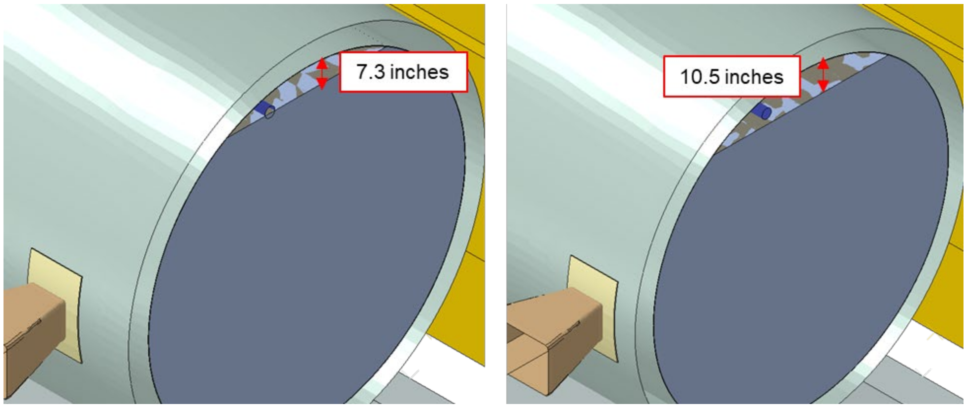

Figure D12. Reference Measurements for Outage Heights at 3% (left) and 5% (right)

Appendix E.
Modeling Techniques

This appendix describes the FE modeling techniques that were used in both the pre- and post-test models.

E1. Rigid Impactor Boundary Conditions

The rigid impactor was constrained against all motion except for longitudinal displacement. The pre-test models were run at various speeds ranging from 18 to 23 mph, and the post-test model was run at the measured test speed of 22.1 mph.

E2. Rigid Wall Boundary Conditions

The rigid wall was constrained against motion in all six DOF.

E3. Rigid Ground Boundary Conditions

The ground was constrained in all six DOF.

E4. Bolster and Stub Sill Coupling

The bolster and stub sill were tied to the outer tank as shown in Figure E1 with the tied connections displayed in red. The tied locations approximately aligned with the weld locations in the actual DOT-113 tank car. A position tolerance of 4 inches was used to connect nearby nodes between the parts.

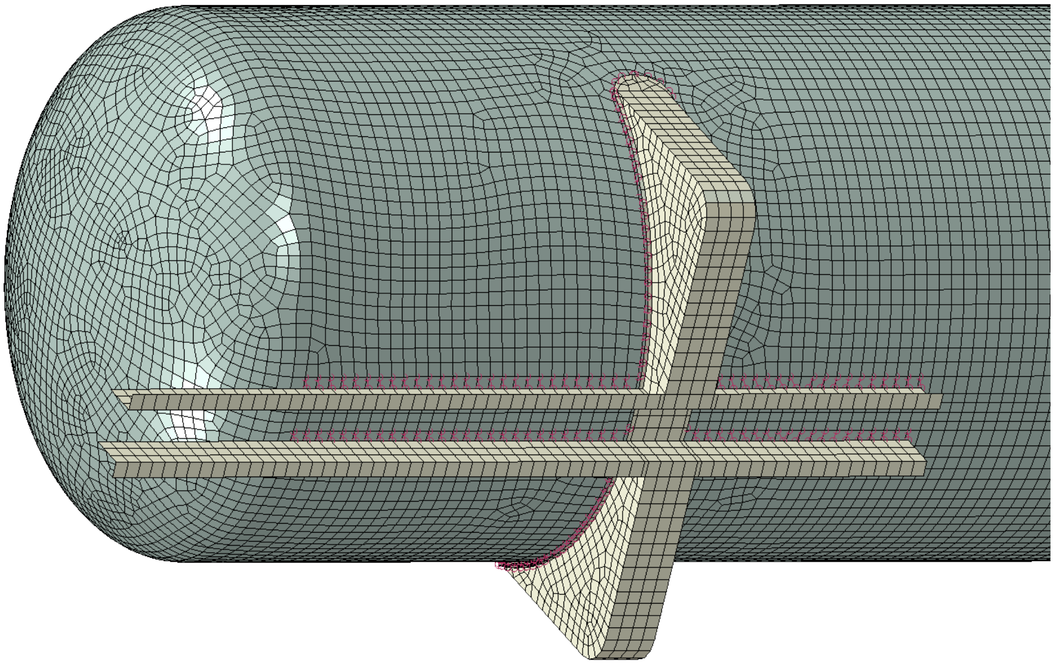

Figure E1. Tied Constraint between East End Bolster-Stub Sill and Outer Tank (Bottom View Only Showing Tied Parts)

E5. Skid Coupling

A beam-type multi-point constraint (MPC) was used to attach the bolster at each end of the tank car to the corresponding skid. The rigid body reference node on each skid was used as the control point of the MPC. The bolster nodes subject to the constraint included nodes on the bottom where the bolster was rigidly attached to the skids during the test. The B-End MPC constraint is shown in Figure E2 with the beam connectors displayed in red.

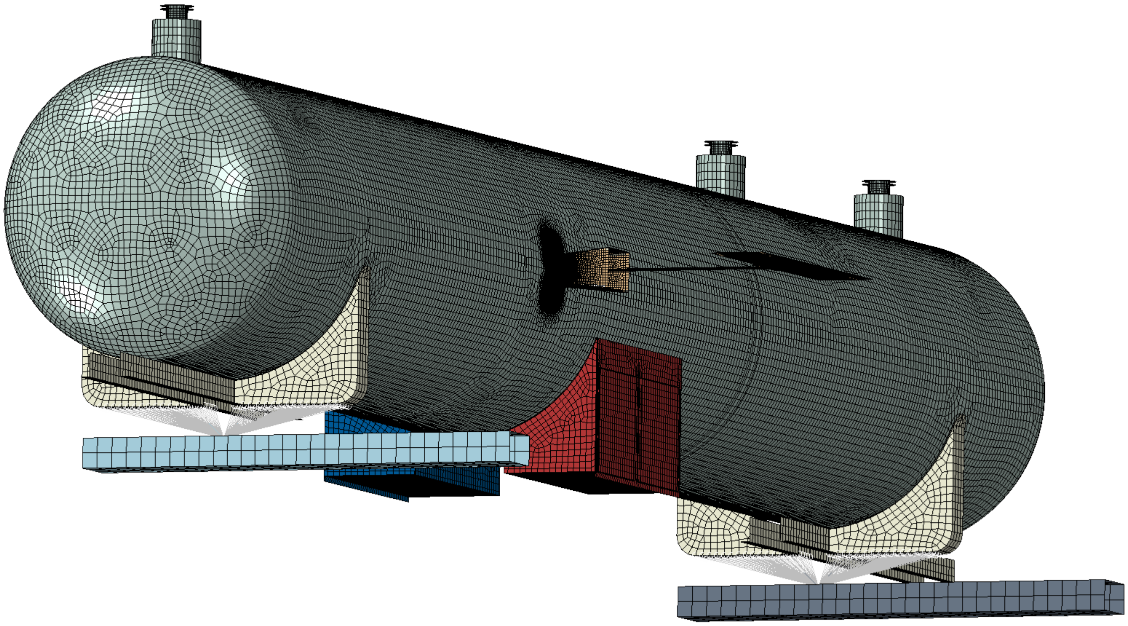

Figure E2. MPC between Bolsters and Skids (Wall and Ground Hidden)

Additionally, a “Cartesian” type of connector was used to constrain the motion of the skid both vertically and longitudinally (i.e., the direction of impactor travel). A nonlinear damper was defined between the skid and ground to constrain longitudinal motion. This damper defined the longitudinal resistance force as a function of skid speed, such that the skid had to overcome an initially high force when it was moving slowly. Once this initial peak was overcome, the resistance offered to skid motion diminished as the skid moved more quickly. This simplified model was intended to approximate the effect of static friction being overcome as the skid initially begins its motion, followed by a reduced resistance from kinetic friction. The longitudinal relationship used in the Cartesian connector is shown in Table E1 and plotted in Figure E3.

Table E1. Longitudinal Skid Behavior

Reaction Force *lbf*	Skid Velocity *in/s*
-100	-10
-38,000	-1
0	0
38,000	1
100	10

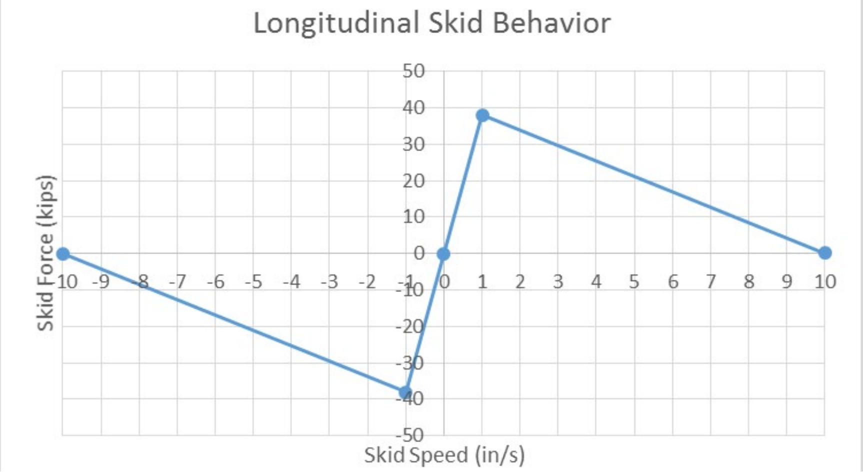

Figure E3. Longitudinal Skid Behavior

In the vertical direction, the skid used a "Stop" behavior assigned to a connector element between skid and ground to limit its range of motion. In the vertical downward direction, the reference point of the skid was prevented from having any displacement. In the upward direction, a limit of 100 inches was used. This number is arbitrary, but it was chosen to be larger than any anticipated vertical motion of the skid. These two vertical stops approximated the behavior of the skid on the ground during the physical test, where the skid was prevented from moving downward through contact with the ground but was free to lift upward if sufficient lifting forces overcame the weight resting on it.

E6. Inner and Outer Tanks SSC

SSC constraints were used on the inner tank and the outer tank to attach each patch of solid elements in the vicinity of the impact zone to the rest of the shell-meshed tank. This type of constraint is necessary to ensure a smooth transition from solid elements that possess only translational DOF to shell elements that possess translational and rotational DOF. The shell part of each tank featured a refined mesh in the vicinity of the SSC constraint. Since the shell part corresponded to the mid-plane thickness of the tank, the shell part was aligned with the mid-plane of the solid patch. The interface between the solid elements and shell elements is shown in Figure E4 for the outer tank and Figure E5 for the inner tank.

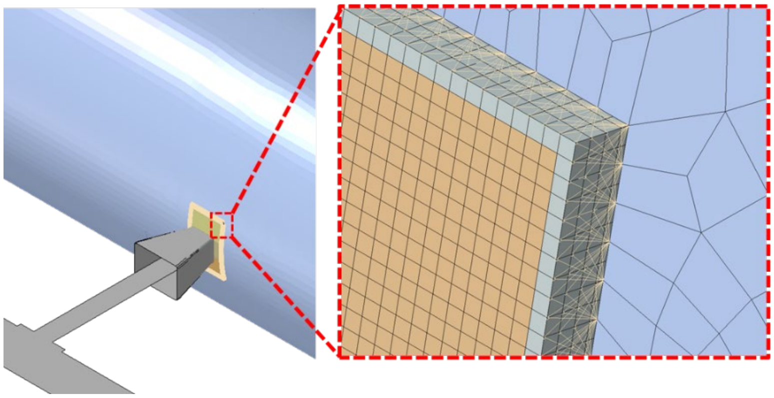

Figure E4. Shell-to-Solid Coupling Region on Outer Tank Geometry (left) and Detailed Mesh View of Corner (right)

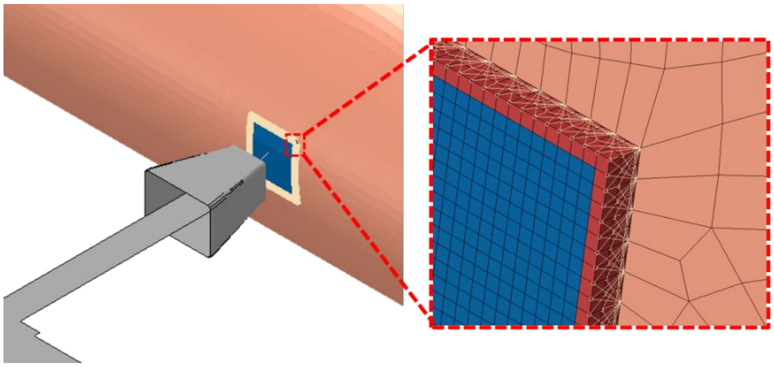

Figure E5. Shell-to-Solid Coupling Region on Inner Tank Geometry (left) and Detailed Mesh View of Corner (right) with Outer Tank Hidden

E7. Pressures and Temperatures

The tested DOT-113 tank car had an initial pressure above atmospheric pressure within the inner tank and the annular space between the tanks was held under vacuum. The pre- and post-test FE models attempted to replicate these pressure conditions as initial conditions on the model. Initial values for lading temperature were defined in the models.

The LN2 lading and GN2 outage within the inner tank were each given an initial pressure of 30 psig in the pre-test models and 22 psig for the post-test model. As the surfaces describing the boundaries of the liquid and gas phases deformed, the pressure was free to change in response. The models also require the definition of the ambient pressure on the outer tank. A value of 12.3 psi, corresponding to the atmospheric pressure [28] at the Pueblo, CO, altitude of approximately 4,700 feet [29], was used for ambient pressure. Initial temperatures were defined for both the LN2 and GN2. These initial temperatures were used to determine the appropriate material properties for each fluid type. The pre-test models used temperatures of −304.9 °F (86 K) for the LN2 and −290.5 °F (94 K) for the GN2. The post-test models used temperatures of −306.7 °F (85 K) for the LN2 and −290.5 °F (94 K) for the GN2. The temperature of the LN2 was updated in the post-test model so that it was below the saturation temperature at the lower initial pressure (22 psig) measured during the test.

E8. Mass Scaling

Variable mass scaling was used in the puncture-capable models. Because of the need for a refined mesh of solid elements in the impact zone on both the inner and outer tanks, the puncture-capable models feature many very small elements. Variable mass scaling was employed in the FE models to decrease the runtime without decreasing either the span or the resolution of the refined meshes.

Variable mass scaling is a technique in which the user sets a target time increment for a set of elements within the model (up to and including all elements within the model) and the Abaqus solver increases the mass of any element required to bring the minimum time step up to the user-defined minimum. “Variable” refers to the software’s ability to increase the mass of each element by a different amount, based on the material and geometry of each element. While mass scaling is an efficient way of reducing runtime without re-meshing a model, care must be exercised when using this technique with highly dynamic simulations. If an overly aggressive mass scaling is applied, the amount of artificial mass added to the model in the refined mesh area can significantly affect both the overall dynamic response as well as the puncture behavior of the model.

The tensile coupon models of TC-128 and T304 steels used a variable mass scaling with a target time increment of 1 x 10^{-6} seconds. The puncture-capable FE models used a variable mass scaling to achieve a target time increment of 9 x 10^{-7} seconds over the entire model. The mass scaling factors were re-calculated for the full-scale puncture models every 2,000 increments (i.e., approximately every 1.8 milliseconds).

E9. Contact

A general contact definition was used in all models. The global contact used frictionless contact, except for regions of metal-on-metal contact where a coefficient of friction of 0.3 was defined. Contact exclusions were defined between the shell tank and the solid tank patch for both the inner and outer tanks. A contact thickness reduction was used on the membrane mesh in the vicinity of the impact zone.

Appendix F.
Material Behaviors in FE Models

F1. Introduction

Pre- and post-test FE models used TC-128 carbon steel and T304 stainless steel material inputs which were calibrated from ASTM-E8 tensile test results. The TC-128 tensile tests were conducted on samples that were excised from a previous DOT-113 surrogate tank car tested with water in June 2020 (Test 11). The TC-128 material inputs were identical between the Test 11, Test 12, and Test 13 FE models because the outer tank was at room temperature in all the tests, and the mechanical properties from the TC-128 samples in the Test 11 surrogate tank car were determined to be typical. The T304 material input was updated with tensile test results from Test 13. While the Test 12 FE model also used T304 stainless steel at a cryogenic temperature, the material test report from the Test 13 tank car showed a higher ductility. The research team therefore determined that the Test 13 FE model should be updated as the higher T304 ductility could increase the predicted puncture speed. Information regarding the TC-128 material inputs is available in the Test 11 report [4]. This appendix focuses on the process used to create the cryogenic T304 material inputs for the FE model.

F2. Material Calibration Coupon Models

FE simulations of the T304 stainless steel ASTM-E8 subsize rectangular (i.e., DB) uniaxial tensile tests were used to calibrate the material definitions in Abaqus/Explicit for the full-scale models of the DOT-113 side impact test with LN2. First, the plastic true stress-plastic equivalent strain (PEEQ) characteristic was specified. Then, the damage initiation envelope was calculated. Finally, a reasonable damage progression was determined empirically.

As the material responses developed using coupon models were planned for implementation in the full-scale DOT-113 model with LN2, modeling techniques for performing the coupon simulations were deliberately chosen to be similar to the modeling techniques planned for side impact analyses of the DOT-113 tank car. Where possible, the same solver (Abaqus/Explicit), element types (C3D8R), and mesh sizes were chosen for the coupon models and the DOT-113 side impact models. This was done to attempt to minimize the uncertainty associated with calibrating a material behavior using one set of modeling techniques but applying that behavior to model puncture in the full-scale tank car impact simulation with a different set of techniques. If the tank car model was run using a different solver or different mesh density, for example, it is expected that the material behaviors would need to be recalibrated using coupon simulations that used similar solvers and mesh density.

For all tensile coupon simulations, a soft (1×10^{-6} lbf/in) discrete spring was attached to the ends of the gauge. This spring was a representation of an extensometer in the model and simplified the process of requesting the change-in-length of the gauge section from the model.

The ASTM E8 DB tensile coupon FE model used for the T304 stainless steel calibration is shown in Figure F1. The T304 DB coupon had a 2-inch gauge length, 0.5-inch width, and approximate 0.24-inch thickness (refer to Appendix Section B4). The FE model used planes of symmetry across the width and length, which are not shown in Figure F1.

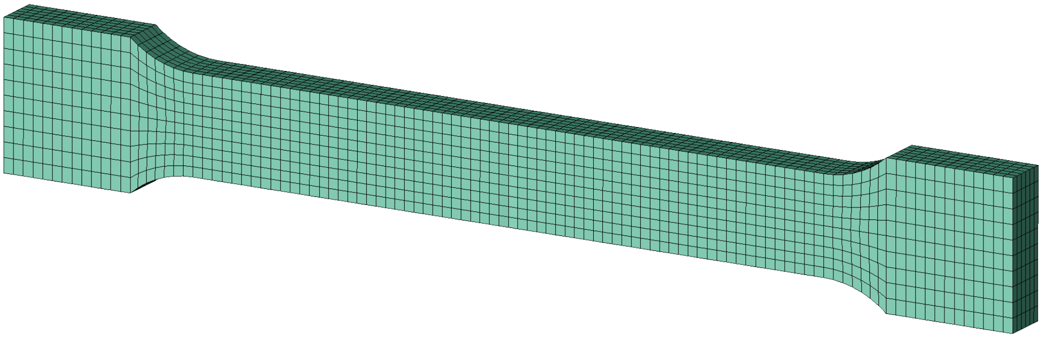

Figure F1. FE Model of T304 Stainless Steel DB ASTM E8 Coupon with 2-inch Gauge Length

The 0.296-inch-thick T304 stainless steel inner tank shell was meshed with six elements across the thickness corresponding to a mesh size of 0.059 inch (refer to Appendix Section D6).

F2.1 Plastic Hardening

Abaqus requires metal plasticity to be defined in terms of true stress and PEEQ. The plastic behavior of each steel was input to the Abaqus model as isotropic hardening using a discrete number of data points. True stress and PEEQ can be calculated from nominal stress-strain tensile coupon data according to Equation F1.

Equation F1. True Stress-strain Transformation

$$\sigma_{true} = \sigma_{nom} \cdot (1 + \varepsilon_{nom})$$
$$\varepsilon^{pl} = \ln(1 + \varepsilon_{nom}) - \frac{\sigma_t}{E}$$

σ_{nom}	nominal (engineering) stress
ε_{nom}	nominal (engineering) strain
σ_{true}	true stress
ε^{pl}	plastic equivalent strain

Because necking dominates the nominal stress-strain response of the tensile coupon characteristic after the maximum force is achieved, the true stress-PEEQ relationship was extrapolated for strains beyond the strain at maximum force using the inverse method. The inverse method involves iteratively adjusting the true stress-PEEQ relationship until agreement is achieved between the tensile coupon simulation and test results. Two methods were used to describe the true stress-PEEQ relationships for TC-128 and T304, respectively.

Paredes et al. [30] applied a Mixed Swift-Voce Law hardening expression to extrapolate true stress at high strains for TC-128. The Mixed Swift-Voce Law is a conjunction of the Swift (power) Law [31] and the Voce (exponential/saturation) Law [32] which describe plastic hardening. The Mixed Swift-Voce Law is a function of PEEQ (ε^{pl}) and is formed by combining the Swift term (σ_t^{Swift}) with the Voce term (σ_t^{Voce}) using a weighting factor (α) as shown in Equation F2.

Equation F2. Swift (Power), Voce (Exponential/Saturation), and Mixed Swift-Voce Laws for Plastic Hardening

$$\sigma_t^{Swift}\left(\varepsilon^{pl}\right) = A \cdot \left(\varepsilon_0 + \varepsilon^{pl}\right)^n$$

$$\sigma_t^{Voce}\left(\varepsilon^{pl}\right) = K_0 + Q \cdot \left(1 - e^{-\beta \varepsilon^{pl}}\right)$$

$$\sigma_t^{Mixed} = \alpha \cdot \sigma_t^{Swift} + (1-\alpha)\sigma_t^{Voce}$$

The Swift-Voce constants are calibrated using the calculated true stress-PEEQ (see Equation F1) from a tensile test and performing a least squares regression fit on the Swift and Voce equations. The Swift and Voce expressions are independently fit on the test data from a PEEQ close to zero to the PEEQ at max force because the plastic behavior of the coupon is not dominated by necking for that range of strains. After the constants for the Swift and Voce expressions are independently determined by least-squares regression, a FE model of the uniaxial tensile test is iteratively executed while varying α until the nominal stress-strain output from the model agrees with the test results up to the point of crack initiation.

In the previous test of a DOT-113 surrogate tank car filled with water (Test 11), researchers calibrated Swift Law Plastic Hardening constants for TC-128 and Swift-Voce Law Plastic Hardening constants for T304 at room temperature [4]. The team determined that these extrapolation methods captured the post-necking behavior of the tensile coupons better than linear extrapolation. They applied the same TC-128 material definition from Test 11 [4] to the DOT-113 surrogate filled with LN2 (Test 12) [6] and the current DOT-113C120W9 filled with LN2 (Test 13). However, they calibrated different Voce Law Plastic Hardening constants for T304 (see Section F3) in Test 12 because T304 has a much higher strength at cryogenic temperature than the previously calibrated room temperature material model. From Test 12 to Test 13, the T304 calibration was updated again because the strength and ductility was slightly higher.

Ductile damage initiation and progression can be used in Abaqus to simulate the crack initiation and propagation experienced in the actual coupon test through element stiffness degradation and deletion. The process of calibrating a damage initiation envelope and then empirically determining a suitable damage progression value is explained in the following section.

F2.2 Bao-Wierzbicki (B-W) Damage Initiation

Figure F2 shows a schematic of the B-W triaxiality (η)-based damage initiation envelope [24] that was used in the TC-128 material failure models. Triaxiality is defined as the ratio of the hydrostatic stress (i.e., mean stress) divided by the von Mises stress (i.e., equivalent stress) and describes the general stress state of an element. The B-W envelope consists of three regions: I – Ductile Fracture, II – Mixed Fracture, and III – Shear Fracture.

When $\eta<0$ the element is in a state of compression, and when $\eta>0$ the element is in a state of tension. A triaxiality of $\eta=-1/3$ corresponds to a stress state of hydrostatic compression and $\eta=0$ corresponds to pure shear. The cusp of the B-W envelope is intended to be located at the average triaxiality on the fracture surface of a smooth round bar specimen under uniaxial tension at $\eta=x_0$ and is typically close to a value of 0.4.

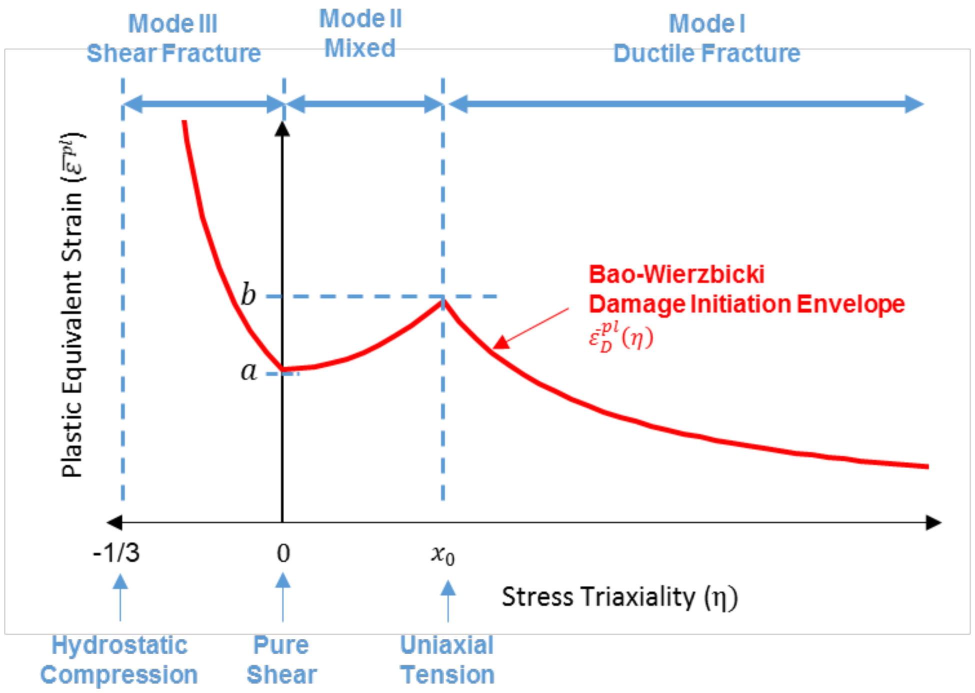

Figure F2. Schematic of Bao-Wierzbicki Damage Initiation Envelope

Three constants (a, b, x_0) govern the shape of the B-W damage initiation envelope (Equation F3) and are calibrated based on coupon test results. The critical strain to fracture in pure shear (a) corresponds to the PEEQ on the B-W envelope (ε^{pl}) when η=0 (pure shear). The critical strain to fracture in uniaxial tension (b) corresponds to ($\varepsilon_D{}^{pl}$) at the cusp of the B-W envelope when η=x_0.

Equation F3. B-W Damage Initiation Envelope

$$\varepsilon_D^{pl}(\eta) = \begin{cases} \dfrac{a}{1 + 3 \cdot \eta} & -\dfrac{1}{3} \leq \eta \leq 0 \\ (b - a) \cdot \left(\dfrac{\eta}{x_0}\right)^2 + a & 0 \leq \eta \leq x_0 \\ \dfrac{b \cdot x_0}{\eta} & x_0 \leq \eta \end{cases}$$

The complete damage initiation envelope can be developed through a series of mechanical tests on 11 unique specimen geometries intended to cover a wide range of stress triaxialities, but a simplified “quick calibration” approach that requires only one uniaxial tensile geometry to estimate the entire failure envelope was developed for industrial use by Lee and Wierzbicki [33], [34]. According to Lee, the quick calibration approach is intended to be within 10 percent agreement with a failure envelope that was developed using the complete set of 11 specimens.

The quick calibration procedure for smooth round bar tensile tests allows the calculation of the B-W envelope constants (a, b, x_0) by measuring the initial radius (a_0), final radius (a_f), displacement at max force (δ_d), and initial gauge length (L_0). For flat (i.e., DB) coupons the calculation is performed by measuring initial thickness (t_0) and final thickness (t_f) instead of initial and final radius. As seen in Equation F4, the quick calibration procedure also uses the hardening exponent (n) which is used to describe the plastic hardening behavior of metals by the power law. The hardening exponent is estimated as a function of engineering strain at maximum force.

Equation F4. Quick Calibration Procedure for Smooth Round Bar (left) and Flat DB (right) Uniaxial Tensile Coupons

Smooth Round Bar

$$
\begin{aligned}
n &= \ln\left(1+\frac{\delta_d}{L_0}\right)\\
b &= 2\cdot\ln\frac{a_o}{a_f}\\
x_0 &= \frac{1}{3}+\frac{0.22}{b}\cdot(b-n)^{1.8}\\
a &= b\cdot\left(\frac{\sqrt{3}}{2}\right)^{1/n}
\end{aligned}
$$

Flat (Dogbone) Coupon

$$
\begin{aligned}
n &= \ln\left(1+\frac{\delta_d}{L_0}\right)\\
b &= \frac{2}{\sqrt{3}}\cdot\ln\frac{t_o}{t_f}+\frac{2\cdot n}{\sqrt{3}}\cdot\left(\sqrt{3}-1\right)\\
x_0 &= \frac{1}{\sqrt{3}}-\frac{2\cdot n}{3\cdot b}\cdot\left(\sqrt{3}-1\right)\\
a &= b\cdot\left(\frac{\sqrt{3}}{2}\right)^{1/n}
\end{aligned}
$$

For ductile metals in Abaqus, the damage threshold is reached when the ductile criterion (DUCTCRT) reaches a value of 1. The DUCTCRT is calculated by integrating the change in PEEQ divided by the PEEQ where damage initiates as a function of triaxiality (i.e., the B-W envelope) according to Equation F5.

Equation F5. Calculation of the Ductile Damage Criterion (DUCTCRT) in Abaqus

$$
DUCTCRT = \int \frac{d\varepsilon^{pl}}{\varepsilon_D^{pl}(\eta)}
$$

After DUCTCRT reaches a value of 1 the stiffness of the element is degraded according to the damage progression in the material definition. In this report, exponential displacement-based damage progression values are calibrated for each material; however, previous puncture simulations have used linear energy-based damage progressions [12, 13].

F3. Cryogenic T304 Stainless Steel

The T304 stainless steel stress-strain behavior at 77 K and 0.1 s^{-1} presented in Section 4.7.2 was used to calibrate a material model for the full-scale DOT-113C120W9 with LN2 puncture model. A temperature of 77 K, corresponding to the saturation temperature of nitrogen at atmospheric pressure, was chosen for the coupon FE model and DOT-113 FE model. While this temperature is colder than the actual temperature in the tank car, it is easier for a test lab to achieve a temperature corresponding to the saturation temperature of LN2 at atmospheric pressure because the sample can be fully immersed in LN2. The team chose this approach for simplicity due to the short time frame for material testing prior to the side impact test. Previous cryogenic tensile testing after Test 11 showed that there was very little difference in the measured fracture toughness at 77 K between strain rates which were above QS strain rate [4]. Therefore, researchers chose an elevated strain rate of 0.1 s^{-1} for calibrating the FE model.

The team scaled the true stress-PEEQ strain curve calibrated for Test 12 [6] because extensometer data was not available up to the elongation at break for the Test 13 T304 stainless tensile coupons. A scaling factor of 1.05 resulted in good agreement with the YS and UTS measured from the Test 13 tank car. In the Test 12 T304 material input, the true stress-PEEQ strain curve was directly calculated from the nominal stress-strain test data up to a true strain of 0.2 in/in. For higher strains, a Voce (i.e., saturation) plastic hardening equation was fit onto a calculated true stress-PEEQ strain curve. The Voce constants which resulted in the best fit were determined by a least-squares regression similar to Paredes et al. [35]. The Voce curve was used to extrapolate the true stress-PEEQ strain behavior after the UTS occurred (i.e., necking) up to PEEQ strains as high as 2.0 in/in. Figure F4 shows the updated plastic hardening input for cryogenic (77 K) T304 stainless steel at 0.1 s^{-1} from the Test 13 tank car which was scaled from the Test 12 surrogate tank car. The resulting saturation true stress was 247 ksi.

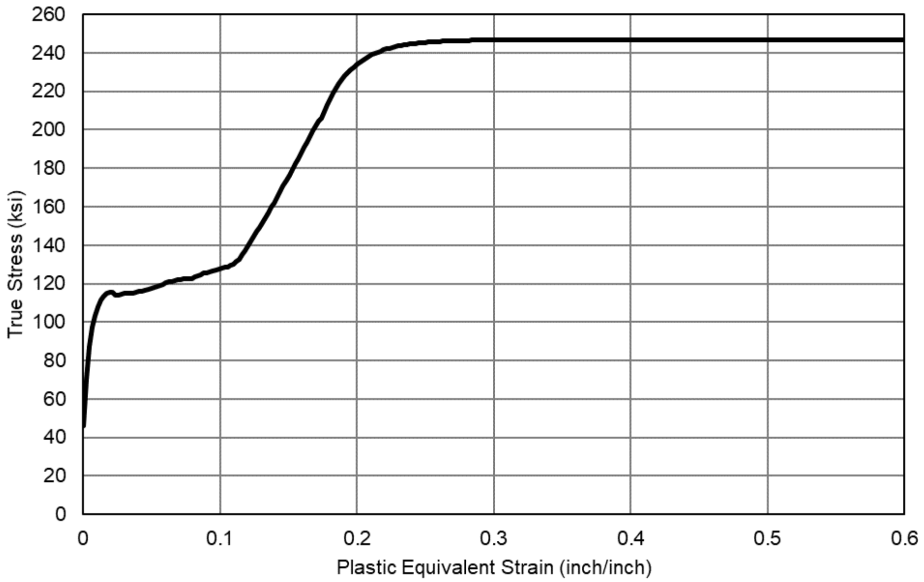

Figure F3. True Stress-PEEQ Strain FE Input for Test 13 T304 Stainless Steel at 77 K and 0.1 s^{-1}

The updated constants for the Voce plastic hardening expression (see Equation F2) are given in Table F1. Note that the Voce plastic hardening expression was only used to extrapolate true stress for PEEQ strains above 0.2 in/in. Refer to Table F2 for the true stress-PEEQ strain behavior up to a PEEQ strain of 0.2 in/in which was directly calculated using Equation F1 on regularized test data.

Table F1. Constants for Voce Plastic Hardening Greater than 0.2 in/in of Test 13 T304 Stainless Steel at 77 K and 0.1 s^{-1}

k_0	Q	β
ksi	*ksi*	-
-1.0767×10^5	1.0791×10^5	3.8900×10^1

Table F2. Plastic Equivalent Strain Versus True Stress Input up to 0.2 in/in for Test 13 T304 Stainless Steel at 77 K and 0.1 s^{-1}

PEEQ *in/in*	True Stress *ksi*	PEEQ *in/in*	True Stress *ksi*	PEEQ *in/in*	True Stress *ksi*
0.00E+00	4.62E+01	6.88E-02	1.22E+02	1.38E-01	1.60E+02
2.15E-03	7.05E+01	7.10E-02	1.22E+02	1.40E-01	1.62E+02
4.30E-03	8.73E+01	7.31E-02	1.22E+02	1.42E-01	1.65E+02
6.45E-03	9.72E+01	7.53E-02	1.23E+02	1.44E-01	1.68E+02
8.60E-03	1.04E+02	7.74E-02	1.23E+02	1.46E-01	1.71E+02
1.08E-02	1.08E+02	7.96E-02	1.23E+02	1.48E-01	1.74E+02
1.29E-02	1.11E+02	8.17E-02	1.23E+02	1.51E-01	1.76E+02
1.51E-02	1.14E+02	8.39E-02	1.24E+02	1.53E-01	1.79E+02
1.72E-02	1.15E+02	8.60E-02	1.25E+02	1.55E-01	1.82E+02
1.94E-02	1.16E+02	8.82E-02	1.25E+02	1.57E-01	1.85E+02
2.15E-02	1.15E+02	9.03E-02	1.26E+02	1.59E-01	1.88E+02
2.37E-02	1.14E+02	9.25E-02	1.26E+02	1.61E-01	1.91E+02
2.58E-02	1.14E+02	9.46E-02	1.27E+02	1.63E-01	1.94E+02
2.80E-02	1.15E+02	9.68E-02	1.27E+02	1.66E-01	1.96E+02
3.01E-02	1.15E+02	9.89E-02	1.28E+02	1.68E-01	1.99E+02
3.23E-02	1.15E+02	1.01E-01	1.28E+02	1.70E-01	2.02E+02
3.44E-02	1.15E+02	1.03E-01	1.28E+02	1.72E-01	2.05E+02
3.66E-02	1.15E+02	1.05E-01	1.29E+02	1.74E-01	2.06E+02
3.87E-02	1.16E+02	1.08E-01	1.30E+02	1.76E-01	2.10E+02
4.09E-02	1.16E+02	1.10E-01	1.30E+02	1.79E-01	2.13E+02
4.30E-02	1.16E+02	1.12E-01	1.32E+02	1.81E-01	2.16E+02
4.52E-02	1.17E+02	1.14E-01	1.33E+02	1.83E-01	2.19E+02
4.73E-02	1.17E+02	1.16E-01	1.35E+02	1.85E-01	2.22E+02
4.95E-02	1.18E+02	1.18E-01	1.37E+02	1.87E-01	2.24E+02
5.16E-02	1.18E+02	1.20E-01	1.40E+02	1.89E-01	2.26E+02
5.38E-02	1.18E+02	1.23E-01	1.42E+02	1.91E-01	2.28E+02
5.59E-02	1.19E+02	1.25E-01	1.45E+02	1.94E-01	2.30E+02
5.81E-02	1.20E+02	1.27E-01	1.47E+02	1.96E-01	2.31E+02
6.02E-02	1.20E+02	1.29E-01	1.49E+02	1.98E-01	2.33E+02
6.24E-02	1.21E+02	1.31E-01	1.52E+02	2.00E-01	2.34E+02
6.45E-02	1.21E+02	1.33E-01	1.54E+02		
6.67E-02	1.22E+02	1.36E-01	1.57E+02		

The B-W damage initiation envelope from the Test 12 T304 was also scaled to match the average elongation at break from the Test 13 samples. The updated constants for the B-W damage envelope are given in Table F3, and the resulting B-W envelope is plotted in Figure F5.

Table F3. Bao-Wierzbicki Damage Initiation Envelope Constants for Test 13 T304 Stainless Steel at 77 K and 0.1 s^{-1}

a	*b*	x_0
0.3235	0.5906	0.3333

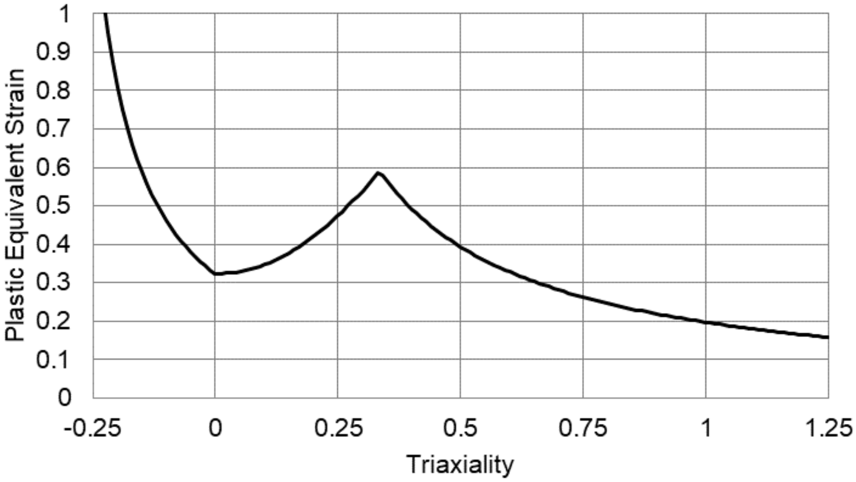

Figure F4. Bao-Wierzbicki Damage Initiation Envelope for Test 13 T304 Stainless Steel at 77 K and 0.1 s^{-1}

Figure F6 shows the resulting nominal stress-strain responses from the T304 DB FE model. A displacement-based exponential damage progression was selected at 0.005 in/in^2 with an exponent of −2 because it gave a reasonable nominal stress-strain slope after damage initiation. Qualitatively, the nominal stress-strain response from the FE model matches the average UTS and EB measurements from the T304 DB tensile coupons response below.

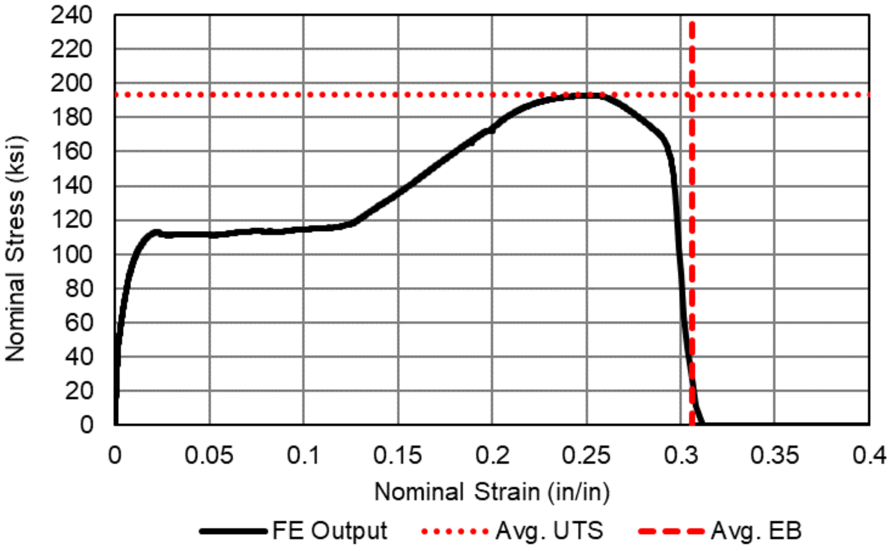

Figure F5. Nominal Stress-Strain Output of T304 Stainless Steel DB (2-inch GL) FE Model with Average UTS and EB Shown for Comparison at 77 K and 0.1 s^{-1}

Appendix G.
Outage Volume and Pressures

The DOT-113 tank car was filled with LN2 between May 10 and May 13, then allowed to settle until the test on May 14, 2022. Digital pressure, temperature, and weight measurements were recorded while the tank car was being filled. Additionally, readings from the mechanical pressure and filling level gauges (static head pressure gauges) installed on the DOT-113 were manually recorded periodically during filling. These measurements are presented in Section G1. The post-test calculations to estimate the filling volume at the start of the test are shown in Section G2.

G1. Pre- and Post-test Pressures and Temperatures

Pressure, temperature, and weight data collected while the tank car was being filled were intended to provide an estimate of the filling level and outage pressure with a high level of confidence. Unfortunately, there were several inconsistencies in the data and challenges with making the measurements that led to uncertainty in the actual filling level at the time of the test.

The same internal pressure transducers and thermocouples used in the impact test were used to record filling data, but at a lower rate of 1 Hz. Pressure and temperature data were recorded from the start of filling on May 10 until the morning of the test on May 14. Pressure data from the instrumentation system was supplemented by intermittent manual recordings from the two mechanical pressure gauges on the exterior of the tank car. Four load cells were installed between the tank car and its skids to measure the weight of LN2 added to the car. While the load cells were measuring weight continuously, the weight data were not recorded continuously.

The pressure data was post-processed to produce an average pressure from each measurement device over the course of an hour. Figure G1 shows a plot of the hourly average pressure measured by each of the three pressure transducers at the top of the inner tank, an average of these three measurements for each hour, and discrete measurements read from the mechanical pressure gauges on the exterior of the tank car.

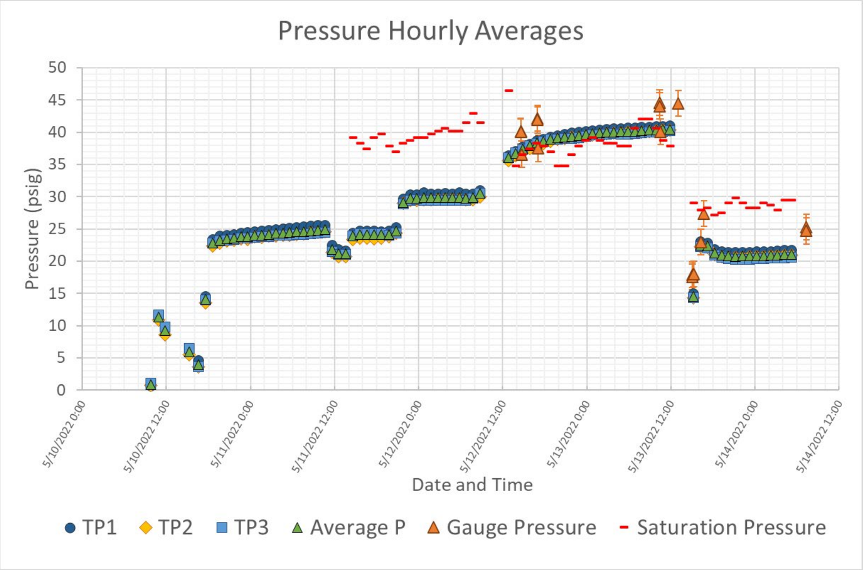

Figure G1. Hourly Average Pressures During Filling and Settling

This plot also includes the saturation pressure (i.e., the pressure that LN2 must remain above for a given temperature) as a point of reference. The saturation pressure was calculated by averaging the temperature readings from three thermocouples positioned below the filling level (TT1L, TT2L, and TT3L) and looking up the corresponding saturation pressure using a public database from NIST [20]. Note that as the average liquid temperature within the tank car changed during the filling process (see subsequent discussion in this Appendix) the saturation pressure also changed.

Figure G1 shows that the inner tank was initially close to atmospheric pressure at the start of the filling process, as expected. The pressure was allowed to build as LN2 was introduced into the car. On the day before the test, the pressure was decreased by venting vapor as the car was being filled with liquid. By the morning of the test the pressure was stable at approximately 22 psig. This figure also shows that while the pressure transducers were consistent with one another there was typically a difference of 2-3 psi between the transducers and the mechanical pressure gauge readings at the same time.

The temperature data were post-processed to produce an average temperature from each measurement device over the course of an hour. Figure G2 shows a plot of the hourly average temperature measured by each of the three thermocouples positioned below the liquid level of the tank car, as well as the average of these three measurements for each hour. This plot also includes the calculated saturation temperature (i.e., the temperature that LN2 must remain below for a given pressure). The saturation temperature was calculated by averaging the pressure measurements from the outage (TP1, TP2, and TP3) and looking up the corresponding saturation temperature using the same public database from NIST [20]. Note that as the internal pressure of the tank car changed during the filling process (see Figure G1) the saturation temperature also changed.

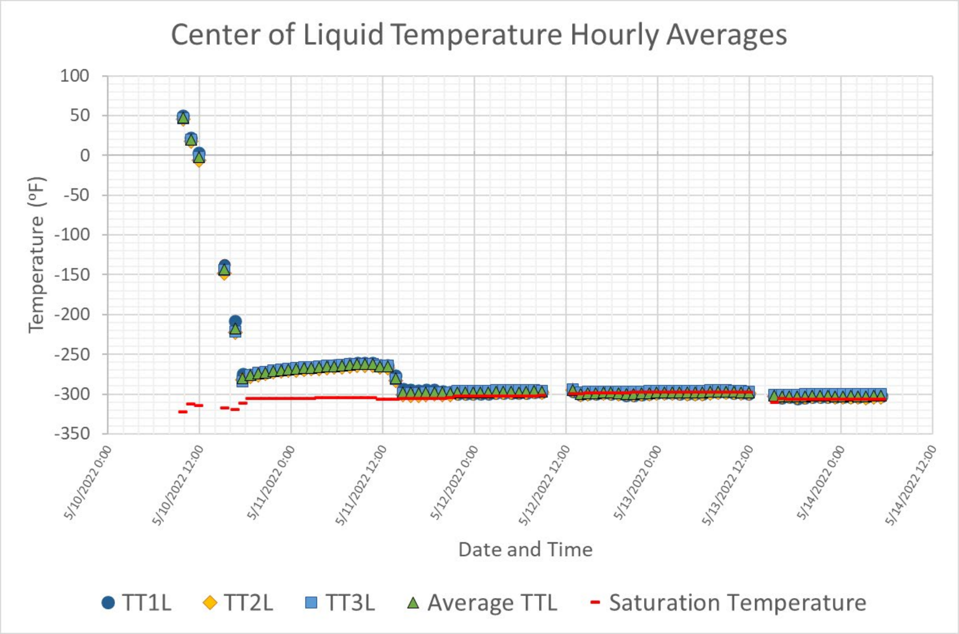

Figure G2. Hourly Average Temperature from Thermocouples at Center of Liquid During Filling and Settling

Initially, the thermocouples near the center of the tank measured the initial ambient temperature of the tank. This temperature rapidly dropped as LN2 was introduced into the tank. The temperature at the center of the tank was significantly above the saturation temperature until approximately 3 PM on May 11. It is likely that the level of LN2 reached the level of the thermocouples in the center of the tank around this time, submerging the thermocouples below the liquid for the rest of the filling process.

Figure G3 shows the same data as the previous figure, but on a re-scaled set of axes to focus on the relationship between measured temperatures and calculated saturation temperatures. From this figure it is apparent that except for a period on May 12-13, the measured temperatures in the center of the tank car remained above the saturation temperature of LN2. While this difference was typically less than 10 degrees Fahrenheit, any temperature measured in a liquid above its saturation temperature is suspicious as that condition cannot exist.

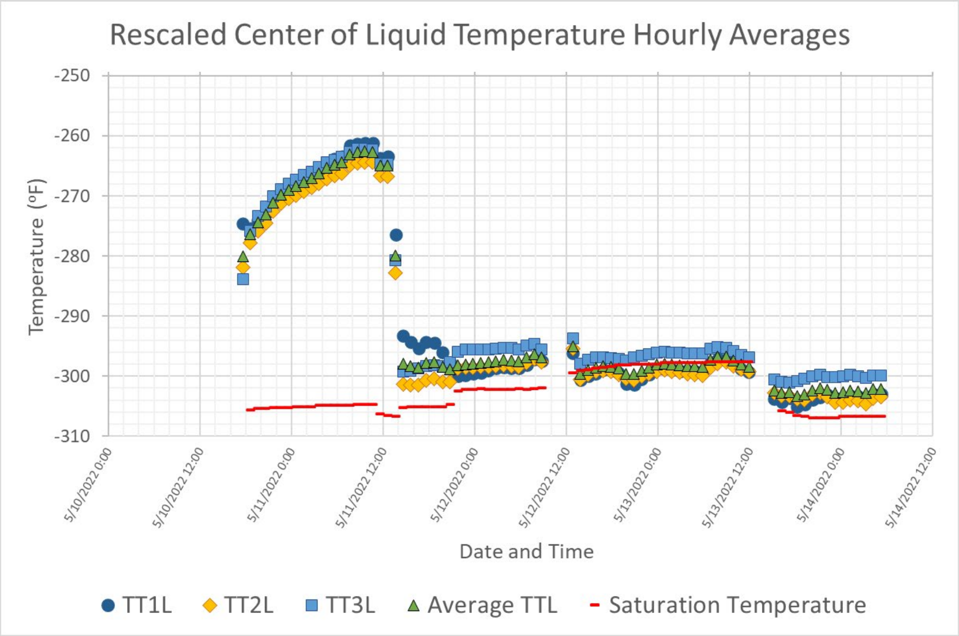

Figure G3. Rescaled Hourly Average Temperature from Thermocouples at Center of Liquid During Filling and Settling

Figure G4 shows a plot of the hourly average temperature measured by each of the three thermocouples (TT1VS, TT2VS, and TT3VS) positioned in the vapor space of the tank car, as well as the average of these three measurements for each hour and the saturation temperature for the pressure at that time. This figure shows that the initial temperature was consistent with the initial temperature measured by the thermocouples in the center of the liquid, as the tank was initially empty. The vapor space temperature initially decreased quickly as LN2 was introduced into the tank car, but the rate of change slowed after the initial decrease. The thermocouples in the vapor space recorded temperatures above the saturation temperature throughout the filling process, which is consistent with these transducers not being submerged in LN2.

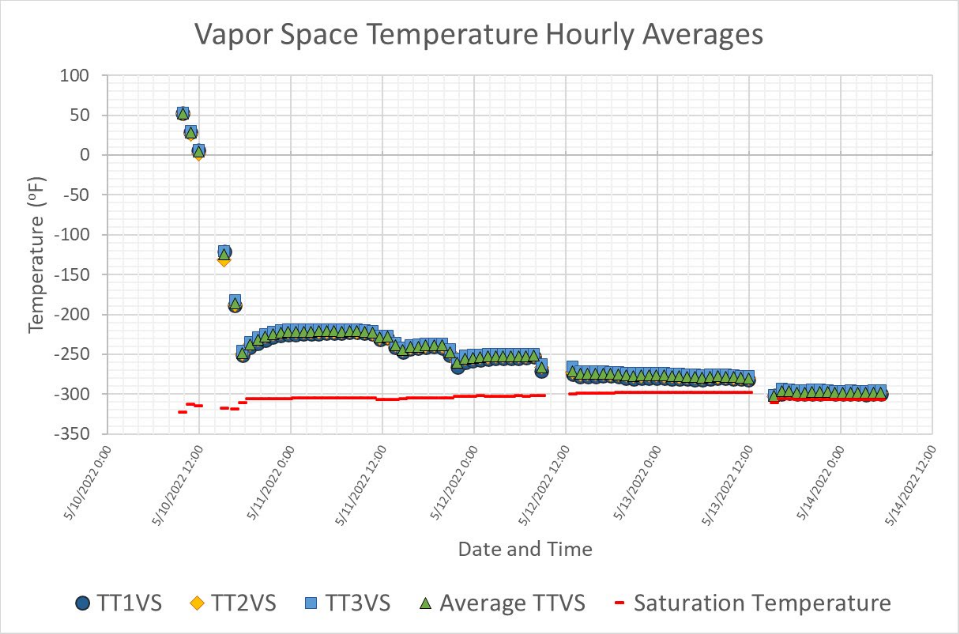

Figure G4. Hourly Average Temperature from Thermocouples in Vapor Space During Filling and Settling

Figure G5 contains a plot of the hourly average temperatures from the transducers at the top of the inner tank, the average of these three transducers, and the saturation temperature for reference.

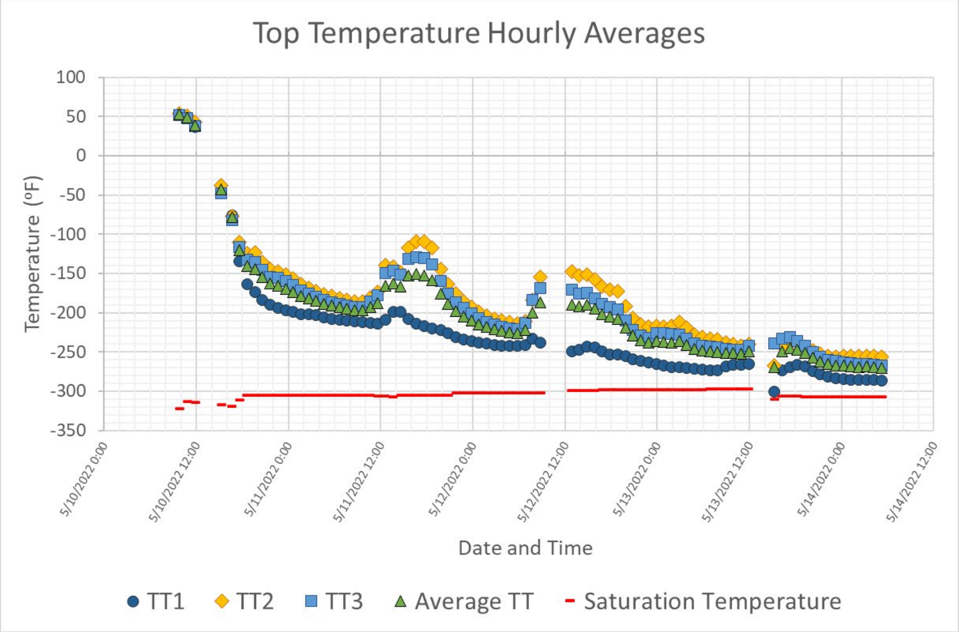

Figure G5. Hourly Average Temperature from Transducers at the Top of the Tank During Filling and Settling

Like the data from the temperature transducers in the vapor space and below the liquid, the initial temperature is consistent with the ambient temperature within the tank prior to the introduction of LN2. The transducers at the top of the tank measured daily increases in temperature that corresponded with increases in the outdoor temperature. For example, between noon and 6 PM on May 11 the average temperature increased by approximately 50 degrees Fahrenheit. This increase in temperature may be related to the transducers' location at the top of the tank near where passthroughs allow instrumentation and cables to pass into the sealed inner tank. These structures may introduce a path for heat to transfer from the exterior tank into the inner tank. Note that these structures were installed on the test car to facilitate the instrumentation used in this test and would not be installed on a typical DOT-113 tank car.

Figure G6 shows a plot of the lading weight in the tank car throughout the day prior to the test. The lading weight is taken as the sum of the four load cells supporting the tank car minus the empty weight of the tank car. Since the weight of the empty tank car has been subtracted from the total load cell measurements, this plot only represents the weight of the GN2 and LN2 that have been added to the tank car. As discussed previously, the tank was both filled and vented on this date (May 13) to decrease both the temperature and pressure of the N2 within the tank. The final weight measurement at 4:30 PM on the day before the test was 211,100 lbf.

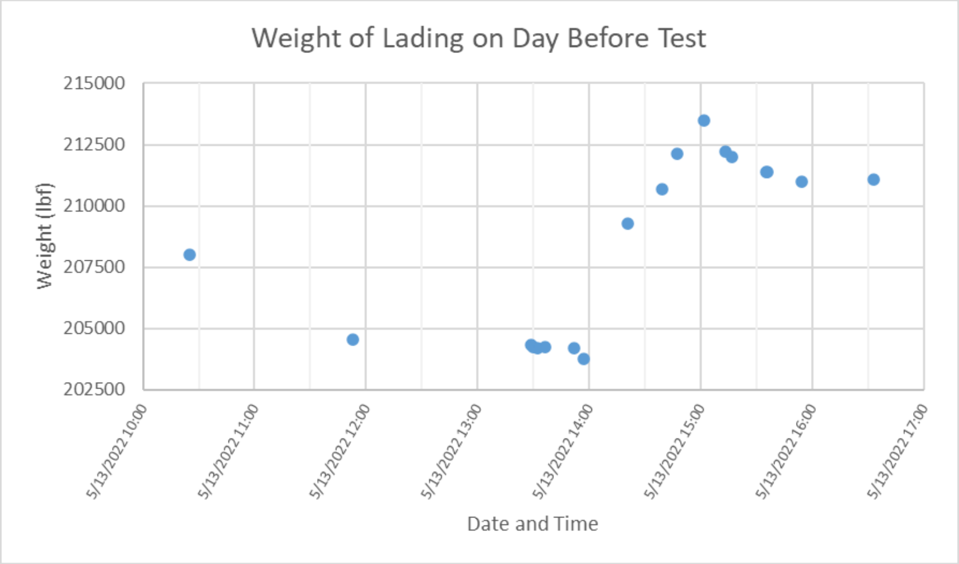

Figure G6. Total Weight of Lading in Tank on Day Before Test

The volume occupied by a given mass of liquid (and thus, the height of the liquid/vapor interface within the tank) depends on the density of the liquid. The density, in turn, depends on both the temperature and pressure of the liquid. In addition to the electronic instrumentation, the DOT-113 was also equipped with two mechanical level gauges (i.e., static head pressure gauges). These gauges used the differential pressure between the top and bottom of the tank to report the filling level in equivalent inches of water. Since LN2 has a lower density than water, a higher filling level of LN2 is necessary to generate the same differential pressure as reported by a gauge calibrated in inches of water. The mechanical gauge readings were recorded intermittently during the filling process as shown in Figure G7. The last reading recorded was 76.5 inches of water, taken on the morning of the test (May 14).

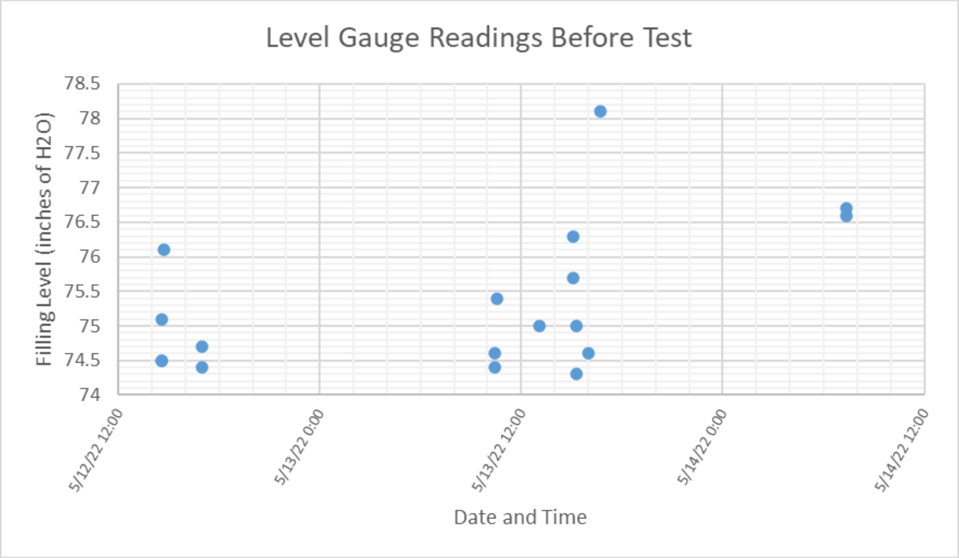

Figure G7. Filling Level Gauge Readings Before Test

Pressure measurements were recorded by the data acquisition system in the second before impact until 30 seconds after impact. The pressure measurements in the second before impact are shown in Figure G8 and the pressure measurements from 29 to 30 seconds post-impact are shown on the right side. In the second prior to impact the pressure measured by each transducer is stable, with some noise. At 29 seconds post-impact the pressures are still elevated above atmospheric pressure, but they are lower than the initial pressures. There is also a slightly negative slope in the post-impact measurements, indicating that the pressure is continuing to decrease as the punctured tank car drains. Each pressure transducer showed a consistent drop in pressure between the start of the test and after the test.

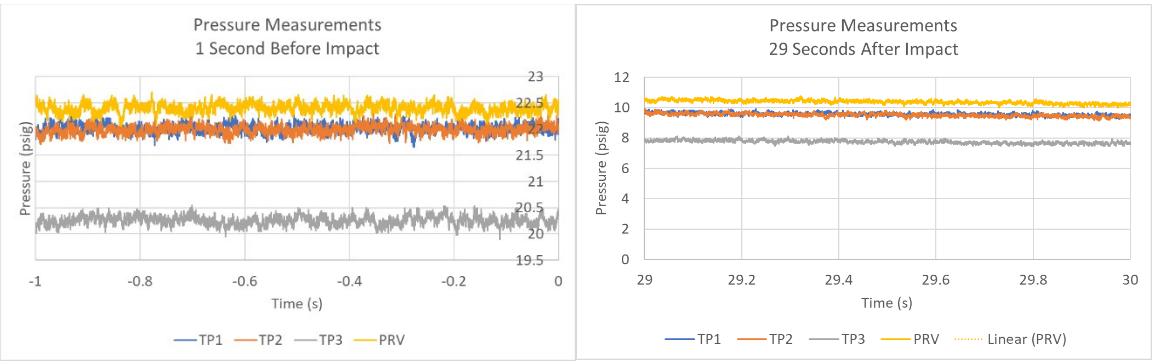

Figure G8. Pressure Measurements Recorded in the Second Before Impact (left) and Twenty-nine Seconds After Impact (right)

The temperature measurements made in the second leading up to impact are shown in Figure G9. While each transducer measured a stable temperature at its location, all the measured temperatures are once again above the saturation temperature at 22 psig [20]. A temperature above the saturation temperature is expected for the thermocouples in the vapor space (TT1VS, TT2VS, and TT23VS) and the combination gauges (TT1, TT2, and TT3). The temperature measurements below the liquid line (TT1L, TT2L, and TT3L) are suspicious since LN2 cannot exist at the measured temperatures and a pressure of 22 psig, but LN2 was known to exist within the tank. This means there is some inconsistency in the measured values of pressure and temperature inside the tank.

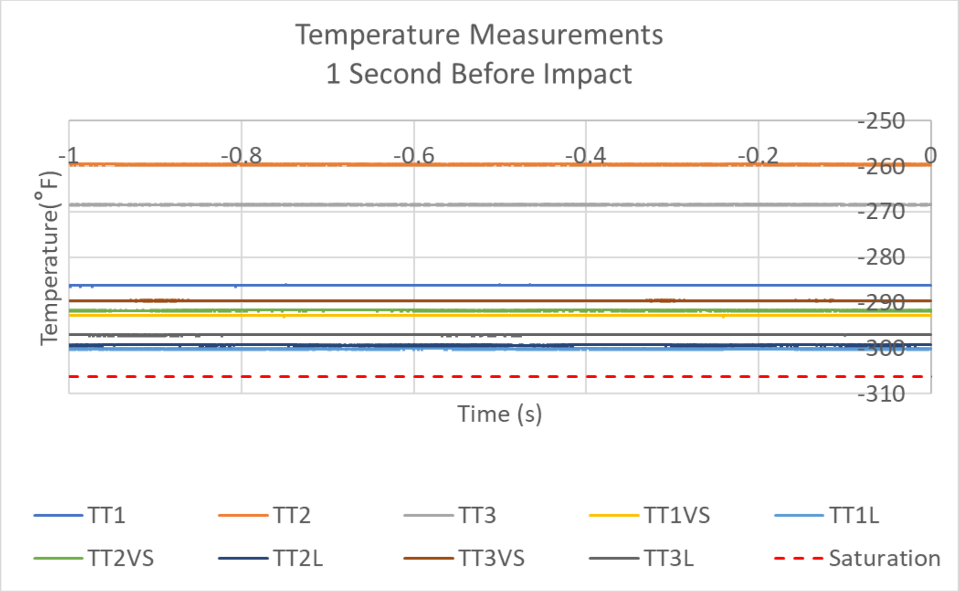

Figure G9. Temperature Measurements from Thermocouples Measured in the Second Prior to Impact

G1.1 Average Pre- and Post-test Measurements

The average pressures over the second before the time of impact and between 29 and 30 seconds after the impact are shown in Table G1. In the second before impact the conditions within the tank were stable, and the average value represents a steady-state value over the entire second. Between 29 and 30 seconds after impact, the tank was still actively draining. Therefore, the pressure within the tank was not at a steady value over the 1-second averaging window. The average value of pressure over this period was included in the table to illustrate that the difference in pressure was consistent over each measurement location, and to indicate that after 30 seconds the pressure had not yet returned to atmospheric pressure (i.e., 0 psig).

Table G1. Summary of Pressures Measured Before and After Impact

Channel	Before Impact	After Impact	Change
TP1	22.0 psig	9.6 psig	-12.4 psig
TP2	22.0 psig	9.5 psig	-12.5 psig
TP3	20.3 psig	7.7 psig	-12.5 psig
PRV	22.4 psig	10.4 psig	-12.0 psig
Average	21.7 psig	9.3 psig	-12.4 psig

Between 29 and 30 seconds after impact, the pressure had decreased by an average of 12.4 psi, but they had not yet decreased to 0 psig (i.e., one atmosphere). The difference between the initial and final pressures are also shown in Table G1. Overall, the change in pressure from beginning of impact to 30 seconds after is consistent for each transducer. The average pressure measured at the time of impact was approximately 22 psig and the average pressure between 29 and 30 seconds after impact was 9.3 psig. Regardless of its initial pressure, each pressure transducer measured a consistent pressure reduction of between 12.0 and 12.5 psi.

Researchers encountered several challenges while interpreting the temperature data from the nine temperature sensors inside the inner tank. Six thermocouples were installed at various positions inside the inner tank to determine the average bulk temperature of the LN2 and GN2. Three thermocouples were submerged below the liquid and three thermocouples were initially positioned within the vapor space. An additional three combination pressure and temperature transducers were installed at the very top of the vapor space. The locations of these thermocouples are shown in Figure 11 and Figure 12.

Test data were recorded for 30 seconds following the impact. This duration captured the impact event itself (approximately 1 second) and 29 seconds of the LN2 and GN2 response after impact. At 22 psig, LN2 can only exist at a temperature at or below the saturation temperature. All the recorded temperatures measured via thermocouple remained above the saturation temperature throughout the test, despite several thermocouples being installed below the liquid level of the inner tank.

The temperatures measured at each location averaged over the second before impact and between 29 and 30 seconds after impact are shown in Table G2 in Fahrenheit and Table G3 in Kelvin. In the second prior to impact the conditions within the tank were stable, while between 29 and 30 seconds after impact the tank was still draining. The temperature over the last second of measurement is therefore expected to fluctuate, while the temperature one second prior to impact is expected to remain relatively close to this average value. This table also shows the difference between the initial and final temperatures measured in each location.

Table G2. Average Temperatures Measured Before and After Impact in Fahrenheit

Channel	**Units**	**Average 1 second Before Impact**	**Average Value from 29-30 Seconds After Impact**	**Final – Initial Difference**
TT1	°F	−286.2	−303.1	−16.9
TT1VS	°F	−292.9	−314.0	−21.2
TT1L	°F	−300.2	−306.0	−5.8
TT2	°F	−259.6	−287.7	−28.1
TT2VS	°F	−291.7	−310.1	−18.4
TT2L	°F	−299.3	−312.4	−13.1
TT3	°F	−268.5	−286.3	−17.8
TT3VS	°F	−289.6	−310.8	−21.2
TT3L	°F	−297.1	−317.1	−20.0
Average – Top	**°F**	**−271.4**	**−292.4**	**−20.9**
Average – Vapor Space	**°F**	**−291.4**	**−311.6**	**−20.2**
Average – Liquid	**°F**	**−298.9**	**−311.8**	**−13.0**
Saturation Temperature [20]	**°F**	**~−306 (at 22 psig)**	**−314.5 (at 9 psig)**	**-**

Table G3. Average Temperatures Measured Before and After Impact in Kelvin

Channel	Units	Average 1 second Before Impact	Average Value from 29-30 Seconds After Impact	Final – Initial Difference
TT1	K	96.4	87.0	−9.4
TT1VS	K	92.7	80.9	−11.7
TT1L	K	88.6	85.4	−3.2
TT2	K	111.2	95.5	−15.6
TT2VS	K	93.3	83.1	−10.2
TT2L	K	89.1	81.8	−7.3
TT3	K	106.2	96.3	−9.9
TT3VS	K	94.5	82.7	−11.8
TT3L	K	90.3	79.2	−11.1
Average – Top	**K**	**104.6**	**92.9**	**−11. 7**
Average – Vapor Space	**K**	**93.5**	**82.3**	**−11.2**
Average – Liquid	**K**	**89.3**	**82.1**	**−7.2**
Saturation Temperature [20]	**K**	**~85.4 (at 22 psig)**	**~80.7 (at 9 psig)**	**-**

Researchers determined that the temperatures recorded within the inner tank could not be relied upon to describe the temperature of the LN2 since prior to impact the sensors reported temperatures at which LN2 could not exist, yet LN2 was known to exist within the tank. One possibility considered was that the surfaces of the thermocouples below the liquid level were not in contact with liquid, but rather with a thin film of vapor that had formed between the tank and the LN2. While the thermocouples do not appear to have malfunctioned, the temperatures measured prior to and during the test do not directly describe the conditions in the LN2.

There are several trends observable in the temperature data. First, at both the pre- and post-test periods the average temperature at each location (top, vapor space, and submerged in liquid) decreases moving from top to bottom. The bottom location was 27.4 °F (15.3 K) colder than the top location before the impact and 19.5 °F (10.8 K) colder after the impact. Prior to the test, the thermocouples in the vapor space and thermocouples in the liquid space had a much larger average temperature difference than after the test.

The average temperature at each location decreased between the second prior to impact and the period 29 to 30 seconds after impact. The difference in temperature was largest at the top of the tank, with the vapor space having only 0.7 °F (0.4 K) less of a temperature drop. Both locations were initially in the vapor space, surrounded by GN2. During the test, LN2 could have splashed or sloshed through the outage, or GN2 could have condensed into LN2 due to a pressure increase. In either case, cold LN2 would have been introduced onto thermocouples that had previously been surrounded by relatively warm GN2, causing a temperature drop over the course of the test.

At the same time, the average temperature measured by the thermocouples that were submerged under liquid also dropped during the test. Two possible behaviors may explain this measurement. First, the thermocouples submerged below the liquid were approximately midway through the height of the liquid phase. The data in Table G2 and Table G3 show a degree of thermal stratification from the vapor space to the liquid, where temperature decreases from the top of the tank to the thermocouples at the middle of the tank. If this stratification continued down to the bottom of the tank, the LN2 at the bottom of the tank would have been colder than the LN2 at the location of the submerged thermocouples. During the test the deformation of the tank could have led to mixing the LN2, dropping the temperature of the LN2 at the center of the tank, near the thermocouples.

Another possible explanation for this decrease in temperature at a location that was submerged below liquid involves a phase change. During the test, researchers believe GN2 condensed into LN2 due to the increase in pressure caused by the impactor reducing the tank's volume. Following puncture, the pressure within the tank decreased as the inner tank was exposed to atmosphere. Between 29 and 30 seconds after impact, the average pressure in the outage had decreased to 9.3 psig. This reduction in pressure could have caused some volume of LN2 to evaporate into GN2. As evaporation is an endothermic process, the bulk temperature of the LN2 that did not evaporate would have decreased.

G2. Post-test Estimate of Actual Filling Level

The critical value for input into the FE model is the height of the outage (i.e., the distance from the top of the tank to the liquid-vapor interface). Unfortunately, the measurements summarized in Table G1 cannot be used to directly determine the filling level because the combination of temperature and pressure corresponds to the inner tank being full of GN2, which is impossible based on the weight. The team determined that the average LN2 temperature measurement was incorrect and likely the result of a thin layer of vapor surrounding the submerged thermocouples. Researchers therefore had to bound the possible range of average LN2 temperature using the information that was available to estimate the filling level and subsequently the outage volume (See Table G4).

Table G4. Summary of Final Measurements of Lading Parameters Prior to Impact

Measurement	**Value**	**Date of Measurement**	**Reference**
Filling Level from Static Head Pressure Gauge	76.5 inches H2O	Day of test, morning	Figure G7
Weight of Lading from Load Cells	211,100 lbf[†]	Day before test, afternoon	Figure G6
Average LN2 Temperature	−298.9 °F[††] (89.3 K[††])	Day of test, averaged 1 second before impact	Figure G9
Average GN2 Pressure	22 psig	Day of test, averaged 1 second before impact	Figure G8

[†] Subjected to drift (see Section 2.2.1 and Section 4.6.3)

[††] Incorrect measurement due to vapor surrounding thermocouple

An additional source of uncertainty comes from the dimensions of the inner tank. At ambient temperature, the inner tank of the tested DOT-113 tank car had a volume of 34,500 gallons. Due to thermal contraction the tank has a lower volume when filled with cryogenic liquid. A pre-test simulation was used to estimate the volume of the tank when cooled to −320 °F (77.6 K), the saturation temperature of LN2 at atmospheric pressure. This pre-test model produced a cold tank volume of 34,150 gallons, or approximately 1 percent less than the warm volume. While this decrease in volume is not substantial compared to the total volume of the tank, this change in volume is a substantial difference compared to the target outage volume of 5 percent. The cold-temperature tank also had an inner diameter of approximately 106.7 inches, slightly less than the diameter at ambient temperatures.

To bound the possible outage volume, the team estimated the

(1) **maximum outage volume** using the height of the trycock which was known to be submerged in LN2 and

(2) **minimum outage volume** using the lowest possible density of LN2 at its saturation temperature.

The height of the trycock (96.2 inches in the chilled tank) corresponds to an outage volume of 5 percent. The density of LN2 would need to be 6.591 lbf/gal (789.8 kg/m^3) to achieve this filling level using the geometry of the chilled inner tank. The team therefore proposed that this was the maximum possible density of LN2 prior to the test because they checked the trycock valve and verified that liquid was ejected. At a pressure of 22 psig, the temperature that corresponds to this maximum density is −314 °F (80.9 K) which is 8 °F (4.5 K) below the saturation temperature. This is physically reasonable, as liquids can exist at temperatures below their saturation temperature.

At the measured pressure of 22 psig, N2's saturation temperature is −306 °F (85.4 K). This is the highest temperature that LN2 can be assuming that the pressure measurement is correct. Therefore, LN2 has a minimum density of approximately 6.413 lbf/gal (768.5 kg/m^3) [20]. Using this density, the filling level can be calculated using the measurement from the static head pressure gauge or the weight from the load cells.

While the trycock height (i.e., maximum outage volume) was used to calculate the minimum temperature (i.e., maximum density) of LN2, the team used the reverse calculation for the minimum outage volume. Table G5 shows the maximum and minimum initial outage volume. The team calculated the minimum outage volume using the filling gauge because the load cells experienced drift. The filling gauge (3 percent outage) resulted in a more extreme estimate of the minimum outage volume compared to the load cells (3.5 percent outage), which was beneficial in attempting to bound the possible outage volume.

Table G5. Minimum and Maximum Outage Volume Estimates

Case	**Assumed LN2 Temperature**	**Density of LN2** [20]	**Filling Level Height**	**Outage Height**	**Outage Volume**
Minimum Outage	−314 °F (80.9 K)	6.413 lbf/gal (768.5 kg/m^3)	99.5 inches	7.2 inches	~3%
Maximum Outage	−306 °F (85.4 K)	6.591 lbf/gal (789.8 kg/m^3)	96.2 inches	10.5 inches	~5%

To summarize, there was uncertainty in the outage volume due to inaccurate measurement of the average LN2 temperature even though the initial pressure was credible. The outage volume was estimated to be between 3 percent, based on the filling volume gauge assuming saturated LN2, and 5 percent, based on the lowest LN2 height that could produce liquid from the trycock.

Abbreviations and Acronyms

ACRONYM	DEFINITION
AAR	Association of American Railroads
ASTM	American Society for Testing and Materials
B-W	Bao-Wierzbicki
CFC	Channel Frequency Class
DB	DogBone
DOF	Degrees-of-Freedom
DOT	Department of Transportation
EOS	Equations of State
FE	Finite Element
FEA	Finite Element Analysis
FRA	Federal Railroad Administration
HD	High Definition
HHFT	High-hazard Flammable Trains
HMR	Hazardous Materials Regulations
HS	High-speed
LIDAR	Light Detection and Ranging
LNG	Liquefied Natural Gas
MLI	Multi-layer Insulation
MMC	Modified Mohr Coulomb
MPC	Multi-Point Constraint
NPRM	Notice of Proposed Rulemaking
PEEQ	Plastic Equivalent
PHMSA	Pipeline and Hazardous Materials Safety Administration
PRV	Pressure Relief Valve
PWHT	Post-weld Heat Treated
QS	Quasi-Static
RA	Reduction in Area

ACRONYM	DEFINITION
SAE	Society of Automotive Engineers
SCFM	Standard Cubic Feet per Minute
SPH	Smoothed Particle Hydrodynamics
SRB	Smooth Round Bar
SSC	Shell-to-solid Coupling
STD	Start-to-discharge
TC	Transport Canada
TRIAX	Stress Triaxiality
TTC	Transportation Technology Center
TTCI	Transportation Technology Center, Inc. (now MxV Rail)
UTS	Ultimate Tensile Strength
Volpe	Volpe National Transportation Systems Center
YS	Yield Strength